Alleviation of the Response of Slender Bridges to Wind Action Using Different Types of Controlled Actuators

by

Arno Kirch

born 10 April 1974

from Zell (Mosel), Germany

Dissertation submitted to and approved by the Department of Architecture, Civil Engineering and Environmental Sciences of the University of Braunschweig - Institute of Technology and the Department of Civil and Environmental Engineering of the University of Florence in candidacy for the degree of a Doktor-Ingenieur (Dr.-Ing.) / Dottore di Ricerca in Mitigation of Risk due to Natural Hazards on Structures and Infrastructures*)

Submitted on	6 March 2013
Oral examination on	22 April 2013
Professorial advisors	Prof. Udo Peil Prof. Claudio Borri

*) Either the German or the Italian form of the title may be used.

Schriftenreihe des Instituts für Stahlbau

Heft 1

Arno Kirch

Alleviation of the Response of Slender Bridges to Wind Action Using Different Types of Controlled Actuators

Shaker Verlag
Aachen 2014

Bibliografische Information der Deutschen Nationalbibliothek
Die Deutsche Nationalbibliothek verzeichnet diese Publikation in der Deutschen Nationalbibliografie; detaillierte bibliografische Daten sind im Internet über http://dnb.d-nb.de abrufbar.

Zugl.: Braunschweig, Techn. Univ., Diss., 2013

ISBN 978-3-8440-2479-1
ISSN 2198-8722

Shaker Verlag GmbH • Postfach 101818 • 52018 Aachen
Telefon: 02407 / 95 96 - 0 • Telefax: 02407 / 95 96 - 9
Internet: www.shaker.de • E-Mail: info@shaker.de

'*... nondum omnium dierum solem occidisse.*'

Philip II of Macedonia (Livy, Ab urbe condita, 39, 26, 9)

Preface

This doctoral thesis was written during the final period of my employment at the Institute of Steel Structures of the Technische Universität Braunschweig. Preliminary studies were financed by the German Research Foundation (DFG), when I was a member of an Italo-German research training group. I started investigating controlled aeroelastic systems at the Hamburg University of Technology.

Prof. Udo Peil deserves my gratitude first and foremost. Under his supervision and as a part of his wind-engineering research group, all the knowledge and freedom were offered to me that are essential for writing a reasonable dissertation. His continuous technical and non-technical support and advice facilitated my research significantly.

Furthermore, I would like to thank Prof. Klaus Thiele. He gave me the opportunity to finish my work at Braunschweig. Additionally, he took on the stressful role of chairman of my examination board. I am also very grateful to Prof. Claudio Borri for being my Italian tutor and for his cordial hospitality during my stay at the University of Florence. Especially at the beginning of my membership in the international research training group, his support was very valuable. Further thanks go to Prof. Dieter Dinkler, Prof. Gianni Bartoli, and Prof. Francesco Ricciardelli for being members of my examination board.

At the Institute of Steel Structures, I particularly appreciated the pleasant and relaxed atmosphere among the colleagues of the scientific and the non-scientific staff. This was the basic prerequisite for a wonderful time and a lot of very productive technical discussions. Above all, I would like to mention the helpful collaboration with Mr Hodei Aizpurua Aldasoro, Dr Mathias Clobes, Mr Thomas Höbbel, and Dr Tobias Wagner concerning topics of wind engineering and structural dynamics. The Italo-German research training group, on the other hand, has provided a fantastic framework not only for the scientific work but also for an intercultural exchange among the doctoral candidates. In this respect, I have really treasured the contact to Dr Claudio Mannini, Dr Enzo Marino, Dr Antonino Marra, and Dr Chiara Pozzuoli.

Finally, I would like to thank my former colleagues Dr Thomas Löhning and Mr Jochen Schenk for the long-lasting friendship. Besides that to my family and my native region, this contact has been an invaluable support during the last years.

Braunschweig, July 2013 Arno Kirch

Abstract

The theoretical work presented here describes how the dynamic characteristics of slender bridges under wind action can be improved through the use of controlled actuators. First, models for the aerodynamic forces are introduced that are based on linear time-invariant transfer elements. Hence, a force representation is available in both the time and the frequency domain. These models are similar to those of the aerodynamic forces acting on a flat plate in a theoretical potential flow. Therefore, the theoretical flat-plate forces are extensively reviewed and consistently presented within the framework of linear system theory. For a selection of bridge cross sections in real flow, measured coefficients of aerodynamic forces are taken from the technical literature.

Rational function approximations of the aerodynamic transfer functions allow for force representations with state-space models. On the basis of partial fraction expansions, general matrix-based rational function approaches are defined. Two approaches, which are commonly applied in aerospace and bridge engineering, are derived as special cases. Their suitability is limited for the variety of possible bridge cross sections. For an evaluation of the approximation quality, several parameter studies are conducted and comprehensively explained.

In the next step, a cable-stayed bridge is introduced as an example of a slender bridge structure. Two different spatial discretisations with element-wise and global shape functions are applied for modelling this bridge. The aeroelastic system as the combination of aerodynamic forces and the bridge structure is described in terms of a state-space model. Stability and transfer behaviour, the most important characteristics of the aeroelastic system, are theoretically investigated. Emphasis is laid on the effect of the rational function approximations on the quality of the results.

Reaction wheels, control moment gyroscopes, and aerodynamically effective flaps are employed as actuators. The state-space model of the aeroelastic system is extended in order to incorporate these devices. When the actuator motions are controlled in a closed loop, the system response to disturbances can be attenuated. For the controller design, classical algorithms of multivariable systems with state feedback are applied. Pole-placement design and linear-quadratic control lead to active controllers. A particular focus of the work is on finding fundamental limits for the stabilisation of the actuator-extended aeroelastic systems. Furthermore, the performance of the controlled system in a turbulent wind field is compared for the different types of actuators. In the last steps, the effect of state observers is investigated, a disturbance feedforward is analysed, and the feasibility of an integral control is explored.

Contents

Notation

If the variable of a matrix, which is always denoted with a bold letter, is used in normal font and not explicitly defined in another way, it represents an arbitrary element of the matrix. Matrix elements can be additionally specified with indices.

The term Eq. ( ) is not only used as a reference to a mathematical equation but rather as a placeholder throughout this work.

Greek Variables

α, α_j ..... torsional rotation

$\boldsymbol{\alpha}^{\mathrm{g}}$ ..... fluctuating wind velocities of the turbulent freestream wind field

β ..... real part of the reduced complex frequency

γ ..... specific weight

γ_j ..... negative value of a pole of the rational function approximation

δ ..... Dirac impulse with respect to the time t

$\bar{\delta}$ ..... Dirac impulse with respect to the reduced time $\bar{t}$

δ_{s} ..... logarithmic decrement of structural damping

$\theta_{\mathrm{fl},l}$, $\theta_{\mathrm{fl},l,j}$ ..... flap rotation

θ_{gy}, θ_{gy_j} ..... tilting angle of a gimbal

θ_{rw} ..... rotation angle of the reaction wheel

κ ..... variously used index

λ ..... variously used index

μ ..... variously used index

μ_j ..... mean of the physical quantity j

ν ..... kinematic viscosity

ν_μ ..... pole multiplicity of the rational function approximation

ξ_{e} ..... non-dimensional element coordinate

$\boldsymbol{\xi}_{\mathrm{c}}$ ..... actuator degrees of freedom

$\boldsymbol{\xi}_{\mathrm{s}}$ ..... structural degrees of freedom

$\boldsymbol{\xi}_{\mathrm{s}}^{\mathrm{a}}$ ..... aerodynamically effective structural degrees of freedom

ξ_a, $\xi_{\mathrm{a},j}$ ..... aerodynamic states of the rational function approximation

ρ ..... air density

σ ..... real part of the complex frequency

σ_j ..... standard deviation of a physical quantity

τ ..... time

$\bar{\tau}$ ..... reduced time

φ, φ_j ..... bending rotation

ϕ_coh ..... non-dimensional frequency for the coherence function

$\mathbf{\Phi}$ ..... modal matrix of the aeroelastic system

$\mathbf{\Phi}_\mathrm{s}$ ..... modal matrix of the undamped structural system

$\mathbf{\Psi}$ ..... block matrix for element properties

ω ..... imaginary part of the complex frequency

ω_s ..... eigenfrequency of the undamped structural system

Ω ..... global shape function

Ω_gy ..... spin speed of a rotor

$\mathbf{\Omega}^\mathrm{e}$, $\mathbf{\Omega}^\mathrm{e}_j$ ..... element shape function

$\mathbf{\Omega}^{\mathrm{g,e}}$ ..... element shape function for gust velocities

Latin Variables, Constants, and Numbers

$\mathbf{a}$ ..... transformation matrix

$\mathbf{a}_\chi$ ..... matrix for the coupling of the actuator degrees of freedom

$\mathbf{a}^\mathrm{g}$ ..... vector containing the gust velocities and their derivatives

$\mathbf{a}_\mathrm{Kü}$ ..... matrix for the transformation between aerofoil (Küssner & Göllnitz 1964) and bridge variables

$\mathbf{a}_\mathrm{Th}$ ..... matrix for the transformation between aerofoil (Theodorsen & Garrick 1941) and bridge variables

A ..... area

A^*_j ..... aerodynamic derivatives, i. e. aerodynamic coefficients of motion-induced aerodynamic forces, according to the notation in Simiu & Scanlan (1996)

$\mathbf{A}_j$, $\mathbf{A}_{\mu\kappa}$ ..... various coefficient matrices of the rational function approximation

$\mathbf{A}_\mathrm{sys}$ ..... system matrix of the system sys

b ..... half-width of the bridge-girder cross section

b_fl ..... half-width of the flaps

$\mathbf{B}_\mathrm{sys}$ ..... input matrix of the system sys

c ..... real part of the integration path of the inverse Laplace transform $\mathscr{L}_s^{-1}$

$\bar{c}$ ..... real part of the integration path of the inverse Laplace transform $\mathscr{L}_p^{-1}$

coh_w ..... coherence function of the vertical gust component w^{g} along the girder axis

C ..... consistent Theodorsen function

C_{coh} ..... wind-field parameter for the coherence function

$\bar{\mathbf{C}}$ ..... modified damping of the aeroelastic system

$\mathbf{C}_{\mathrm{ae}}$ ..... normalised aerodynamic derivative matrix, i. e. normalised aerodynamic coefficient matrix of motion-induced aerodynamic forces

$\mathbf{C}_{\mathrm{ae}}^{\mathrm{g}}$ ..... normalised aerodynamic coefficient matrix of gust-induced aerodynamic forces

$\mathbf{C}_{\mathrm{c}}$ ..... gyroscopic matrix

$\mathbf{C}_{\mathrm{r}}$ ..... output matrix of the integrated state variables

$\mathbf{C}_{\mathrm{s}}$ ..... structural damping

$\mathbf{C}_{\mathrm{sys}}$ ..... output matrix of the system sys

$\mathbf{C}_j^{\mathrm{uc}}$ ..... coefficients of the third-order system for the displacement input

$d_{\mathrm{h},j}$ ..... distance between the flap hinge and the middle of the flap cross section

$\mathbf{d}_{\mathrm{ae}}^{\mathrm{g}}$ ..... gust-induced aerodynamic forces

$\mathbf{d}_{\mathrm{ae}}^{\mathrm{s}}$ ..... static aerodynamic forces that are not represented by $\mathbf{f}_{\mathrm{ae}}$ and $\mathbf{d}_{\mathrm{ae}}^{\mathrm{g}}$

D ..... horizontal aerodynamic force

$\mathbf{D}, \mathbf{D}_j$ ..... various coefficient matrices of the rational function approximation

e ..... Euler's number

E ..... Young's modulus

$\mathbf{E}, \mathbf{E}_j$ ..... various coefficient matrices of the rational function approximation

$\mathbf{E}^{\mathrm{e,c}}$ ..... continuous structural element stiffness

$\mathbf{E}_{\mathrm{sys}}$ ..... input matrix of the system sys

f ..... arbitrary function

$\mathbf{f}$ ..... force

$\mathbf{f}_{\mathrm{ae}}$ ..... motion-induced aerodynamic forces

$\mathbf{f}_{\mathrm{c}}$ ..... force input of an actuator

$\mathbf{f}_{\mathrm{d}}$ ..... damping force

$\mathbf{f}^{\mathrm{e}}$ ..... element nodal forces

g ..... hysteretic damping factor

G ..... shear modulus

$\mathbf{G}_{\mathrm{ae}}$ ..... transfer function or impulse response of motion-induced aerodynamic forces

$\mathbf{G}_{\mathrm{ae}}^{\mathrm{g}}$ ..... transfer function or impulse response of gust-induced aerodynamic forces

$\mathbf{G}_{\mathrm{mod,j}}$ ..... modification matrix of the closed-loop transfer function due to the observer

$\mathbf{G}_{\mathrm{sys}}$ ..... transfer function or impulse response of the system sys

h, h_j ..... vertical bending displacement

H_j^* ..... aerodynamic derivatives, i. e. aerodynamic coefficients of motion-induced aerodynamic forces, according to the notation in Simiu & Scanlan (1996)

i ..... imaginary unit

I ..... mass moment of inertia of the bridge girder per unit length with respect to the centre of gravity of the girder cross section

I_φ ..... area moment of inertia of the bridge girder

I_{fl} ..... double moment of inertia of a flap

$I_{\mathrm{gy,h}}$, $I_{\mathrm{gy,l}}$ ..... double moments of inertia of a rotor

$I_{\mathrm{rw,h}}$, $I_{\mathrm{rw,l}}$ ..... moments of inertia of a reaction wheel

I_{t} ..... torsional moment of inertia of the bridge girder

$\mathbf{I}$ ..... identity matrix

j ..... variously used index

J ..... total least-squares approximation error

J_{m}^2 ..... joint acceptance function

k ..... imaginary part of the reduced complex frequency

K ..... Küssner function

K_j ..... Bessel functions of the second kind and integer order j

$\mathbf{K}$ ..... controller matrix

$\bar{\mathbf{K}}$ ..... modified stiffness of the aeroelastic system

$\mathbf{K}_{\mathrm{d}}$ ..... feedforward controller matrix

$\mathbf{K}^{\mathrm{e}}$ ..... structural element stiffness

$\mathbf{K}_{\mathrm{I}}$ ..... proportional-integral controller matrix

$\mathbf{K}_{\mathrm{r}}$ ..... controller matrix for the feedback of the integrator state

$\mathbf{K}_{\mathrm{s}}$ ..... structural stiffness

$\mathbf{K}_{\mathrm{sys}}^{\infty}$ ..... zero frequency or static gain of the system sys

l ..... variously used index

l_{b} ..... length of the bridge girder

l_{e} ..... element length

L ..... total vertical aerodynamic force

L_{wx} ..... integral length scale of the vertical gust component w^{g} along the girder axis

$\mathbf{L}$ ..... observer feedback matrix

m ..... mass of the bridge girder per unit length

m_{fl} ..... double mass of a flap

m_{gy} ..... mass of a twin control moment gyroscope

m_{rw} ..... mass of a reaction wheel

M ..... total aerodynamic moment around the centre of the bridge girder

$M_{\mathrm{fl},j}, M_{\mathrm{fl},j,l}$ .... hinge moments between girder and flaps

M_{gy} ..... difference between the torques on the gimbals

$M_{\mathrm{gy},j}$ ..... torque on a gimbal

M_j ..... aerodynamic moment acting on the flap around its hinge

M_{rw} ..... moment between the reaction wheel and the bridge girder

$\bar{\mathbf{M}}, \bar{\bar{\mathbf{M}}}$ ..... modified mass of the aeroelastic system

$\mathbf{M}_{\mathrm{c}}$ ..... actuator mass

$\mathbf{M}_{\mathrm{c}}^{\mathrm{e}}$ ..... element mass of the flaps

$\mathbf{M}_{\mathrm{c}}^{\mathrm{e,c}}$ ..... continuous element mass of the flaps

$\mathbf{M}^{\mathrm{e}}$ ..... structural element mass

$\mathbf{M}^{\mathrm{e,c}}$ ..... continuous structural element mass

$\mathbf{M}_{\mathrm{s}}$ ..... structural mass

n_γ ..... number of different poles of the rational function approximation

n_k ..... number of reduced frequencies where the original aerodynamic admittance is available

N ..... static axial force

p ..... reduced complex frequency or index for the $\mathscr{L}_p$ domain

p ..... horizontal displacement of the bridge-girder cross section

$\mathbf{p}^{\mathrm{e}}$ ..... external distributed element loads

P ..... power

P_j^* ..... aerodynamic derivatives, i. e. aerodynamic coefficients of motion-induced aerodynamic forces, according to the notation in Sarkar & al. (1994)

q_0 ..... factor to normalise aerodynamic force coefficients

$\mathbf{Q}$ ..... normalised admittance of motion-induced aerodynamic forces, i. e. matrix of normalised aerodynamic derivatives, or its corresponding impulse response

$\mathbf{Q}^{\mathrm{e}}$ ..... normalised element admittance of motion-induced aerodynamic forces or its corresponding impulse response

$\mathbf{Q}^{\mathrm{g}}$ ..... normalised admittance of gust-induced aerodynamic forces or its corresponding impulse response

$\mathbf{Q}^{\mathrm{g,e}}$ ..... normalised element admittance of gust-induced aerodynamic forces or its corresponding impulse response

$\mathbf{Q}_{\mathrm{lqr}}$ ..... state weighting of the lqr design

$\mathbf{Q}^{\mathrm{s}}$ ..... vector of normalised coefficients of static aerodynamic forces

r_j ..... arbitrary variable

r_{rw}, r_{gy} ..... rotor radii

$\mathbf{r}_{\mathrm{st}}$ ..... measurement noise in the output

Re ..... Reynolds number

$\mathbf{R}$, $\mathbf{R}_j$ ..... various pole matrices of the rational function approximation

$\mathbf{R}_{\mathrm{lqr}}$ ..... input weighting of the lqr design

s ..... complex frequency or index for the $\mathscr{L}_s$ domain

S ..... consistent Sears function

$\mathbf{s}^{\mathrm{e}}$, $\mathbf{s}^{\mathrm{e}}_j$ ..... element nodal forces

$\mathbf{S}$ ..... spectral density matrix

t ..... time

$\bar{t}$ ..... reduced time

$\mathbf{t}^{\mathrm{e}}$ ..... external nodal element loads

T ..... length of the finite sample function of an ergodic stochastic process

$T_{\mathrm{Kü}}$ ..... wake-vortex function

$\mathbf{T}_j$ ..... permutation matrix

u^{g} ..... fluctuating horizontal wind velocity

$\mathbf{u}_{\mathrm{c}}$ ..... displacement input of the actuator equipped aeroelastic system

$\mathbf{u}^{\mathrm{e}}$ ..... continuous element displacements

$\mathbf{u}^{\mathrm{g,e}}$ ..... continuously distributed gust velocities

$\mathbf{u}_{\mathrm{ob}}$ ..... observer input

U ..... constant reference wind velocity

$\mathbf{v}^{\mathrm{e}}$, $\mathbf{v}^{\mathrm{e}}_j$ ..... element nodal displacements

$\mathbf{v}^{\mathrm{g,e}}$ ..... discretised element gust velocities

w^{g}, w^{g}_j ..... fluctuating vertical wind velocity

$w_{jl\lambda}$ ..... weights of the least-squares approximation

W ..... Wagner function

x, y, z ..... coordinates

$\mathbf{x}_{\mathrm{c}}$ ..... actuator state of the actuator-equipped aeroelastic system with a displacement input

$\mathbf{x}_\mathrm{r}$ ..... integrator state

$\mathbf{x}_\mathrm{sys}$ ..... state of the system sys

$\mathbf{y}_\mathrm{sys}$ ..... output vector of the system sys

Other Symbols

$|\ |$, arg( ) ..... absolute value and argument of a complex variable

Re( ), Im( ) ... real and imaginary part of a complex variable

diag( ) ..... main diagonal blocks of a block diagonal matrix

d ..... differential operator

Δ ..... difference

$\mathscr{F}$ ..... Fourier transform

$\mathscr{F}^{-1}$ ..... inverse Fourier transform

$\mathscr{L}$ ..... Laplace transform

$\mathscr{L}^{-1}$ ..... inverse Laplace transform

$\circ\!\!-\!\!\bullet$ ..... symbol connecting corresponding time domain $\circ$ and frequency domain $\bullet$ functions

$\overset{t}{*}$ ..... convolution with respect to time t

$\overset{\bar{t}}{*}$ ..... convolution with respect to the reduced time $\bar{t}$

$\dot{(\ )}$, $\overset{(j)}{(\ )}$ ..... generalised differentiation with respect to time t

$(\ )'$, $(\ )^{(j)}$ ..... generalised differentiation with respect to the reduced time $\bar{t}$

$(\ )^\mathrm{c}$ ..... complex conjugate

$(\ )^\mathrm{T}$ ..... transpose of a matrix

$(\ )^0$ ..... special value of a variable

$\overline{(\ )}$ ..... arithmetic mean

$\breve{(\ )}$ ..... eigenvector

$\hat{(\ )}$ ..... amplitude of a harmonic motion

$\tilde{(\ )}$ ..... alternative definition of a variable

Abbreviations

2d ..... two dimensional

3d ..... three dimensional

as ..... index for the state-space model of the aeroelastic system

asg ..... index for the state-space model of the aeroelastic system including the state-space model of the gust forces

asu ..... index for the state-space model of the actuator-equipped aeroelastic system with a displacement input

A, B, C, etc. ... hinge positions of the flaps
b ..... bending
cl ..... index for the closed-loop system matrix
fl ..... flap
g ..... bridge girder
gy ..... control moment gyroscope
I ..... index for a system that is extended with an integrator part
Kü ..... abbreviation for aerodynamic forces according to Küssner & Göllnitz (1964) or index for variables used in this reference
lee ..... index for leeward variables
le, mi, ri ..... indices for a value of a finite element at $x = 0$, $x = l_e/2$, and $x = l_e$, respectively
lqr ..... linear-quadratic regulator
m ..... index for modal variables
max ..... maximum value
min ..... minimum value
ob ..... index for the observer state and output
oga, sga ..... kinds of gaps between bridge and flaps
o ..... index for original, not approximated data
pl ..... index for a quantity per unit length of an otherwise discrete actuator property
red ..... index for reduced degrees of freedom in the case of kinematic couplings
ref ..... index for a reference value when finite elements with different properties b and U are used
rel ..... index for the relative difference
rfa ..... rational function approximation according to the Roger or Karpel approach in combination with the identification procedure described in Section 3.4
rw ..... reaction wheel
sd, od ..... kinematic couplings between windward and leeward flaps
st ..... index for the state-space model of the structural system
t ..... torsion
TaS, ChS, etc. .. abbreviations for the idealised cross sections given in Figure 2.7
Th ..... abbreviation for aerodynamic forces according to Theodorsen & Garrick (1941) or index for variables used in this reference
uc ..... index for the state-space model of the third-order system for the displacement input
win ..... index for windward variables

1 Introduction

1.1 Motivation and Research Objectives

Bridges with slender girders are sensitive structures which can considerably respond to a variety of impacting loads. Examples are cable-stayed bridges and suspension bridges, whose girders are supported by thin tension elements within their column-free span. In addition to their flexibility, these bridges usually exhibit only a low structural damping, which makes them extremely prone to vibration problems. Both long-span road bridges and filigree pedestrian bridges are affected. Especially the vibration behaviour under wind action can crucially determine their design. Not only static displacements and vibration amplitudes have to be limited but also aeroelastic instabilities must be avoided. Particularly the flutter phenomenon is supposed to be the reason for several bridge collapses during the nineteenth century. Nevertheless, it was not until some time after the famous collapse of the first Tacoma Narrows Bridge / USA in 1940 that this instability phenomenon was recognised to be important for the design of slender bridges. In bridge engineering, there is a broad consensus that aeroelastic instabilities according to a linear theory must be avoided even if a non-linear theory or an experiment indicate limited displacements or limit cycle oscillations. Currently, the commonly applied methods to prevent flutter vibrations are to provide a sufficiently high torsional girder stiffness or to streamline the shape of the girder cross section. Early examples of bridges with these girders are the second Tacoma Narrows Bridge and the Severn Bridge / UK, respectively. In the context of streamlining, the latest executed idea is to split the girder into separated streamlined boxes, as done for the Xihoumen Bridge / China in the form of a twin deck. A comprehensive overview of the history of long-span suspension bridges against the background of bridge flutter is given in Scott (2001). As foreseeable, the foregoing methods reach their limits for very slender bridges.

To overcome these limits, a number of sophisticated techniques have been proposed in the past. With the help of controlled actuators, additional forces can be systematically imposed on the bridge to improve its dynamic characteristics. In theoretical investigations (e. g. Miyata & al. 1994), external forces are often applied without sufficiently accounting for their origin. Due to the inherent function of a bridge to span a distance without a contact to the ground, only the use of specific actuating elements is allowed. The theoretical work presented here describes three different types of actuators and investigates their capabilities. For the controller design, their

dynamic behaviour must be explicitly taken into account. The investigations are structured as follows. Further sections of the introduction briefly explain the risk management framework and address special aspects of mechanics and mathematics. In Chapter 2, models of the aerodynamic forces are defined. Chapter 3 describes the mathematically advantageous approximation of the aerodynamic transfer function with rational functions. A cable-stayed bridge is modelled in Chapter 4 as an aeroelastic system and its dynamic characteristics are examined. Chapter 5 starts with an introduction of the actuators. Subsequently, controllers are determined and the controlled aeroelastic systems are analysed.

Although structural control is a relatively young discipline, there are a large number of publications in this field. For initial reading, Housner & al. (1997), Preumont & Seto (2008), and Preumont (2011) are recommendable references. Control theory, moreover, is an interdisciplinary branch of engineering and mathematics. The methods developed in numerous fields of engineering have to be applied to analyse a controlled aeroelastic system. For a limitation of the investigations presented in this work to an acceptable degree, the chosen models and numerical examples only cover those system parts which are considered to be decisive for a phenomenological investigation of a controlled bridge within streaming air. An experimental check of the theoretical results, as obligatory in natural sciences, still needs to be done.

In advance, some of the gained insights have already been published in a shortened form (e. g. Kirch & Peil 2009, Kirch & Peil 2011, Kirch & Peil 2012). The revealed shortcomings of later cited publications of other authors are usually not mentioned because an appropriate, well-founded review would go far beyond the scope of this work. It is up to the reader to compare the models and results of the work presented here with those of other researchers.

1.2 Integration into the Risk Management Framework

Natural hazards like storms, earthquakes, and floods can lead to significant losses in an affected system. For civil engineering purposes, the term risk management framework describes a general approach to assess, compare, and treat the consequences of the impacting hazards. Definitions of technical terms that are used in this context vary in the technical literature. Risk management principles and guidelines for general applications are codified in ISO 31000 (2009). Moreover, a framework and a glossary for civil engineering problems were developed by members of the International Research Training Group 802 of the German Research Foundation (DFG) (Pliefke & al. 2007). Besides the latter tools, statements given in Augusti & al. (2001) are used to roughly explain the risk management framework in the following paragraphs for wind-loaded slender bridges. A detailed analysis, however, is not performed here.

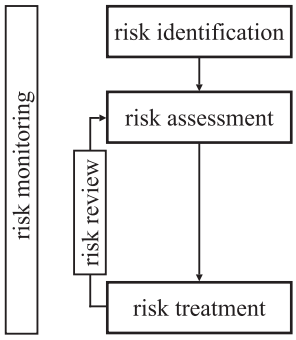

Figure 1.1: Risk management framework (Pliefke & al. 2007).

The natural wind, which is the relevant hazard in this work, can cause major losses. Currently, statistical data is provided online by the NatCatSERVICE database of the Munich Reinsurance Company (Munich RE), for instance. Within the period 1980–2012, 40 % of the overall losses and even 72 % of the insured losses due to natural catastrophes worldwide originated from meteorological events, according to that database. This is much more than the losses caused by other natural events. Geophysical events like earthquakes, tsunamis, and volcanic eruptions, which come in second, have a percentage of 25 % and 11 %, respectively. Concerning fatalities, wind events cause 19 % of the total number, which is a bit behind those due to climatological (32 %) and geophysical (39 %) events. These few numbers indicate the importance of considering wind events and their consequences for a coordinated application of the usually limited resources of a society.

Figure 1.1 shows the three major steps of the risk management framework, which are connected as a chain. The risk identification step defines what can happen and where. The system under consideration cannot only be the bridge itself and its structural components but also a whole region that is influenced by the bridge as a component of the infrastructure. System parts are called elements at risk. The natural wind as a source of an event that can negatively affect the system is called hazard.

Details of the risk assessment step, which is the second step of the risk management chain, are displayed in Figure 1.2. Risk assessment consists of the risk analysis and the risk evaluation phase. Results that are obtained with probabilistic methods can be illustrated with exceedance probability curves, for instance. First, the hazard is analysed with an intensity measure per time unit like the 10 min average wind speed that is exceeded per time unit. Exposure factors can weight the impact of the hazard on different elements at risk due to local effects. The hazard is not constant in the long run. Against the background of global warming, an increase of the hazard cannot be excluded due to a higher number, or even an increasing intensity, of wind events. In the following steps, risk is quantified with a measure per time unit. The link between the risk measure and the hazard intensity is called the vulnerability of the system. Two substeps have to be distinguished. Structural risk, which is determined in the first substep, only covers the

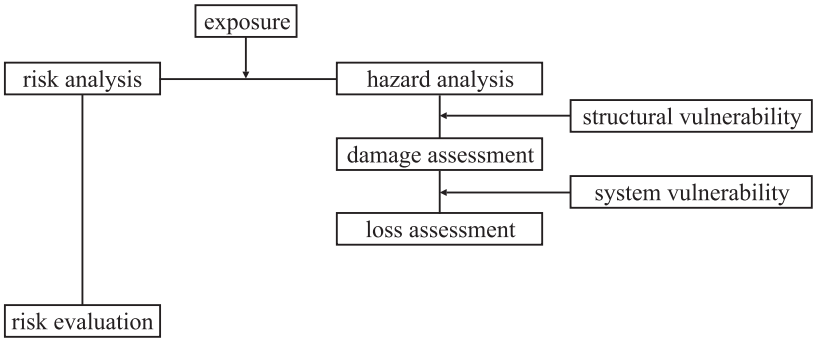

Figure 1.2: Risk assessment (Pliefke & al. 2007).

damage to the structure itself. It is described with a damage measure per time unit. Structural vulnerability, which is measured in damage per hazard intensity, links the structural risk to the hazard. For bridges, not only rare catastrophic storm events have to be considered that can lead to a collapse of the whole structural system or important parts of it. Also more frequent moderate wind events can cause structural damage in terms of fatigue problems, unacceptable vibration amplitudes, or traffic-disturbing conditions, for instance. In the second substep, the consequences of the structural damage are considered. Some consequences occur immediately after the damage arises, and others occur with a time shift. Examples for instantaneous consequences of a bridge collapse are the damaged structure and fatalities. If the bridge is a part of a traffic artery, a disruption due to a collapse usually has negative economic effects on a larger surrounding area. These effects depend on the local traffic situation and increase with the duration in which the gap exists. In contrast to the structural risk, the total risk covers all consequences and is described with an adequate loss measure per time unit. Usually a monetary unit is used for the loss. Loss and damage are linked by the system vulnerability of each element at risk. In the risk evaluation phase, different risks determined in separated risk analyses are made comparable. Moreover, risk classes based on individual risk perceptions are introduced.

The risk assessment results in the decision as to how the risk is treated in presence of other competing risks. Therefore, the third step of the risk management chain shown in Figure 1.1 is called risk treatment. Different reactions to the outcome of the risk assessment are possible. A low risk can simply be judged to be acceptable and no action is required. If the risk caused by a special project is considered to be far too high, the project and, thus, the risk can be rejected. Between these two extremes, there are two alternatives. Either the risk is transferred for instance to an insurance company or the risk is mitigated. For risk mitigation, pre-disaster and post-disaster interventions and combinations of them are possible. Technical prevention belongs to the first group of interventions. The application of controlled actuators to bridges for influencing their structural vulnerability, which is analysed in the work presented here, is an example of technical prevention.

Figure 1.1 contains two more elements. Risk monitoring means the information exchange among all persons who are involved in the risk management process. A risk review is necessary to include new information, knowledge, and experience after running through the risk management chain at least once. With such a review, the effectiveness of possibly implemented risk mitigation measures can be evaluated.

1.3 Employed Mechanics and Mathematics

The dynamic systems are analysed here with methods of the linear system theory. Concerning this branch of mechanics and mathematics, the textbooks Föllinger (2003), Lunze (2004), and Lunze (2005) have been primarily used. Some of these methods are based on the theory of complex functions, which is, for instance, dealt with in Remmert & Schumacher (2002). For problems in the field of structural mechanics, the contents of Gasch & Knothe (1987), Gasch & Knothe (1989), Clough & Penzien (1993), and Krätzig & Başar (1997) have been adopted. Different kinds of eigenvalue problems are studied in Zurmühl & Falk (1984). The contents of the books on control theory Lunze (2004) and Lunze (2005) have been mainly used concerning the manipulation of the system behaviour. All this textbook knowledge is usually applied without any citation. The developed or employed algorithms have been programmed and evaluated with the software MATLAB (2007).

To cite one of the pioneers of aeroelasticity almost literally: ‘Owing to the rather extensive field covered’ here ‘it has been considered necessary to omit many elementary proofs, it being left to the reader to verify certain specific statements’ (Theodorsen 1934). In the paragraphs below, some special mathematical aspects are explained that are used throughout this work.

All investigations of the following chapters are based on continuous-time descriptions of the flow and the structural systems. Two different time-domain variables are employed. The first one is the physical time t. Additionally, the second, the dimensionless or reduced time

$$\bar{t} = t\,U/b \tag{1.1}$$

is used in the sense of a substitution of variables. The constant reference wind velocity is denoted as U, and b is the nominal half-width of a typical bridge-girder cross section. A function f, which is unique in the time domain, can be described using the time t or the reduced time $\bar{t}$. The function value remains the same for both options. Depending on the used time variable, the differentiation is defined either as $(\dot{\ })$ with respect to time t or as

$$(\ )' = (\dot{\ })\,b/U \tag{1.2}$$

with respect to the reduced time $\bar{t}$. Higher derivatives of the order j are symbolised with $\overset{(j)}{(\ )}$ and $(\ )^{(j)}$, respectively. For the integration, similar aspects have to be taken into account.

$$\int_{\bar{t}_1=t_1 U/b}^{\bar{t}_2=t_2 U/b} f(\bar{\tau})\,\mathrm{d}\bar{\tau} = \int_{t_1=\bar{t}_1 b/U}^{t_2=\bar{t}_2 b/U} f(\tau)\,\mathrm{d}\tau\, U/b \tag{1.3}$$

All differentiations are considered as generalised if not otherwise specified. That means Dirac impulses are used if a jump discontinuity occurs in the time history of a physical quantity. Dirac impulses

$$\bar{\delta}(t) = \delta(t)\, b/U \tag{1.4}$$

are defined with respect to the used time-domain variable to ensure the following integrals.

$$\int_{-\infty}^{\infty} \delta(t)\,\mathrm{d}t = 1\ , \quad \int_{-\infty}^{\infty} \bar{\delta}(t)\,\mathrm{d}\bar{t} = 1 \tag{1.5}$$

Based on the two time-domain variables, two different unilateral Laplace transforms $\mathscr{L}_s$, $\mathscr{L}_p$ and accordingly two different frequency domains are defined.

$$\begin{aligned} f(t) &= f(\bar{t}) \\ &= \mathscr{L}_s^{-1}\{f_s(s)\} \\ &= \frac{1}{2\pi\mathrm{i}} \int_{c-\mathrm{i}\infty}^{c+\mathrm{i}\infty} f_s(s)\mathrm{e}^{ts}\,\mathrm{d}s \end{aligned} \quad \overset{t,s}{\circ\!\!-\!\!\bullet} \quad \begin{aligned} f_s(s) &= f_s(p) \\ &= \mathscr{L}_s\{f(t)\} \\ &= \int_0^{\infty} f(t)\mathrm{e}^{-st}\,\mathrm{d}t \end{aligned} \tag{1.6a}$$

$$\begin{aligned} f(t) &= f(\bar{t}) \\ &= \mathscr{L}_p^{-1}\{f_p(p)\} \\ &= \frac{1}{2\pi\mathrm{i}} \int_{\bar{c}-\mathrm{i}\infty}^{\bar{c}+\mathrm{i}\infty} f_p(p)\mathrm{e}^{\bar{t}p}\,\mathrm{d}p \end{aligned} \quad \overset{\bar{t},p}{\circ\!\!-\!\!\bullet} \quad \begin{aligned} f_p(p) &= f_p(s) \\ &= \mathscr{L}_p\{f(\bar{t})\} \\ &= \int_0^{\infty} f(\bar{t})\mathrm{e}^{-p\bar{t}}\,\mathrm{d}\bar{t} \end{aligned} \tag{1.6b}$$

The variable $s = \sigma + \mathrm{i}\omega$ is the complex frequency and

$$p = \beta + \mathrm{i}k = s\, b/U \tag{1.7}$$

its dimensionless or reduced version. Corresponding time-domain $\circ$ and frequency-domain $\bullet$ functions are connected with the symbol $\circ\!\!-\!\!\bullet$. The superscript variables indicate the variables

of the transform. The integration path of the inverse transform is a straight line parallel to the imaginary axis, and c or $\bar{c}$ must be located within the region of absolute convergence of the Laplace transforms. Within the two frequency domains, the frequency variables can be substituted according to Eq. (1.7). The two function values f_s and f_p are, however, not the same. Since the products $\bar{t}p$ and ts are equal, it follows from Eq. (1.6) that

$$\mathscr{L}_p^{-1} = \mathscr{L}_s^{-1}\, b/U \qquad \circ\!\!-\!\!\bullet \qquad \mathscr{L}_p = \mathscr{L}_s\, U/b \tag{1.8}$$

and thus

$$f_p = f_s\, U/b \quad . \tag{1.9}$$

The same variable is used for both the two frequency-domain versions and the time-domain representation of the function. If necessary, an index points to the special frequency domain.

Depending on the chosen time-domain variable, two different convolution integrals are possible.

$$f_1(t) \overset{t}{*} f_2(t) = \int_0^t f_1(\tau) \cdot f_2(t-\tau)\,\mathrm{d}\tau \qquad \overset{t,s}{\circ\!\!-\!\!\bullet} \qquad f_{1,s}(s) \cdot f_{2,s}(s) \tag{1.10a}$$

$$f_1(\bar{t}) \overset{\bar{t}}{*} f_2(\bar{t}) = \int_0^{\bar{t}} f_1(\bar{\tau}) \cdot f_2(\bar{t}-\bar{\tau})\,\mathrm{d}\bar{\tau} \qquad \overset{\bar{t},p}{\circ\!\!-\!\!\bullet} \qquad f_{1,p}(p) \cdot f_{2,p}(p) \tag{1.10b}$$

The convolution is abbreviated as a product with the operator $*$ and the superscript convolution variable. Eq. (1.10) additionally shows the corresponding products in the two frequency domains pursuant to the convolution theorem of Laplace transforms. Comparing Eq. (1.10a) with Eq. (1.10b) leads to

$$f_1(\bar{t}) \overset{\bar{t}}{*} f_2(\bar{t}) = f_1(t) \overset{t}{*} f_2(t)\, U/b \tag{1.11}$$

if the integration intervals correspond to each other. For the evaluation of the convolution integral, it should be noted that digital computers cannot work with Dirac impulses and generalised differentiations. For digital calculations, it is, thus, necessary to remove the Dirac impulses from the integrands, which leads to additional summands.

The unilateral Laplace transform is usually applied to solve the differential equation of a linear time-invariant transfer element. With the differentiation theorem, arbitrary non-zero initial conditions at $t = 0$ can be easily taken into account. This is a major advantage of the unilateral Laplace transform over the bilateral Laplace transform or the Fourier transform.

If the variables f_1 and f_2 denote zero-mean stationary stochastic processes in the time domain, the functions themselves and relations between them can be described by statistical properties

in terms of ensemble averages like correlation functions. If, moreover, the stochastic processes are ergodic, ensemble averages can be simply determined as time averages of individual sample functions or pairs of them. Let

$$\begin{aligned} f^T(t) &= \mathscr{F}^{-1}\{f^T(\mathrm{i}\omega)\} \\ &= \frac{1}{2\pi}\int_{-\infty}^{\infty} f^T(\mathrm{i}\omega)\mathrm{e}^{t\,\mathrm{i}\omega}\,\mathrm{d}\omega \end{aligned} \quad \overset{t,\mathrm{i}\omega}{\circ\!\!-\!\!\bullet} \quad \begin{aligned} f^T(\mathrm{i}\omega) &= \mathscr{F}\{f^T(t)\} \\ &= \int_{-\infty}^{\infty} f^T(t)\mathrm{e}^{-\mathrm{i}\omega t}\,\mathrm{d}t \end{aligned} \tag{1.12}$$

be the Fourier transform of a finite sample function of an ergodic stochastic process. As shown in Eq. (1.12), Fourier transforms are usually defined only with respect to the non-reduced frequency-domain variable ω. The finite sample function is recorded during a time interval $[-T/2;T/2]$, which is indicated with the superscript $(\ )^T$. In the frequency domain, the two-sided spectral density function S, which is the Fourier transform of the correlation function, can also be determined as the following limit.

$$S_{f_1 f_2} = \lim_{T\to\infty}\left(\frac{1}{T}(f_1^T(\mathrm{i}\omega))^{\mathrm{c}} f_2^T(\mathrm{i}\omega)\right) \tag{1.13}$$

The superscript $(\ )^{\mathrm{c}}$ indicates the complex conjugate. Based on this definition with Fourier transforms, the spectral density function between the derivatives of f_1 and f_2 can be found as

$$S_{f_1^{(j)} f_2^{(l)}} = (-1)^j(\mathrm{i}\omega)^{j+l}\, S_{f_1 f_2} \tag{1.14}$$

with the restriction that the ordinary differentiation and not the generalised one has to be used (Föllinger 2003). The treatment of stochastic processes follows the contents of Bendat & Piersol (2000).

The next theorem is important for the transformations of structural degrees of freedom applied in this work. A structural system can be completely described with different sets of linearly independent degrees of freedom, for instance $\boldsymbol{\xi}_{\mathrm{s},1}$ and $\boldsymbol{\xi}_{\mathrm{s},2}$. If the associated forces $\mathbf{f}_1$ and $\mathbf{f}_2$ are chosen in an energetically corresponding manner and there are no redundancies, the total work done by a force along a displacement can be described in two ways.

$$W = \mathbf{f}_1^{\mathrm{T}}\boldsymbol{\xi}_{\mathrm{s},1} = \mathbf{f}_2^{\mathrm{T}}\boldsymbol{\xi}_{\mathrm{s},2} \tag{1.15}$$

The superscript $(\ )^{\mathrm{T}}$ denotes the transpose. If a linear transformation of the degrees of freedom is given with

$$\boldsymbol{\xi}_{\mathrm{s},1} = \mathbf{a}\boldsymbol{\xi}_{\mathrm{s},2} \quad , \tag{1.16}$$

Eq. (1.15) leads to the linear transformation

$$\mathbf{f}_2 = \mathbf{a}^{\mathrm{T}} \mathbf{f}_1 \tag{1.17}$$

of the forces. The theorem is used in similar forms, for instance in Argyris (1957), for the transformation of internal and external variables of a structure. It also holds true if kinematic couplings are used for the degrees of freedom. For this case, the transformation in Eq. (1.17) includes amplifying effects on the forces due to gears.

Throughout the work, a special formulation is used that must be explained to avoid confusion. In an eigenvalue analysis of a quadratic matrix, multiple eigenvalues can occur. If the rank deficiency of the characteristic matrix of the special linear eigenvalue problem equals one for these eigenvalues, only one eigenvector can be determined. Some authors (e. g. Gasch & Knothe 1987) say that the multiple eigenvalues are connected to identical eigenvectors. This formulation is used here because it is in line with the displayed numerical solution of MATLAB (2007).

Another term, steady, also needs to be defined. Here, steady is related to something like a flow pattern or a displacement, for instance, that is time invariant, constant. It must not be mixed with the similar term steady-state. The latter is employed for the part of the output of a linear time-invariant transfer element that is not transient.

2 Aerodynamic Forces

2.1 Types of Aerodynamic Forces and Aerodynamic Transfer Equations

Several structural components of a bridge are subjected to wind loads. The particular focus of the work presented here is on bridges with slender girders. Wind loading on the girder decisively influences the dynamic characteristics of this kind of bridges. Strong vibrations of other structural bridge components can also be excited by the wind. These phenomena, like rain-wind-induced vibrations of stay cables, for instance, are not discussed here. Special attention is given to the bridge behaviour when wind is acting on the girder.

A mathematical description of the total flow around the bridge girder with a system of coupled non-linear partial differential equations based on sufficiently realistic model assumptions is possible in principle (e. g. Walther & Larsen 1997, Hübner 2003, Thiesemann 2008, Mannini & al. 2010, Bai & al. 2010). The development of efficient and precise numerical solution algorithms is, however, part of the ongoing research in computational fluid dynamics. Moreover, these numerical methods are not appropriate for the application of standard procedures of control engineering for the design of a controller. Although these numerical flow models can be used for an additional, independent check of the controlled system behaviour, they are not adopted in this work.

For the majority of the current issues in bridge engineering, the aerodynamic forces and, thus, the flow around the girder are usually divided into different types. In real flow, whether in nature or in laboratory experiments, there is an interaction between these types, which is normally not directly accounted for. Each of the force types can be described with semi-empirical models for arbitrary aerodynamically effective girder shapes. Motion-induced aerodynamic forces, which are also called self-excited aerodynamic forces, are caused by the motion of the bridge girder itself. Due to the direct relation between forces and displacements, motion-induced wind forces change the dynamic characteristics of the structural system. Gust-induced aerodynamic forces, also termed buffeting forces, are generated by the turbulence of the natural wind. Vortex-induced aerodynamic forces, a further force type, arise from vortex shedding behind bluff bodies. These special vortices detach mainly at obtuse downstream-oriented cross-section sides of the girder.

Whereas the first two kinds of aerodynamic forces are taken into account in the further studies, the third force type is neglected here. This simplifying assumption can be justified to some extent by the following statement. Before applying the different types of moved actuators that are investigated for the improvement of the dynamic behaviour of the bridge, the presumably simpler method of streamlining the girder cross section geometry should be taken into account. Streamlining can be directly applied in the design process or later as a measure of retrofitting. It covers the shape modification of the load-bearing cross section, the shape modification with additional fixed elements like cladding panels (Barelli & al. 2006), and the flow modification with guide vanes (Ostenfeld & al. 1970). The size of vortex-induced aerodynamic forces is assumed to be insignificant for girders with such cross sections. Nevertheless, it must be mentioned that streamlining with respect to a significant reduction of vortex-induced aerodynamic forces is much more challenging than streamlining for an improvement of the bridge stability (Larsen & al. 2000).

The relation between motion-induced aerodynamic forces $\mathbf{f}_{\mathrm{ae}}$ and the degrees of freedom of the structural system $\boldsymbol{\xi}_{\mathrm{s}}$, as well as the dependency of gust-induced aerodynamic forces $\mathbf{d}_{\mathrm{ae}}^{\mathrm{g}}$ on fluctuating freestream wind velocities $\boldsymbol{\alpha}^{\mathrm{g}}$ can be described in the frequency domain with deterministic transfer equations of linear time-invariant transfer elements.

$$\mathbf{f}_{\mathrm{ae}}(s) = \mathbf{G}_{\mathrm{ae}}(s)\boldsymbol{\xi}_{\mathrm{s}}(s) \tag{2.1a}$$

$$\mathbf{d}_{\mathrm{ae}}^{\mathrm{g}}(s) = \mathbf{G}_{\mathrm{ae}}^{\mathrm{g}}(s)\boldsymbol{\alpha}^{\mathrm{g}}(s) \tag{2.1b}$$

Due to the low ratio between the wavelength of the relevant fluctuating flow components and the width of the girder cross section, these unsteady formulations are necessary. For the aerodynamic forces, vector-matrix equations are used that can be applied to rigid bodies or discretised continua. The aerodynamic transfer functions $\mathbf{G}_{\mathrm{ae}}(s)$ and $\mathbf{G}_{\mathrm{ae}}^{\mathrm{g}}(s)$, which are here alternatively termed aerodynamic admittances, contain the transfer characteristics of the air flow. In general, both aerodynamic admittance matrices are not square. For the transfer of motion-induced aerodynamic forces, the input and the output vector are often defined in an energetically corresponding way. If all elements of these corresponding vectors are taken into account, the associated admittance matrix is square.

The frequency-domain functions are unilateral Laplace transforms. Transfer equations describe the input-output performance of a dynamic system, which means the transfer of the input to the forced system response. The natural system response, which occurs if the system state does not equal zero prior to time $t = 0$, is not included. If the system has a history prior to $t = 0$, the effect of the input on the system output is not unique and an additional summand must be inserted into the equations. Since only the transfer functions of the flow are used, there is, moreover, no information available about the total internal structure and a corresponding adequate system state

of the flow, which can affect its natural response. Usually, only the effect of the input on the flow is of interest and, thus, the chosen input-output relation is sufficient.

A multiplication with the complex-valued transfer function changes the phase and the magnitude of the complex-valued input. For motion-induced aerodynamic forces, the phase shift is important because it activates a damping-force character. For gust-induced forces, however, the phase shift has no comparable effects. In bridge engineering (e. g. Simiu & Scanlan 1996), the latter transfer function is, thus, often simplified by neglecting its phase and using the maximum of its frequency-dependent magnitude for a simplification in terms of a quasi-steady approach.

The aerodynamic transfer relations in Eq. (2.1) can either be seen as $\mathscr{L}_s$ or $\mathscr{L}_p$ transforms. Taking for instance Eq. (2.1a), it must be possible to transform the two variants

$$\mathbf{f}_{\mathrm{ae},s} = \mathbf{G}_{\mathrm{ae},s}\boldsymbol{\xi}_{\mathrm{s},s} \;, \quad \mathbf{f}_{\mathrm{ae},p} = \mathbf{G}_{\mathrm{ae},p}\boldsymbol{\xi}_{\mathrm{s},p} \tag{2.2}$$

into each other with Eq. (1.8). Keeping in mind that the input and the output is unique in the time domain due to its physical nature, it follows that $\mathbf{G}_{\mathrm{ae},s} = \mathbf{G}_{\mathrm{ae},p}$. The representations of the aerodynamic transfer function are, thus, the same in both Laplace domains.

Corresponding to the multiplications in the frequency domain given in Eq. (2.1), convolutions of the system input with the aerodynamic impulse responses $\mathbf{G}_{\mathrm{ae}}(t)$ and $\mathbf{G}^{\mathrm{g}}_{\mathrm{ae}}(t)$ represent the unsteady aerodynamic transfer behaviour in the time domain. Assuming Eq. (2.1), for instance, as an $\mathscr{L}_s$ transform, the convolution follows related to the time t.

$$\mathbf{f}_{\mathrm{ae}}(t) = \mathbf{G}_{\mathrm{ae}}(t) \overset{t}{*} \boldsymbol{\xi}_{\mathrm{s}}(t) \tag{2.3a}$$

$$\mathbf{d}^{\mathrm{g}}_{\mathrm{ae}}(t) = \mathbf{G}^{\mathrm{g}}_{\mathrm{ae}}(t) \overset{t}{*} \boldsymbol{\alpha}^{\mathrm{g}}(t) \tag{2.3b}$$

Respective variables in Eq. (2.1) and in Eq. (2.3) are $\mathscr{L}_s$ Laplace pairs. Usually, the matrices $\mathbf{G}_{\mathrm{ae}}$ and $\mathbf{G}^{\mathrm{g}}_{\mathrm{ae}}$ are defined as frequency-domain functions of the reduced frequency p. As derived, the aerodynamic transfer functions can be understood either as $\mathscr{L}_s$ or $\mathscr{L}_p$ transforms. Hence, the corresponding aerodynamic impulse responses differ according to Eq. (1.8). In combination with the corresponding convolutions from Eq. (1.10), both variants, however, lead to the same results in the time domain. Eq. (2.4) clarifies this statement for the gust-induced aerodynamic forces.

$$\mathscr{L}_s\{\mathbf{d}^{\mathrm{g}}_{\mathrm{ae}}\} = \mathbf{G}^{\mathrm{g}}_{\mathrm{ae}}(p)\mathscr{L}_s\{\boldsymbol{\alpha}^{\mathrm{g}}\} \quad \bullet\!\!-\!\!\overset{s,t}{-}\!\!\circ \quad \mathbf{d}^{\mathrm{g}}_{\mathrm{ae}} = \mathscr{L}_s^{-1}\{\mathbf{G}^{\mathrm{g}}_{\mathrm{ae}}\} \overset{t}{*} \boldsymbol{\alpha}^{\mathrm{g}} \tag{2.4a}$$

$$\begin{aligned}\mathscr{L}_p\{\mathbf{d}^{\mathrm{g}}_{\mathrm{ae}}\} = \mathbf{G}^{\mathrm{g}}_{\mathrm{ae}}(p)\mathscr{L}_p\{\boldsymbol{\alpha}^{\mathrm{g}}\} \quad \bullet\!\!-\!\!\overset{p,\bar{t}}{-}\!\!\circ \quad \mathbf{d}^{\mathrm{g}}_{\mathrm{ae}} &= \mathscr{L}_p^{-1}\{\mathbf{G}^{\mathrm{g}}_{\mathrm{ae}}\} \overset{\bar{t}}{*} \boldsymbol{\alpha}^{\mathrm{g}} \\ &= U/b\,\mathscr{L}_p^{-1}\{\mathbf{G}^{\mathrm{g}}_{\mathrm{ae}}\} \overset{t}{*} \boldsymbol{\alpha}^{\mathrm{g}} \\ &= \mathscr{L}_s^{-1}\{\mathbf{G}^{\mathrm{g}}_{\mathrm{ae}}\} \overset{t}{*} \boldsymbol{\alpha}^{\mathrm{g}}\end{aligned} \tag{2.4b}$$

When Eq. (2.1b) is again assumed as an $\mathscr{L}_s$ transform and expanded in the following way

$$\mathbf{d}_{\mathrm{ae}}^{\mathrm{g}} = \left(s^{-j}\mathbf{G}_{\mathrm{ae}}^{\mathrm{g}}\right)\left(s^{j}\boldsymbol{\alpha}^{\mathrm{g}}\right) \quad , \tag{2.5}$$

where j is an integer, the corresponding time-domain equation shows that the convolution with aerodynamic impulse responses can be replaced by suitable convolutions with, for instance, step responses, which are also called indicial functions, or ramp responses.

$$\mathbf{d}_{\mathrm{ae}}^{\mathrm{g}} = \mathscr{L}_s^{-1}\{s^{-j}\mathbf{G}_{\mathrm{ae}}^{\mathrm{g}}\} \overset{t}{*} \boldsymbol{\alpha}^{\mathrm{g}(j)} \tag{2.6}$$

If Eq. (2.1b) is understood as an $\mathscr{L}_p$ transform, Eq. (2.6) has to be replaced as follows.

$$\mathbf{d}_{\mathrm{ae}}^{\mathrm{g}} = \mathscr{L}_p^{-1}\{p^{-j}\mathbf{G}_{\mathrm{ae}}^{\mathrm{g}}\} \overset{\bar{t}}{*} \boldsymbol{\alpha}^{\mathrm{g}(j)} \tag{2.7}$$

As already shown for the impulse response, the other characteristic time-domain responses differ as well. Applying a derivation in the sense of Eq. (2.4) under consideration of Eq. (1.2) and Eq. (1.3) proves that both time-domain variants are again equivalent.

Due to the used input-output descriptions of the flow and the causality of the transfer elements, the input functions, output functions, impulse responses, step responses, and system states of this work are in most cases assumed to be zero prior to time $t = 0$. If not otherwise specified, this has to be kept in mind for all following considerations.

The aerodynamic admittances are usually split up as follows.

$$\mathbf{G}_{\mathrm{ae}}(s) = q_0\mathbf{Q}(p) \tag{2.8a}$$

$$\mathbf{G}_{\mathrm{ae}}^{\mathrm{g}}(s) = q_0\mathbf{Q}^{\mathrm{g}}(p) \tag{2.8b}$$

Geometrical data of a typical girder cross section and information about the flow is included in the factor q_0.

$$q_0 = \pi\rho b^2 U^2 \tag{2.9}$$

The variable ρ stands for the density of the streaming air and is set to $\rho = 1.25\ \mathrm{kg/m^3}$ here. As already defined in Section 1.3, the nominal half-width of a typical bridge-girder cross section is denoted with b, and U symbolises the constant reference wind velocity. In order to avoid a multiple representation of parts of the air flow, it is important to define a reference wind velocity whose absolute value and direction do not vary with time. Moreover, the ratio between the absolute values of the fluctuating wind velocities and the reference wind velocity, as well as the values of the structural degrees of freedom must, in general, be small enough to ensure a sufficiently

precise linearisation in the sense of Eq. (2.1). Taking proper and identical dimensions for both the different types of input entries and output entries leads to matrices of dimensionless aerodynamic force coefficients $\mathbf{Q}(p)$ and $\mathbf{Q}^{\mathrm{g}}(p)$. In this work, the aerodynamic force coefficient matrices are alternatively called normalised aerodynamic admittances. Additionally, the coefficients of the matrix $\mathbf{Q}(p)$ of motion-induced aerodynamic forces are termed normalised aerodynamic derivatives. A non-dimensionalisation with respect to other factors of the same dimension is also possible. For instance, the advantage of alternatively using the steady admittances of motion-induced or gust-induced aerodynamic forces — if they do not equal zero — for this purpose is that the aerodynamic coefficients at $p = 0$ equal one. The unsteady behaviour of different structures can then be better compared to one another. The exclusive dependency of the aerodynamic force coefficients on the reduced complex frequency p is based on similarity characteristics in the description of incompressible two-dimensional flows with methods of the potential theory. If the reduced frequency is identical for geometrically similar structures, identical aerodynamic force coefficients are assumed, at least based on Eq. (2.8). In aerospace engineering, the notation of Eq. (2.8a) for motion-induced aerodynamic forces has been used especially for purely imaginary frequencies since early publications on aerodynamics (e. g. Küssner 1936). In the time domain, the normalised aerodynamic impulse responses $\mathbf{Q}(t)$ and $\mathbf{Q}^{\mathrm{g}}(t)$ are inverse Laplace transforms of the normalised aerodynamic admittances $\mathbf{Q}(p)$ and $\mathbf{Q}^{\mathrm{g}}(p)$.

There are also other ways to split up the transfer functions of the aerodynamic forces. The following alternative has often been applied to model the motion-induced aerodynamic forces for many decades (e. g. Theodorsen & Garrick 1941).

$$\mathbf{G}_{\mathrm{ae}}(s) = -\pi\rho b^4 s^2 \mathbf{C}_{\mathrm{ae}}(p) \tag{2.10a}$$

$$\mathbf{G}^{\mathrm{g}}_{\mathrm{ae}}(s) = -\pi\rho b^4 s^2 \mathbf{C}^{\mathrm{g}}_{\mathrm{ae}}(p) \tag{2.10b}$$

The aerodynamic force coefficients in $\mathbf{C}_{\mathrm{ae}}(p)$ and $\mathbf{C}^{\mathrm{g}}_{\mathrm{ae}}(p)$ are called normalised aerodynamic admittances as well, and the elements in $\mathbf{C}_{\mathrm{ae}}(p)$ are also moreover termed derivatives. In contrast to the matrices in Eq. (2.8), $\mathbf{C}_{\mathrm{ae}}(p)$ and $\mathbf{C}^{\mathrm{g}}_{\mathrm{ae}}(p)$ have no corresponding impulse responses because they are not complete frequency-domain functions due to the separation of the complex frequency s. Comparing Eq. (2.8a) and Eq. (2.10) leads to the following conversions.

$$\mathbf{Q}(p) = -p^2 \mathbf{C}_{\mathrm{ae}}(p) \tag{2.11a}$$

$$\mathbf{Q}^{\mathrm{g}}(p) = -p^2 \mathbf{C}^{\mathrm{g}}_{\mathrm{ae}}(p) \tag{2.11b}$$

The notations in Eq. (2.8) and Eq. (2.10a) have also long been, and still are, the basis for lots of investigations in bridge engineering (e. g. Sakata 1971, Ukeguchi & al. 1966, Klöppel & Thiele 1967). For the sake of brevity, the term normalised is usually omitted in the following for the variables $\mathbf{Q}$, $\mathbf{Q}^{\mathrm{g}}$, $\mathbf{C}_{\mathrm{ae}}$, and $\mathbf{C}^{\mathrm{g}}_{\mathrm{ae}}$.

Moreover, there are several notations introduced by Scanlan for motion-induced aerodynamic forces of special two-dimensional systems, which are the preferred notations in bridge engineering (e. g. Simiu & Scanlan 1996). These notations are only valid for purely harmonic motions. They can be seen as ostensibly more illustrative representations of the frequency response behaviour, which use displacements and velocities instead of complex values to describe the change in phase and magnitude. Since both time and frequency-domain information are incorporated in the formulas, they are inconsistent from a mathematical point of view and can lead to misinterpretations. Hence, they are not used here. For purely harmonic motions, the Scanlan notation can be converted to those in Eq. (2.8a) and Eq. (2.10a).

Assuming negligible vortex-induced aerodynamic forces and zero inputs in Eq. (2.1), there are, in general, still static aerodynamic forces $\mathbf{d}_{\mathrm{ae}}^{\mathrm{s}}$ that act on the structure. For instance, there can be a constant lift force due to an unsymmetrical flow around a structure though the inputs $\boldsymbol{\xi}_{\mathrm{s}}$ and $\boldsymbol{\alpha}^{\mathrm{g}}$ are zero. The static aerodynamic forces $\mathbf{d}_{\mathrm{ae}}^{\mathrm{s}}$ have to be distinguished from the steady motion-induced and gust-induced aerodynamic forces at $p = 0$. Usually a notation with a vector of normalised constant coefficients $\mathbf{Q}^{\mathrm{s}}$ is chosen for these static aerodynamic forces.

$$\mathbf{d}_{\mathrm{ae}}^{\mathrm{s}} = q_0 \mathbf{Q}^{\mathrm{s}} \tag{2.12}$$

If, again, proper and identical dimensions are used for the different types of entries in $\mathbf{d}_{\mathrm{ae}}^{\mathrm{s}}$, a vector of dimensionless aerodynamic force coefficients is possible. A non-dimensionalisation can again also be managed with respect to another factor of the same dimension. The aerodynamic forces $\mathbf{d}_{\mathrm{ae}}^{\mathrm{s}}$ must be added to the other above-mentioned types of aerodynamic forces to obtain a full representation of the effect of the air flow.

Due to the complexity of the flow, the aerodynamic force coefficients in $\mathbf{Q}$, $\mathbf{Q}^{\mathrm{g}}$, and $\mathbf{Q}^{\mathrm{s}}$ generally depend on the definition of the zero values of the degrees of freedom $\boldsymbol{\xi}_{\mathrm{s}}$. The latter are identical to the points of linearisation for the input-output relations in Eq. (2.1). Moreover, the linear approach in Eq. (2.1) has to be adjusted to cover the non-linear behaviour of the real flow with reference to another aspect. The coefficients in $\mathbf{Q}$ and $\mathbf{Q}^{\mathrm{g}}$ must be considered as functions of a characteristic value of the input. For a harmonic input, for instance, this value can be related to the amplitude of the input.

The aerodynamic force coefficients basically depend on the aerodynamically effective shape of the three-dimensional structure. They can be derived analytically only for a few simple two-dimensional problems when the flow is described with the methods of potential theory. For real, more or less bluff bodies, the aerodynamic force coefficients are either experimentally determined with scaled models in wind or water tunnels or numerically calculated with methods of computational fluid dynamics. Respective studies can be found, for instance, in Ukeguchi & al. (1966) and in Larsen & Walther (1998) for the motion-induced aerodynamic forces of two-

dimensional problems. A system identification of the unsteady aerodynamic forces is possible in both the frequency and the time domain based on the aerodynamic transfer relations in Eq. (2.1) and Eq. (2.3), respectively. Usually the aerodynamic frequency responses $\mathbf{G}_{\mathrm{ae}}(\mathrm{i}k)$ and $\mathbf{G}^{\mathrm{g}}_{\mathrm{ae}}(\mathrm{i}k)$ are determined in the sense of a non-parametric model for a set of discrete purely imaginary frequencies without any further assumptions on the values of the aerodynamic transfer functions for other, arbitrary complex reduced frequencies.

The aerodynamic strip theory is used here in order to simplify the description of the three-dimensional air flow around the girder. This theory assumes that the flow can be separated into strips where it can be considered to be two-dimensional and that the flow between two neighbouring strips can be neglected. The theory is usually assumed to be applicable to elongated parts of a structure with a constant cross section. Hence, the aerodynamic force coefficients are related to a specific girder cross section. In a fluctuating wind field, however, depending on the cross section of the elongated body, the correlation of the gust-induced forces has been observed to be remarkably higher than the correlation of the corresponding gust speeds (e. g. Larose & Mann 1998, Matsuda & al. 1999). A main reason is the balancing effect of the occurring vortices. For the investigations given here, such effects, which are contrary to the strip assumption, are not taken into account. The following pages of this chapter describe the coefficients of the cross sections that are used in this work.

2.2 Theoretical Aerodynamic Forces on Flat Plates

2.2.1 Characteristic Aerodynamic Transfer Functions of Flat Plates

The determination of the aerodynamic forces acting on an aerofoil in a two-dimensional incompressible flow is a classical topic in aerospace engineering. The aerodynamic forces are caused either by a motion of the aerofoil components or by a vertical gust. If the aerofoil is modelled as a combination of rigid flat plates, the two problems can be solved analytically with the potential flow theory (von Kármán & Sears 1938). Some important details of the results are explained below.

One way to solve the problems is to divide the flow into a non-circulatory and a circulatory part and to combine both parts using the Kutta condition. As one result, characteristic transfer functions are obtained that connect the circulatory aerodynamic lift either with a specific non-circulatory downwash due to motions of the plates or with a vertical gust velocity. The first, to some extent, comprehensive treatment of these problems, which leads to consistent transfer functions of linear time-invariant aerodynamic systems, was published in Sears (1940). For motion-induced aerodynamic forces, these derivations are further analysed and extended in Edwards (1977). By

applying unilateral Laplace transforms, the derivations result in two frequency-domain functions whose only variable is the reduced complex frequency p. No restrictive assumptions are made for the time-domain behaviour of the system input, apart from the existence of the Laplace transform. The function $C(p)$ is related to the problem of the moved plates and is here termed consistent Theodorsen function. The gust problem leads to the function $S(p)$, the here called consistent Sears function.

$$C(p) = \frac{K_1(p)}{K_0(p) + K_1(p)} \tag{2.13a}$$

$$S(p) = \frac{1}{K_0(p) + K_1(p)} \cdot \frac{1}{p\,\mathrm{e}^{p}} \tag{2.13b}$$

Both functions depend on the principle branch of the modified Bessel functions K_j of the second kind and integer order j, whose definition and behaviour is comprehensively described, for instance, in Abramowitz & Stegun (1984). The region of absolute convergence of the transforms is the right complex half-plane where $\mathrm{Re}(p) = \beta > 0$. As usual, the notations Re( ), Im( ), | |, and arg( ) are used for the real part, the imaginary part, the absolute value, and the argument of a complex variable, respectively. To guarantee a complex-conjugate behaviour for $C(p)$ and $S(p)$ as transfer functions, not only the principle branch of the modified Bessel functions is defined as usual with $-\pi < \arg(p) \leq \pi$ but also the frequencies along the negative real axis must be excluded. Moreover, the definitions of the characteristic aerodynamic transfer functions with modified Bessel functions lead to a removable singularity at the origin of the frequency plane. The characteristic aerodynamic transfer functions described in this manner are both defined and holomorphic throughout the complex frequency plane, except for the negative real axis and the origin. According to the uniqueness of holomorphic functions and Laplace transforms, these functions, or mathematically equivalent ones, are the only solutions of the mathematical problems in terms of transfer functions. Figure 2.1 illustrates the real and imaginary part of the consistent Theodorsen and the consistent Sears function. To avoid misunderstandings, it should be mentioned that the values of the functions, as displayed in the figures, do not tend to infinity. The values along the imaginary frequency axis are accentuated with the black lines. Although the region of absolute convergence of the Laplace transforms is the frequency half-plane right to the imaginary axis, the functions can be extended to all other frequencies at which they are defined and holomorphic with the concept of analytic continuation. For inputs of these frequencies, the illustrated function values themselves show the steady-state transfer behaviour of the flow. Figure 2.2(a) illustrates the Nyquist plots of the functions, where their real against their imaginary parts are displayed for frequencies along the positive part of the imaginary axis. Against those frequencies, Figure 2.2(b) additionally depicts the absolute values of both functions.

In the definition of the consistent Theodorsen function C in Eq. (2.13a), the modified Bessel functions of the variable p can be replaced with Hankel functions of the second kind that depend

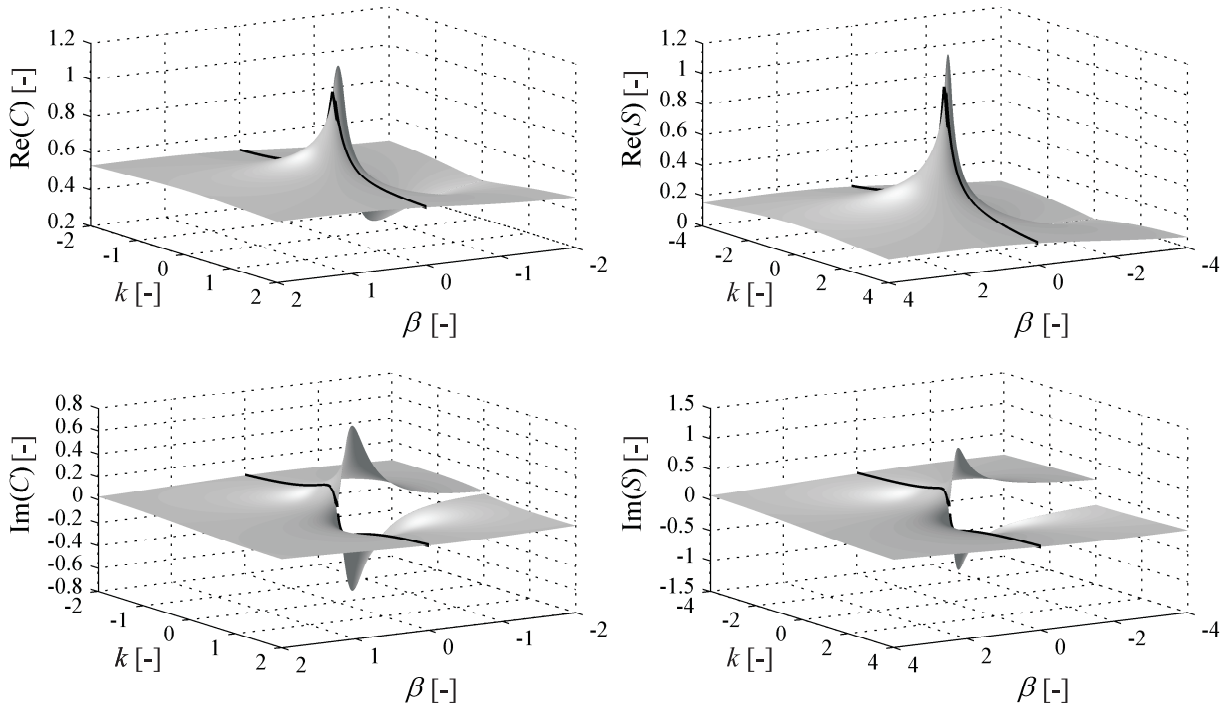

(a) Consistent Theodorsen function. (b) Consistent Sears function.

Figure 2.1: Characteristic aerodynamic transfer functions of the flat-plate problem above the complex reduced frequency plane.

on the variable $(-\mathrm{i}p)$. The converted function, which is also given in Luke & Dengler (1951), equals the consistent Theodorsen function C in the complex frequency plane, except for the third quadrant and the adjacent half imaginary frequency axis. In the latter region, not the principal but another branch of the modified Bessel functions is activated through the use of the principal branch of the Hankel functions. The converted function can, thus, not be seen as a transfer function for $\mathrm{Re}(p) = \beta \leq 0$. For positive purely imaginary frequencies, the converted function takes the form of the original Theodorsen function given in Theodorsen (1934).

In Sears (1940), the characteristic aerodynamic step responses $W(\bar{t})$ and $K(\bar{t})$ are connected to the characteristic aerodynamic transfer functions $C(p)$ and $S(p)$, respectively, with Laplace transforms.

$$\begin{pmatrix} W \\ K \end{pmatrix} = \mathscr{L}_p^{-1}\left\{\frac{1}{p}\begin{pmatrix} C \\ S \end{pmatrix}\right\} \quad \circ\!\!-\!\!\bullet \quad \frac{1}{p}\begin{pmatrix} C \\ S \end{pmatrix} = \mathscr{L}_p\left\{\begin{pmatrix} W \\ K \end{pmatrix}\right\} \tag{2.14}$$

Accordingly, the respective characteristic aerodynamic impulse responses $W'(\bar{t})$ and $K'(\bar{t})$ and the characteristic aerodynamic transfer functions $C(p)$ and $S(p)$ form Laplace pairs.

$$\begin{pmatrix} W' \\ K' \end{pmatrix} = \mathscr{L}_p^{-1}\left\{\begin{pmatrix} C \\ S \end{pmatrix}\right\} \quad \circ\!\!-\!\!\bullet \quad \begin{pmatrix} C \\ S \end{pmatrix} = \mathscr{L}_p\left\{\begin{pmatrix} W' \\ K' \end{pmatrix}\right\} \tag{2.15}$$

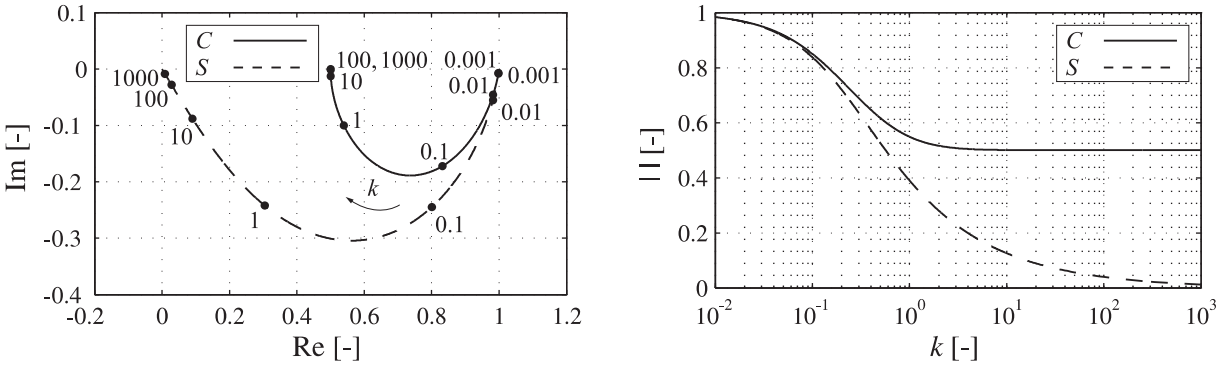

(a) Nyquist plots. (b) Absolute values.

Figure 2.2: Consistent Theodorsen and Sears function for purely imaginary positive reduced frequencies $p = 0 + \mathrm{i}k,\ k > 0$.

When applying the inverse Laplace transform, the integration path must be located within the region of absolute convergence. In Eq. (2.14), the factor $1/p$ additionally limits this region to $\beta > 0$. The full information on the transfer is incorporated in either the frequency-domain function in an infinite straight line parallel to the imaginary axis within the convergence region or in the full characteristic time-domain function. Since the imaginary axis is not within the region of absolute convergence, Eq. (2.14) and Eq. (2.15) cannot be interpreted as a Fourier transforms as done in Garrick (1938), which is usually cited. Cauchy's integral theorem allows for choosing alternative integration paths in the complex frequency plane. Examples of alternative paths, like hook integrals and others, are given in Sears (1940) and in a mathematically more cumbersome way in Schwarz (1940).

The characteristic aerodynamic step response of the moved-plates problem W is known as the Wagner function (Wagner 1925) and the one of the gust problem K as the Küssner function (Küssner 1940). Contrary to Küssner (1940), $\bar{t} = 0$ is the instant when the upstream edge begins to penetrate the boundary of the vertical gust. For an explanation within the framework of linear system theory, the step responses must be zero prior to $\bar{t} = 0$ to ensure causality.

According to the time-shift theorem of unilateral Laplace transforms, a multiplication of the consistent Sears Function by e^p can be interpreted as applying a time shift of $\bar{t} = -1$ to the gust transfer without taking the information in the time interval $\bar{t} \in [0;1)$ into account. Shifting the time by this amount means that the instant when the gust boundary reaches the middle of the plate becomes the new origin of the step response time axis. The resulting function $S\mathrm{e}^p$ coincides with the original Sears function given in Sears (1941) if the representations of the latter are formally generalised by replacing k with $(-\mathrm{i}p)$. As the time-shift theorem is incorrectly applied for unilateral Laplace transforms, the function $S\mathrm{e}^p$ is not such a transform of the shifted and truncated version of the function K'. For shifting K' to the left without losing the information in the interval $\bar{t} \in [0;1)$, S must be considered as a bilateral Laplace transform. In so doing, $S\mathrm{e}^p$

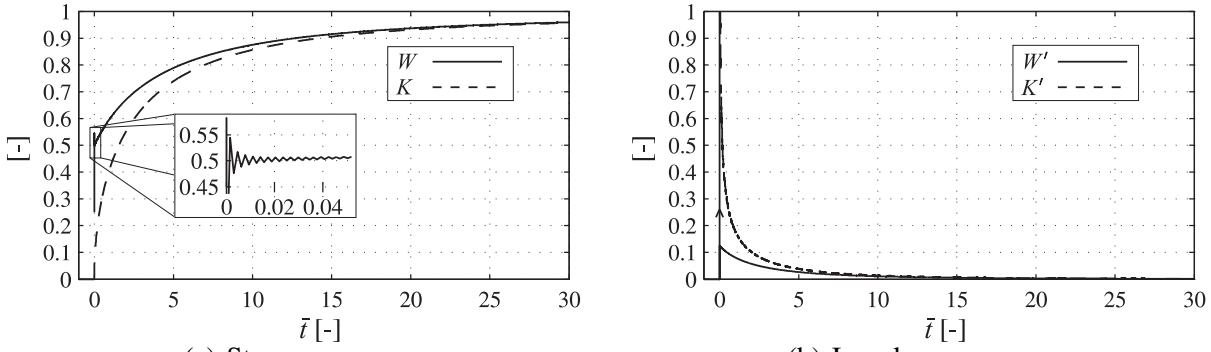

(a) Step responses. (b) Impulse responses.

Figure 2.3: Characteristic aerodynamic time-domain functions of the flat-plate problem.

fully corresponds to the transform of the shifted and not truncated version of K'. When displaying the original Sears function in the sense of Figure 2.2(a), the time shift, as with transfer functions in general, leads to the often cited spiral behaviour shown in Sears (1941) (Giesing & al. 1970).

Numerical values of the characteristic aerodynamic step responses W and K can be determined with contemporary mathematical procedures without problems. Figure 2.3(a) shows the result obtained with a numerical inverse Laplace transform (Brigham 1997) that utilises a negatively damped inverse discrete Fourier transform (`ifft` in MATLAB (2007)). The used frequency spacing is $\Delta k = 0.01$, the Nyquist frequency is set to $k = 2000$, and the integration is done along a straight line parallel to the imaginary axis with $\bar{c} = 0.03$ according to Eq. (1.6b). The small value of $\bar{c}$ is necessary to sufficiently suppress the procedure-typical oscillating error, which rises with increasing time, within the displayed time range. With the ad hoc-chosen parameters, the relative difference of the values in Figure 2.3(a) from the discrete values given in Küssner (1940) is less than $7 \cdot 10^{-2}\,\%$ for W and less than $4 \cdot 10^{-3}\,\%$ for K. The single value of the Wagner function $W(\bar{t} = 0)$ is calculated as 0.25, which is only 0.5 times the correct value, as it is typical for an inverse Laplace transform. As displayed in the zoomed area of Figure 2.3(a), the jump discontinuity of W is followed by a small oscillating error, known as the Gibbs phenomenon. This oscillation in the vicinity of $\bar{t} = 0$ is responsible for the larger differences.

When comparing the characteristic aerodynamic step responses and transfer functions for $\bar{t} \to \infty$, $p \to 0$ and $\bar{t} \to 0$, $p \to \infty$, their values can be transformed into each other with the initial and the final value theorem of Laplace transforms.

Figure 2.3(b) additionally illustrates the result of the inverse Laplace transform for the characteristic aerodynamic impulse responses W' and K' when the same numerical parameters are chosen as for the characteristic aerodynamic step responses. Due to the discontinuity of the Wagner Function at $\bar{t} = 0$, its derivative W' starts with a scaled Dirac impulse. In the figure, the

Dirac impulse is marked with an arrowhead. Directly to the right of the impulse, the function approaches a finite limit.

$$W'(\bar{t}) \to 0.125 \qquad \text{for} \qquad \bar{t} \to 0\,, \quad \bar{t} > 0 \tag{2.16}$$

This right-hand limit corresponds to the following limit in the frequency domain.

$$\mathrm{Re}(pC(p)) \to 0.125 \qquad \text{for} \qquad p = 0 + \mathrm{i}k\,, \quad k \to \pm\infty \tag{2.17}$$

By contrast, the derivative K' tends to infinity for $\bar{t} \to 0$. When the singularities of C and S at the origin are removed, it can be easily proven with Cauchy's integral theorem that for determining the characteristic aerodynamic impulse responses W' and K' from the characteristic aerodynamic transfer functions C and S with inverse Laplace transforms, the integration paths can also be fully identical to the imaginary frequency axis. The Laplace pairs are also Fourier pairs in this case.

In Küssner (1936), the aerodynamic forces are divided in another way than used above, leading for the moved-plate problem to the so-called wake-vortex function. The consistent wake-vortex function $T_{\mathrm{Kü}}$ can be derived from the consistent Theodorsen function of Eq. (2.13).

$$T_{\mathrm{Kü}}(p) = 2C(p) - 1 \tag{2.18}$$

A proof can be easily given when comparing the resulting forces of both approaches. The consistent wake-vortex function $T_{\mathrm{Kü}}$ is not further addressed because all investigations of the consistent Theodorsen function C can be transferred to it using Eq. (2.18).

2.2.2 Aerodynamic Forces on the Single Flat Plate

The aerodynamic force coefficients of the rigid flat plate in a two-dimensional incompressible flow can be analytically determined with the potential theory. In accordance with Figure 2.4, the input and output vectors of Eq. (2.1) are defined as follows.

$$\mathbf{f}_{\mathrm{ae}} = \begin{pmatrix} Lb & M \end{pmatrix}^{\mathrm{T}}, \quad \boldsymbol{\xi}_{\mathrm{s}} = \begin{pmatrix} h/b & \alpha \end{pmatrix}^{\mathrm{T}} \tag{2.19a}$$

$$\mathbf{d}^{\mathrm{g}}_{\mathrm{ae}} = \begin{pmatrix} Lb & M \end{pmatrix}^{\mathrm{T}}, \quad \boldsymbol{\alpha}^{\mathrm{g}} = \begin{pmatrix} w^{\mathrm{g}}/U \end{pmatrix} \tag{2.19b}$$

A constant horizontal reference wind velocity U and a vertical fluctuating wind velocity w^{g} represent the wind field. The direction of the reference wind velocity is perpendicular to the vertical symmetry axis of the undeflected cross section. The degrees of freedom are denoted with h and α. The variable L stands for the vertical aerodynamic force and M for the aerodynamic moment around the middle of the plate. Forces and displacements are defined in an energetically

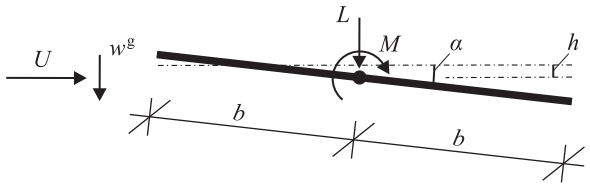

Figure 2.4: Geometry, degrees of freedom, aerodynamic forces, and wind velocity components concerning the flow around a flat plate.

corresponding way. A drag force is not generated according to the results of potential flow theory, a contradiction known as d'Alembert's paradox.

The first independently derived but equivalent analytical solutions for the aerodynamic coefficients $\mathbf{Q}(p)$ or $\mathbf{C}_{\mathrm{ae}}(p)$ of motion-induced aerodynamic forces were published in Theodorsen (1934) and Küssner (1936). The results are derived there for a wing-aileron system. It is modelled with two flat plates that are joined at their ends with a hinge. The solution for a single flat plate can be extracted as a special case.

In the two references, the solutions are given for purely harmonic motions of the reduced frequency k. With respect to the explanations of the last section, the generalisation to arbitrary complex frequencies p can easily be carried out using the consistent characteristic functions in Eq. (2.13a) and in Eq. (2.18) and replacing ik with p or k with $(-\mathrm{i}p)$ (Edwards 1977). According to Theodorsen (1934), for instance, the result is as follows.

$$\begin{aligned}\mathbf{Q}(p) = &\begin{pmatrix} 0 & -1 \\ 0 & -\frac{1}{2} \end{pmatrix} p + \begin{pmatrix} -1 & 0 \\ 0 & -\frac{1}{8} \end{pmatrix} p^2 + \\ &+ \begin{pmatrix} 0 & -2 \\ 0 & 1 \end{pmatrix} C(p) + \begin{pmatrix} -2 & -1 \\ 1 & \frac{1}{2} \end{pmatrix} C(p) p\end{aligned} \tag{2.20}$$

The aerodynamic admittances $\mathbf{Q}(p)$ contain the reduced frequency not only implicitly in the consistent Theodorsen function but also as a free variable in terms of p and p^2. Since the motion-induced aerodynamic forces thus depend not only on the displacements ξ_{s} themselves but also on their first two derivatives, there is a non-causal, differentiating part in the aerodynamic transfer behaviour of Eq. (2.1a). When the equation of motion of a structural system under the effect of aerodynamic forces is assembled, the problem of non-causality disappears due to other input and output variables.

As mentioned in Section 2.1, the motion-induced aerodynamic forces in the two-dimensional flow can also be described in another way. For the flat plate, the relation between the aerodynamic

derivatives A_j^* and H_j^* of the notation defined in Simiu & Scanlan (1996) and the aerodynamic derivatives in $\mathbf{Q}(p)$ and $\mathbf{C}_{\mathrm{ae}}(p)$ can be given for purely harmonic motions.

$$\mathbf{Q}(\mathrm{i}k) = k^2\mathbf{C}_{\mathrm{ae}}(\mathrm{i}k) = \frac{k^2}{\pi}\begin{pmatrix} 2(H_4^*(\mathrm{i}k)+\mathrm{i}H_1^*(\mathrm{i}k)) & 4(H_3^*(\mathrm{i}k)+iH_2^*(\mathrm{i}k)) \\ 4(A_4^*(\mathrm{i}k)+\mathrm{i}A_1^*(\mathrm{i}k)) & 8(A_3^*(\mathrm{i}k)+iA_2^*(\mathrm{i}k)) \end{pmatrix} \tag{2.21}$$

The aerodynamic admittances $\mathbf{Q}^{\mathrm{g}}(p)$ of the gust-induced aerodynamic forces on the flat plate, according to Küssner (1936) or von Kármán & Sears (1938), generalised to arbitrary complex frequencies, can be calculated as follows.

$$\mathbf{Q}^{\mathrm{g}}(p) = \mathbf{Q}(p\to 0)\begin{pmatrix} 0 & -1 \end{pmatrix}^{\mathrm{T}} S(p) \tag{2.22}$$

At the right side of the equation, the first two factors lead to the steady normalised motion-induced aerodynamic forces due to a rotation of the angle $\alpha = -1$. Since the singularity of the Theodorsen function at the origin is removable, the limit of the derivatives for $p \to 0$ exists. The frequency-dependent behaviour of $\mathbf{Q}^{\mathrm{g}}(p)$ is only governed by the consistent Sears function. In connection with Eq. (2.1b), the aerodynamic transfer behaviour has thus no differentiating character.

Static aerodynamic forces

$$\mathbf{d}_{\mathrm{ae}}^{\mathrm{s}} = \begin{pmatrix} Lb & M \end{pmatrix}^{\mathrm{T}} \tag{2.23}$$

are not generated if the zero position of the cross section, which is determined by the zero values of the degrees of freedom, is defined as given in Figure 2.4.

For another zero position of the cross section, however, static aerodynamic forces $\mathbf{d}_{\mathrm{ae}}^{\mathrm{s}}$ have to be taken into account. For the other zero position, other degrees of freedom $\tilde{\boldsymbol{\xi}}_{\mathrm{s}}$ have to be defined that correspond to those of the position in Figure 2.4 in the following way.

$$\tilde{\boldsymbol{\xi}}_{\mathrm{s}} = \boldsymbol{\xi}_{\mathrm{s}} - \boldsymbol{\xi}_{\mathrm{s}}^0 \tag{2.24}$$

The aerodynamic coefficients $\mathbf{Q}^{\mathrm{s}}$ of the other position can be easily determined.

$$\mathbf{Q}^{\mathrm{s}} = \mathbf{Q}(p\to 0)\boldsymbol{\xi}_{\mathrm{s}}^0 \tag{2.25}$$

As the first column of $\mathbf{Q}(p\to 0)$ is always a zero vector for all types of structures, only an inclination of the cross section leads to static aerodynamic forces $\mathbf{d}_{\mathrm{ae}}^{\mathrm{s}}$. The aerodynamic force coefficients $\mathbf{Q}$ and $\mathbf{Q}^{\mathrm{g}}$ remain the same for all zero positions of the flat plate in incompressible potential flow. The latter finding directly follows from the linear force-displacement description

of the potential flow theory. The case of an inclined angle of attack of the reference wind velocity is equivalent to the inclined zero position of the cross section.

Since the aerodynamic force descriptions Eq. (2.1) and Eq. (2.8) are based on the results of the flat plate in incompressible potential flow, the described analytical solutions completely fit in the assumed, linear form of the aerodynamic transfer equations. With the results of Section 2.2.1 and tables of Laplace transforms, the exact aerodynamic impulse responses $\mathbf{Q}(t)$ and $\mathbf{Q}^{\mathrm{g}}(t)$ can be found in the time domain. The flat-plate results only apply to real cross sections in real flow if the preconditions for a description with the potential theory are almost complied with. Streamlined narrow profiles of aircraft wings with rounded leading edges and sharp trailing edges conform to these assumptions far better than flat-plate profiles or large-width, more or less bluff bridge cross sections in the natural wind field. Statements that are based on the results of the potential flow theory can thus not generally be applied to the various kinds of cross sections occurring in bridge engineering. In Bleich (1949), the flat-plate results of the motion-induced aerodynamic forces were used for the analysis of the dynamic behaviour of bridges for the first time.

2.2.3 Aerodynamic Forces on Three Coupled Flat Plates

For the description of the aerodynamic forces acting on a streamlined bridge girder that is equipped with movable aerodynamically effective flaps, theoretical aerodynamic force coefficients of the two-dimensional flow around a system of flat plates are used in this work. When the potential flow theory is applied, analytical expressions can be derived, which are similar to those of the single flat plate. The system consists of rigid flat plates that are coupled in a line with kinks and steps, as shown in Figure 2.5. Again, the direction of the reference wind velocity is parallel to the horizontally aligned undeflected cross section. The large middle plate models the streamlined girder cross section. Aerodynamically effective flaps are represented by the two small outer plates. These flaps, which are directly attached to the edges of the girder, generate additional aerodynamic forces and, moreover, modify the air flow around the girder. In Figure 2.5, the subscripted abbreviations win and lee indicate windward and leeward edge variables, respectively. The half-width of the flaps is denoted with b_{fl}, the distance of the hinges from the middle of the flaps with $d_{\mathrm{h},j}$. The input and output vectors of Eq. (2.1) are defined as follows.

$$\mathbf{f}_{\mathrm{ae}} = \begin{pmatrix} Lb & M & M_{\mathrm{win}} & M_{\mathrm{lee}} \end{pmatrix}^{\mathrm{T}}, \quad \boldsymbol{\xi}_{\mathrm{s}} = \begin{pmatrix} h/b & \alpha & \theta_{\mathrm{fl,win}} & \theta_{\mathrm{fl,lee}} \end{pmatrix}^{\mathrm{T}} \tag{2.26a}$$

$$\mathbf{d}_{\mathrm{ae}}^{\mathrm{g}} = \begin{pmatrix} Lb & M & M_{\mathrm{win}} & M_{\mathrm{lee}} \end{pmatrix}^{\mathrm{T}}, \quad \boldsymbol{\alpha}^{\mathrm{g}} = \begin{pmatrix} w^{\mathrm{g}}/U \end{pmatrix} \tag{2.26b}$$

The vertical aerodynamic force on the whole system is denoted with L, and M is the moment on the whole system around the middle of the deck. The components of $\mathbf{f}_{\mathrm{ae}}$ and $\boldsymbol{\xi}_{\mathrm{s}}$ are defined in an

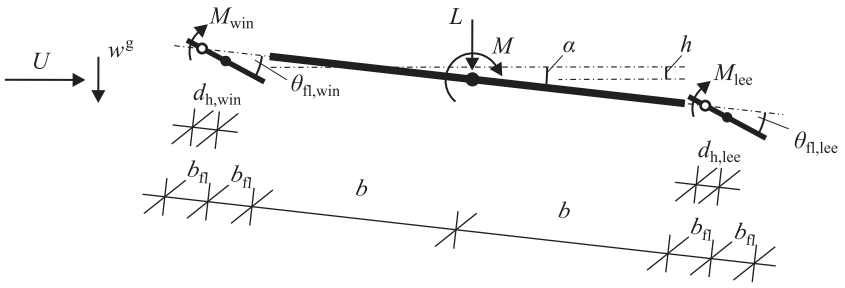

Figure 2.5: Geometry, degrees of freedom, aerodynamic forces, and wind velocity components concerning the flow around three coupled flat plates.

energetically corresponding way without redundancies. Accordingly, the flap rotations $\theta_{\text{fl},j}$ are defined relative to the rotation α of the whole system, and the aerodynamic moments acting on the flaps around their hinges are denoted with M_j.

Similar systems have already been used in aerospace engineering to describe the motion-induced aerodynamic forces on a wing that has leading and trailing edge ailerons (e. g. Nissim 1971, Edwards 1977). The aerodynamics of this problem can be modelled with the transformed description of a usual aerofoil in incompressible potential flow. In Theodorsen & Garrick (1941), the analytical formulas of which are usually employed, the aerofoil consists of a wing with an aerodynamically balanced aileron-tab combination. The aerofoil is modelled with flat plates. Aerodynamically balanced means that the hinges are not positioned between the ends of neighbouring plates but somewhere within the plates. This measure leads to a diminution of the aerodynamic moments around the hinges. Based on the publications of aerospace engineering, the transformed analytical aerofoil forces have also been applied to investigations of bridges with attached flaps (e. g. Kwon 1996, Wilde & al. 2001).

The implementation of the analytical results in a computer code is highly error prone because the aerodynamic force coefficients include a huge number of analytical expressions. Hence, in addition to the results given in Theodorsen & Garrick (1941), an alternative derivation of the aerodynamics is used in this work as a second set of theoretical coefficients. In Küssner & Göllnitz (1964), the motion-induced aerodynamic forces of the wing-aileron-tab problem are published as well. The report is basically the revised and extended version of Küssner & Schwarz (1940), and it includes lots of precise tables of aerodynamic derivatives that can be used to check the developed computer codes. Unlike the derivations in Theodorsen & Garrick (1941), the gap between the neighbouring plates is not only modelled as sealed but also as open. Taking a flow through these gaps into account seems to be also appropriate for an application in bridge aerodynamics where the neighbouring edges of the flaps and the streamlined bridge girder can be both acute and obtuse. The transformations between motion-induced aerodynamic forces of the aerofoil problem and the system in Figure 2.5 are given in Appendix A.1.

As shown for the single flat plate, the aerodynamic force coefficients $\mathbf{Q}^{\mathrm{g}}(p)$ of the gust-induced aerodynamic forces can be derived from the steady normalised motion-induced forces due to a rotation of the angle $\alpha = -1$.

$$\mathbf{Q}^{\mathrm{g}}(p) = \mathbf{Q}(p \to 0) \begin{pmatrix} 0 & -1 & 0 & 0 \end{pmatrix}^{\mathrm{T}} S(p) \tag{2.27}$$

The statements on the differentiating character of the aerodynamic transfer in Eq. (2.1) that are given for the single flat plate also apply to the coupled flat plates. Static aerodynamic forces

$$\mathbf{d}_{\mathrm{ae}}^{\mathrm{s}} = \begin{pmatrix} Lb & M & M_{\mathrm{win}} & M_{\mathrm{lee}} \end{pmatrix}^{\mathrm{T}} \tag{2.28}$$

are not generated if the zero values of the degrees of freedom are defined as shown in Figure 2.5. The aerodynamic coefficients of another zero position can again be determined with Eq. (2.25). In addition to the inclination of the main cross section, also the rotations of the flaps lead to static aerodynamic forces $\mathbf{d}_{\mathrm{ae}}^{\mathrm{s}}$. All other remarks for the single flat plate concerning another zero position hold for the coupled flat plates as well.

Again, the aerodynamic forces only apply to real cross sections with flaps if the flow around them is similar to the potential flow around the system of flat plates. Conditions have to be considered that go beyond those for the single flat plate. For the trailing-edge flap, it has to be ensured, for instance, that there is no separated flow region at its position on the downstream side of the bridge girder.

2.3 Measured Aerodynamic Forces on Various Cross Sections in Real Flow

The aerodynamic forces per unit length acting in real flow on a cross-section model and the input vectors of the unsteady aerodynamic forces can be defined in connection with Figure 2.6 as follows.

$$\mathbf{f}_{\mathrm{ae}} = \begin{pmatrix} Lb & Db & M \end{pmatrix}^{\mathrm{T}}, \quad \boldsymbol{\xi}_{\mathrm{s}} = \begin{pmatrix} h/b & p/b & \alpha \end{pmatrix}^{\mathrm{T}} \tag{2.29a}$$

$$\mathbf{d}_{\mathrm{ae}}^{\mathrm{g}} = \begin{pmatrix} Lb & Db & M \end{pmatrix}^{\mathrm{T}}, \quad \boldsymbol{\alpha}^{\mathrm{g}} = \begin{pmatrix} u^{\mathrm{g}}/U & w^{\mathrm{g}}/U \end{pmatrix}^{\mathrm{T}} \tag{2.29b}$$

$$\mathbf{d}_{\mathrm{ae}}^{\mathrm{s}} = \begin{pmatrix} Lb & Db & M \end{pmatrix}^{\mathrm{T}} \tag{2.29c}$$

In addition to the variables used for the flat-plate problem, the horizontal force component D, the horizontal displacement p, and the horizontal gust component u^{g} should in general be taken into

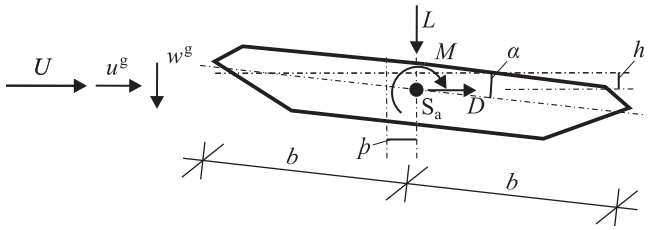

Figure 2.6: Geometry, degrees of freedom, aerodynamic forces, and wind velocity components concerning the flow around an arbitrarily shaped cross section.

account due to friction effects. Consequently, the position in thickness direction of the reference point S_a of the aerodynamic moment must also be specified.

The relation between the Scanlan derivatives A_j^*, H_j^*, and P_j^* given in Sarkar & al. (1994) and the aerodynamic derivatives in $\mathbf{Q}(p)$ and $\mathbf{C}_{ae}(p)$ is in extension of Eq. (2.21) as follows.

$$\begin{aligned}\mathbf{Q}(\mathrm{i}k) &= k^2\mathbf{C}_{ae}(\mathrm{i}k)\\ &= \frac{k^2}{\pi}\begin{pmatrix} 2(H_4^*(\mathrm{i}k)+\mathrm{i}H_1^*(\mathrm{i}k)) & 2(H_6^*(\mathrm{i}k)+\mathrm{i}H_5^*(\mathrm{i}k)) & 4(H_3^*(\mathrm{i}k)+\mathrm{i}H_2^*(\mathrm{i}k))\\ 2(P_6^*(\mathrm{i}k)+\mathrm{i}P_5^*(\mathrm{i}k)) & 2(P_4^*(\mathrm{i}k)+\mathrm{i}P_1^*(\mathrm{i}k)) & 4(P_3^*(\mathrm{i}k)+\mathrm{i}P_2^*(\mathrm{i}k))\\ 4(A_4^*(\mathrm{i}k)+\mathrm{i}A_1^*(\mathrm{i}k)) & 4(A_6^*(\mathrm{i}k)+\mathrm{i}A_5^*(\mathrm{i}k)) & 8(A_3^*(\mathrm{i}k)+\mathrm{i}A_2^*(\mathrm{i}k)) \end{pmatrix}\end{aligned} \tag{2.30}$$

For the work presented here, experimentally determined coefficients of static aerodynamic forces and admittances of motion-induced aerodynamic forces are taken from Bergmann (2004). They were measured on scaled rigid cross-section models in a water tunnel in smooth flow. The finite length of the rigid cross-section models across the water-tunnel width allows for taking periodical spatial flow effects into account, which are averaged in the measured forces. For a variety of cross sections, data sets are available. This data, together with numerically determined aerodynamic derivatives according to Thiesemann (2008), is currently also accessible on the website of the Structural Analysis and Steel Structures Institute of the Hamburg University of Technology (www.tu-harburg.de/sdb). The idealised cross sections shown in Figure 2.7 have been selected from those given in Bergmann (2004). As often done, the motion-induced drag force D and the influence of the horizontal motion $\dot{p}$ on the other force components were assumed to be negligible in the experiments. Hence, the definition of the motion-induced aerodynamic forces is reduced to the notation given in Eq. (2.19a). The measured static aerodynamic forces, however, include all components given in Eq. (2.29c).

The used aerodynamic admittances were obtained from measurements with the forced vibration method. In detail, the frequency responses $\mathbf{G}_{ae}(\mathrm{i}k)$ were measured for several single-frequency inputs. Since the force-displacement relation is more or less non-linear, as explained in Section 2.1, the aerodynamic derivatives depend on the zero position of the cross section and the amplitudes of the harmonic input. In the zero position that aerodynamic derivatives were extracted for, the

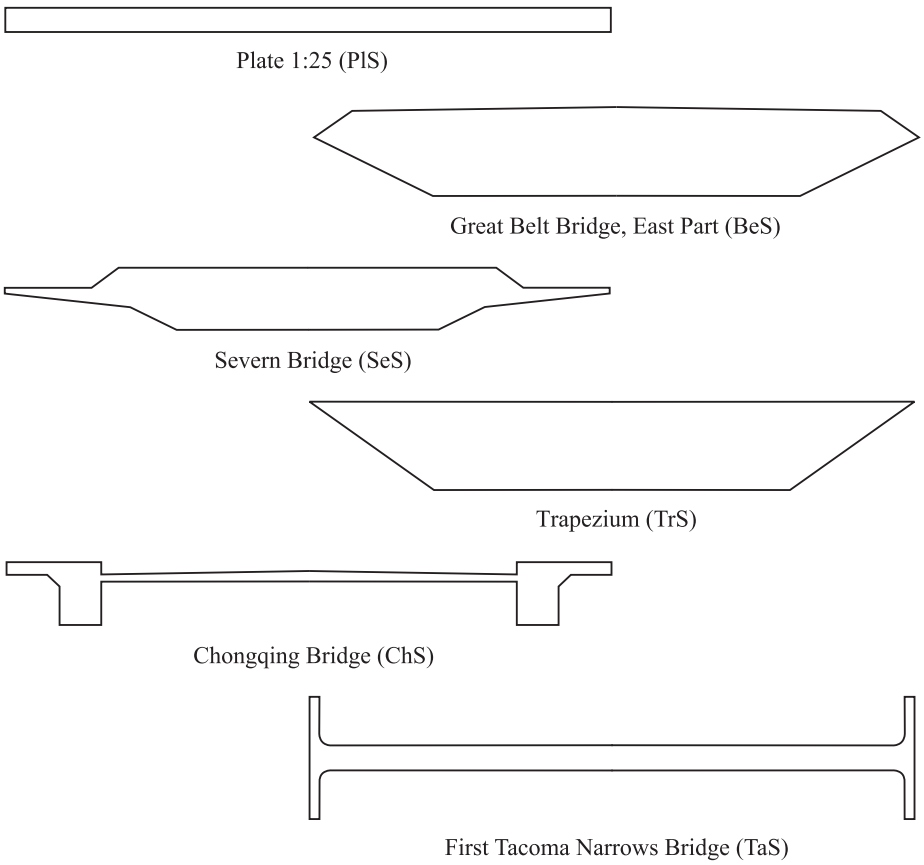

Figure 2.7: Selection of idealised cross sections which measured aerodynamic derivatives are available for in Bergmann (2004). Abbreviations are defined within brackets.

vertical symmetry axis of the cross section is perpendicular to the constant horizontal reference flow velocity U, as shown in Figure 2.6. Hence, the change of the aerodynamic derivatives due to a non-zero mean deflection of the cross section is not taken into account here. The data determined at $\hat{h}/b = 0.04$ and $\hat{\alpha} = 5.0°$, which are in the middle of the measured amplitude range, is used. The aerodynamic derivatives have been readout in the frequency intervals $[k_{\min}, k_{\max}]$ whose endpoints are given in Table 2.1.

Table 2.1: Frequency interval endpoints of the readout derivatives.

	PlS	BeS	SeS	TrS	ChS	TaS
$k_{\min}$	0.188	0.175	0.187	0.187	0.187	0.189
$k_{\max}$	0.941	1.051	1.028	1.026	1.026	1.038

Some more problems concerning this kind of measurement of aerodynamic derivatives with scaled models should be mentioned. These occur in connection with the model assumptions of Eq. (2.1) and Eq. (2.8). To some extent, they are also addressed in Bergmann (2004).

According to Eq. (2.8), the reduced frequency p is the only parameter that determines the unsteady flow field. If this parameter is identical for geometrically similar cross sections, identical

aerodynamic derivatives are assumed. The influence of other similarity parameters is neglected. For the similarity of the air flow as a viscous fluid, however, especially the Reynolds number $Re = U(2b)/\nu$, as a measure of the ratio of inertial forces to viscous forces, plays a decisive role. In the definition of the Reynolds number, ν stands for the kinematic viscosity. The numerical value of the Reynolds number crucially determines the structure of the boundary layer around and the flow behind the body. It affects the occurrence of a separated and a reattached flow and the existence of three-dimensional flow patterns. The water-tunnel experiments were carried out for Reynolds numbers within the range $Re \approx 10^5 \div 10^6$. Aerodynamic derivatives used here were measured at $Re \approx 2 \cdot 10^5$. The water-tunnel experiments show Reynolds numbers that are similar to those in usual wind-tunnel measurements because the advantage of a fifteen-fold lower kinematic viscosity is compensated by a comparably lower speed of the oncoming flow. The Reynolds numbers of the flow around girder cross sections of large-span bridges, however, have values of roughly $Re \approx 10^8$. Contrary to the often heard statement that the flow around sharp-edged cross sections is independent of the Reynolds number, even the steady flow around an unmoved trapezoidal cross section significantly changes in the range of $Re \approx 10^5 \div 10^6$ (Schewe 2001). Consequently, the aerodynamic force coefficients also change noticeably. A comparable behaviour cannot be excluded for unsteady flows. In Bergmann (2004), it is mentioned that a minimum Reynolds number was kept for the experiments with most cross sections. A flow condition similar to the original situation should thus have occurred. The statement is further justified with a low influence of the Reynolds number on the measured unsteady aerodynamic force coefficients. Only at low values of the imaginary part k of the reduced frequency, the aerodynamic derivatives of the cross sections ChS and TaS considerably depend on the Reynolds number.

A further problem appears if the frequency of the motion is around the Strouhal frequency. The Strouhal frequency is the frequency of the vortex-induced aerodynamic forces that occur due to the flow separation behind bluff bodies. In this case, motion-induced and vortex-induced aerodynamic forces cannot be clearly separated. At high frequency ranges, the measured data is additionally skewed by the resonance of the force balance. The distortion of the experimental data due to the two latter phenomena should be low or negligible in the intervals given in Table 2.1.

The stochastical nature of the aerodynamic derivatives is not investigated in Bergmann (2004). The lack of a reliable data basis for a stochastic representation of the aerodynamic transfer is one reason for the chosen deterministic formulation. Mainly, idealised cross sections were used in the experiments. The influence of geometric details like railings and traffic barriers was not comprehensively examined. In the work presented here, the aerodynamic effect of snow banks or ice accretion on railings, as well as the flow modification due to vehicles is not taken into account either.

Beyond the described aerodynamic derivatives and the coefficients of the static aerodynamic forces, no other experimentally determined aerodynamic force coefficients are used. Especially for bridge cross sections with flaps, no experimental data sets comparable to those described in Bergmann (2004) exist. Here, all gust-induced aerodynamic forces are described with the theoretical flat-plate values for the sake of simplicity, though values in real flow can strongly differ. In Jancauskas & Melbourne (1986), for instance, it is shown that the measured absolute values of the admittance of gust-induced aerodynamic forces on rectangular cross sections along the imaginary frequency axis are higher than the theoretical flat-plate values based on the Sears function. For the comparison, it has to be kept in mind that the absolute value of the original Sears function $|S(\mathrm{i}k)e^{\mathrm{i}k}|$ equals the absolute value of the consistent Sears function $|S(\mathrm{i}k)|$ at purely imaginary frequencies.

3 Approximation of Aerodynamic Admittances with Rational Functions

3.1 Analytical Approaches for Aerodynamic Transfer Functions

Chapter 2 shows that the aerodynamic transfer functions $\mathbf{G}_{\mathrm{ae}}(s)$ and $\mathbf{G}_{\mathrm{ae}}^{\mathrm{g}}(s)$ of most aerodynamically effective structural shapes in real flow are only known in the sense of a non-parametric model for a limited number of complex-conjugate frequencies within finite intervals on the imaginary axis. An approximation with analytical functions, which should be defined for almost arbitrary complex frequencies, allows for a continuous description in the complex frequency plane. This kind of parametric system identification with a black-box model does not only exist in the field of aerodynamics but for all physical phenomena which are described with transfer equations like Eq. (2.1). If the analytical approximation functions meet the requirements for Laplace transforms, continuous and causal time-domain descriptions in terms of impulse responses can be obtained. Moreover, approximation functions can have advantages concerning their mathematical handling even if more exact analytical transfer functions are available.

In aerospace as well as in bridge engineering, rational functions are usually employed to represent the aerodynamic transfer behaviour of Eq. (2.1) in the frequency domain. Several aspects of this approach are described in the next sections. The first proposal of using rational functions is given in Jones (1938) for approximating the Theodorsen function. There, the rational function is obtained from the approximation of the corresponding step response, the Wagner function, in the time domain. Another example of an analytical approach for the aerodynamic transfer behaviour is published in Garrick (1938), again in the time domain for the Wagner function. This kind of approximation, which leads in the frequency domain to a transfer function with a logarithmic term, is generalised to other shapes of aircraft wings in Stark (1984). Both latter approaches are not dealt with here. A further interesting idea is presented in Jung & al. (2012). Cubic splines are used for approximating the frequency response of the motion-induced aerodynamic forces of bridge decks. In the fitting procedure, the approximation functions are selected so that the corresponding impulse responses satisfy the causality condition in a weak sense. From the results presented there, the aerodynamic transfer function can be determined for arbitrary complex

frequencies within the region of absolute convergence with a numerical Laplace transform. Since classical methods of control theory cannot be applied together with such a transfer function representation, it is not considered herein.

3.2 Rational Function Approaches for Single Matrix Elements of the Aerodynamic Admittance

Complex-valued rational functions are the most commonly used analytical expressions for approximating the aerodynamic transfer behaviour in aerospace and in bridge engineering. Since q_0 is an explicitly known factor, only the normalised aerodynamic admittances $\mathbf{Q}(p)$ and $\mathbf{Q}^{\mathrm{g}}(p)$ as functions of the reduced complex frequency must be approximated. The rational functions can be split up into a polynomial and a purely rational part. Using the finite series of a complex partial fraction expansion of the latter part is most suitable for an explanation. For single elements of the aerodynamic admittances, the chosen approximation functions are as follows.

$$Q(p) = A_0 + A_1 p + A_2 p^2 + \sum_{\mu=1}^{n_\gamma} \sum_{\kappa=1}^{\nu_\mu} \frac{A_{\mu\kappa}}{\left(p+\gamma_\mu\right)^\kappa} \tag{3.1a}$$

$$Q^{\mathrm{g}}(p) = A_0 + \sum_{\mu=1}^{n_\gamma} \sum_{\kappa=1}^{\nu_\mu} \frac{A_{\mu\kappa}}{\left(p+\gamma_\mu\right)^\kappa} \tag{3.1b}$$

In order to avoid using too many indices, the same approximation variables are used for both kinds of aerodynamic admittances despite the approximation being carried out separately. The n_γ different poles of the rational functions are denoted with $(-\gamma_\mu)$ and their order or multiplicity with ν_μ. For the coefficients of the polynomial part and the partial fractions, the variables A_j and $A_{\mu\kappa}$ are respectively employed.

A rational function is a meromorphic function on the whole complex frequency plane. That means it is a function which is holomorphic at all complex frequencies except for its poles. If the rational function is seen as a Laplace transform, a straight line parallel to the imaginary axis through the pole with the largest real part is the open boundary of the region of absolute convergence. In order to extend the Laplace transform to all other points of the complex frequency plane where the rational function is holomorphic, the concept of analytical continuation can be applied.

The degrees of the polynomial parts of the rational function approximations in Eq. (3.1) are chosen according to the results of the theoretically described flat plate. As explained for the flat plate in Section 2.2.2, its transfer behaviour of the motion-induced aerodynamic forces is twice differentiating whereas that of the gust-induced aerodynamic forces does not differentiate. The

following derivations are shown for the admittance of motion-induced aerodynamic forces. The results can be adjusted to the gust-induced aerodynamic forces without any difficulty.

Using tables of Laplace transforms, the aerodynamic impulse responses that correspond to the analytical approximation function of the aerodynamic admittances in Eq. (3.1) can be determined. The matrix elements of the aerodynamic impulse response $\mathbf{Q}(\bar{t})$ of the motion-induced aerodynamic forces have the following form.

$$Q(\bar{t}) = A_0\bar{\delta}(\bar{t}) + A_1\bar{\delta}'(\bar{t}) + A_2\bar{\delta}''(\bar{t}) + \sum_{\mu=1}^{n_\gamma}\sum_{\kappa=1}^{\nu_\mu} A_{\mu\kappa}\frac{\bar{t}^{\kappa-1}}{(\kappa-1)!}\mathrm{e}^{-\gamma_\mu\bar{t}} \tag{3.2}$$

Since the inverse $\mathscr{L}_p$ transform is adopted, this impulse response has to be used in connection with the $\overset{\bar{t}}{*}$ convolution.

In the aerodynamic impulse responses, only the terms that correspond to the partial fractions in Eq. (3.1) do not equal zero for $t > 0$. Therefore, the partial fractions are often called lag terms. Regarding the location of their poles $(-\gamma_\mu)$, the partial fractions can be separated into several types. The mandatory pole location in the left complex half-plane ensures impulse responses that decrease with time according to a stable transfer behaviour. Since the imaginary frequency axis is part of the region of absolute convergence, the frequency and time-domain representations are also Fourier pairs. The coefficients A_j of the polynomial part must be real to obtain real time-domain results. Usually, simple $(\nu_\mu = 1)$ real poles with real coefficients $A_{\mu\kappa}$ are applied. As a result, the associated aerodynamic impulse responses are decaying exponential functions. Pairs of simple complex-conjugate poles with complex-conjugate coefficients are, however, possible as well. Complex conjugates are necessary to ensure a real aerodynamic impulse response in the time domain. Concerning their partial fractions, the pairs of complex impulse responses can be rewritten as follows.

$$A_{\mu\kappa}\mathrm{e}^{-\gamma_\mu\bar{t}} + A^{\mathrm{c}}_{\mu\kappa}\mathrm{e}^{-\gamma^{\mathrm{c}}_\mu\bar{t}} = \left|A_{\mu\kappa}\right| e^{-\mathrm{Re}(\gamma_\mu)\bar{t}} 2\cos\left(\mathrm{Im}(\gamma_\mu)\bar{t} - \arg(A_{\mu\kappa})\right) \tag{3.3}$$

Accordingly, the pairs of aerodynamic impulse responses can be considered as a decaying cosine function. In bridge engineering, a similar approach is used for instance in Sternberg (1991) for the admittances of motion-induced aerodynamic forces. The poles described so far can also be multiple $(\nu_\mu > 1)$. For this case, the aerodynamic impulse responses include an additional factor in the form of $\bar{t}^{\kappa-1}/(\kappa-1)!$, which is dominant for small time values. The proposal to use multiple real poles is published in Eversman & Tewari (1991a) and recommended there for aerodynamic derivatives of aerofoils. A systematic investigation of the suitability of complex-conjugate or multiple poles in the rational function approximations of aerodynamic admittances still needs to be done for applications in bridge engineering.

Since the partial fraction expansion is chosen for the representation of the rational function approximation, the poles, but not the zeros of the aerodynamic transfer functions, can be a priori constrained. Hence, the aerodynamic transfer can have a non-minimum phase behaviour.

Concerning the constant summand of the polynomial parts and the partial fractions of Eq. (3.1), which form the causal portion of the approximation, it would be interesting to find more or less realistic mechanical systems that possess a similar transfer behaviour. This is attempted in Omenzetter & al. (2000a) for a simple real pole. Certainly, this kind of analogy would help to understand the rational function approach in a better way.

From the mathematical point of view, rational functions have a major advantage compared to other functions. When using them, the input-output transfer in Eq. (2.1) can be described in the time domain with a system of linear differential equation with constant coefficients. If, in addition, the transfer is causal, it can be realised with a linear time-invariant state-space model. Hence, an alternative to the convolution in Eq. (2.3) is available in the time domain. Based on the form of Eq. (3.1), the realisation is derived below for the transfer of the motion-induced aerodynamic forces from one element ξ_s of the input vector to one element f_ae of the output vector. Analogously, the state-space model for the gust-induced aerodynamic forces can be found. This kind of realisation from a partial fraction expansion of a rational transfer function to a state-space model is shown, for instance, in Unbehauen (2007) for an abstract dynamic system in a similar way.

After inserting Eq. (3.1a) into Eq. (2.1a), an aerodynamic state $\xi_{\mathrm{a},\mu\kappa}$ for each summand of the inner series of the expansion can be defined for each pole $(-\gamma_\mu)$. These mathematically introduced aerodynamic states are also called lag states. They possess the mathematical descriptions of first-order lag elements. The lag state $\xi_{\mathrm{a},\mu 1}$ of the first summand ($\kappa = 1$) is connected to the input ξ_s.

$$\xi_{\mathrm{a},\mu 1} = \frac{1}{(p+\gamma_\mu)}\xi_\mathrm{s} \qquad \bullet\!\!-\!\!\circ \qquad \xi'_{\mathrm{a},\mu 1} = -\gamma_\mu \xi_{\mathrm{a},\mu 1} + \xi_\mathrm{s} \tag{3.4}$$

For the lag states $\xi_{\mathrm{a},\mu\kappa}$ of all other summands ($\kappa > 1$), the definition of the preceding lag states $\xi_{\mathrm{a},\mu(\kappa-1)}$ is used.

$$\begin{aligned} \xi_{\mathrm{a},\mu\kappa} &= \frac{1}{(p+\gamma_\mu)^\kappa}\xi_\mathrm{s} \\ &= \frac{1}{(p+\gamma_\mu)}\xi_{\mathrm{a},\mu(\kappa-1)} \end{aligned} \qquad \bullet\!\!-\!\!\circ \qquad \xi'_{\mathrm{a},\mu\kappa} = -\gamma_\mu \xi_{\mathrm{a},\mu\kappa} + \xi_{\mathrm{a},\mu(\kappa-1)} \tag{3.5}$$

Eq. (3.4) and Eq. (3.5) additionally show the corresponding first-order differential equations in the time domain. They are derived assuming that the frequency-domain functions are $\mathscr{L}_p$ transforms. For the inverse transform and the function values of the time $t < 0$, the statements of

Section 2.1 have to be kept in mind. A combination of the time-domain expression in Eq. (3.4) and Eq. (3.5) with the inverse Laplace transforms of all the other parts of Eq. (2.1a) and Eq. (3.1a) leads to the following state-space model.

$$\boldsymbol{\xi}_\mathrm{a}' = \mathbf{R}\boldsymbol{\xi}_\mathrm{a} + \begin{pmatrix} \mathbf{0} & \mathbf{0} & \mathbf{E} \end{pmatrix} \begin{pmatrix} \xi_\mathrm{s}'' \\ \xi_\mathrm{s}' \\ \xi_\mathrm{s} \end{pmatrix} \tag{3.6a}$$

$$f_\mathrm{ae} = q_0 \mathbf{D}\boldsymbol{\xi}_\mathrm{a} + q_0 \begin{pmatrix} A_2 & A_1 & A_0 \end{pmatrix} \begin{pmatrix} \xi_\mathrm{s}'' \\ \xi_\mathrm{s}' \\ \xi_\mathrm{s} \end{pmatrix} \tag{3.6b}$$

Replacing the differentiation $(\ )'$ with $\dot{(\ )}$ through the use of Eq. (1.2) gives the same result as that obtained if the frequency domain descriptions of the aerodynamic states are considered as $\mathscr{L}_s$ transforms. The relationship to the explanations of Section 2.1 can be established when the differentiation is seen as a convolution with the derivative of the Dirac impulse. To circumvent the problem of the differentiating, non-causal terms in Eq. (3.1a), the first two derivatives of the input are additionally listed in the input vector of the state-space model. The vectors and matrices in Eq. (3.6) are defined as follows.

$$\boldsymbol{\xi}_\mathrm{a} = \begin{pmatrix} \boldsymbol{\xi}_{\mathrm{a},1} \\ \vdots \\ \boldsymbol{\xi}_{\mathrm{a},\mu} \\ \vdots \\ \boldsymbol{\xi}_{\mathrm{a},n_\gamma} \end{pmatrix}, \quad \boldsymbol{\xi}_{\mathrm{a},\mu} = \begin{pmatrix} \xi_{\mathrm{a},\mu\nu_\mu} \\ \vdots \\ \xi_{\mathrm{a},\mu 1} \end{pmatrix}, \qquad \mathbf{E} = \begin{pmatrix} \mathbf{E}_1 \\ \vdots \\ \mathbf{E}_\mu \\ \vdots \\ \mathbf{E}_{n_\gamma} \end{pmatrix}, \quad \mathbf{E}_\mu = \begin{pmatrix} 0 \\ \vdots \\ 0 \\ 1 \end{pmatrix} \tag{3.7a}$$

$$\mathbf{R} = \mathrm{diag}\begin{pmatrix} \mathbf{R}_1 & \cdots & \mathbf{R}_\mu & \cdots & \mathbf{R}_{n_\gamma} \end{pmatrix}, \quad \mathbf{R}_\mu = \begin{pmatrix} -\gamma_\mu & 1 & & 0 \\ & -\gamma_\mu & \ddots & \\ & & \ddots & 1 \\ 0 & & & -\gamma_\mu \end{pmatrix} \tag{3.7b}$$

$$\mathbf{D} = \begin{pmatrix} \mathbf{D}_1 & \cdots & \mathbf{D}_\mu & \cdots & \mathbf{D}_{n_\gamma} \end{pmatrix}, \quad \mathbf{D}_\mu = \begin{pmatrix} A_{\mu\nu_\mu} & \cdots & A_{\mu 1} \end{pmatrix} \tag{3.7c}$$

The mathematically introduced state vector $\boldsymbol{\xi}_\mathrm{a}$ and the state-space model only guarantee the chosen input-output transfer approach in the sense of one possible state-space realisation. As dealing with black-box models, the vector $\boldsymbol{\xi}_\mathrm{a}$ is not a system state that describes the internal structure of the flow with physical quantities. A natural response due to a non-zero initial system state, thus, lacks any physical basis. The length of the state vector $\boldsymbol{\xi}_\mathrm{a}$ equals the number of partial fractions in Eq. (3.1a). According to the described realisation technique, the system matrix $\mathbf{R}$ results in the general complex Jordan normal form whose eigenvalues are the poles of the

admittance function. The case of eigenvalues of the same value but different eigenvectors, which are, thus, not multiple in the sense used before, is included in the model. In Eq. (3.1a), this case corresponds to a summand that is subdivided into several summands.

When transforming Eq. (3.6) into the Laplace domain, the defined matrices can be used to equivalently rewrite the rational function approach of Eq. (3.1a) in an elegant way.

$$Q(p) = A_0 + A_1 p + A_2 p^2 + \mathbf{D}(p\mathbf{I} - \mathbf{R})^{-1}\mathbf{E} \tag{3.8}$$

3.3 Matrix-Based Rational Function Approaches

The main disadvantage of the separated approximation of single admittance-matrix elements is the huge size of the corresponding state-space model. For each element of the aerodynamic admittance matrix, as many aerodynamic states have to be defined as partial fractions are used. To overcome this shortcoming, two commonly used matrix-based rational function approaches have been developed in the past for applications in aerospace engineering. They are addressed at the end of this section and applied afterwards. These approaches can be seen as special cases of the two more general matrix-based approaches that are derived first.

The starting point for the first approach is Eq. (3.1a). Using the same poles with the same multiplicity for all elements of the aerodynamic admittance leads to a partial fraction expansion with matrix coefficients.

$$\mathbf{Q}(p) = \mathbf{A}_0 + \mathbf{A}_1 p + \mathbf{A}_2 p^2 + \sum_{\mu=1}^{n_\gamma} \sum_{\kappa=1}^{\nu_\mu} \frac{\mathbf{A}_{\mu\kappa}}{\left(p+\gamma_\mu\right)^\kappa} \tag{3.9}$$

The aerodynamic impulse response $\mathbf{Q}(\bar{t})$ is just the matrix version of the scalar form in Eq. (3.2).

Vectorial aerodynamic states $\xi_{\mathrm{a},\mu\kappa}$ can be defined as shown for the scalar case in Eq. (3.4) and Eq. (3.5). The length of these aerodynamic states equals that of the input vector ξ_s. With the help of these states, a representation with a state-space model can again be assembled in the time domain, which is just the extended version of the model for the element-wise transfer shown in Eq. (3.6).

$$\xi_\mathrm{a}' = \mathbf{R}\xi_\mathrm{a} + \begin{pmatrix} \mathbf{0} & \mathbf{0} & \mathbf{E} \end{pmatrix} \begin{pmatrix} \xi_\mathrm{s}'' \\ \xi_\mathrm{s}' \\ \xi_\mathrm{s} \end{pmatrix} \tag{3.10a}$$

$$\mathbf{f}_{\mathrm{ae}} = q_0 \mathbf{D} \boldsymbol{\xi}_{\mathrm{a}} + q_0 \begin{pmatrix} \mathbf{A}_2 & \mathbf{A}_1 & \mathbf{A}_0 \end{pmatrix} \begin{pmatrix} \xi_{\mathrm{s}}'' \\ \xi_{\mathrm{s}}' \\ \xi_{\mathrm{s}} \end{pmatrix} \tag{3.10b}$$

In detail, the model vectors and matrices are defined as follows.

$$\boldsymbol{\xi}_{\mathrm{a}} = \begin{pmatrix} \xi_{\mathrm{a},1} \\ \vdots \\ \xi_{\mathrm{a},\mu} \\ \vdots \\ \xi_{\mathrm{a},n_\gamma} \end{pmatrix}, \quad \xi_{\mathrm{a},\mu} = \begin{pmatrix} \xi_{\mathrm{a},\mu\nu_\mu} \\ \vdots \\ \xi_{\mathrm{a},\mu 1} \end{pmatrix}, \quad \mathbf{E} = \begin{pmatrix} \mathbf{E}_1 \\ \vdots \\ \mathbf{E}_\mu \\ \vdots \\ \mathbf{E}_{n_\gamma} \end{pmatrix}, \quad \mathbf{E}_\mu = \begin{pmatrix} \mathbf{0} \\ \vdots \\ \mathbf{0} \\ \mathbf{I} \end{pmatrix} \tag{3.11a}$$

$$\mathbf{R} = \mathrm{diag} \begin{pmatrix} \mathbf{R}_1 & \cdots & \mathbf{R}_\mu & \cdots & \mathbf{R}_{n_\gamma} \end{pmatrix}, \quad \mathbf{R}_\mu = \begin{pmatrix} -\gamma_\mu \mathbf{I} & \mathbf{I} & & \mathbf{0} \\ & -\gamma_\mu \mathbf{I} & \ddots & \\ & & \ddots & \mathbf{I} \\ \mathbf{0} & & & -\gamma_\mu \mathbf{I} \end{pmatrix} \tag{3.11b}$$

$$\mathbf{D} = \begin{pmatrix} \mathbf{D}_1 & \cdots & \mathbf{D}_\mu & \cdots & \mathbf{D}_{n_\gamma} \end{pmatrix}, \quad \mathbf{D}_\mu = \begin{pmatrix} \mathbf{A}_{\mu\nu_\mu} & \cdots & \mathbf{A}_{\mu 1} \end{pmatrix} \tag{3.11c}$$

Compared to the scalar entries of the matrices in Eq. (3.7), the matrices in Eq. (3.11) contain matrix blocks. The system matrix $\mathbf{R}$ shows a block version of the Jordan form that can be converted to the usually used Jordan matrix notation by regrouping the entries of the state vector. In addition to the chosen multiplicity ν_μ, the eigenvalues are multiple according to the size of the identity matrix $\mathbf{I}$, which equals the length of the input vector $\boldsymbol{\xi}_{\mathrm{s}}$ of the aerodynamic transfer equation. This multiplicity is, however, harmless because it is in connection with different eigenvectors. Through the use of the matrix-based rational function approximation, the total length of the state vector $\boldsymbol{\xi}_{\mathrm{a}}$ is significantly reduced to the length of the input vector times the number of partial fraction in Eq. (3.9).

Employing the matrices of Eq. (3.11), the approach in Eq. (3.9) can again be rewritten in the following short form.

$$\mathbf{Q}(p) = \mathbf{A}_0 + \mathbf{A}_1 p + \mathbf{A}_2 p^2 + \mathbf{D}(p\mathbf{I} - \mathbf{R})^{-1}\mathbf{E} \tag{3.12}$$

In addition to the direct transformation of Eq. (3.9), the matrix of aerodynamic impulse responses $\mathbf{Q}(\bar{t})$ can also be obtained from the state-space representation by applying standard procedures.

The identity matrices in $\mathbf{R}_\mu$ are a sign of an information redundancy in the approach of Eq. (3.9). Hence, a second approach in the form of Eq. (3.12) and Eq. (3.10) that uses the matrix $\mathbf{R}_\mu$ of Eq. (3.7b) seems to be promising. For the second approach, the employed vectors and matrices are defined as follows.

$$\xi_{\mathrm{a}} = \begin{pmatrix} \xi_{\mathrm{a},1} \\ \vdots \\ \xi_{\mathrm{a},\mu} \\ \vdots \\ \xi_{\mathrm{a},n_\gamma} \end{pmatrix}, \quad \xi_{\mathrm{a},\mu} = \begin{pmatrix} \xi_{\mathrm{a},\mu\nu_\mu} \\ \vdots \\ \xi_{\mathrm{a},\mu 1} \end{pmatrix}, \qquad \mathbf{E} = \begin{pmatrix} & \vdots & \\ \cdots & E_{jl} & \cdots \\ & \vdots & \end{pmatrix} \tag{3.13a}$$

$$\mathbf{R} = \operatorname{diag}\begin{pmatrix} \mathbf{R}_1 & \cdots & \mathbf{R}_\mu & \cdots & \mathbf{R}_{n_\gamma} \end{pmatrix}, \quad \mathbf{R}_\mu = \begin{pmatrix} -\gamma_\mu & 1 & & 0 \\ & -\gamma_\mu & \ddots & \\ & & \ddots & 1 \\ 0 & & & -\gamma_\mu \end{pmatrix} \tag{3.13b}$$

$$\mathbf{D} = \begin{pmatrix} & \vdots & \\ \cdots & D_{jl} & \cdots \\ & \vdots & \end{pmatrix} \tag{3.13c}$$

The approach goes along with a further considerable reduction of the number of elements in the state vector ξ_{a}, which is equal to the number of partial fractions in Eq. (3.9). The first approach in Eq. (3.9) and Eq. (3.12) uses common poles but separated coefficients for each element of the aerodynamic admittance matrix $\mathbf{Q}$, whereas this approach also accesses a common pool of coefficients in the matrices $\mathbf{D}$ and $\mathbf{E}$. To avoid too strong couplings between the single elements of the aerodynamic admittance matrix $\mathbf{Q}$, all the elements of the matrices $\mathbf{D}$ and $\mathbf{E}$ can have non-zero values. The total number of these elements is, however, considerably smaller than the number of non-zero entries of the matrix $\mathbf{D}$ in Eq. (3.11) if the aerodynamic transfer model shows more than one element in the input and the output vector and $\mathbf{Q}$ is not a square matrix with four elements. Whether the already mentioned couplings are not too restrictive for a sufficiently flexible approximation when all kinds of poles are applied has not been investigated.

An additional reduction of the number of aerodynamic states can only be achieved if the aerodynamic admittances of motion-induced and gust-induced aerodynamic forces are combined, like $(\mathbf{Q}\ \mathbf{Q}^{\mathrm{g}})$, and approximated together with the second general approach. This procedure requires that both aerodynamic admittances are approximated in the same way with the same poles. The physical background of this step is at least questionable. An approximation of the combined admittances is not considered here.

Other kinds of general matrix-based approaches of the rational function approximation are given, for instance, in Morino & al. (1995). One major disadvantage of these approaches is that the system matrices do not feature the Jordan normal form. Hence, the kinds of poles and their values cannot be a priori constrained.

The matrix approach in Eq. (3.9) for the special case of simple real poles essentially corresponds to the formulas proposed in Sevart (1975), Roger (1977), and Abel (1979). It is given in the following form in Tiffany Hoadley & Adams Jr. (1988).

$$\mathbf{Q}(p) = \mathbf{A}_0 + \mathbf{A}_1 p + \mathbf{A}_2 p^2 + \sum_{\mu=1}^{n_\gamma} \mathbf{A}_{\mu+2} \frac{p}{p+\gamma_\mu} \tag{3.14}$$

Here, this approach is referred to as the Roger approach, as it is usually done in engineering publications. Employing simple real poles for the rational function approximation of aerodynamic admittances is most common in aerospace engineering and has also found its way into bridge engineering (e. g. Xie & Xiang 1985, Wilde & al. 1996, Boonyapinyo & al. 1999, Chen & al. 2000). Compared to those in Eq. (3.9), the nominators of the lag terms in Eq. (3.14) additionally contain the complex reduced frequency p. A polynomial division shows that Eq. (3.14) is equivalent to the special case of Eq. (3.9). The nominator modification allows identifying the steady values $\mathbf{Q}(p=0)$ of the aerodynamic admittances with the elements of the $\mathbf{A}_0$ matrix, as can also be seen when looking at the following aerodynamic step response.

$$\mathscr{L}_p^{-1}\{\mathbf{Q}(p)/p\} = \int_0^{\bar{t}} \mathbf{Q}(\bar{\tau})\,\mathrm{d}\bar{\tau} = \mathbf{A}_0 + \mathbf{A}_1 \bar{\delta}(\bar{t}) + \mathbf{A}_2 \bar{\delta}'(\bar{t}) + \sum_{\mu=1}^{n_\gamma} \mathbf{A}_{\mu+2}\, \mathrm{e}^{-\gamma_\mu \bar{t}} \tag{3.15}$$

Since Eq. (3.14) is considered as a $\mathscr{L}_p$ transform and the aerodynamic admittance $\mathbf{Q}(p)$ is divided by p, this step response has to be adopted in connection with the $\overset{\bar{t}}{*}$ convolution and the $(\ )'$ differentiation of the input. Analogously, the aerodynamic impulse response can be found.

$$\begin{aligned}\mathscr{L}_p^{-1}\{\mathbf{Q}(p)\} = \mathbf{Q}(\bar{t}) = \left(\mathbf{A}_0 + \sum_{\mu=1}^{n_\gamma} \mathbf{A}_{\mu+2}\right) \bar{\delta}(\bar{t}) + \mathbf{A}_1 \bar{\delta}'(\bar{t}) + \mathbf{A}_2 \bar{\delta}''(\bar{t}) \\ - \sum_{\mu=1}^{n_\gamma} \mathbf{A}_{\mu+2} \gamma_\mu\, \mathrm{e}^{-\gamma_\mu \bar{t}}\end{aligned} \tag{3.16}$$

Due to the additional factor in the nominator of the lag terms in Eq. (3.14), the short version of the general approach in Eq. (3.12) must be modified.

$$\mathbf{Q}(p) = \mathbf{A}_0 + \mathbf{A}_1 p + \mathbf{A}_2 p^2 + \mathbf{D}(p\mathbf{I} - \mathbf{R})^{-1}\mathbf{E}p \tag{3.17}$$

Consequently, the position of the matrix $\mathbf{E}$ in the state equation of the state-space model in Eq. (3.10) changes.

$$\xi_\mathrm{a}' = \mathbf{R}\xi_\mathrm{a} + \begin{pmatrix} \mathbf{0} & \mathbf{E} & \mathbf{0} \end{pmatrix} \begin{pmatrix} \xi_\mathrm{s}'' \\ \xi_\mathrm{s}' \\ \xi_\mathrm{s} \end{pmatrix} \tag{3.18}$$

The form of the output equation remains the same. Using only simple real poles leads to the following reduced entries in the model vectors and matrices.

$$\boldsymbol{\xi}_\mathrm{a} = \begin{pmatrix} \xi_{\mathrm{a},1} \\ \vdots \\ \xi_{\mathrm{a},n_\gamma} \end{pmatrix}, \quad \mathbf{E} = \begin{pmatrix} \mathbf{I} \\ \vdots \\ \mathbf{I} \end{pmatrix}, \qquad \begin{aligned} \mathbf{R} &= \operatorname{diag}\begin{pmatrix} -\gamma_1\mathbf{I} & \cdots & -\gamma_{n_\gamma}\mathbf{I} \end{pmatrix} \\ \mathbf{D} &= \begin{pmatrix} \mathbf{A}_3 & \cdots & \mathbf{A}_{n_\gamma+2} \end{pmatrix} \end{aligned} \tag{3.19}$$

In Karpel & Strul (1996), for instance, the matrices are defined in another way.

$$\boldsymbol{\xi}_\mathrm{a} = \begin{pmatrix} \xi_{\mathrm{a},1} \\ \vdots \\ \xi_{\mathrm{a},n_\gamma} \end{pmatrix}, \quad \mathbf{E} = \begin{pmatrix} \mathbf{A}_3 \\ \vdots \\ \mathbf{A}_{n_\gamma+2} \end{pmatrix}, \qquad \begin{aligned} \mathbf{R} &= \operatorname{diag}\begin{pmatrix} -\gamma_1\mathbf{I} & \cdots & -\gamma_{n_\gamma}\mathbf{I} \end{pmatrix} \\ \mathbf{D} &= \begin{pmatrix} \mathbf{I} & \cdots & \mathbf{I} \end{pmatrix} \end{aligned} \tag{3.20}$$

In this notation, the length of the state vector is not connected to length of the input vector, as explained for the state-space model of Eq. (3.10) with the matrices in Eq. (3.11), but to the length of the output vector. Hence, using this notation is advantageous if the length of the output vector is shorter than the length of the input vector. A general matrix approach in Jordan normal form including all the other kinds of poles, however, cannot be derived in this format. The notation of Eq. (3.20) should, thus, only be seen as an alternative arrangement of the approximation matrices in the state-space model when the explained advantage can be achieved.

With the notation of Eq. (3.17), the aerodynamic step response in Eq. (3.15) and impulse response in Eq. (3.16) can be rewritten.

$$\mathscr{L}_p^{-1}\{\mathbf{Q}(p)/p\} = \int_0^{\bar{t}} \mathbf{Q}(\bar{\tau})\,\mathrm{d}\bar{\tau} = \mathbf{A}_0 + \mathbf{A}_1\bar{\delta}(\bar{t}) + \mathbf{A}_2\bar{\delta}'(\bar{t}) + \mathbf{D}\mathrm{e}^{\mathbf{R}\bar{t}}\mathbf{E} \tag{3.21a}$$

$$\mathscr{L}_p^{-1}\{\mathbf{Q}(p)\} = \mathbf{Q}(\bar{t}) = (\mathbf{A}_0 + \mathbf{D}\mathbf{E})\bar{\delta}(\bar{t}) + \mathbf{A}_1\bar{\delta}'(\bar{t}) + \mathbf{A}_2\bar{\delta}''(\bar{t}) + \mathbf{D}\mathbf{R}\mathrm{e}^{\mathbf{R}\bar{t}}\mathbf{E} \tag{3.21b}$$

Since the system matrix $\mathbf{R}$ is diagonal for the Roger approach, the matrix exponential function $\mathrm{e}^{\mathbf{R}\bar{t}}$ can easily be obtained by exponentiating every element on the main diagonal of $\mathbf{R}\bar{t}$.

Combining Eq. (3.17) with the matrices

$$\boldsymbol{\xi}_\mathrm{a} = \begin{pmatrix} \xi_{\mathrm{a},1} \\ \vdots \\ \xi_{\mathrm{a},n_\gamma} \end{pmatrix}, \quad \mathbf{D} = \begin{pmatrix} \vdots & & \\ \cdots & D_{jl} & \cdots \\ \vdots & & \end{pmatrix}, \quad \mathbf{E} = \begin{pmatrix} \vdots & & \\ \cdots & E_{jl} & \cdots \\ \vdots & & \end{pmatrix} \tag{3.22a}$$

$$\mathbf{R} = \operatorname{diag}\begin{pmatrix} -\gamma_1 & \cdots & -\gamma_{n_\gamma} \end{pmatrix} \tag{3.22b}$$

leads to the formula proposed in Karpel (1981), which can be seen as a reduction of the second general approach in Eq. (3.12) and Eq. (3.13) to the case of simple real poles. In the following sections, the approach combining Eq. (3.17) and Eq. (3.22) is addressed as the Karpel approach. The typical couplings between the elements of the aerodynamic admittance matrix become also apparent when the Karpel approach in the form of Eq. (3.17) is converted into the Roger form in Eq. (3.14). The elements of the lag-term matrix coefficients are then as follows.

$$A_{\mu+2,\,jl} = D_{j\mu} E_{\mu l} \tag{3.23}$$

For aerodynamic transfer functions with a single input or a single output, the Karpel approach essentially leads to the same results as the Roger approach because the Karpel approach has more free parameters and the Roger approach can be transformed into the Karpel form. For multiple-input multiple-output transfer systems, however, the Roger form cannot be converted into the Karpel form, in general. It can be expected that the common pool of coefficients in the Karpel approach leads to a worse approximation, especially when the different elements of an aerodynamic admittance matrix strongly differ in their order of magnitude. To assess a possible lowering of the approximation quality due to the Karpel approach, a comparison with the results of the Roger approach is always recommendable.

3.4 Identification Procedure

After deciding which rational function approach and which special kinds of poles are employed, the free values of the coefficients and the poles must be determined in order to fit the rational functions to the original values. For this purpose, all kinds of optimisation procedures can, in principle, be applied, taking into account various constraints. The use of complicated and time-consuming methods should, however, be avoided as far as possible.

As mentioned at the beginning of Section 3.3, the matrix-based approaches of Roger and Karpel are used in the following. In aerospace engineering, multilevel linear and non-linear optimisation procedures have been developed for the identification of these approaches that determine as many free parameters as possible by solving linear least-squares approximation problems (Karpel 1981, Tiffany Hoadley & Adams Jr. 1988). The procedure used here combines and adjusts the recommendations of several publications. It is implemented for an arbitrary size of the aerodynamic admittance matrix.

First, the identification procedure is described for the fit of the Karpel approach. An overview of the procedure is shown in Figure 3.1. The elements of the aerodynamic frequency-response matrix $\mathbf{Q}^{\mathrm{o}}(\mathrm{i}k)$ form the database of the original values. They must be available for a finite number n_k of purely imaginary reduced frequencies with positive values k. The number n_k must be at least

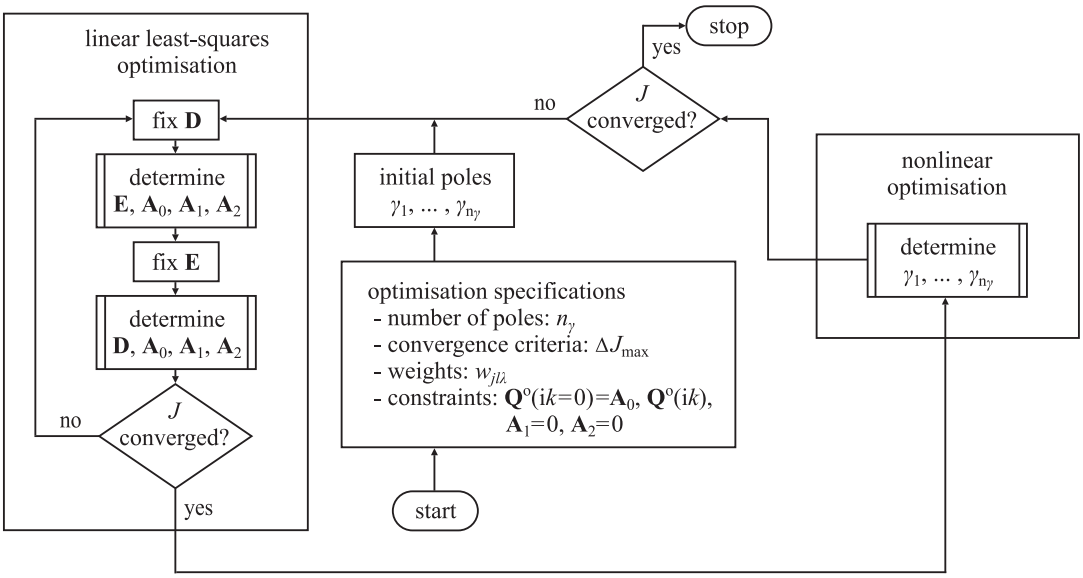

Figure 3.1: Flowchart of the parameter identification procedure for the Karpel approach.

large enough to determine all free parameters of the approximation problems. In the initial step of the identification, the number of employed poles is fixed and reasonable pole values are assumed. In contrast to the values of most matrix coefficients, this assumption is possible for the poles, as is explained in the next sections. While keeping the pole values constant, the matrix coefficients $\mathbf{A}_0$, $\mathbf{A}_1$, $\mathbf{A}_2$, $\mathbf{D}$, and $\mathbf{E}$ are determined by solving linear least-squares approximation problems with matrix techniques. Since the matrices $\mathbf{D}$ and $\mathbf{E}$ cannot be evaluated simultaneously with these techniques, they are determined iteratively until a convergence criterion is fulfilled. The linear least-squares approximation is implemented in a computer code as described in Karpel & Strul (1996). Several optional constraints can be taken into account. The $\mathbf{A}_0$ matrix can be identified with the original steady matrix $\mathbf{Q}^{\mathrm{o}}(p=0)$. To exactly match the approximation function with the original data $\mathbf{Q}^{\mathrm{o}}(\mathrm{i}k)$ at one non-zero purely imaginary reduced frequency, the values of the $\mathbf{A}_1$ and $\mathbf{A}_2$ matrices can be constrained. Finally, $\mathbf{A}_1$ and $\mathbf{A}_2$ can be set to be zero matrices in order to allow an approximation without them, as it is necessary for the gust admittance $\mathbf{Q}^{\mathrm{g}}$. Additionally, weights $w_{jl\lambda}$ can be used to improve the fit of the aerodynamic admittance matrix elements Q_{jl} at selected frequencies k_λ. The approximation error J, which is also used in the overall procedure to define a convergence criterion of the solution, is chosen exactly in the weighted least-squares sense (Karpel & Strul 1996).

$$J = \sqrt{\sum_{j,l,\lambda} \left| Q_{jl}(\mathrm{i}k_\lambda) - Q^{\mathrm{o}}_{jl}(\mathrm{i}k_\lambda) \right|^2 w^2_{jl\lambda}} \tag{3.24}$$

This error depends on the number n_k of selected frequencies, the number of elements in the aerodynamic admittance matrix $\mathbf{Q}$ and the size of these elements. To start the iteration loop, an

initial **D** matrix has to be defined. Here, all its elements are set to one and thus non-zero. The recommendation that is given in Tiffany Hoadley & Adams Jr. (1988), for instance, to use also zero elements, seems to be too restrictive for starting the approximation process. The iteration stops if the difference between the current and the previous-loop approximation error is lower than a predefined limit $\Delta J_{\max}$. As already mentioned above for the approximation error J, the numerical value of the tolerance $\Delta J_{\max}$ is always connected with the number n_k of selected frequencies and the specific **Q** matrix.

A problem occurs due to the simultaneous linear least-squares fitting of the **Q** matrix elements. These elements can significantly differ in their magnitudes, especially for three-dimensional problems in modal coordinates. Elements with large magnitudes have a higher portion of the minimised total approximation error J than smaller ones, and their approximation function is thus better fitted to the original data. In Karpel & Tiffany Hoadley (1991), a two-step weighting procedure is proposed to overcome this shortcoming. In the first step, weights w_{jl} are defined to normalise the data set of large matrix elements Q^{o}_{jl} to the maximum absolute value of one.

$$w_{jl} = 1 / \max_{\lambda} \left(Q_{\min}; \left| Q^{\mathrm{o}}_{jl}(\mathrm{i}k_{\lambda}) \right| \right) \ , \quad Q_{\min} \geq 0 \tag{3.25}$$

Hence, the weights are bounded above by $1/Q_{\min}$. Matrix elements with a maximum magnitude lower than $Q_{\min}$, which are expected to have a negligible influence on a later investigated physical property, are not weighted too high in order to avoid a worse fit of more important matrix elements. In contrast to the original publication, this limit is not restricted to having the value one. If not otherwise specified, it is set to zero. Even if the weights in Eq. (3.25) are applied, the approximation error is still influenced by the way the single elements of **Q** change their size for increasing values of the frequency imaginary part k. The second step weights the different $\mathbf{Q}^{\mathrm{o}}$ matrix elements at the single purely imaginary reduced frequencies k in accordance with their influence on a later investigated physical property. This step is not implemented because the sufficiently precise determination of that physical property is checked with an alternative aerodynamic transfer model.

After determining the matrix coefficients and keeping them constant, the initially estimated poles are improved with a non-linear optimisation in order to minimise the approximation error J. Hence, the same criterion is employed for both the linear and the non-linear optimisation. As proposed in Tiffany Hoadley & Adams Jr. (1988), a non-gradient simplex method based on Nelder & Mead (1965) is used for the calculation of the improved poles (`fminsearch` in MATLAB (2007)). One disadvantage of this simplex method is that the range of poles cannot be directly constrained. If the seldom case of optimised poles with positive values occurs, another non-linear optimisation procedure must be chosen. The gradient-based algorithm that is implemented in the function `fmincon` of MATLAB (2007), which allows for constraining the

optimised parameters, is employed in this case. The non-linear optimisation step is programmed so that the mentioned constraints of the linear least-squares fit can be also taken into account. The termination tolerance is again determined by the limit $\Delta J_{\max}$. Subsequent to the convergence of the non-linear optimisation, the difference of the current and a previous approximation error is checked. If it is lower than the already mentioned limit $\Delta J_{\max}$, the identification procedure ends. Otherwise a new linear least-squares fit of the matrix coefficients with the optimised and fixed set of poles starts.

The fitting procedure of the Roger approach is just a reduced version of the one described above (Karpel & Strul 1996). Since either the **E** or the **D** matrix, depending on the use of Eq. (3.19) or Eq. (3.20), does not include free parameters, the linear least-squares step can be carried out without iterations. In the following, especially the Roger and Karpel approach, in combination with the described identification procedure, is termed rational function approximation and abbreviated as rfa.

3.5 Approximation of the Theoretical Aerodynamic Admittances of Flat Plates

3.5.1 Approximation of the Characteristic Aerodynamic Transfer Functions

In order to demonstrate some main features of the rational function approximation, it is applied in its scalar form to the characteristic aerodynamic transfer functions C and S of the flat plate. Though exact analytical expressions of these transfer functions are available for almost arbitrary complex frequencies, the approximations allow for a mathematically favourable representation. The following explanations refer to the scalar version of the Roger approach in Eq. (3.14). As explained at the end of Section 3.3, the Karpel approach leads to the same results if applied to a scalar transfer function. Both aerodynamic transfer functions have no differentiating character, as can be seen, for instance, by means of the step responses in Figure 2.3(a). Hence, the coefficients A_1 and A_2 of the corresponding summands are set to zero. The A_0 coefficients are constrained to the original steady values.

For the identification procedure, a reasonable database has to be defined first. With respect to the Nyquist plots in Figure 2.2(a), original values in the frequency interval $k \in [0.01; 10]$ for the consistent Theodorsen function C and in $k \in [0.01; 100]$ for the consistent Sears function S seem to sufficiently cover the original functions on the entire imaginary frequency axis. A logarithmic interval spacing avoids a too non-uniform distribution to the disadvantage of low

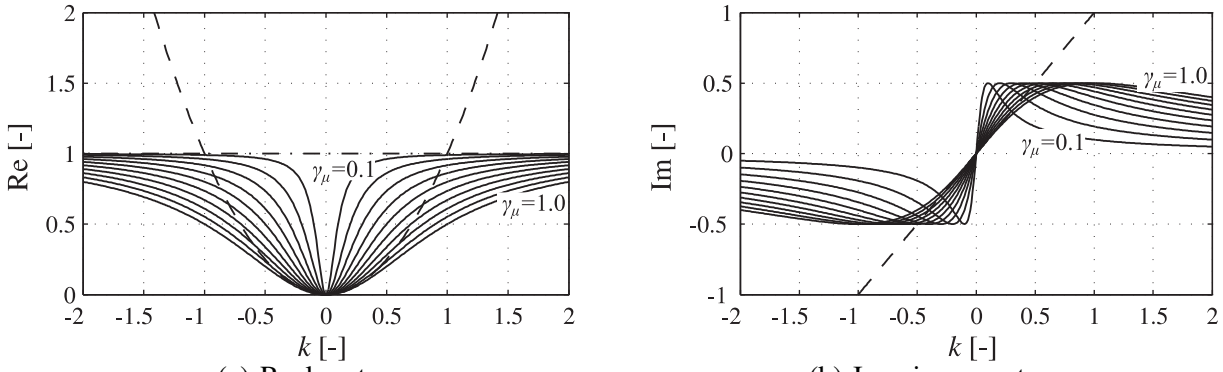

(a) Real parts. (b) Imaginary parts.

Figure 3.2: Summands of the Roger approach according to Eq. (3.26).

purely imaginary reduced frequencies. Since there is no restriction concerning the number of frequencies with original values, except from the computation time, $n_k = 200$ frequencies are chosen in the way explained before. For the fitting procedure, the convergence limit is set to $\Delta J_{\max} = 10^{-5}$.

As lots of local minima exist when optimising the approximation error J, the approximation results depend on the initial settings, especially for a higher number of employed poles. Nearly independent of the initial values, the range of optimised poles is limited to the intervals on the negative real axis where the imaginary parts of the characteristic aerodynamic transfer functions show distinct discontinuities. The initial pole range of the flat-plate function approximations can thus be limited to corresponding small intervals. The discontinuities can be seen in Figure 2.1. For the consistent Theodorsen function, this discontinuity tends faster to zero for decreasing real parts β of the reduced frequency than for the consistent Sears function. Hence, the range of optimised poles is larger for the latter function. The setting of the initial pole values can also be explained by considering the real and imaginary parts of the approximation function values directly along the identification axis, the imaginary frequency axis. For the Roger approach they read as follows.

$$\mathrm{Re}(Q(\mathrm{i}k)) = A_0 - A_2 k^2 + \sum_{\mu=1}^{n_\gamma} A_{\mu+2} \frac{k^2}{k^2+\gamma_\mu^2} \tag{3.26a}$$

$$\mathrm{Im}(Q(\mathrm{i}k)) = A_1 k + \sum_{\mu=1}^{n_\gamma} A_{\mu+2} \frac{k\gamma_\mu}{k^2+\gamma_\mu^2} \tag{3.26b}$$

Eq. (3.26) additionally includes the non-causal summands that are not used in this section. In Figure 3.2, the function values of the individual summands are graphically represented for $A_j = 1$, $j \neq 2$ and $A_2 = -1$. The curves of $n_\gamma = 10$ lag terms are displayed for poles equally spaced in the interval $[-1.0; -0.1]$. It can be seen that the maximum and minimum values of the real and imaginary parts of the lag terms are independent of the location of the poles on the negative

real axis. The extrema of all lag-term real parts are located at the origin. The absolute values of the location k of the extrema of the lag-term imaginary parts, however, equal the absolute values β of the lag-term poles. Along the imaginary frequency axis, the influence of the lag terms is thus crucially determined by the bandwidth of poles on the real axis. Regarding the behaviour of the imaginary parts of the characteristic aerodynamic transfer functions along the real and the imaginary frequency axis in Figure 2.1, it seems to be reasonable to set the initial poles within the interval $[k_{\min}; 1.5]$. The foregoing explanation can be transferred to the Karpel approach using Eq. (3.23).

When carrying out the approximation procedure for both characteristic aerodynamic transfer functions C and S, a special phenomenon concerning the detailed pole locations often occurs. When the consistent Theodorsen function is approximated for instance with $n_\gamma = 3$ poles and the initial poles are uniformly distributed in the interval given before, the approximation algorithm converges to the result given in Table 3.1. The optimised poles show two almost equal values

Table 3.1: Rfa of the consistent Theodorsen function C with a double pole.

n_γ	J	A_0	$A_{\mu+2}$	γ_μ	$A_0+\sum_{\mu=1}^{n_\gamma} A_{\mu+2}$
3	0.12818	1.0000	−0.17752	0.051784	0.50616
			8099498.12020	0.29813331341431	
			−8099498.43652	0.29813331355914	

that are connected to huge almost equal coefficients with opposite signs. The associated terms of the rational function approximation have the following form.

$$A\frac{p}{p+\gamma} - (A+\Delta A)\frac{p}{p+(\gamma+\Delta\gamma)} \tag{3.27}$$

The huge magnitude of the coefficients can lead to numerical problems when the aerodynamic forces are determined with the state-space model in the time domain, for instance. To avoid these problems, the two poles can be replaced by one double pole with coefficients whose size is comparable to that of the single pole.

$$A\frac{p\Delta\gamma}{(p+\gamma)(p+(\gamma+\Delta\gamma))} - \Delta A\frac{p}{p+(\gamma+\Delta\gamma)} \overset{\Delta\gamma\ll}{\approx} A\Delta\gamma\frac{p}{(p+\gamma)^2} - \Delta A\frac{p}{p+\gamma} \tag{3.28}$$

For the numerical approximation example, the derived coefficients of the double pole have the values $A\Delta\gamma = 0.0011731$ and $\Delta A = 0.31632$. In this case, the multiplicity can be neglected because the first coefficient is very small. In other cases, the multiplicity can also be significant. The approximation finally equals the one with two poles given in Table 3.2. Since the focus is on rational functions with simple poles here, it has not been investigated if an a priori approach with a single and a double pole can reduce the approximation error. If the fitting procedure leads to multiple poles, the different values of the optimised poles can be used as an initial set for an

Table 3.2: Rfa of the consistent Theodorsen function C. Marked values are taken from *Jones (1938), †Eversman & Tewari (1991b), ‡Peterson & Crawley (1988), and §Vepa (1977).

n_γ	J	A_0	$A_{\mu+2}$	γ_μ	$A_0+\sum_{\mu=1}^{n_\gamma} A_{\mu+2}$
2	0.12821	1.0000	−0.18577	0.054234	0.50566
			−0.30857	0.31053	
3	0.03528	1.0000	−0.061878	0.020486	0.50182
			−0.26013	0.12689	
			−0.17617	0.46757	
5	0.011841	1.0000	−0.033492	0.011955	0.50058
			−0.15178	0.073164	
			−0.34421	0.26410	
			0.26481	0.43158	
			−0.23474	0.56849	
(5)	0.0027306	1.0000	−0.016818	0.0063994	0.50017
			−0.06311	0.036002	
			−0.18364	0.11784	
			−0.19127	0.31094	
			−0.044992	0.89440	
2*	0.14749	1.0000	−0.16500	0.04550	0.50000
			−0.33500	0.30000	
3†	0.074668	0.9994	−0.10550	0.03710	0.50270
			−0.28790	0.18590	
			−0.10330	0.58860	
3‡	0.16554	1.0000	−0.15240	0.04900	0.51760
			−0.22120	0.23850	
			−0.10880	0.35760	
4§	0.072971	1.0000	−0.011286	0.0044482	0.50000
			−0.043281	0.027697	
			−0.21640	0.096055	
			−0.22904	0.40380	

approach with a lower number of poles. In this way, the results are obtained which are given in the first three blocks of Table 3.2 and Table 3.3 for $n_\gamma = 2$, $n_\gamma = 3$, and $n_\gamma = 5$ poles.

The connection of nearly equal poles with large coefficients is typical for the fitting procedure described in Section 3.4 where the poles and the coefficients are optimised in different steps. As soon as the non-linear optimisation finds narrow-spaced poles, the linear least-squares step minimises the approximation error by strongly increasing the magnitudes of the corresponding coefficients. The non-linear iteration step has almost no chance to escape from these isolated solutions because these kinds of large coefficients necessitate narrow-spaced poles. An optimisation of the poles with other non-linear procedures cannot change this unfavourable behaviour. For example, a genetic algorithm can find significantly different values for the narrow-spaced poles, but they remain still narrow spaced. The only way for the iteration process to potentially

Table 3.3: Rfa of the consistent Sears function S. Marked values are taken from *Bisplinghoff & al. (1951) and §Vepa (1977).

n_γ	J	A_0	$A_{\mu+2}$	γ_μ	$A_0+\sum_{\mu=1}^{n_\gamma} A_{\mu+2}$
2	0.50240	1.0000	−0.54822	0.14297	0.068069
			−0.38372	1.4207	
3	0.21660	1.0000	−0.30344	0.07795	0.042627
			−0.48634	0.46667	
			−0.16759	5.3524	
5	0.050684	1.0000	−0.10003	0.03005	0.021534
			−0.40836	0.17849	
			−0.29911	0.73630	
			−0.11927	4.2672	
			−0.051693	33.881	
(5)	0.04463	1.0000	−0.070287	0.022207	0.024147
			−0.34324	0.13829	
			−0.35171	0.52968	
			−0.14816	2.9579	
			−0.062455	25.403	
2*	0.99284	1.0000	−0.50000	0.13000	0.00000
			−0.50000	1.0000	
4§	0.86000	1.0000	−0.012994	0.0049896	0.00000
			−0.06232	0.034931	
			−0.40921	0.13797	
			−0.51548	1.1646	

find new solutions is to reduce the convergence limit $\Delta J_{\max}$ in order to provoke a numerical problem in the linear least-squares step due to too narrow-spaced poles. Such an irregular linear least-squares optimisation leads to a zero coefficient in connection with one of the narrow-spaced poles, which enables the non-linear optimisation step to find a different set of poles.

The problem of narrow-spaced poles with huge coefficients is also described in Eversman & Tewari (1991a) for the approximation of aerofoil derivatives and in Eversman & Tewari (1991b) for the approximation of the original Theodorsen function. The explanations given above can be seen as an extension and correction of their findings.

Since the amount of coefficients is low for the approximation of the scalar aerodynamic transfer functions, it is also possible to determine all parameters with a non-linear optimisation procedure. For instance, the mentioned simplex-based algorithm can be used to minimise the approximation error J of Eq. (3.24). With this method, solutions can often be found that show narrow-spaced poles with corresponding normal-sized coefficients. According to Eq. (3.27) and Eq. (3.28), these poles should not be considered as multiple in the sense discussed above but rather be related to an approximation term that is subdivided into several summands. In other words, the

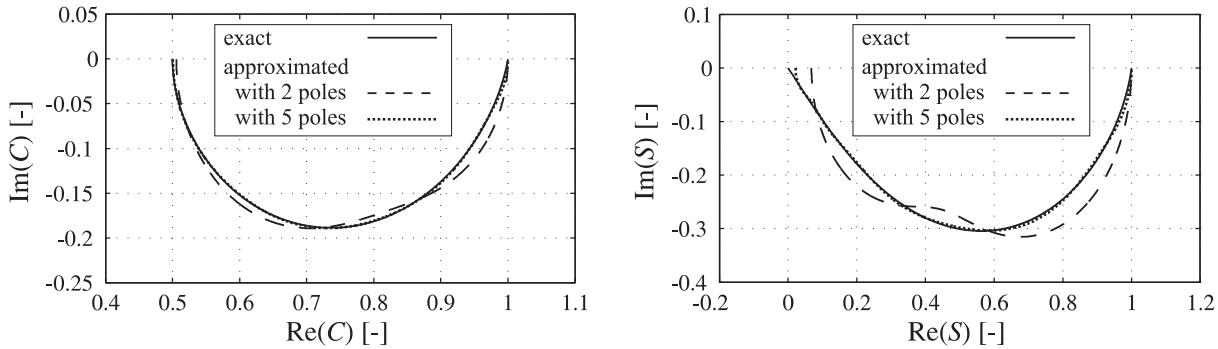

(a) Consistent Theodorsen function (b) Consistent Sears function

Figure 3.3: Rfa compared to the exact values of the characteristic aerodynamic transfer functions of the flat-plate problem for purely imaginary positive reduced frequencies $p = 0 + \mathrm{i}k$, $k > 0$ (Nyquist plots).

corresponding eigenvalues of the matrix $\mathbf{R}$ are connected to different eigenvectors.

If the convergence limit $\Delta J_{\max}$ is reduced and the approximation results of the fitting procedure described in Section 3.4 are used as initial values of a fully non-linear parameter optimisation and vice versa, the rational function approximation with $n_\gamma = 5$ poles can be noticeably improved in contrast to the given approximations with fewer poles. The solutions with the lowest approximation error found in this way are additionally given in Table 3.2 and Table 3.3 labelled with brackets. As the simplex method always converges to local minima, a fully non-linear parameter optimisation with a genetic algorithm (`ga` in MATLAB (2007)) has been additionally carried out. In spite of many days of calculation, only solutions with a higher approximation error have been found.

The approximation quality of the rational functions along the identification axis can be seen in the Nyquist plots of Figure 3.3. Expectedly, the higher the selected number of poles, the better the approximation. For $n_\gamma = 5$ poles, almost no difference to the original values is visible. The dependency of the approximation error J on the number of poles can be seen in the numerical results of Table 3.2 and Table 3.3, too. A further, extensive increase of the number of poles leads to a problem that is addressed in the next section. The figure and the approximation error also show that the chosen kind of rational function is more capable to approximate the consistent Theodorsen than the consistent Sears function. As the A_0 coefficients are constrained to the original steady values, the approximation for $k \to 0$ exactly tends to the limit C, $S \to 1$. It is known from the theory of dynamic systems that the Nyquist plots of the summands $p/(p+\gamma_\mu)$ can only cross the horizontal coordinate axis at a right angle. The original curves, in contrast, do not cross this axis at a right angle. Hence, the rational function approximations tend a little bit faster to the limit 1 for $k \to 0$. According to the final value theorem of Laplace transforms, the corresponding approximations of the step responses also tend a little bit faster to the steady values. The relative differences of the step responses in Figure 3.4, thus, remain positive for times

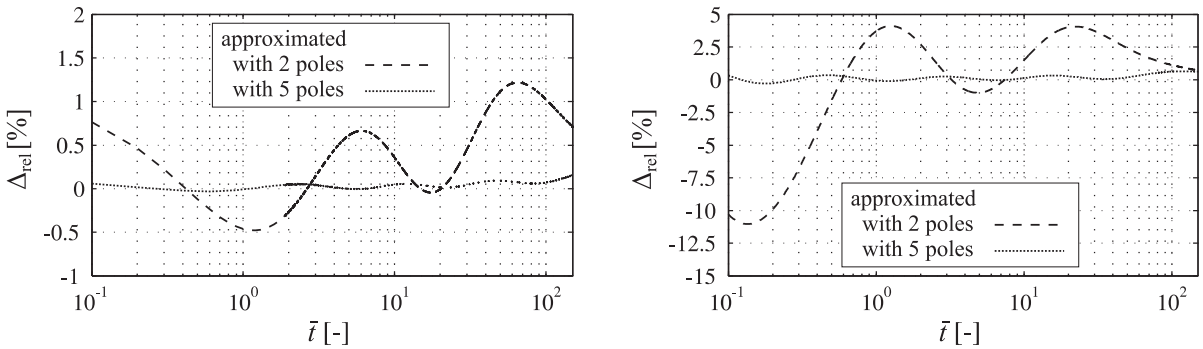

(a) Wagner function (b) Küssner function

Figure 3.4: Relative differences of the approximated characteristic aerodynamic step responses of the flat-plate problem from the exact values.

$\bar{t}$ greater than the displayed ones. When comparing both characteristic aerodynamic transfer functions, especially the consistent Sears function crosses the horizontal axis for $k \to \infty$ at an angle that strongly differs from a right one. This can be seen as one reason for the lower approximation quality. Since the approximation values are not constrained for $k \to \infty$, they slightly differ there from the original ones $C(\mathrm{i}k \to \infty) = 0.5$ and $S(\mathrm{i}k \to \infty) = 0$. As a result of the initial value theorem of Laplace transforms, the corresponding approximated step responses do not exactly match the original ones at the time $t = 0$. Concerning the chosen rational function approach, both limit values are identical to the sum $(A_0 + \sum_{\mu=1}^{n_\gamma} A_{\mu+2})$ of its coefficients, as can be seen in Eq. (3.15). Table 3.2 and Table 3.3 give these values in their right column for the different rational function approximations.

The behaviour of the rational functions above the complex frequency plane, which is shown in Figure 3.5 for the approximations with $n_\gamma = 5$ poles, corresponds to the behaviour along the imaginary frequency axis — or every other parallel line within the region of absolute convergence — due to their holomorphic character. The values above the imaginary frequency axis are accentuated with black lines. In all the three-dimensional plots of this chapter, the large function values around the poles are limited to the displayed extrema of the vertical axis. If the coefficient of a lag term has a very small magnitude, the function values only diverge in a very small area around the pole. Partly, the resolution of the figures is not high enough to display those needle-like surfaces. Comparing the approximations with the original values in Figure 2.1 shows that the only difference occurs in the vicinity of the poles. As already indicated at the beginning of the section, the approximations try to imitate the discontinuity of the imaginary parts of the characteristic aerodynamic transfer functions along the negative real frequency axis with their distorted function behaviour around the poles though the identification is carried out along the imaginary axis. For the real parts of the characteristic aerodynamic transfer functions, which only show a removable singularity along the negative real frequency axis, the poles consequently also lead to a distortion of the approximations. Figure 3.6 additionally illustrates

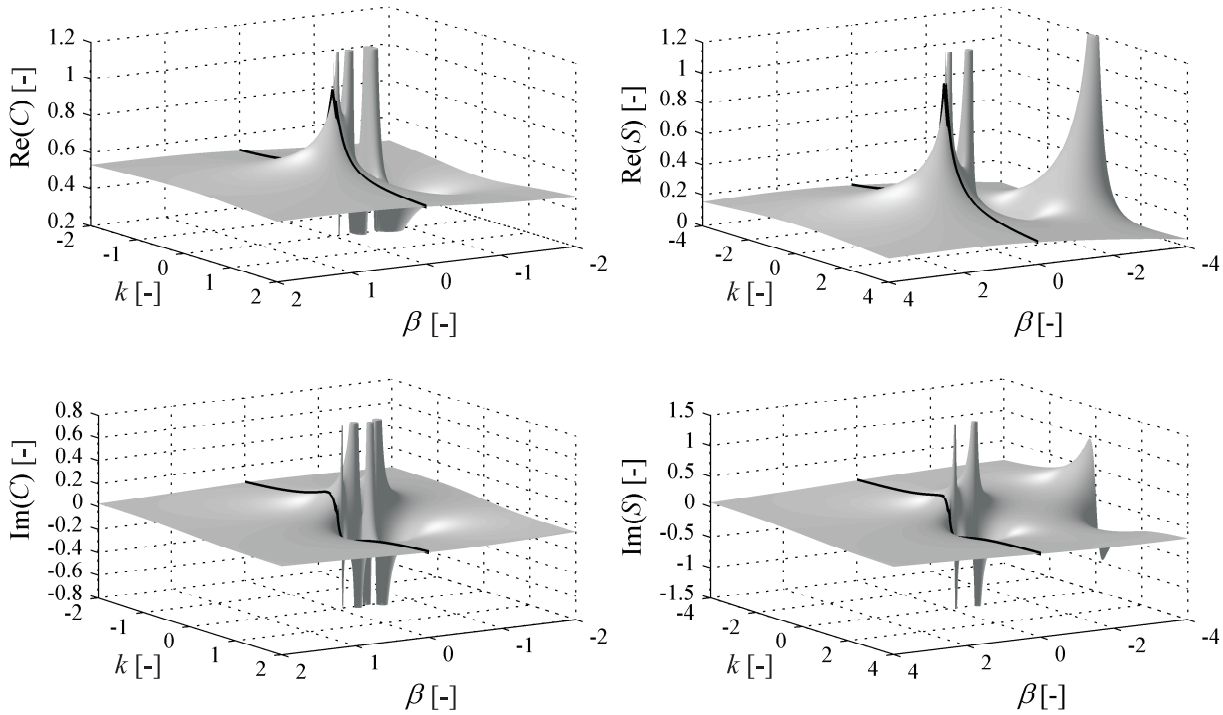

(a) Consistent Theodorsen function. (b) Consistent Sears function.

Figure 3.5: Rfa with $n_\gamma = 5$ poles of the characteristic aerodynamic transfer functions of the flat-plate problem above the complex reduced frequency plane.

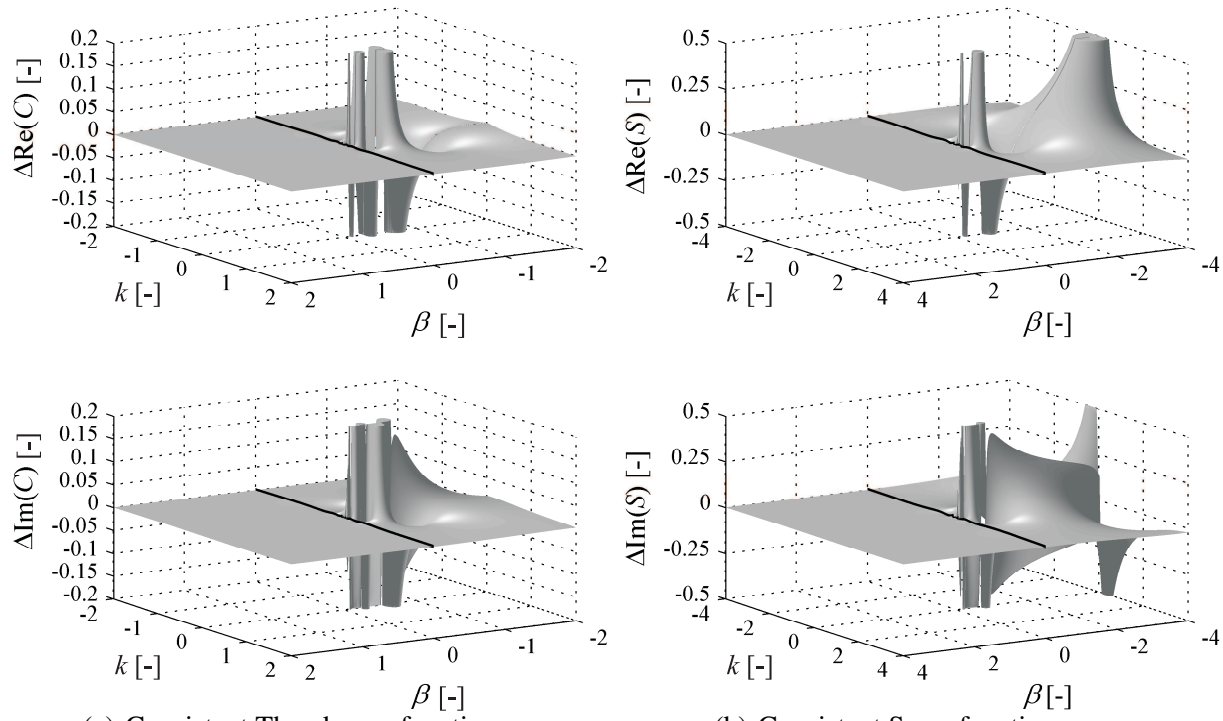

(a) Consistent Theodorsen function. (b) Consistent Sears function.

Figure 3.6: Difference of the rfa with $n_\gamma = 5$ poles from the original characteristic aerodynamic transfer functions of the flat-plate problem.

the differences of the approximation from the original values. For reduced frequencies with positive real parts and frequencies with sufficiently large absolute values of the imaginary parts, almost no difference is visible. For the characteristic aerodynamic transfer functions of the flat plate, the particular suitability of the rational function approximation with negative simple real poles can be qualitatively explained in the time domain. The decaying exponential functions can describe the effect of the drifting vortices arising at the leeward edge and their girder-bound counterpart very well.

Table 3.2 and Table 3.3 also give some approximations from other references. In these references, the original Sears function multiplied by $e^{-\mathrm{i}k}$ or the original Theodorsen function are approximated for positive purely imaginary reduced frequencies. As explained in Section 2.2.1, these functions coincide with the consistent functions S and C along the positive imaginary axis. Compared to the approximation results of this work, all cited rational functions show larger approximation errors J for the database used here.

3.5.2 Approximation of the Aerodynamic Admittances of Flat Plates

Even for the aerodynamic admittances of flat plates, the mathematical representation in terms of a state-space model is mathematically advantageous. As can be seen in Eq. (2.22) and Eq. (2.27), the different elements of the gust admittance $\mathbf{Q}^{\mathrm{g}}$ of flat plates are similar to the consistent Sears function S that is only multiplied by a constant factor. The rational function approximation of this theoretical gust admittance can thus simply be calculated from the approximation of the consistent Sears function. The transformation of the results works for both the Roger and the Karpel approach, as it has to be for a single-input multiple-output transfer system.

The rational function approximation of the theoretical admittance of motion-induced aerodynamic forces of the single flat plate, however, can only be obtained in a more complicated way from the approximation of the consistent Theodorsen function because C occurs in the elements of the aerodynamic admittance matrix in Eq. (2.20) in different ways and it is partly multiplied by the reduced complex frequency p. For the Roger approach, the result of the transformation is as follows.

$$\begin{aligned}\mathbf{Q}(p) = &\begin{pmatrix} 0 & -2A_0 \\ 0 & A_0 \end{pmatrix} + \\ &+ \begin{pmatrix} -2(A_0+\sum_{\mu=1}^{n_\gamma} A_{\mu+2}) & -1-(A_0+\sum_{\mu=1}^{n_\gamma} A_{\mu+2}) \\ (A_0+\sum_{\mu=1}^{n_\gamma} A_{\mu+2}) & -\frac{1}{2}+\frac{1}{2}(A_0+\sum_{\mu=1}^{n_\gamma} A_{\mu+2}) \end{pmatrix} p + \\ &+ \begin{pmatrix} -1 & 0 \\ 0 & -\frac{1}{8} \end{pmatrix} p^2 + \sum_{\mu=1}^{n_\gamma} \begin{pmatrix} 2\gamma_\mu & 2(\frac{1}{2}\gamma_\mu - 1) \\ -\gamma_\mu & -(\frac{1}{2}\gamma_\mu - 1) \end{pmatrix} A_{\mu+2} \, \frac{p}{p+\gamma_\mu}\end{aligned} \tag{3.29}$$

Using the C approximation with $n_\gamma = 5$ poles given in the third block of Table 3.2, for instance, the approximation of the flat-plate derivatives has the following entries.

$$\begin{aligned}
&\mathbf{A}_0 = \begin{pmatrix} 0 & -2 \\ 0 & 1 \end{pmatrix}, \quad \mathbf{A}_1 = \begin{pmatrix} -1.0012 & -1.5006 \\ 0.50058 & -0.24971 \end{pmatrix} \\
&\mathbf{A}_2 = \begin{pmatrix} -1 & 0 \\ 0 & -0.125 \end{pmatrix}, \qquad \mathbf{E} = \begin{pmatrix} -0.0008008 & 0.066584 \\ 0.0004004 & -0.033292 \\ -0.022209 & 0.29245 \\ 0.011105 & -0.14622 \\ -0.18181 & 0.59752 \\ 0.090905 & -0.29876 \\ 0.22857 & -0.41533 \\ -0.11429 & 0.20767 \\ -0.26690 & 0.33604 \\ 0.13345 & -0.16802 \end{pmatrix} \\
&\gamma_1 = 0.011955 \\
&\gamma_2 = 0.073164 \\
&\gamma_3 = 0.26410 \\
&\gamma_4 = 0.43158 \\
&\gamma_5 = 0.56849 \\
&J = 0.0049856
\end{aligned} \tag{3.30a}$$

$$\mathbf{A}_0 + \sum_{\mu=1}^{n_\gamma} \mathbf{A}_{\mu+2} = \begin{pmatrix} -0.24315 & -1.1227 \\ 0.12157 & 0.56137 \end{pmatrix} \tag{3.30b}$$

For the matrix coefficients of the lag terms, the notation with the $\mathbf{E}$ matrix of Eq. (3.20) is applied in Eq. (3.30a). The approximation error J refers to the original values at the purely imaginary reduced frequencies that are used for the approximation of the consistent Theodorsen function. The sum of coefficients given in Eq. (3.30b) equals the right-hand limit at $t = 0$ of the aerodynamic step response in Eq. (3.15).

With the results of the foregoing section, the exact theoretical values of the matrix coefficients $\mathbf{A}_0$, $\mathbf{A}_1$, and $\mathbf{A}_2$ of the polynomial part of the approximation in Eq. (3.29) can be found. Moreover, the exact theoretical elements of the mentioned limit of the aerodynamic step response can be determined from Eq. (2.20) and Figure 2.3 in combination with the initial value theorem of Laplace transforms.

$$\mathbf{A}_0 = \begin{pmatrix} 0 & -2 \\ 0 & 1 \end{pmatrix}, \quad \mathbf{A}_1 = \begin{pmatrix} -1 & -1.5 \\ 0.5 & -0.25 \end{pmatrix}, \quad \mathbf{A}_2 = \begin{pmatrix} -1 & 0 \\ -0 & -0.125 \end{pmatrix} \tag{3.31a}$$

$$\mathbf{A}_0 + \sum_{\mu=1}^{n_\gamma} \mathbf{A}_{\mu+2} = \begin{pmatrix} -0.25 & -1.125 \\ 0.125 & 0.5625 \end{pmatrix} \tag{3.31b}$$

The approximation of the $\mathbf{A}_1$ matrix in Eq. (3.30) corresponds to the approximation of the initial value of the Wagner function W given in the right column of Table 3.2. Interestingly, the

right-hand limit of the initial value of the aerodynamic step response of the flat plate, in which not only the coefficients but also the poles of the approximated consistent Theodorsen function are involved, is also sufficiently well approximated.

As can be seen when comparing the signs of the elements of the right hand limit $(\mathbf{A}_0 + \sum_{\mu=1}^{n_\gamma} \mathbf{A}_{\mu+2})$ of the initial value of the aerodynamic step response with those of the final, steady value $\mathbf{A}_0$, the causal parts of the flat-plate derivatives show a minimum-phase behaviour. A non-minimum-phase behaviour occurs due to the polynomial coefficients $\mathbf{A}_1$ and $\mathbf{A}_2$. In the aerodynamic step response according to Eq. (3.15), their elements produce Dirac impulses and derivatives of Dirac impulses that are partly oriented opposite to the final direction of the aerodynamic step response. As usual, the non-minimum-phase behaviour can also be detected when converting the matrix element description of the approximation of the aerodynamic admittance function $\mathbf{Q}$ into a ratio of two polynomials and searching for zeros of the nominators in the right frequency plane.

The aerodynamic derivatives of the single flat plate can be directly approximated as well without taking the roundabout way over the approximation of the consistent Theodorsen function. The direct matrix-based approximation is possible by employing both the Roger and the Karpel approach. To demonstrate the direct approximation and to compare it with the foregoing results, it is carried out with the Roger approach under the same settings that are used in the last section. That means the original aerodynamic derivatives are calculated at the frequencies k that are used for the C approximation. The convergence limit is again set to $\Delta J_{\max} = 10^{-5}$. In contrast to the approximation of the consistent Theodorsen function, the $\mathbf{A}_1$ and $\mathbf{A}_2$ matrix must be employed for the approximation of aerodynamic derivatives. The $\mathbf{A}_0$ matrix is again constrained to the original steady matrix. For the first linear least-squares step, the initial poles are uniformly distributed within the range $[k_{\min}; 1.5]$. Using $n_\gamma = 5$ poles, the following result is obtained.

$$
\begin{aligned}
&\mathbf{A}_0 = \begin{pmatrix} 0 & -2 \\ 0 & 1 \end{pmatrix}, \quad \mathbf{A}_1 = \begin{pmatrix} -1.0002 & -1.5001 \\ 0.50010 & -0.24995 \end{pmatrix} \\
&\mathbf{A}_2 = \begin{pmatrix} -0.99997 & 0.00001 \\ -0.00001 & -0.12501 \end{pmatrix}, \quad \mathbf{E} = \begin{pmatrix} -0.0013876 & 0.093732 \\ 0.00069378 & -0.046866 \\ -0.37813 & 2.7321 \\ 0.18907 & -1.3660 \\ 0.41821 & -2.7324 \\ -0.20910 & 1.3662 \\ -0.19101 & 0.71520 \\ 0.095505 & -0.35760 \\ -0.095505 & 0.067235 \\ 0.047753 & -0.033617 \end{pmatrix} \\
&\gamma_1 = 0.016256 \\
&\gamma_2 = 0.12254 \\
&\gamma_3 = 0.13381 \\
&\gamma_4 = 0.22884 \\
&\gamma_5 = 0.84472 \\
&J = 0.0027711
\end{aligned}
\tag{3.32a}
$$

$$\mathbf{A}_0 + \sum_{\mu=1}^{n_\gamma} \mathbf{A}_{\mu+2} = \begin{pmatrix} -0.24782 & -1.1242 \\ 0.12391 & 0.56209 \end{pmatrix} \tag{3.32b}$$

With respect to the approximation error J, the approximation quality is similar to that in Eq. (3.30). Although the direct approximation seems to lead to a slightly lower approximation error, it has to be kept in mind that the used C approximation is not the best one that has been found for $n_\gamma = 5$ poles. Deriving the aerodynamic admittances from the C approximation with $n_\gamma = 3$ poles in the second block of Table 3.2, for instance, leads to an approximation error of $J = 0.015988$. A direct approximation with the same number of poles leads to a slightly larger error $J = 0.019227$. For the same number of poles, both approximation errors are, hence, at least within the same order of magnitude.

Concerning the influence of the initial poles on the range of optimised poles, the process of the direct fitting of the aerodynamic derivatives shows the behaviour that is described for the C approximation in the foregoing section. That justifies the use of the selected initial position also for the direct approximation. A major difference in the approximation processes occurs due to the non-causal parts of the aerodynamic transfer function. They dominate the magnitude of the aerodynamic derivatives for high imaginary parts k of the reduced frequency and hence the approximation error. For the selected convergence limit $\Delta J_{\max}$, the fitting process thus does not lead to multiple poles with huge coefficients. If the convergence limit is reduced, the problem of this kind of multiple poles can, however, also arise. Due to the existence of lots of local minima of the approximation error J, the optimised poles of the direct approximation of the aerodynamic derivatives and the corresponding coefficients differ from those of the approximation of the consistent Theodorsen function.

In contrast to the exact values in Eq. (3.30), the entries in the $\mathbf{A}_2$ matrix are now approximations. The matrix $\mathbf{A}_1$ and the right-hand limit $(\mathbf{A}_0 + \sum_{\mu=1}^{n_\gamma} \mathbf{A}_{\mu+2})$ of the initial value of the aerodynamic step response in Eq. (3.32) are even a little bit closer to the exact values than in Eq. (3.30).

As an example, Figure 3.7(a) shows the approximation of the aerodynamic derivative Q_{hh} given in Eq. (3.32) above the complex frequency plane. The function values along the imaginary frequency axis are accentuated with black lines. On the right side, Figure 3.7(b) shows the difference from the original values of Eq. (2.20). As explained for the characteristic transfer functions, differences are only visible around the negative real axis in the vicinity of the poles. Figure 3.8 illustrates the time-domain versions of the approximation of the aerodynamic derivative Q_{hh} in terms of the aerodynamic step and impulse response.

To describe and to compare the direct approximations with the Roger approach for different numbers n_γ of poles, the results are given in Table 3.4. The fitting process is carried out with the settings mentioned for the approximation given in Eq. (3.32). The elements of the matrix

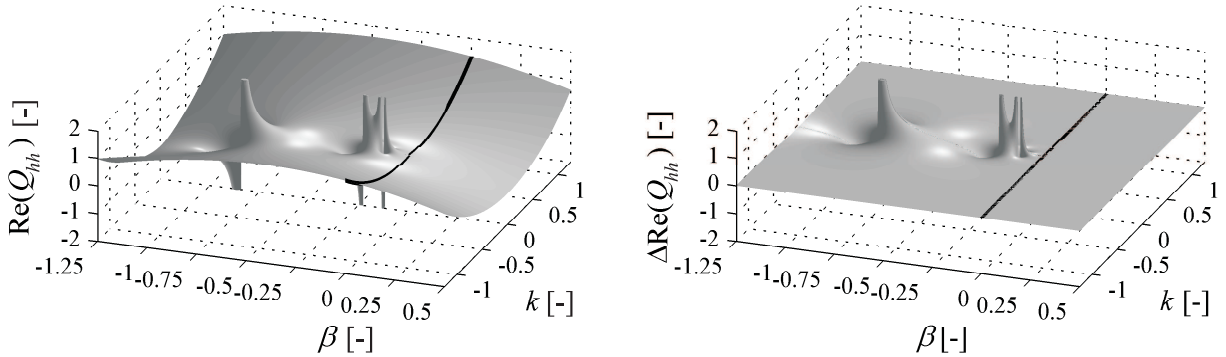

(a) Rfa according to the Roger approach with $n_\gamma = 5$ poles.

(b) Difference between the rfa and the original theoretical values.

Figure 3.7: Real part of the aerodynamic derivative Q_{hh} of the single flat plate above the complex reduced frequency plane.

coefficients $(\mathbf{A}_0 \;\; \mathbf{A}_1 \;\; \mathbf{A}_2)$ of the polynomial part, the elements of the lag-term matrix coefficients in the matrix $\mathbf{E}$, and the elements of the right-hand limit $(\mathbf{A}_0 + \sum_{\mu=1}^{n_\gamma} \mathbf{A}_{\mu+2})$ of the initial value of the aerodynamic step response are only shown with the arithmetic mean $\overline{(\;)}$ of their absolute values. A large, confusing amount of numerical data is avoided in this way. The approximation error J is divided by the number n_k of frequencies at which original aerodynamic derivatives are calculated.

Table 3.4: Rfa of the theoretical flat-plate derivatives with the Roger approach.

n_γ	$J/n_k \cdot 10^4$	$\overline{\lvert(\mathbf{A}_0 \;\; \mathbf{A}_1 \;\; \mathbf{A}_2)_{jl}\rvert}$	$\overline{\lvert(\mathbf{E})_{jl}\rvert}$	$\overline{\lvert(\mathbf{A}_0 + \sum_{\mu=1}^{n_\gamma} \mathbf{A}_{\mu+2})_{jl}\rvert}$	$\gamma_{\max} - \gamma_{\min}$
3	0.96135	0.61470	0.22550	0.51498	0.34208
5	0.13856	0.61461	0.55686	0.51450	0.82846
7	0.16664	0.61459	0.59218	0.51580	0.92498
10	0.22681	0.61461	173.95	0.51336	1.4735
17	0.073669	0.61457	5449629	0.51803	1.4890

The values of the coefficients of the polynomial part and the right hand limit of the initial value of the aerodynamic step response are almost independent of the number of employed poles. This fact again indicates the suitability of this type of rational function for the approximation of the flat-plate derivatives. The approximations of the right-hand limit of the aerodynamic impulse response at $t = 0$, which equal $(-\sum_{\mu=1}^{n_\gamma} \mathbf{A}_{\mu+2}\gamma_\mu)$ according to Eq. (3.16), are not shown in the table. Due to the roughening effect of the differentiation, these values scatter slightly more.

The approximation error J does not monotonically decay with an increasing number of poles, but globally, a higher number of poles usually leads to a better approximation of the original values along the imaginary frequency axis. Considering the approximation quality and remembering the number of aerodynamic states in the state-space model, an approximation with $n_\gamma = 5$ poles

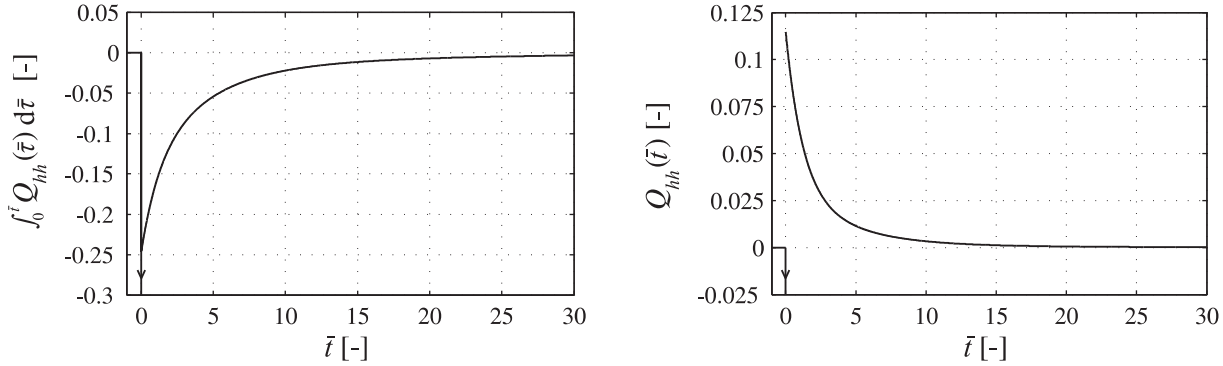

(a) Aerodynamic step response. (b) Aerodynamic impulse response.

Figure 3.8: Time-domain functions of the approximated aerodynamic derivative Q_{hh} of the flat plate according to the Roger approach with $n_\gamma = 5$ poles.

seems to be ideal for the flat-plate derivatives. Although the number of $n_\gamma = 10$ and $n_\gamma = 17$ poles is, thus, too high and therefore not recommendable, the corresponding results are used to show a typical behaviour of the rational function approximation. The range of the related poles is merely altered by the non-linear optimisation steps, as can be seen in the right column of the tables. The absolute values of the coefficients of the lag terms, however, drastically increase. Figure 3.9(a) demonstrates that a better approximation of the original values along the imaginary axis is caused by a strong weighting of the lag terms and thus the distorted function values around the poles. Hence, the approximation quality outside the identification line gets really bad, as can be seen in Figure 3.9(b). When the number of frequencies with original values is drastically reduced, for instance from $n_k = 200$ to $n_k = 10$, the effect of strongly weighted terms is additionally slightly increased for the approximations with a high number of poles. The high weighting of the lag terms is a second, more important reason, not to employ too many poles. As already mentioned in the foregoing section, the problem of strongly weighted lag terms also arises if too many poles are employed for the approximation of the consistent Theodorsen function and the consistent Sears function. The huge coefficients that occur in combination with double poles, by the way, do not lead to distorted areas, because the corresponding summands can be equivalently transformed into terms with small coefficients.

For an aerodynamic transfer problem with two inputs and two outputs, the Roger approach cannot, in general, be converted into the Karpel approach, although both approaches use the same number of free coefficients. For the theoretical flat-plate derivatives, however, the columns of the $\mathbf{A}_{\mu+2}$ matrix $(1 < \mu < n_\gamma)$ in the approximation with the Roger approach just differ in a scalar factor, as can be seen in Eq. (3.30a) and in Eq. (3.32a). The same holds for the rows. These similarities are a direct consequence of the similarities in the original aerodynamic derivatives shown in Eq. (2.20). In this special case, the Roger approach can be converted into the Karpel form. An approximation with the Karpel approach thus leads to the same results as explained

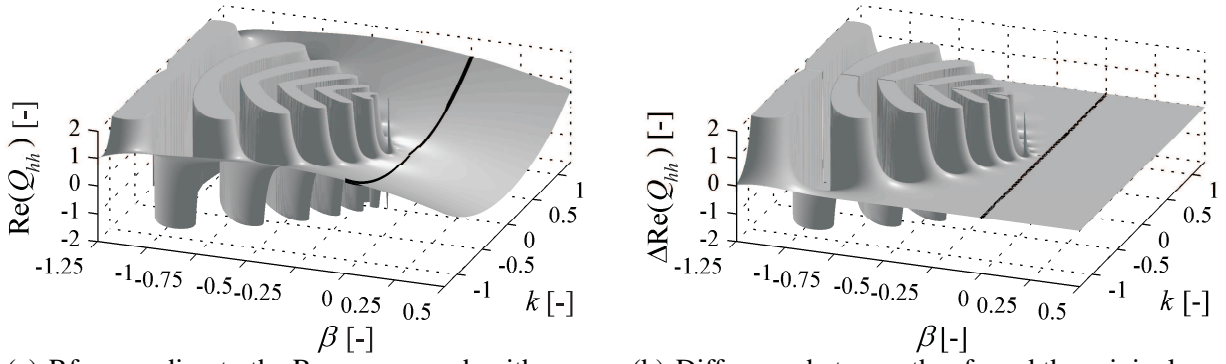

(a) Rfa according to the Roger approach with $n_\gamma = 17$ poles.

(b) Difference between the rfa and the original theoretical values.

Figure 3.9: Real part of the aerodynamic derivative Q_{hh} of the single flat plate above the complex reduced frequency plane.

before. For instance, the following matrices of the Karpel approach can be derived from the Roger approach in Eq. (3.29).

$$\mathbf{D} = \begin{pmatrix} \mathbf{D}_1 & \cdots & \mathbf{D}_\mu & \cdots & \mathbf{D}_{n_\gamma} \end{pmatrix}, \quad \mathbf{D}_\mu = r_\mu \begin{pmatrix} -2 \\ 1 \end{pmatrix} \tag{3.33a}$$

$$\mathbf{E} = \begin{pmatrix} \mathbf{E}_1 \\ \vdots \\ \mathbf{E}_\mu \\ \vdots \\ \mathbf{E}_{n_\gamma} \end{pmatrix}, \quad \mathbf{E}_\mu = -\frac{A_{\mu+2}}{r_\mu} \begin{pmatrix} \gamma_\mu & \frac{1}{2}\gamma_\mu - 1 \end{pmatrix} \tag{3.33b}$$

The variable r_μ represents an arbitrary non-zero real number. With the help of Eq. (3.23), the expressions in Eq. (3.29) can be retrieved.

The aerodynamic derivatives of three coupled flat plates depend on the special system configuration, like hinge positions and the ratio of the plate widths. As shown for the single flat plate, their approximation in terms of the Roger approach can again be derived from the approximation of the consistent Theodorsen function. An advantage of taking this way is that the analytical dependency of the aerodynamic derivatives on the special system configuration still exists. As explained for the single flat plate, the transformation from the Roger to the Karpel approach is also possible for the derivatives of Section 2.2.3, due to the similarities in the $\mathbf{A}_{\mu+2}$ matrix $(1 < \mu < n_\gamma)$, though it is a multiple-input multiple-output transfer system. Using the C approximation, however, is very laborious and error prone and is not performed here. Again, the direct approximation is much simpler and can be carried out with both the Roger and the Karpel approach with the same accuracy. In contrast to the derivation from the approximated consistent

Theodorsen function, the system configuration cannot be varied after the direct approximation. The direct rational function approximation is, thus, related to a special configuration. Due to all the parallels with the approximation of the aerodynamic derivatives of the single flat plate, the approximation of the aerodynamic derivatives of the addressed coupled flat plates shows a similar quality.

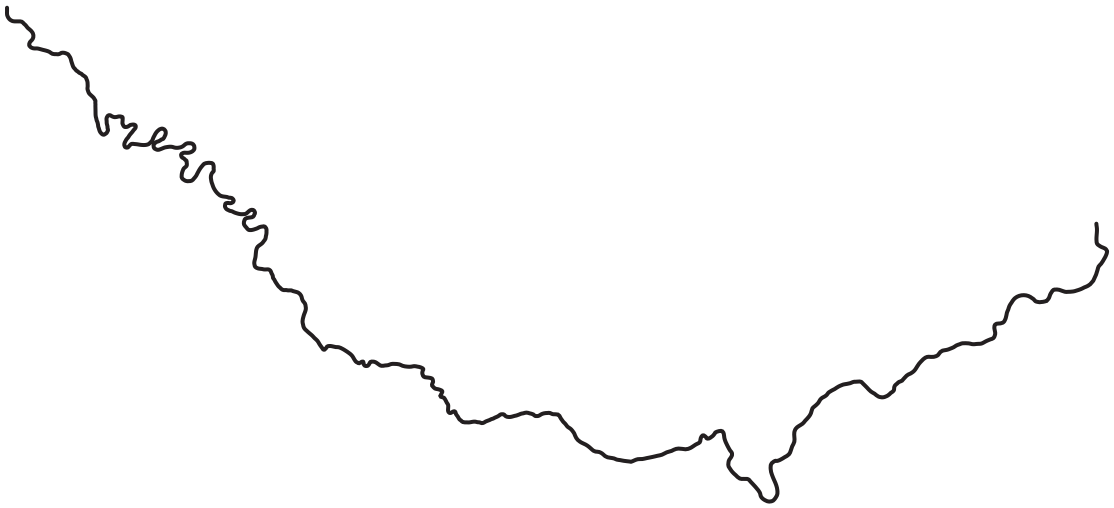

3.6 Approximation of the Aerodynamic Derivatives of Cross Sections in Real Flow

Approximating the aerodynamic derivatives of cross sections in real flow differs from the approximation of those of the flat plates described in the last section. The original, measured data is usually only available at a few frequencies within a limited interval along the imaginary frequency axis. For each cross section in real flow that is addressed here, aerodynamic derivatives are accessible at about $n_k = 10$ frequencies within the intervals of Table 2.1. An approximation with analytical functions is, thus, requisite when values of the aerodynamic transfer functions are needed at arbitrary frequencies.

The initial settings of the poles cannot be justified as explained for the flat-plate derivatives because the original measured data is neither known above the complex frequency plane nor along a sufficiently long interval of the imaginary frequency axis. A recommendation can, however, be derived based on the Roger approach when looking at Eq. (3.26) and Figure 3.2. The initial range of pole magnitudes $|-\gamma_\mu|$ along the negative real frequency axis should equal the range of frequency magnitudes $|k|$ where aerodynamic derivatives were measured. In so doing, the lag terms have their highest influence within the bandwidth of the original data along the imaginary

frequency axis. This explanation also applies to the Karpel approach. Similar recommendations for the poles are given in publications of aerospace engineering like Tiffany Hoadley & Adams Jr. (1988). For this reason, the initial poles are here equidistantly distributed in the interval $[-k_{\max}; -k_{\min}]$. For the following approximations, the $\mathbf{A}_0$ matrix is constrained to the original steady matrix and the convergence limit is set to $\Delta J_{\max} = 10^{-5}$, again.

Since the approximation of the TaS derivatives differs most significantly from the approximation of the flat-plate derivatives, it is addressed first. A fitting of the TaS derivatives with the Roger approach for $n_\gamma = 5$ poles leads to the following approximation.

$$
\begin{aligned}
&\mathbf{A}_0 = \begin{pmatrix} 0 & -3.1378 \\ 0 & -0.5258 \end{pmatrix}, \quad \mathbf{A}_1 = \begin{pmatrix} -2.9394 & 37.607 \\ 13.070 & 3.7920 \end{pmatrix} \\
&\mathbf{A}_2 = \begin{pmatrix} -1.1375 & -11.455 \\ -3.5253 & -1.1125 \end{pmatrix}, \qquad \mathbf{E} = \begin{pmatrix} 6.1074 & 23.056 \\ -18.313 & -2.3993 \\ -76.763 & -26.610 \\ 150.28 & 40.943 \\ 327.56 & -405.70 \\ -506.18 & -185.84 \\ -541.76 & 1197.7 \\ 765.44 & 329.72 \\ 295.47 & -882.82 \\ -422.75 & -193.96 \end{pmatrix} \\
&\gamma_1 = 0.30585 \\
&\gamma_2 = 0.48824 \\
&\gamma_3 = 0.68630 \\
&\gamma_4 = 0.88850 \\
&\gamma_5 = 1.0937 \\
&J = 0.84916
\end{aligned}
\tag{3.34a}
$$

$$
\begin{aligned}
&\mathbf{A}_0 + \sum_{\mu=1}^{n_\gamma} \mathbf{A}_{\mu+2} = \begin{pmatrix} 10.606 & -97.470 \\ -31.532 & -12.064 \end{pmatrix} \\
&-\sum_{\mu=1}^{n_\gamma} \gamma_\mu \mathbf{A}_{\mu+2} = \begin{pmatrix} -30.994 & 185.74 \\ 61.904 & 27.469 \end{pmatrix} \\
&\sum_{\mu=1}^{n_\gamma} \gamma_\mu^2 \mathbf{A}_{\mu+2} = \begin{pmatrix} 62.314 & -305.79 \\ -105.75 & -49.725 \end{pmatrix}
\end{aligned}
\tag{3.34b}
$$

In addition to the right hand limit of the initial value of the step response, Eq. (3.34b) also displays those of the impulse response and the derivative $\mathbf{Q}'(\bar{t})$ of the impulse response.

Figure 3.10(a) shows the original values and the approximation along the imaginary frequency axis. Within the interval of the original values, which is grey shaded together with the constrained steady value, a qualitatively acceptable approximation is visible although the aerodynamic derivatives strongly differ from the theoretical ones of the flat plate. A total evaluation of the approximation based only on this small interval is, however, inadequate.

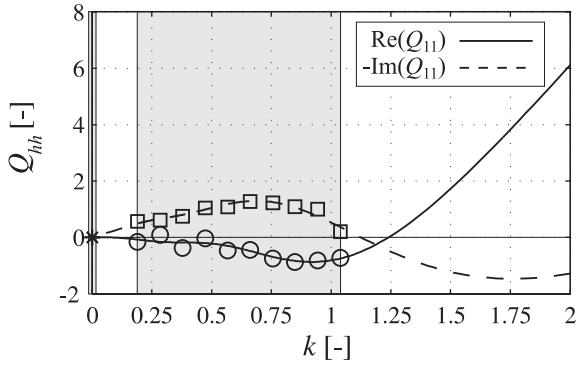

(a) Rfa and original values along the imaginary axis.

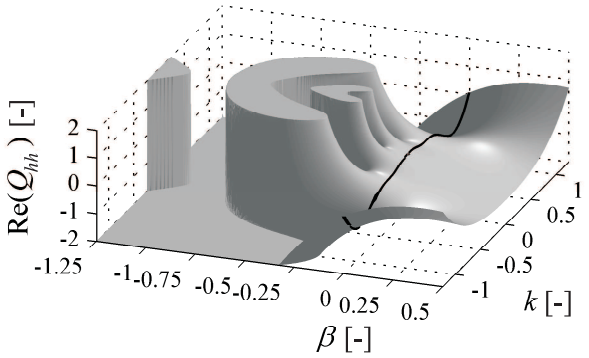

(b) Rfa above the complex reduced frequency plane.

Figure 3.10: Rfa real part of the aerodynamic derivative Q_{hh} of the TaS cross section according to the Roger approach with $n_\gamma = 5$ poles.

In contrast to the theoretical flat-plate case, no exact values are known for the matrices that are given in Eq. (3.31). To better judge the approximation quality, the approximation with $n_\gamma = 3$ poles is also shown.

$$
\begin{aligned}
&\mathbf{A}_0 = \begin{pmatrix} 0 & -3.1378 \\ 0 & -0.5258 \end{pmatrix}, \quad \mathbf{A}_1 = \begin{pmatrix} 3.1541 & -7.8502 \\ 2.8287 & -2.0845 \end{pmatrix} \\
&\mathbf{A}_2 = \begin{pmatrix} -2.4755 & 3.1774 \\ -0.92103 & 0.52666 \end{pmatrix}, \qquad \mathbf{E} = \begin{pmatrix} -0.58494 & 2.7784 \\ -0.54117 & 0.31174 \\ 3.2860 & -9.1890 \\ 2.9423 & -0.44713 \\ -9.6371 & 19.904 \\ -6.3730 & 3.8323 \end{pmatrix} \\
&\gamma_1 = 0.094009 \\
&\gamma_2 = 0.37135 \\
&\gamma_3 = 0.85783 \\
&J = 1.0296
\end{aligned}
\tag{3.35a}
$$

$$
\begin{aligned}
&\mathbf{A}_0 + \sum_{\mu=1}^{n_\gamma} \mathbf{A}_{\mu+2} = \begin{pmatrix} -6.9360 & 10.356 \\ -3.9719 & 3.1711 \end{pmatrix} \\
&-\sum_{\mu=1}^{n_\gamma} \gamma_\mu \mathbf{A}_{\mu+2} = \begin{pmatrix} 7.1018 & -13.923 \\ 4.4252 & -3.1507 \end{pmatrix} \\
&\sum_{\mu=1}^{n_\gamma} \gamma_\mu^2 \mathbf{A}_{\mu+2} = \begin{pmatrix} -6.6438 & 13.404 \\ -4.2888 & 2.7612 \end{pmatrix}
\end{aligned}
\tag{3.35b}
$$

Obviously, neither the matrices $\mathbf{A}_1$ and $\mathbf{A}_2$ nor the right-hand limit $(\mathbf{A}_0 + \sum_{\mu=1}^{n_\gamma} \mathbf{A}_{\mu+2})$ of the aerodynamic step response bear any resemblance when both approximations are compared. The

matrix elements differ in value and sign. When comparing in both approximations the signs of the $\mathbf{A}_1$ and $\mathbf{A}_2$ matrix, which give the orientations of the Dirac impulses and the derivatives of the Dirac impulses in the step response, with those of the $\mathbf{A}_0$ matrix, it can be seen that the associated non-minimum-phase behaviour amazingly depends on the number of used poles. The same defect can be observed when comparing the right hand limit $(\mathbf{A}_0 + \sum_{\mu=1}^{n_\gamma} \mathbf{A}_{\mu+2})$ of the initial value of the aerodynamic step response with the final, steady value $\mathbf{A}_0$. Corresponding to the initial behaviour of the aerodynamic step response, the matrices $\mathbf{A}_1$ and $\mathbf{A}_2$ determine the behaviour of the aerodynamic derivatives for large frequencies along the imaginary frequency axis, as can be seen in Figure 3.2.

Based on the measured aerodynamic frequency response, it cannot be decided which of the two approximations describes the flow effect in a more realistic way. For a full description of the aerodynamic transfer behaviour, the aerodynamic frequency response must be known along the whole imaginary axis or at least along a sufficiently long interval of it, as it is used for the flat plate. Complete sets of aerodynamic step responses, which would be an alternative, sound basis for an evaluation, are usually not measured and are not available in Bergmann (2004). Especially within the range of small time values, the determination of aerodynamic step responses, whether numerical (e. g. Eusani 2005) or experimental (e. g. Yoshimura & Nakamura 1979 and Caracoglia & Jones 2003), is much more challenging than the determination of the aerodynamic frequency response. The kind of harmonic fluctuation that is observable in the measured aerodynamic step response given in Caracoglia & Jones (2003) hints at employing not only poles on the negative real axis but also complex-conjugate ones.

Looking at the size of the lag-term coefficients in the $\mathbf{E}$ matrix, it is questionable whether rational functions with simple real poles are capable of approximating the aerodynamic transfer behaviour of the flow around bluff, non-streamlined cross sections at all. Unlike the flat-plate case, the frequency range of the poles is not essentially changed by the non-linear optimisation of their location. The rational functions obviously try to approximate the aerodynamic derivatives in the identification interval with strongly weighted lag terms. For the different poles, the large coefficients of the lag terms appear with changing signs. Thus, the sum of the lag terms results in the desired behaviour along parts of the imaginary axis. Figure 3.10(b) displays the approximation with $n_\gamma = 5$ poles for the real part of the aerodynamic derivative Q_{hh} over an area of the complex frequency plane. In contrast to Figure 3.7 of the flat plate, the areas around the poles where the approximation functions are strongly distorted are widely extended, even more than in Figure 3.9(a). The effect of highly weighted lag terms is not only caused by the aerodynamic behaviour that strongly differs from the flat-plate one. To some small extent, also the low number of frequencies with original data and the scatter of data provoke an approximation with the large lag terms. Since the effect of highly weighted lag terms also appears for an approximation of a single aerodynamic derivative, it is not a result of the matrix-based Roger approach.

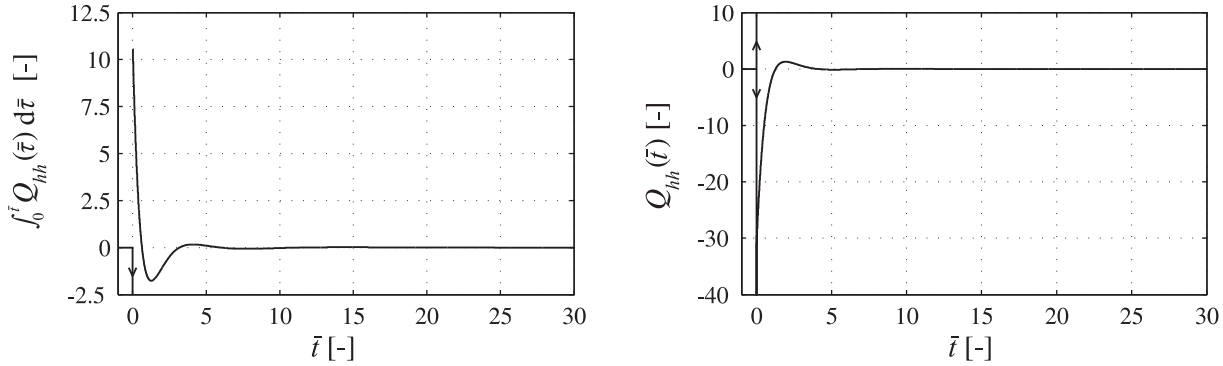

(a) Aerodynamic step response. (b) Aerodynamic impulse response.

Figure 3.11: Time-domain functions of the approximated aerodynamic derivative Q_{hh} of the cross section TaS according to the Roger approach with $n_\gamma = 5$ poles.

Another presumably artificial phenomenon that is visible in Eq. (3.34b) and Eq. (3.35b) occurs in connection with the large lag-term coefficients. The average magnitude of the entries of the right hand limit $(\mathbf{A}_0 + \sum_{\mu=1}^{n_\gamma} \mathbf{A}_{\mu+2})$ of the aerodynamic step response at $t = 0$ is distinctly higher than that of the flat plate. These initial values correspond to the limit of the sum of the $\mathbf{A}_0$ matrix and the lag terms for infinitely high reduced frequencies according to the initial value theorem of Laplace transforms. Moreover, these high values are in connection with large magnitudes of the right hand limits of the initial values of the aerodynamic impulse response and its derivative, which are $(-\sum_{\mu=1}^{n_\gamma} \gamma_\mu \mathbf{A}_{\mu+2})$ and $\sum_{\mu=1}^{n_\gamma} \gamma_\mu^2 \mathbf{A}_{\mu+2}$, respectively. That means that both the aerodynamic step response and impulse response strongly vary for small times. Figure 3.11 illustrates both time-domain functions that correspond to the aerodynamic derivative Q_{hh}. On the one hand, this approximated behaviour of the fluid forces is questionable from the physical point of view. On the other hand, it entails a large numerical effort if the aerodynamic forces are determined via convolution in the time domain. In the convolution integral, which has to be solved for every time step, the time around the starting time of the aerodynamic step or impulse response must be discretised with a high number of time points to take the strong variations into account.

In the frequency domain, the distorted behaviour of the approximated aerodynamic derivatives for large frequencies along the imaginary axis is connected to the distorted behaviour in the frequency plane by the holomorphic character of the rational functions. In contrast to the approximations of the flat-plate derivatives, the approximation of the TaS derivatives is only trustworthy within the ranges of the imaginary frequency axis where original data is used for the fitting. Independent of the special approximation function, whether rational or another one, it could also be that a description of the aerodynamic transfer with a linear time-invariant transfer element is simply impossible for such a non-streamlined cross section.

Table 3.5: Rfa of the aerodynamic derivatives of cross sections in real flow with the Roger approach. For the marked approximations, the optimised poles are determined with the gradient-based algorithm.

	n_γ	$J/n_k \cdot 10^4$	$\overline{\lvert(\mathbf{A}_0 \;\; \mathbf{A}_1 \;\; \mathbf{A}_2)_{jl}\rvert}$	$\overline{\lvert(\mathbf{E})_{jl}\rvert}$	$\overline{\lvert(\mathbf{A}_0 + \sum_{\mu=1}^{n_\gamma} \mathbf{A}_{\mu+2})_{jl}\rvert}$	$\gamma_{\max} - \gamma_{\min}$
PlS	3	44.591	0.62490	0.31880	0.60511	0.45220
	5	27.238	0.65189	4.0730	1.4033	0.75404
	7	22.517	0.92413	349.41	3.9293	0.75307
	10	18.094	2.6014	43591	17.987	0.75305
BeS	3	143.09	0.45519	0.27572	0.41040	0.47849
	5	130.91	0.53351	5.7815	1.4863	1.0139
	7	129.95	0.50306	170.80	1.7684	0.87552
	10	115.53	7.7779	255567	74.900	0.87539
SeS	3	49.374	0.54483	0.53450	0.78342	1.0831
	5*	37.408	0.56152	0.73879	0.63202	0.85275
	7	37.618	0.62170	226.78	1.2141	0.84129
	10	19.221	4.3710	181515	40.520	0.84115
TrS	3	97.654	0.52295	0.46033	0.60951	0.84155
	5	85.204	0.52988	0.93221	0.52392	0.63190
	7	90.563	0.59729	256.30	1.5452	0.85205
	10	75.823	4.6425	255115	44.456	0.83905
ChS	3*	172.35	0.51347	0.84526	1.1963	1.2871
	5	107.83	0.98129	8.9383	3.3147	0.91920
	7	108.40	1.0501	685.15	4.5540	0.83924
	10	74.498	4.6265	139421	39.117	0.83910
TaS	3	1029.6	2.2235	4.9856	6.1087	0.76382
	5	849.16	6.5252	319.97	37.918	0.78787
	7	813.69	8.8274	6457.5	67.454	0.84894
	10	699.29	62.412	1235281	544.58	0.84905

For the aerodynamic derivatives of cross sections in real flow, the effect of an approximation with large lag-term coefficients increases when measuring data is not only extracted for the intervals given in Table 2.1 but also for higher frequencies. This also indicates that rational functions with simple real poles are not the adequate function type for the approximation of the transfer behaviour of the flow around non-streamlined cross sections. In Bergmann (2004) measured aerodynamic derivatives are given up to the imaginary part $k \approx 1.9$ of the reduced frequency. Since the rational function approximation with simple real poles is mainly used in this work to find instabilities of bridge girders in streaming air, the intervals of original data are limited to the range where these instabilities usually begin (Kirch 2010).

As done for the flat plate, Table 3.5 shows the shortened results of the approximation with the Roger approach for the cross sections of Figure 2.7 for different numbers n_γ of poles. All approximations are based on the settings that are described for the TaS section. Only for the approximations that are labelled with *, has the non-linear optimisation been carried out with

Table 3.6: Rfa of the aerodynamic derivatives of cross sections in real flow with the Karpel approach. For the marked approximation, the optimised poles are determined with the gradient-based algorithm.

	n_γ	$J/n_k \cdot 10^4$	$\overline{\lvert(\mathbf{A}_0 \;\; \mathbf{A}_1 \;\; \mathbf{A}_2)_{jl}\rvert}$	$\overline{\lvert(\mathbf{E})_{jl}\rvert}$	$\overline{\lvert(\mathbf{A}_0+\sum_{\mu=1}^{n_\gamma}\mathbf{A}_{\mu+2})_{jl}\rvert}$	$\gamma_{\max}-\gamma_{\min}$
PlS	3	60.749	0.62536	0.31385	0.56213	0.40035
	5	61.082	0.70110	2.6434	0.65935	0.75278
	7	32.423	0.77458	96.036	0.90233	0.75318
	10	21.098	2.4334	86436	15.882	0.75304
BeS	3	145.24	0.45539	0.27047	0.40506	0.46409
	5	138.42	0.48998	5.8221	0.97457	0.87682
	7	137.89	0.48617	28.493	0.96221	0.87540
	10	121.15	5.1286	109804	46.517	0.87540
SeS	3	63.108	0.53741	0.27643	0.53276	0.90025
	5	35.111	0.55471	0.45711	0.54113	0.86494
	7	38.905	0.57692	266.58	1.5001	0.84153
	10	28.896	1.8969	19876	13.717	0.84119
TrS	3	99.421	0.52387	0.37223	0.64936	0.79211
	5	93.886	0.52994	1.4406	0.39599	0.72089
	7	97.252	0.84668	167.86	4.2558	0.84670
	10	85.218	0.87730	64300	3.8376	0.83906
ChS	3	236.90	0.78640	5.2695	2.8840	0.64029
	5*	176.00	0.72238	3.7044	2.2683	0.83910
	7	124.12	0.64459	185.53	2.0606	0.83921
	10	89.616	6.2324	86246	52.534	0.83909
TaS	3	1155.5	2.3133	4.8331	7.0149	0.97557
	5	949.21	4.7229	138.67	24.201	0.84313
	7	872.90	3.9291	2324.7	15.855	0.84891
	10	741.65	59.785	379813	527.05	0.84905

the alternative procedure described in Section 3.4 and $\gamma_\mu \geq 0.05$ because the simplex-based algorithm converges to a solution with poles in the right, unstable frequency plane.

For all cross sections, the relative approximation error J/n_k is much greater than in the flat-plate case, mainly due to the scatter of the measured values. As to be expected, a higher number of lag terms reduces the approximation error in most cases. It can be seen that for the more or less streamlined cross sections SeS and TrS, the effect of highly weighted lag terms does not occur if $n_\gamma = 3$ or $n_\gamma = 5$ poles are employed. For the cross sections PlS and BeS, $n_\gamma = 5$ or more poles should not be used to exclude this effect, though these cross sections are not less streamlined than the two ones addressed before. Increasing the number of lag terms always results in higher lag-term coefficients. For the bluff, non-streamlined TaS cross section, only approximations with highly weighted lag terms occur. In the flow around this cross section, large vortices arise not only at the downstream but also at the upstream side, and when drifting downstream, the latter vortices significantly interact with the downstream side of the cross section (Larsen 2000). The

approximation of the aerodynamic derivatives of the bluff ChS cross section shows a behaviour that is somewhere between those of the streamlined ones and the TaS cross section. Contrary to the theoretical flat-plate case, the entries in the matrices $\mathbf{A}_0$, $\mathbf{A}_1$, and $\mathbf{A}_2$ and the right hand limit $(\mathbf{A}_0 + \sum_{\mu=1}^{n_\gamma} \mathbf{A}_{\mu+2})$ of the initial value of the aerodynamic step response depend on the number of employed poles. When no highly weighted lag terms occur, the averaged entries are at least within the order of magnitude of the theoretically described flat plate. As explained at the end of Section 2.2.2, the original values of the plate cross section PlS slightly differ from those of the theoretically described flat plate. Hence, the approximation results in the first block of Table 3.5 and in Table 3.4 are not the same. According to the results in Table 3.5, an approximation with $n_\gamma = 7$ or more poles is not recommendable for all cross sections because the poles are otherwise not changed at all and the original aerodynamic derivatives are only approximated with highly weighted lag terms.

Table 3.6 gives the approximations based on the Karpel approach. All settings are the same as explained before. To compare the results with the Roger approach, the matrix coefficients **D** and **E** are converted from the Karpel approach in the Roger form with Eq. (3.23) and then, as before, gathered in the matrix **E** from Eq. (3.20). Hence, the initial value limit is also given in the Roger notation. Comparing the approximation errors J with those in Table 3.5 reveals that approximations with the Karpel approach lead to worse results than those with the Roger approach, as can be expected for multiple-input multiple-output transfer systems in general. The approximation of the aerodynamic derivative of the bluff ChS cross section shows highly weighted lag terms also for $n_\gamma = 3$ poles. Apart from that, all other findings explained for the Roger approach still hold true for the Karpel approach.

4 Dynamic Characteristics of the Bridge

4.1 Numerical Example and Finite-Element Discretisation

In the following chapters, the investigations are carried out using a long-span cable-stayed bridge taken from Starossek (1992) as a numerical example. One-dimensional structural models are employed for the different structural components of the bridge. In detail, the bridge girder, the pylons, and the stay cables are included in the model.

The equations of motion of classical continuum models are difficult to solve analytically, especially for structures with a complex spatial topology. Spatially discretised models of such structures are, however, appropriate for a numerical matrix-based solution on a digital computer. Currently, the finite-element method is the most widely used concept for a spatial discretisation. In this section, the employed solid continuum models and the finite elements are introduced. Apart from different sign conventions, they comply for rigid cross sections with those used in Starossek (1992), which in turn are oriented on the contents of Clough & Penzien (1993).

For all structural components, it is assumed that the material behaviour is linear elastic and the displacements are small. The bending of the girder and the pylons is modelled according to the beam theory, without taking into account the shear deformation due to shear forces. Moreover, neither the deformation under axial forces nor bending inertia effects in axial direction are incorporated in the model. Later addressed restrictions on the topology of the bridge and the investigated forces allow considering uniaxial bending only. The linearised influence of the axial forces on the bending stiffness is included in the model, based on an assumed dominance of the static loading. As feasible for closed box-girder cross sections, warping torsion is assumed to be negligible for the girder and only St. Venant's torsion is considered. The stay cables are modelled as ties. Only their stiffness is included in the bridge model. Neglecting cable vibrations, the softening effect of the cable sag is accounted for by modifying the elastic modulus in the sense of a tangent modulus according to Ernst (1965).

Figure 4.1 shows the straight-lined finite element of the length l_e that is used for the combined bending and torsion of the bridge girder without flaps and the bending of the pylons. All following

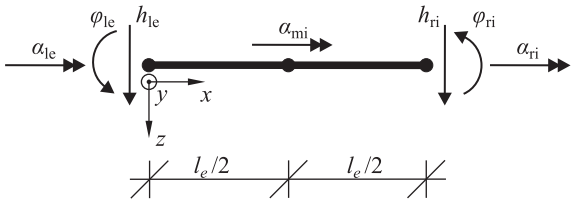

Figure 4.1: Finite element and nodal displacements.

values are defined with respect to the single finite element and the local element coordinates x, y, and z. The nodal displacements are arranged in the vector $\mathbf{v}^{\mathrm{e}}$ as follows.

$$\mathbf{v}^{\mathrm{e}} = \begin{pmatrix} \mathbf{v}_h^{\mathrm{e}} \\ \mathbf{v}_\alpha^{\mathrm{e}} \end{pmatrix}, \quad \mathbf{v}_h^{\mathrm{e}} = \begin{pmatrix} h_{\mathrm{le}} & \varphi_{\mathrm{le}} & h_{\mathrm{ri}} & \varphi_{\mathrm{ri}} \end{pmatrix}^{\mathrm{T}}, \quad \mathbf{v}_\alpha^{\mathrm{e}} = \begin{pmatrix} \alpha_{\mathrm{le}} & \alpha_{\mathrm{mi}} & \alpha_{\mathrm{ri}} \end{pmatrix}^{\mathrm{T}} \tag{4.1}$$

A notation with entries of the same dimension is possible but not used here, as usually done in a finite-element analysis. The vector of nodal forces $\mathbf{s}^{\mathrm{e}}$, which represents the influence of neighbouring elements, is defined in an energetically corresponding way.

$$\mathbf{s}^{\mathrm{e}} = \begin{pmatrix} \mathbf{s}_h^{\mathrm{e}} \\ \mathbf{s}_\alpha^{\mathrm{e}} \end{pmatrix} \tag{4.2}$$

Due to the unknown displacements and the given loads, a displacement formulation is chosen for the finite element, as usually done in structural mechanics. Along the element length, the continuous displacements $\mathbf{u}^{\mathrm{e}}$ are approximated with shape functions $\mathbf{\Omega}^{\mathrm{e}}$.

$$\mathbf{u}^{\mathrm{e}} = \mathbf{\Omega}^{\mathrm{e}}\mathbf{v}^{\mathrm{e}}, \quad \mathbf{u}^{\mathrm{e}} = \begin{pmatrix} h \\ \alpha \end{pmatrix}, \quad \mathbf{\Omega}^{\mathrm{e}} = \begin{pmatrix} \mathbf{\Omega}_h^{\mathrm{e}} & \mathbf{0} \\ \mathbf{0} & \mathbf{\Omega}_\alpha^{\mathrm{e}} \end{pmatrix} \tag{4.3a}$$

$$\begin{aligned} \mathbf{\Omega}_h^{\mathrm{e}} &= \begin{pmatrix} 1-3\xi_{\mathrm{e}}^2+2\xi_{\mathrm{e}}^3 & (-\xi_{\mathrm{e}}+2\xi_{\mathrm{e}}^2-\xi_{\mathrm{e}}^3)l_{\mathrm{e}} & 3\xi_{\mathrm{e}}^2-2\xi_{\mathrm{e}}^3 & (\xi_{\mathrm{e}}^2-\xi_{\mathrm{e}}^3)l_{\mathrm{e}}) \end{pmatrix} \\ \mathbf{\Omega}_\alpha^{\mathrm{e}} &= \begin{pmatrix} 1-3\xi_{\mathrm{e}}+2\xi_{\mathrm{e}}^2 & 4\xi_{\mathrm{e}}-4\xi_{\mathrm{e}}^2 & -\xi_{\mathrm{e}}+2\xi_{\mathrm{e}}^2 \end{pmatrix} \end{aligned} \tag{4.3b}$$

The variable $\xi_{\mathrm{e}} = x/l_{\mathrm{e}}$ denotes the non-dimensional element coordinate. Usual cubic polynomials are employed for bending. The stability of a slender bridge with a streamlined cross section in streaming air is governed, among other things, by the coupling of structural bending and torsional eigenmodes. In both kinds of displacement, a discretisation error should thus be in the same order of magnitude. This requirement is met because in combination with the used bending approximation, shape functions in terms of quadratic polynomials for torsion are employed (Starossek 1992).

As external forces, distributed loads $\mathbf{p}^{\mathrm{e}}$ and nodal loads $\mathbf{t}^{\mathrm{e}}$ act on the element energetically corresponding to the continuous displacements $\mathbf{u}^{\mathrm{e}}$ and the nodal displacements $\mathbf{v}^{\mathrm{e}}$, respectively.

Along its length, the element has constant mass and stiffness properties, which are gathered in the continuous mass matrix $\mathbf{M}^{\mathrm{e,c}}$ and the continuous stiffness matrix $\mathbf{E}^{\mathrm{e,c}}$.

$$\mathbf{M}^{\mathrm{e,c}} = \begin{pmatrix} m & 0 \\ 0 & I \end{pmatrix}, \quad \mathbf{E}^{\mathrm{e,c}} = \begin{pmatrix} EI_\varphi & 0 \\ 0 & GI_\mathrm{t} \end{pmatrix} \tag{4.4}$$

The variable m represents the mass of the bridge girder, and I is the mass moment of inertia with respect to the centre of gravity of the girder cross section. Both properties are related to a unit length in direction of the torsional axis. Young's modulus is abbreviated with E and the shear modulus with G. The cross section properties I_φ and I_t are the area moment of inertia and the torsional moment of inertia, respectively.

Concerning space, a weak form of the dynamic equilibrium can be derived for the element with the principle of virtual displacements, which allows using the approximated displacements. The virtual displacements are assumed in terms of virtual versions of the approximated displacements. As a result, the semidiscrete equation of motion

$$\mathbf{M}^\mathrm{e}\ddot{\mathbf{v}}^\mathrm{e} + \mathbf{K}^\mathrm{e}\mathbf{v}^\mathrm{e} = \mathbf{f}^\mathrm{e} + \mathbf{s}^\mathrm{e} \tag{4.5}$$

is obtained for the finite element. The mass matrix $\mathbf{M}^\mathrm{e}$, the stiffness matrix $\mathbf{K}^\mathrm{e}$, and the nodal force vector $\mathbf{f}^\mathrm{e}$ can be derived in a consistent way. For simplification purposes, it is assumed that the shear centre of the cross section is identical to its mass centre. Hence, bending and torsion are uncoupled in the mass and the stiffness matrix of the element.

$$\begin{aligned} \mathbf{M}^\mathrm{e} &= \int_0^{l_\mathrm{e}} \boldsymbol{\Omega}^{\mathrm{e}\mathrm{T}} \mathbf{M}^{\mathrm{e,c}} \boldsymbol{\Omega}^\mathrm{e} \,\mathrm{d}x \\ &= l_\mathrm{e} \begin{pmatrix} m\boldsymbol{\Psi}_{hh} & \mathbf{0} \\ \mathbf{0} & I\boldsymbol{\Psi}_{\alpha\alpha} \end{pmatrix} \end{aligned} \tag{4.6a}$$

$$\begin{aligned} \mathbf{K}^\mathrm{e} = \int_0^{l_\mathrm{e}} & \left(\begin{pmatrix} -\frac{\mathrm{d}^2}{\mathrm{d}x^2} & 0 \\ 0 & \frac{\mathrm{d}}{\mathrm{d}x} \end{pmatrix} \boldsymbol{\Omega}^\mathrm{e} \right)^\mathrm{T} \mathbf{E}^{\mathrm{e,c}} \left(\begin{pmatrix} -\frac{\mathrm{d}^2}{\mathrm{d}x^2} & 0 \\ 0 & \frac{\mathrm{d}}{\mathrm{d}x} \end{pmatrix} \boldsymbol{\Omega}^\mathrm{e} \right) \mathrm{d}x + \\ & + \begin{pmatrix} N \int_0^{l_\mathrm{e}} \frac{\mathrm{d}\boldsymbol{\Omega}_h^{\mathrm{e}\mathrm{T}}}{\mathrm{d}x} \frac{\mathrm{d}\boldsymbol{\Omega}_h^\mathrm{e}}{\mathrm{d}x} \,\mathrm{d}x & \mathbf{0} \\ \mathbf{0} & \mathbf{0} \end{pmatrix} \\ = & \begin{pmatrix} \frac{EI_\varphi}{l_\mathrm{e}^3} \tilde{\tilde{\boldsymbol{\Psi}}}_{hh} + \frac{N}{l_\mathrm{e}} \tilde{\boldsymbol{\Psi}}_{hh} & \mathbf{0} \\ \mathbf{0} & \frac{GI_\mathrm{t}}{l_\mathrm{e}} \tilde{\tilde{\boldsymbol{\Psi}}}_{\alpha\alpha} \end{pmatrix} \end{aligned} \tag{4.6b}$$

$$\mathbf{f}^\mathrm{e} = \int_0^{l_\mathrm{e}} \boldsymbol{\Omega}^{\mathrm{e}\mathrm{T}} \mathbf{p}^\mathrm{e} \,\mathrm{d}x + \mathbf{t}^\mathrm{e} \tag{4.6c}$$

Along the element length, the static axial force N in Eq. (4.6b) is assumed to be constant. The symmetric main-diagonal block matrices in Eq. (4.6) read as follows.

$$\boldsymbol{\Psi}_{hh} = \frac{1}{420}\begin{pmatrix} 156 & -22l_\mathrm{e} & 54 & 13l_\mathrm{e} \\ & 4l_\mathrm{e}^2 & -13l_\mathrm{e} & -3l_\mathrm{e}^2 \\ & & 156 & 22l_\mathrm{e} \\ \text{symm.} & & & 4l_\mathrm{e}^2 \end{pmatrix}, \quad \boldsymbol{\Psi}_{\alpha\alpha} = \frac{1}{30}\begin{pmatrix} 4 & 2 & -1 \\ & 16 & 2 \\ \text{symm.} & & 4 \end{pmatrix} \tag{4.7a}$$

$$\tilde{\boldsymbol{\Psi}}_{hh} = \frac{1}{30}\begin{pmatrix} 36 & -3l_\mathrm{e} & -36 & -3l_\mathrm{e} \\ & 4l_\mathrm{e}^2 & 3l_\mathrm{e} & -l_\mathrm{e}^2 \\ & & 36 & 3l_\mathrm{e} \\ \text{symm.} & & & 4l_\mathrm{e}^2 \end{pmatrix} \tag{4.7b}$$

$$\tilde{\tilde{\boldsymbol{\Psi}}}_{hh} = 2\begin{pmatrix} 6 & -3l_\mathrm{e} & -6 & -3l_\mathrm{e} \\ & 2l_\mathrm{e}^2 & 3l_\mathrm{e} & l_\mathrm{e}^2 \\ & & 6 & 3l_\mathrm{e} \\ \text{symm.} & & & 2l_\mathrm{e}^2 \end{pmatrix}, \quad \tilde{\tilde{\boldsymbol{\Psi}}}_{\alpha\alpha} = \frac{1}{3}\begin{pmatrix} 7 & -8 & 1 \\ & 16 & -8 \\ \text{symm.} & & 7 \end{pmatrix} \tag{4.7c}$$

In Eq. (4.6c), the detailed representation of distributed loads in the force vector $\mathbf{f}^\mathrm{e}$ is not given because it depends on the special type of forces. For motion- and gust-induced aerodynamic forces, the entries are addressed in the paragraphs below.

The well known stiffness matrix of the plane two-node truss element, which is employed for the cables, can be taken from the technical literature. When the virtual work principle is formulated for the total discretised structure, the work of the nodal forces $\mathbf{s}^\mathrm{e}$ vanishes. The global matrices and vectors of the structure can be assembled from the derived element values in the sense of the direct stiffness method.

For the description of the continuously distributed aerodynamic forces that act on the bending-torsion element, the aerodynamic strip theory is applied, as mentioned at the end of Section 2.1. The reference wind velocity of the value U blows in direction of the local y axis of the finite element. Static aerodynamic forces are not considered in detail. For real cross sections, they usually cause biaxial bending and the position of the aerodynamic reference point S_a with respect to the shear centre must be known.

The equation for the continuously distributed motion-induced aerodynamic forces can be derived using Eq. (2.1a) and Eq. (2.8a) in connection with the detailed entries given in Eq. (2.19a).

$$\mathbf{p}^\mathrm{e} = q_0 \begin{pmatrix} \frac{1}{b} & 0 \\ 0 & 1 \end{pmatrix} \mathbf{Q} \begin{pmatrix} \frac{1}{b} & 0 \\ 0 & 1 \end{pmatrix} \mathbf{u}^\mathrm{e} \tag{4.8}$$

Along the element length, the value of the reference wind velocity U, the nominal cross-section width b, and the aerodynamically effective cross-section shape are taken as constant. The nodal force vector follows from Eq. (4.6c).

$$\mathbf{f}^{\mathrm{e}} = q_0 \mathbf{Q}^{\mathrm{e}} \mathbf{v}^{\mathrm{e}} \,, \quad \mathbf{Q}^{\mathrm{e}} = \int_0^{l_{\mathrm{e}}} \mathbf{\Omega}^{\mathrm{e}\mathrm{T}} \begin{pmatrix} \frac{1}{b} & 0 \\ 0 & 1 \end{pmatrix} \mathbf{Q} \begin{pmatrix} \frac{1}{b} & 0 \\ 0 & 1 \end{pmatrix} \mathbf{\Omega}^{\mathrm{e}} \, \mathrm{d}x \tag{4.9}$$

Solving the integrals leads to the following entries in the derivative matrix

$$\mathbf{Q}^{\mathrm{e}} = l_{\mathrm{e}} \begin{pmatrix} Q_{hh} \frac{1}{b^2} \mathbf{\Psi}_{hh} & Q_{h\alpha} \frac{1}{b} \mathbf{\Psi}_{h\alpha} \\ Q_{\alpha h} \frac{1}{b} \mathbf{\Psi}_{\alpha h} & Q_{\alpha\alpha} \mathbf{\Psi}_{\alpha\alpha} \end{pmatrix} \quad , \tag{4.10}$$

where the main diagonal block matrices $\mathbf{\Psi}_{hh}$ and $\mathbf{\Psi}_{\alpha\alpha}$ are those from Eq. (4.7a) and the off-diagonal block matrices are

$$\mathbf{\Psi}_{h\alpha} = \frac{1}{60} \begin{pmatrix} 11 & 20 & -1 \\ -l_{\mathrm{e}} & -4l_{\mathrm{e}} & 0 \\ -1 & 20 & 11 \\ 0 & 4l_{\mathrm{e}} & l_{\mathrm{e}} \end{pmatrix} \,, \quad \mathbf{\Psi}_{\alpha h} = \mathbf{\Psi}_{h\alpha}^{\mathrm{T}} \quad . \tag{4.11}$$

These non-zero matrices in Eq. (4.11) show that bending and torsion are coupled in the element by the motion-induced aerodynamic forces. Due to the definition of the entries in the nodal vectors $\mathbf{f}^{\mathrm{e}}$ and $\mathbf{v}^{\mathrm{e}}$, the entries in the derivative matrix $\mathbf{Q}^{\mathrm{e}}$ are neither dimensionless in general nor do they all have the same dimension.

If the value U of the reference wind velocity and the nominal half-width b of the structural member is not constant along the member length, the aerodynamic admittance $\mathbf{G}_{\mathrm{ae}}^{\mathrm{e}} = q_0 \mathbf{Q}^{\mathrm{e}}(p)$ of the finite element has to be described with respect to reference values that are common for all elements in order to obtain a global representation in the form of Eq. (2.8a).

$$\begin{aligned} &\mathbf{G}_{\mathrm{ae}}^{\mathrm{e}} = q_{0,\mathrm{ref}} \tilde{\mathbf{Q}}^{\mathrm{e}}(p_{\mathrm{ref}}) \,, \\ &q_{0,\mathrm{ref}} = \pi \rho b_{\mathrm{ref}}^2 U_{\mathrm{ref}}^2 \,, \quad \tilde{\mathbf{Q}}^{\mathrm{e}}(p_{\mathrm{ref}} = \frac{s b_{\mathrm{ref}}}{U_{\mathrm{ref}}}) = \left(\frac{b}{b_{\mathrm{ref}}} \frac{U}{U_{\mathrm{ref}}} \right)^2 \mathbf{Q}^{\mathrm{e}}(p = \frac{b}{b_{\mathrm{ref}}} \frac{U_{\mathrm{ref}}}{U} p_{\mathrm{ref}}) \end{aligned} \tag{4.12}$$

The dependence of distributed gust-induced aerodynamic forces on gusts $\mathbf{u}^{\mathrm{g,e}}$ that act along the element length can be represented based on Eq. (2.1b) and Eq. (2.8b) with the entries in Eq. (2.19b) as follows.

$$\mathbf{p}^{\mathrm{e}} = q_0 \begin{pmatrix} \frac{1}{b} & 0 \\ 0 & 1 \end{pmatrix} \mathbf{Q}^{\mathrm{g}} \mathbf{u}^{\mathrm{g,e}} \,, \quad \mathbf{u}^{\mathrm{g,e}} = \begin{pmatrix} w^{\mathrm{g}}/U \end{pmatrix} \tag{4.13}$$

Again, the nodal force vector can be derived with the help of Eq. (4.6c).

$$\mathbf{f}^{\mathrm{e}} = q_0 \int_0^{l_\mathrm{e}} \mathbf{\Omega}^{\mathrm{eT}} \begin{pmatrix} \frac{1}{b} & 0 \\ 0 & 1 \end{pmatrix} \mathbf{Q}^{\mathrm{g}} \mathbf{u}^{\mathrm{g,e}} \,\mathrm{d}x \tag{4.14}$$

Along the element, the distribution of the gusts of the natural wind field has a stochastic nature and cannot be given in a form that allows solving the integral in Eq. (4.14) analytically. The first step to get a grip on this problem is the assumption of a distribution shape $\mathbf{\Omega}^{\mathrm{g,e}}$ of the gust velocities with a constant ordinate along the element. For the ordinates $\mathbf{v}^{\mathrm{g,e}}$, the fluctuating gust velocities on a single point of the element — for instance the midpoint — are used.

$$\mathbf{u}^{\mathrm{g,e}} = \mathbf{\Omega}^{\mathrm{g,e}} \mathbf{v}^{\mathrm{g,e}} \,, \qquad \mathbf{\Omega}^{\mathrm{g,e}} = (1) \,, \quad \mathbf{v}^{\mathrm{g,e}} = \begin{pmatrix} w^{\mathrm{g}}_{\mathrm{mi}}/U \end{pmatrix} \tag{4.15}$$

Hence, the discretised input-output equation of the nodal force vector results in the following form.

$$\mathbf{f}^{\mathrm{e}} = q_0 \mathbf{Q}^{\mathrm{g,e}} \mathbf{v}^{\mathrm{g,e}} \,, \quad \mathbf{Q}^{\mathrm{g,e}} = \int_0^{l_\mathrm{e}} \mathbf{\Omega}^{\mathrm{eT}} \begin{pmatrix} \frac{1}{b} & 0 \\ 0 & 1 \end{pmatrix} \mathbf{Q}^{\mathrm{g}} \,\mathrm{d}x \tag{4.16}$$

The problem of reference values for structural members with varying parameters U and b can be solved as shown for the motion-induced aerodynamic forces.

Since the gusts are assumed to be fully correlated along the element length, the gust-induced aerodynamic forces are overestimated. One way to counteract this discretisation error is to limit the element length. Another method is to derive reduction factors in terms of joint acceptance functions. As the effect of gust-induced aerodynamic forces on the bridge is not investigated with the finite-element model in this work, the explanations and references given in Clobes (2008) are referred to.

With the element values derived so far, the equation of motion of the global structure can be assembled in the following form.

$$\mathbf{M}_{\mathrm{s}} \ddot{\boldsymbol{\xi}}_{\mathrm{s}}(t) + \mathbf{K}_{\mathrm{s}} \boldsymbol{\xi}_{\mathrm{s}}(t) = \mathbf{f}(t) \tag{4.17}$$

The variable $\boldsymbol{\xi}_{\mathrm{s}}$ stands for the structural degrees of freedom, and the global mass and stiffness matrices are denoted with $\mathbf{M}_{\mathrm{s}}$ and $\mathbf{K}_{\mathrm{s}}$, respectively. Due to the used finite-element algorithm, both real matrices are symmetric, a form that can finally be obtained for every conservative structural system. For the following derivations, it is assumed that every degree of freedom is connected with a mass. All kinds of forces that are not accounted for with both summands on the left side of the equation are gathered in the global force vector $\mathbf{f}$.

Figure 4.2 shows the discretised model of the investigated cable-stayed bridge together with the numbered global degrees of freedom. The geometry corresponds to the position of the bridge under the effect of its self-weight, and the displacements are defined with respect to this position. All structural components lie in the same plane. The mean wind is blowing perpendicular to the drawing plane against the face of the reader. For such a topology, in consideration of the restrictions mentioned for the used elements, bending and torsion are uncoupled in the global mass and stiffness matrix. Additionally, the horizontal bending must only be considered if there are forces perpendicular to the model plane. The effect of these forces is not the focus of this work. Hence, the corresponding degrees of freedom are usually not addressed in the following. The segmentations of the girder and the pylons are similar to those chosen in Starossek (1992), which are determined by the location of the supports and the cable-girder connections.

In Starossek (1992), the structural properties of the cable-stayed bridge are not given in a way that allows for an exact verification of the numerical results. The input file of the computer programme that had been used for the original investigations, however, was made available to the author of this work. Based on this input file, the structural properties are listed in Table 4.1.

Table 4.1: Structural properties of the bridge model. If parameters vary, they are listed for the left part of the bridge, from the left to the right or from the bottom to the top element. The original value of the torsional moment of inertia of the girder from Starossek (1992) is given in brackets.

cable		girder	pylon	
$E = 200000$ MPa		$E = 200000$ MPa	$E = 200000$ MPa	
$\gamma = 78.5$ kN/m^3		$G = 75000$ MPa	$N = -23.65$ MN	
$A \cdot 10^3$ [m^2]	N [MN]	$I_\varphi = 0.7$ m^4 $I_\mathrm{t} = 0.3818$ m^4	I_φ [m^4]	m [t/m]
2.951	11.23	($= 0.306$ m^4)	1.07	6.3
5.410	2.703	$m = 6.4$ t/m	0.75	4.4
4.611	2.304	$I = 200$ tm^2/m		
3.937	1.961			
3.775	1.873	N [MN]		
3.775	1.873	−9.66		
3.937	1.961	−11.84		
4.611	2.304	−13.50		
5.410	2.703	−14.64		
6.271	3.138	−15.32		
7.190	3.595	−15.32		
8.113	4.068	−14.64		
		−13.50		
		−11.84		
		−9.66		
		−6.96		
		−3.74		
		0		

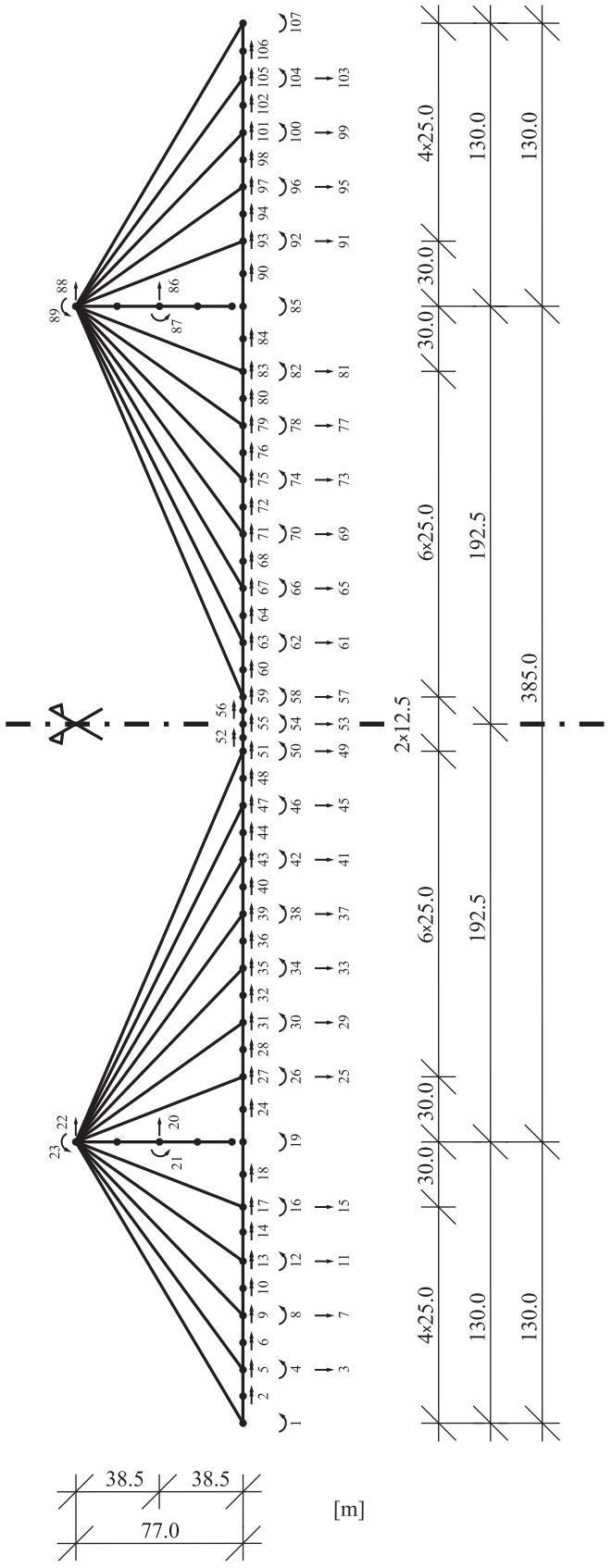

Figure 4.2: Investigated cable-stayed bridge and its discretisation.

They are employed independently of the aerodynamically effective shape of the girder cross section. Although the material properties differ somewhat from those used in current European standards, they have not been changed. The torsional moment of inertia of the girder is varied in Starossek (1992), but only for one value, detailed results are documented. Here, a slightly higher value is chosen. The reason is given later on. For verification purposes, the original value is included in the table. Eq. (4.17) must be seen as the result of a linearisation of the geometrically non-linear behaviour of the structure at the self-weight position. The stiffness of the cables is thus determined by the corresponding normal forces. In the above-mentioned original input file, the cable data is given in terms of stiffness-matrix elements. Hence, the corresponding tabulated values are back-calculated and not the exact original ones. The variables A and γ denote the cross-section area and the specific weight of the cable, respectively.

4.2 Modal Analysis of the Undamped Structural System and Structural Damping

A first step to analyse the dynamic characteristics of the structural system can be taken by solving the generalised linear eigenvalue problem

$$((-\omega_{\mathrm{s}}^2)\mathbf{M}_{\mathrm{s}} + \mathbf{K}_{\mathrm{s}})\breve{\boldsymbol{\xi}}_{\mathrm{s}} = \mathbf{0} \tag{4.18}$$

with the eigenvalues $(-\omega_{\mathrm{s},j}^2) = (\pm \mathrm{i}\omega_{\mathrm{s},j})^2$ and eigenvectors $\breve{\boldsymbol{\xi}}_{\mathrm{s},j}$. The absolute values $\omega_{\mathrm{s},j}$ of the imaginary parts of $(\pm \mathrm{i}\omega_{\mathrm{s},j})$ are called the eigenfrequencies of the undamped structure. According to the size of the eigenfrequencies, the mode numbers j are defined. All eigenvalues and eigenvectors in this work are computed with the function `eig` of MATLAB (2007), which uses routines from the LAPACK (Linear Algebra PACKage) software library. Due to the mentioned decoupling of the degrees of freedom in the mass and the stiffness matrix, the modes have either bending or torsional shapes. As with all conservative structural systems for which rigid-body motions are prevented and static instabilities do not occur, only negative real eigenvalues $(-\omega_{\mathrm{s},j}^2)$ with different real eigenvectors are possible.

Table 4.2 shows some numerical results of the eigenvalue problem for the investigated bridge under its self-weight. Using the original torsional moment of inertia I_{t} leads to the same frequencies for torsional mode shapes that are given in Starossek (1992). Due to the decoupling, the higher I_{t} only changes the frequencies of the torsional vibration. The torsional mode shapes displayed in Figure 4.3 are the same for both values of I_{t} because it is multiplicatively changed in the whole girder. The shapes of the third and fourth torsional mode depend on the special eigenvalue solver. Both different modes have the same eigenvalue, and the corresponding eigenvectors can be replaced by different non-zero linear combinations of them. Since the original cable data is

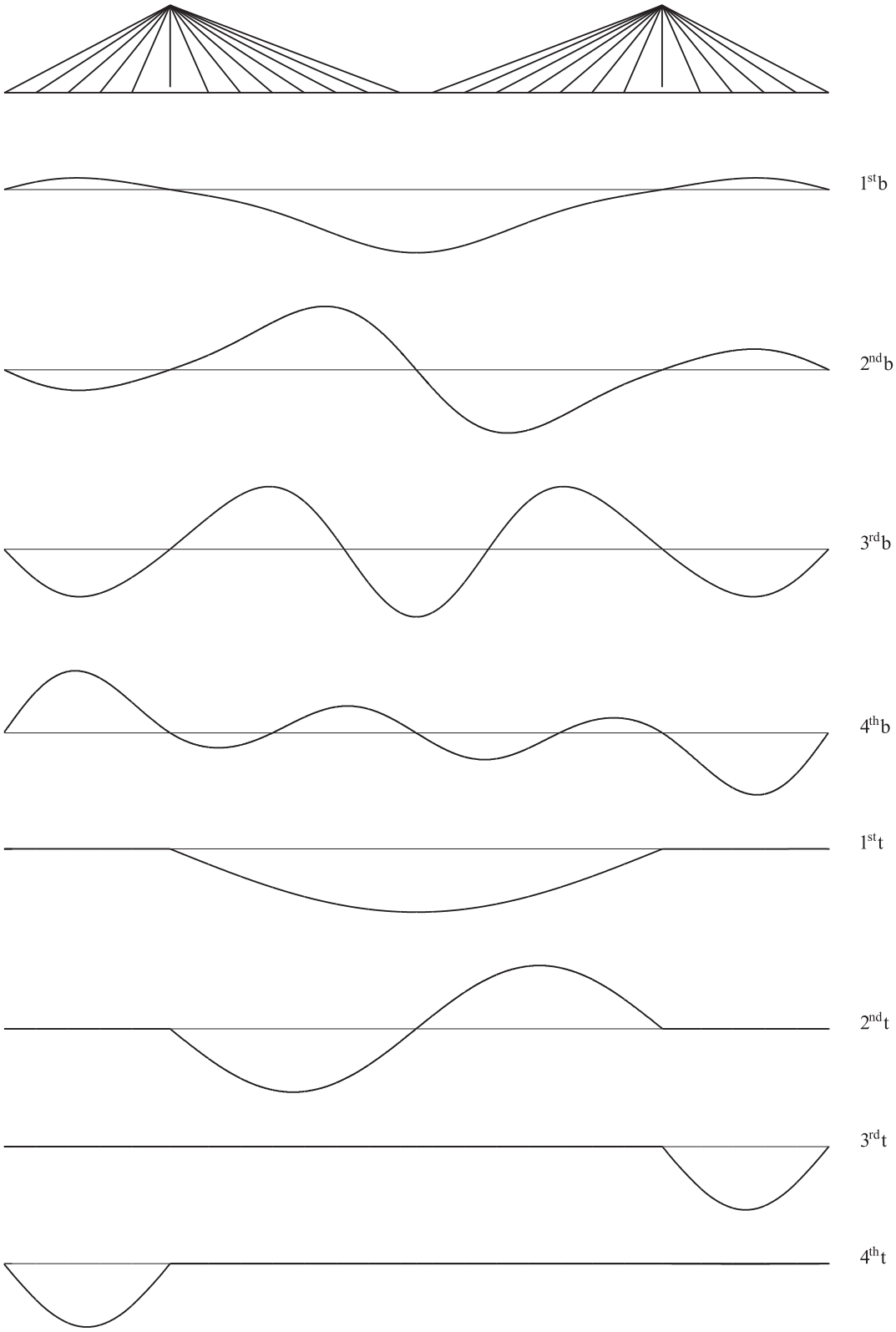

Figure 4.3: Lowest bending and torsional structural eigenmodes (b: bending; t: torsion).

not known exactly, the bending eigenfrequencies, however, differ very slightly from the reference values. The lower the mode number, the more the cables influence the bending stiffness of the structure and, thus, these eigenfrequencies. Hence, the differences increase with decreasing mode numbers. Visually compared, bending and torsional mode shapes in Figure 4.3 comply with those given in Starossek (1992).

Table 4.2: Lowest bending and torsional eigenfrequencies ω_s $[1/s]$ of the undamped structural system. Italic values are taken from Starossek (1992) for a verification.

bending		torsion		
2.4701	*2.468*	3.0876	(2.764)	*2.764*
3.5351	*3.533*	6.1754	(5.528)	*5.528*
5.2411	*5.241*	9.1453		
5.9975	*5.998*	9.1453		

As no multiple eigenvalues with identical eigenvectors occur, both matrices $\mathbf{M}_s$ and $\mathbf{K}_s$ in Eq. (4.18) can be diagonalised. For the special case of symmetric matrices, this can be done with the modal matrix $\mathbf{\Phi}_s$, whose columns are the eigenvectors $\breve{\boldsymbol{\xi}}_{s,j}$. Different eigenvectors of a multiple eigenvalue have to be orthogonal to each other when employed in the modal matrix. Although the function `eig` ensures this orthogonality, the specific choice of orthogonal eigenvectors is processor dependent. Using the transformation

$$\boldsymbol{\xi}_s = \mathbf{\Phi}_s \boldsymbol{\xi}_s^m \tag{4.19}$$

of the degrees of freedom, Eq. (4.17) can be converted into the following form

$$\mathbf{M}_s^m \ddot{\boldsymbol{\xi}}_s^m(t) + \mathbf{K}_s^m \boldsymbol{\xi}_s^m(t) = \mathbf{f}^m(t) \quad , \tag{4.20}$$

where

$$\mathbf{M}_s^m = \mathbf{\Phi}_s^T \mathbf{M}_s \mathbf{\Phi}_s \; , \quad \mathbf{K}_s^m = \mathbf{\Phi}_s^T \mathbf{K}_s \mathbf{\Phi}_s \; , \quad \mathbf{f}^m = \mathbf{\Phi}_s^T \mathbf{f} \quad . \tag{4.21}$$

Modal variables are indicated with the superscript $(\;)^m$. The modal mass and the modal stiffness matrix are diagonal. In the numerical calculations of this work, the eigenvectors in the modal matrix, which are indeterminate with respect to a real scalar factor, are normalised so that $\mathbf{M}_s^m = \mathbf{I}$ unless otherwise specified. Additionally, all matrices that result from a multiplication with the modal matrix are cleaned of very small artificial entries. Not all eigenvectors, whose total number equals the number of entries in the vector $\boldsymbol{\xi}_s$, have to be included in the modal matrix. Depending on the loading and the dynamic characteristics of the structure, only some eigenvectors are necessary to represent Eq. (4.17) with a sufficient accuracy. When reducing the width of the modal matrix, the discretisation with modal degrees of freedom includes, thus, a model simplification.

Structural damping can be accounted for in several ways. Here, modal viscous damping is applied.

$$\mathbf{C}_{\mathrm{s}}^{\mathrm{m}} = \mathrm{diag}\left(\quad \cdots \quad 2\omega_{\mathrm{s},j} M_{\mathrm{s},j}^{\mathrm{m}} \frac{\delta_{\mathrm{s},j}}{2\pi} \quad \cdots \quad \right) \tag{4.22}$$

Eq. (4.22) shows the modal damping matrix with the eigenfrequency $\omega_{\mathrm{s},j}$, the modal mass $M_{\mathrm{s},j}^{\mathrm{m}}$, and the logarithmic decrement $\delta_{\mathrm{s},j}$ of the j^{th} structural eigenmode. Modal damping can be limited to a subset of modes if desired. Corresponding to Eq. (4.21), the transformation of the modal damping matrix from the modal into the physical space is as follows.

$$\mathbf{C}_{\mathrm{s}} = (\mathbf{\Phi}_{\mathrm{s}}^{-1})^{\mathrm{T}} \mathbf{C}_{\mathrm{s}}^{\mathrm{m}} \mathbf{\Phi}_{\mathrm{s}}^{-1} \tag{4.23}$$

Only the columns in $\mathbf{\Phi}_{\mathrm{s}}$ and the rows in $\mathbf{\Phi}_{\mathrm{s}}^{-1}$ have to be considered that correspond to the damped eigenmodes. The inverted modal matrix can be obtained in a numerically efficient way.

$$\mathbf{\Phi}_{\mathrm{s}}^{-1} = (\mathbf{M}_{\mathrm{s}}^{\mathrm{m}})^{-1} \mathbf{\Phi}_{\mathrm{s}}^{\mathrm{T}} \mathbf{M}_{\mathrm{s}} \,, \quad (\mathbf{M}_{\mathrm{s}}^{\mathrm{m}})^{-1} = \mathrm{diag}\left(\quad \cdots \quad 1/M_{\mathrm{s},j}^{\mathrm{m}} \quad \cdots \quad \right) \tag{4.24}$$

With the used eigenvector normalisation, the inverse modal mass matrix equals the identity matrix. Even if not all eigenmodes are considered, Eq. (4.24) can be used with the truncated modal matrix and the truncated modal mass matrix to directly determine the truncated inverse. With the relation

$$\mathbf{f}_{\mathrm{d}}(t) = -\mathbf{C}_{\mathrm{s}} \dot{\boldsymbol{\xi}}_{\mathrm{s}}(t) \quad , \tag{4.25}$$

the viscous damping force $\mathbf{f}_{\mathrm{d}}$ can be inserted into Eq. (4.17).

For assigning damping values to the investigated bridge, the eigenmodes are grouped into bending and torsional modes. As shown in Table 4.3, a logarithmic decrement of $\delta_{\mathrm{s}} = 0.015$ is used for the lowest mode number of each group. The decrements of the other given modes increase according to the proposal given in Petersen (1996). For all modes that are not listed in Table 4.3, the logarithmic decrement of $\delta_{\mathrm{s}} = 0.2$ is chosen.

Table 4.3: Logarithmic decrements δ_{s} for the structural damping of the first eigenmodes. The reference value is $\delta_{\mathrm{s}}^{0} = 0.015$.

$\delta_{\mathrm{s}}/\delta_{\mathrm{s}}^{0}$	1	2	3	4	5	6	7	8	9	10
bending	1	3	4	5	7	8	12	13	15	16
torsion	2	6	9, 10	11	14	19	21, 22	23	25	26

Another way to account for structural damping is the introduction of the imaginary stiffness. In contrast to viscous damping, it aims at a frequency-independent damping formulation. This kind

of damping is applied in Starossek (1992) for the original bridge model. For a numerical check of the described finite-element model, the alternative damping approach needs to be explained.

Imaginary stiffness has been applied to structures in streaming air for a long time (e. g. Theodorsen & Garrick 1938, Klöppel & Thiele 1967, Argyris & Mlejnek 1988). It transfers the structural displacement ξ_s to the damping force f_d.

$$f_d = -\mathrm{i}\,\mathrm{sgn}(\omega) g K_s \xi_s \tag{4.26}$$

The constant g denotes the hysteretic damping factor. With this frequency-domain representation, the imaginary stiffness finally just adds an imaginary part to the matrix $\mathbf{K}_s$. Only for a purely harmonic motion with a single pair of fixed imaginary frequencies, the frequency-domain description in Eq. (4.26) can be transferred into the time domain. The formula is neither a Laplace transform, nor a Fourier transform of a causal time-domain representation, nor the result of employing an exponential approach. Hence, the imaginary stiffness cannot be used as a damping transfer function in a mathematically consistent structure model. Several more complicated, but consistent transfer models have been developed in the past that account for a nearly frequency-independent damping (e. g. Muravskii 2007). Nevertheless, if the structure within streaming air becomes unstable, the imaginary stiffness can be used in a mathematically correct way to determine later explained characteristic values, and it simplifies the equations occurring there.

The imaginary stiffness can be introduced with different hysteretic damping factors g into several kinds of stiffness matrices. In connection with the element stiffness $\mathbf{K}^e$, different damping values can be assigned to different elements. Alternatively, the entries in the global stiffness matrix $\mathbf{K}_s$, for instance separated in bending and torsional stiffness, can be extended with an imaginary part. It is also possible to connect the modal stiffness $\mathbf{K}_s^m$ of several modes with an imaginary stiffness, as it is described for the modal viscous damping.

With reference to the original input file, which is mentioned at the end of the preceding section, a hysteretic damping factor $g = 0.006$ is used for the extension of the elastic element stiffness of all girder and pylon elements instead of viscous damping when further numerical results given in Starossek (1992) are referred to for a check.

4.3 Approximation of the Global Admittance Function of Motion-Induced Aerodynamic Forces

In the same way as mentioned for the mass and the stiffness matrix, the global admittance function $\mathbf{Q}$ of motion-induced aerodynamic forces can be assembled from the element matrices

$\mathbf{Q}^{\mathrm{e}}$ in the sense of the direct stiffness method. According to Eq. (2.1a) and Eq. (2.8a), the transfer equation of the global motion-induced aerodynamic forces takes the following form.

$$\mathbf{f}_{\mathrm{ae}}(s) = q_0 \mathbf{Q}(p) \xi_{\mathrm{s}}(s) \tag{4.27}$$

Since the motion-induced aerodynamic forces are not applied to all structural members, the structural degrees of freedom ξ_{s} can be reduced to aerodynamically effective ones $\xi_{\mathrm{s}}^{\mathrm{a}}$ with a truncated permutation matrix $\mathbf{T}_{\mathrm{ae}}$.

$$\xi_{\mathrm{s}} = \mathbf{T}_{\mathrm{ae}} \xi_{\mathrm{s}}^{\mathrm{a}} \tag{4.28}$$

With respect to Eq. (1.16) and Eq. (1.17), $\mathbf{T}_{\mathrm{ae}}^{\mathrm{T}} \mathbf{Q} \mathbf{T}_{\mathrm{ae}}$ is the reduced admittance matrix. To recover the full admittance matrix, the truncated version of the inverse of the full permutation matrix is necessary. Due to the orthogonality of a permutation matrix, its inverse equals its transpose. This also holds for the truncated matrices.

An approximation of the global aerodynamic admittance matrix $\mathbf{Q}(p)$ with rational functions can be carried out in several ways. For the approximation with the Roger approach, the two-dimensional approximations of Chapter 3 can be used to a limited extent. If the nominal half-width b of the bridge deck, the reference wind velocity U, and the cross-section shape do not vary along the girder, an approximation of the global aerodynamic admittances with the same number and values of poles is possible. For this special case, the global coefficient matrices $\mathbf{A}_j$ in Eq. (3.14) can be obtained from the local ones in the sense of the direct stiffness method. The number of aerodynamic states in ξ_{a} of Eq. (3.18) can be reduced if the bridge is investigated in modal space with a reduced number of modes. For this purpose, the global coefficient matrices $\mathbf{A}_j$ are transferred with the truncated modal matrix

$$\mathbf{A}_j^{\mathrm{m}} = \mathbf{\Phi}_{\mathrm{s}}^{\mathrm{T}} \mathbf{A}_j \mathbf{\Phi}_{\mathrm{s}} \tag{4.29}$$

before the state-space model is assembled according to Eq. (3.19) or Eq. (3.20).

The global aerodynamic admittance matrix in Eq. (4.27) can also be directly approximated with the Roger approach. This way can be applied without the restrictions mentioned above. Usually, the size of the global matrices in the physical space is too large for an approximation within an acceptable computing time, even if the degrees of freedom are limited to the aerodynamically effective ones. If the problem is described in the modal space and only selected modal degrees of freedom are used, the size of the aerodynamic admittance matrix

$$\mathbf{Q}^{\mathrm{m}} = \mathbf{\Phi}_{\mathrm{s}}^{\mathrm{T}} \mathbf{Q} \mathbf{\Phi}_{\mathrm{s}} \tag{4.30}$$

can be significantly reduced. In contrast to the modal mass and the modal stiffness matrix, the modal aerodynamic admittance matrix $\mathbf{Q}^{\mathrm{m}}$ is not diagonal. To allow further investigations of the structure with a different selection of mode shapes, the approximation results $\mathbf{A}_j^{\mathrm{m}}$ must be pumped up to the physical space, though they do not contain the information of all modes. For the Roger approach, two cases have to be distinguished to minimise the length of the aerodynamic state vector $\boldsymbol{\xi}_{\mathrm{a}}$. If the number of modes for further investigations is lower than the number of modes employed for the approximation, the coefficient matrices should be transferred according to

$$\mathbf{A}_j = (\boldsymbol{\Phi}_{\mathrm{s}}^{-1})^{\mathrm{T}} \mathbf{A}_j^{\mathrm{m}} \boldsymbol{\Phi}_{\mathrm{s}}^{-1} \tag{4.31}$$

and, afterwards, treated as explained in connection with Eq. (4.29). In the other case, the coefficient matrices $\mathbf{A}_j^{\mathrm{m}}$ are inserted into the state-space model according to Eq. (3.19) or Eq. (3.20) before the transformation from the modal to the physical space is carried out as follows.

$$\begin{aligned}
\mathbf{A}_0 &= (\boldsymbol{\Phi}_{\mathrm{s}}^{-1})^{\mathrm{T}} \mathbf{A}_0^{\mathrm{m}} \boldsymbol{\Phi}_{\mathrm{s}}^{-1} \,, \quad & \mathbf{D} &= (\boldsymbol{\Phi}_{\mathrm{s}}^{-1})^{\mathrm{T}} \mathbf{D}^{\mathrm{m}} \\
\mathbf{A}_1 &= (\boldsymbol{\Phi}_{\mathrm{s}}^{-1})^{\mathrm{T}} \mathbf{A}_1^{\mathrm{m}} \boldsymbol{\Phi}_{\mathrm{s}}^{-1} \,, \quad & \mathbf{E} &= \mathbf{E}^{\mathrm{m}} \boldsymbol{\Phi}_{\mathrm{s}}^{-1} \\
\mathbf{A}_2 &= (\boldsymbol{\Phi}_{\mathrm{s}}^{-1})^{\mathrm{T}} \mathbf{A}_2^{\mathrm{m}} \boldsymbol{\Phi}_{\mathrm{s}}^{-1} \,, \quad & \mathbf{R} &= \mathbf{R}^{\mathrm{m}}
\end{aligned} \tag{4.32}$$

Then, these entries are transferred to the modal space with another selection of modes.

$$\begin{aligned}
\mathbf{A}_0^{\mathrm{m}} &= \boldsymbol{\Phi}_{\mathrm{s}}^{\mathrm{T}} \mathbf{A}_0 \boldsymbol{\Phi}_{\mathrm{s}} \,, \quad & \mathbf{D}^{\mathrm{m}} &= (\boldsymbol{\Phi}_{\mathrm{s}})^{\mathrm{T}} \mathbf{D} \\
\mathbf{A}_1^{\mathrm{m}} &= \boldsymbol{\Phi}_{\mathrm{s}}^{\mathrm{T}} \mathbf{A}_1 \boldsymbol{\Phi}_{\mathrm{s}} \,, \quad & \mathbf{E}^{\mathrm{m}} &= \mathbf{E} \boldsymbol{\Phi}_{\mathrm{s}} \\
\mathbf{A}_2^{\mathrm{m}} &= \boldsymbol{\Phi}_{\mathrm{s}}^{\mathrm{T}} \mathbf{A}_2 \boldsymbol{\Phi}_{\mathrm{s}} \,, \quad & \mathbf{R}^{\mathrm{m}} &= \mathbf{R}
\end{aligned} \tag{4.33}$$

For the Karpel approach, the two-dimensional results presented in Chapter 3 cannot be transferred to the global structure. Only a direct approximation of the global aerodynamic admittance matrix $\mathbf{Q}$ or its reduced version in Eq. (4.30) is possible. As shown in Eq. (4.32) and Eq. (4.33), the approximation results can be pumped up to the physical space and again transformed with a truncated modal matrix. The length of the aerodynamic state vector is not affected by the modal transformations.

Some features of the rational function approximation of three-dimensional structures are demonstrated in the following for the numerically investigated cable-stayed bridge. Motion-induced aerodynamic forces are only applied to the bridge girder. The girder has a constant half-width of $b = 9.0$ m. Wind is blowing with a reference wind velocity U that is also constant along the girder length. Detailed investigations are carried out with the flat-plate derivatives.

A reduced modal aerodynamic admittance matrix according to Eq. (4.30) is used. In the truncated modal matrix $\mathbf{\Phi}_\mathrm{s}$, the eigenvectors of the 14 lowest torsional modes are taken into account. The two upper torsional modes have identical eigenfrequencies $\omega_\mathrm{s} = 27.620\ 1/\mathrm{s}$. Both different modes are non-zero within the side spans of the girder where they have two nodal points. For the investigations of the following sections, such a set of 14 torsional modes is expected to sufficiently describe the motion-induced aerodynamic forces for the occurring torsional shapes of the structure. Consequently, the eigenvectors of the lowest bending modes up to the 14^{th} mode with $\omega_\mathrm{s} = 21.489\ 1/\mathrm{s}$ are also included in the truncated modal matrix. Despite the derivative normalisation according to Eq. (3.25), numerical problems can occur due to the small size of the aerodynamic derivatives if the eigenvectors are normalised as mentioned in Section 4.2. For the derivative approximation, the modal matrix is, thus, additionally multiplied with a scalar factor so that $\max\limits_{j,l}(|Q^\mathrm{m}_{jl}(p \to 0)|) = 1$.

The original data and the settings of the fitting procedure almost comply with those used for approximating the two-dimensional flat-plate derivatives. However, the number of the frequencies which original derivatives are calculated for is reduced to $n_k = 40$ to accelerate the calculations. The modal $\mathbf{A}^\mathrm{m}_0$ matrix is constrained to the steady value of the reduced modal aerodynamic admittance matrix $\mathbf{Q}^{\mathrm{o,m}}(p \to 0)$. Hence, the pumped-up version $\mathbf{A}_0$ according to Eq. (4.32) does not exactly equal $\mathbf{Q}^\mathrm{o}(p \to 0)$.

Table 4.4 shows the approximation results. Again, the lag-state coefficients of the Karpel approach are transferred with Eq. (3.23) to the Roger form according to Eq. (3.20). For the results in the first block of Table 4.4, all non-zero derivatives are normalised to have the maximum value of one with the weights in Eq. (3.25). As done for the approximation of the two-dimensional derivatives, $Q_\mathrm{min} = 0$ is thus chosen. Alternatively, for the results in the second block, small derivatives are excluded from the full data normalisation to improve the fit of larger derivatives. The limit $Q_\mathrm{min} = 1$ is chosen with respect to the size of the entries in the modal derivative matrix.

In contrast to the two-dimensional derivatives, an approximation of the global derivatives with the Karpel approach leads to significantly different results. Even for the special description of the three-dimensional flow with theoretical flat-plate derivatives, the Roger approach cannot be converted in the Karpel form. This holds for the description in the physical space and for that in the selected reduced modal space. At first, the results in the second block of Table 4.4 are discussed. If $n_\gamma = 5$ poles are employed, the approximation error J is two orders of magnitude higher than for the addressed approximation with the Roger approach. There are simply not enough free coefficients available in the matrices $\mathbf{D}$ and $\mathbf{E}$ for an acceptable approximation. Another interesting phenomenon is caused by the strong coupling of these coefficients, and it occurs at least for the chosen numerical example with its decoupled bending and torsional eigenmodes. The range of poles contracts to a very small interval. Since these poles are connected to small coefficients, they cannot be considered as multiple in the sense of $\nu_\mu > 1$ but rather

Table 4.4: Rfa of the reduced modal aerodynamic derivative matrix $\mathbf{Q}^{\mathrm{m}}$ of the cable-stayed bridge with fully ($Q_{\min} = 0$) and not fully ($Q_{\min} = 1$) normalised data.

		n_γ	$J/n_k \cdot 10^4$	$\overline{\lvert(\mathbf{A}_0 \;\; \mathbf{A}_1 \;\; \mathbf{A}_2)_{jl}\rvert}$	$\overline{\lvert(\mathbf{E})_{jl}\rvert}$	$\gamma_{\max} - \gamma_{\min}$
$Q_{\min} = 0$	Roger	1	102.40	6.4295	4.4673	0
		5	3.0734	6.4271	6.1603	0.82617
	Karpel	5	419.83	6.4362	0.43294	0.0095821
		10	277.62	6.4333	0.77318	0.016577
		15	237.35	6.4368	64.790	1.2930
		16	106.40	6.4305	3.2201	0.15671
		17	208.11	6.4341	207.44	1.2454
$Q_{\min} = 1$	Roger	1	65.745	6.4294	4.4344	0
		5	2.1549	6.4272	7.9329	0.74125
	Karpel	5	328.35	6.4331	0.57291	0.0037898
		10	187.98	6.4308	0.81608	0.0033468
		15	65.686	6.4294	7.7948	0.0058482
		16	64.551	6.4293	133.38	0.020801
		17	63.032	6.4294	41.983	0.15120

related to a single lag term that is divided into five summands. For an increasing number of poles, the contraction phenomenon also occurs. The approximation error does not really decrease for $n_\gamma = 15$ poles or more. More than $n_\gamma = 17$ poles cannot be employed because numerical problems occur in the least-squares steps of the fitting process. The question whether the contraction problem vanishes if more lag-terms are used can thus not be answered. If $n_\gamma = 17$ poles are employed, the convergence limit $\Delta J_{\max}$ is not low enough to enforce a slightly better approximation with more contracted poles. As foreseeable, the lowest approximation error that is achievable with the Karpel approach and contracted poles is comparable to the one that results if the fitting is carried out with the Roger approach and $n_\gamma = 1$ pole. The approximation quality of the Karpel approach is therefore very limited here. As explained for the two-dimensional case, the absolute values of the lag-term coefficients increase with a higher number of employed poles if the convergence limit does not stop the fitting process too early. Again, the coefficients $(\mathbf{A}_0 \;\; \mathbf{A}_1 \;\; \mathbf{A}_2)$ of the polynomial part are independent of the number of lag terms for the flat-plate derivatives.

The results in the first block of Table 4.4 show almost the same behaviour as explained for the second block. Due to the other normalisation, the approximation error is higher. Since the convergence limit is not low enough for $n_\gamma = 15$ and more poles, the fitting process ends before all poles contract to almost one value. Some numerical tests have also shown that the poles also contract if the two-dimensional derivatives of cross sections in real flow of Section 2.3 are used as a basis for the global aerodynamic admittance matrix.

4.4 Discretisation with Global Shape Functions

In Section 4.1, the continuous displacements of the single finite element are discretised with an appropriate set of shape functions. In a similar way, a spatial discretisation of the investigated bridge can also be found if the continuous displacements $h(x,t)$ and $\alpha(x,t)$ of the whole structure are described with a series of suitable global shape functions $\Omega_{h,j}(x)$ and $\Omega_{\alpha,j}(x)$ that are weighted with time-dependent generalised degrees of freedom $h_j(t)$ and $\alpha_j(t)$. Especially the eigenfunctions $\breve{\Omega}_{h,j}$ and $\breve{\Omega}_{\alpha,j}$ of the undamped structural system are particularly suited for this purpose. Within all parts of the linearised structure that have sufficient mass properties, all continuous displacements that meet the displacement boundary conditions can be made up with the following infinite series. Dimensionless shape functions are used.

$$h(x,t) = \sum_{j=1}^{\infty} \breve{\Omega}_{h,j}(x) h_j(t) \tag{4.34a}$$

$$\alpha(x,t) = \sum_{j=1}^{\infty} \breve{\Omega}_{\alpha,j}(x) \alpha_j(t) \tag{4.34b}$$

The main problem of this approach is, of course, the determination of the mode shapes, which are assumed to be known in the following. For the chosen numerical example, as explained in Section 4.2, there are either bending or torsional modes. Eigenfunctions have an additional advantage because they fulfil orthogonality conditions with respect to mass and stiffness properties.

With the principle of virtual displacements, the partial differential equations for the continuous displacements can be transformed into two sets of an infinite number of ordinary differential equations for the modal degrees of freedom $h_j(t)$ and $\alpha_l(t)$.

$$\ddot{h}_j(t) \int_{\mathrm{g}} m(x) \breve{\Omega}_{h,j}^2(x)\,\mathrm{d}x + h_j(t)\ \ \omega_{\mathrm{s},j}^2 \int_{\mathrm{g}} m(x) \breve{\Omega}_{h,j}^2(x)\,\mathrm{d}x = \int_{\mathrm{g}} \breve{\Omega}_{h,j}(x) L(x,t)\,\mathrm{d}x \tag{4.35a}$$

$$\ddot{\alpha}_l(t) \int_{\mathrm{g}} I(x) \breve{\Omega}_{\alpha,l}^2(x)\,\mathrm{d}x + \alpha_l(t)\ \ \omega_{\mathrm{s},l}^2 \int_{\mathrm{g}} I(x) \breve{\Omega}_{\alpha,l}^2(x)\,\mathrm{d}x = \int_{\mathrm{g}} \breve{\Omega}_{\alpha,l}(x) M(x,t)\,\mathrm{d}x \tag{4.35b}$$

The underlying virtual displacements are assumed in terms of virtual versions of the displacements in Eq. (4.34). Damping is omitted in the formulas for the sake of brevity. Modal damping can be assigned to each mode, as shown in Section 4.2. In principal, the integrals in Eq. (4.35) have to be evaluated for the whole structure. For this model it is, however, additionally assumed that the mass is only accounted for those structural members which aerodynamic forces are applied to. Hence, the integrals must be determined only for the bridge girder, which is indicated with the index g. Arbitrary forces acting on the girder can be considered as shown for the aerodynamic lift L and the aerodynamic moment M.

If the mass parameters m and I are, moreover, assumed to be constant, the orthogonality conditions also apply directly to the mode shapes of either bending or torsion. When dividing additionally both equations by appropriate factors, they take the following form.

$$\ddot{h}_j(t)m + h_j(t)\omega_{\mathrm{s},j}^2 m = L_j^{\mathrm{m}}(t)\,, \quad L_j^{\mathrm{m}}(t) = \int_{\mathrm{g}} \breve{\Omega}_{h,j}(x)L(x,t)\,\mathrm{d}x \;/ \int_{\mathrm{g}} \breve{\Omega}_{h,j}^2(x)\,\mathrm{d}x \tag{4.36a}$$

$$\ddot{\alpha}_l(t)I + \alpha_l(t)\omega_{\mathrm{s},l}^2 I = M_l^{\mathrm{m}}(t)\,, \quad M_l^{\mathrm{m}}(t) = \int_{\mathrm{g}} \breve{\Omega}_{\alpha,l}(x)M(x,t)\,\mathrm{d}x \;/ \int_{\mathrm{g}} \breve{\Omega}_{\alpha,l}^2(x)\,\mathrm{d}x \tag{4.36b}$$

As known from Section 4.1, motion-induced aerodynamic forces lead to a coupling of all bending and torsional modes. Assuming that the parameters q_0, b, and $\mathbf{Q}$ do not vary along the girder either, the modal version of these forces is as follows.

$$L_j^{\mathrm{m}}(t)\,b = q_0\,Q_{hh}(t) \overset{t}{*} \frac{h_j(t)}{b} + q_0\,Q_{h\alpha}(t) \overset{t}{*} \frac{\sum_{\kappa=1}^{\infty} \alpha_\kappa(t) \int_{\mathrm{g}} \breve{\Omega}_{h,j}(x)\breve{\Omega}_{\alpha,\kappa}(x)\,\mathrm{d}x}{\int_{\mathrm{g}} \breve{\Omega}_{h,j}^2(x)\,\mathrm{d}x} \tag{4.37a}$$

$$M_l^{\mathrm{m}}(t) = q_0\,Q_{\alpha h}(t) \overset{t}{*} \frac{\sum_{\kappa=1}^{\infty} \frac{h_\kappa(t)}{b} \int_{\mathrm{g}} \breve{\Omega}_{h,\kappa}(x)\breve{\Omega}_{\alpha,l}(x)\,\mathrm{d}x}{\int_{\mathrm{g}} \breve{\Omega}_{\alpha,l}^2(x)\,\mathrm{d}x} + q_0\,Q_{\alpha\alpha}(t) \overset{t}{*} \alpha_l(t) \tag{4.37b}$$

Since the $\overset{t}{*}$ convolution is adopted, the aerodynamic impulse responses have to be determined as inverse $\mathscr{L}_s$ transforms.

Two important special cases can be derived from Eq. (4.37) for the motion-induced aerodynamic forces. If there are only pairs of identical bending and torsional mode shapes, most of the couplings vanish and the following coupled pair of equations remains for the mode $\breve{\Omega}_j(x)$.

$$L_j^{\mathrm{m}}(t)\,b = q_0\,Q_{hh}(t) \overset{t}{*} \frac{h_j(t)}{b} + q_0\,Q_{h\alpha}(t) \overset{t}{*} \alpha_j(t) \tag{4.38a}$$

$$M_j^{\mathrm{m}}(t) = q_0\,Q_{\alpha h}(t) \overset{t}{*} \frac{h_j(t)}{b} + q_0\,Q_{\alpha\alpha}(t) \overset{t}{*} \alpha_j(t) \tag{4.38b}$$

Hence, all these pairs j can be investigated separately. In combination with the left part of Eq. (4.36), the interaction of the structure and the motion-induced aerodynamic forces can moreover be investigated with the physical quantities per unit length. The modal degrees of freedom $h_j(t)$ and $\alpha_j(t)$ represent the modal portions of the physical displacements $h(x,t)$ and $\alpha(x,t)$, respectively, where $\breve{\Omega}_j(x) = 1$. The conclusions of this paragraph are also derived in Starossek (1992) using the differential equation directly. Applying the weak form of the equation of motion, as done here, allows, however, the derivation of approximations especially when further kinds of loads are taken into account.

For the second case, only a limited number of the lower modes are used for a finite series version of Eq. (4.34). This classical approach can be found for instance in Scanlan (1978a) and Scanlan (1978b). Since the finite-element solution of the foregoing sections sufficiently covers this approach, it is not of interest here. However, considering only one bending mode j and one torsional mode l in a bimodal approach often leads to acceptable solutions, even if their shapes are not identical. For this case, Eq. (4.37) takes the following form.

$$L_j^{\mathrm{m}}(t)\,b = q_0\,Q_{hh}(t) \overset{t}{*} \frac{h_j(t)}{b} + q_0\,Q_{h\alpha}(t)\frac{\int_{\mathrm{g}} \breve{\Omega}_{h,j}(x)\breve{\Omega}_{\alpha,l}(x)\,\mathrm{d}x}{\int_{\mathrm{g}} \breve{\Omega}_{h,j}^2(x)\,\mathrm{d}x} \overset{t}{*} \alpha_l(t) \tag{4.39a}$$

$$M_l^{\mathrm{m}}(t) = q_0\,Q_{\alpha h}(t)\frac{\int_{\mathrm{g}} \breve{\Omega}_{h,j}(x)\breve{\Omega}_{\alpha,l}(x)\,\mathrm{d}x}{\int_{\mathrm{g}} \breve{\Omega}_{\alpha,l}^2(x)\,\mathrm{d}x} \overset{t}{*} \frac{h_j(t)}{b} + q_0\,Q_{\alpha\alpha}(t) \overset{t}{*} \alpha_l(t) \tag{4.39b}$$

Compared to the first case, the coupling derivatives are additionally weighted with mode-shape dependent factors. Bimodal approaches of this form can also be found, for instance, in Dyrbye & Hansen (1996). The lower the affinity of the shapes, the lower the magnitude of the coupling terms in the motion-induced aerodynamic forces. Provided that the couplings between these modes and the other ones are distinctly lower in the full approach of Eq. (4.37), this bimodal approach leads to a sufficient solution quality.

Gust-induced aerodynamic forces originate from the speed fluctuations in the natural wind field. The wind velocity components at one single point in space are usually separated into a constant mean and a fluctuating zero-mean part. With sufficient accuracy, the time-varying part can be modelled as an ergodic stochastic process. The following derivations show how modal gust-induced aerodynamic forces that act on the girder can be described with their statistical parameters. Assumptions that are used here for the statistical description of the wind field are taken from Simiu & Scanlan (1996).

First, the following spectral density matrix must be defined according to Eq. (1.13).

$$\begin{aligned}\mathbf{S}_{\mathbf{d}_{\mathrm{ae}}^{\mathrm{g}}} &= \begin{pmatrix} S_{LL}(x_1,x_2,\omega) & S_{LM}(x_1,x_2,\omega) \\ S_{ML}(x_1,x_2,\omega) & S_{MM}(x_1,x_2,\omega) \end{pmatrix} \\ &= \lim_{T\to\infty}\left(\frac{1}{T}\begin{pmatrix} L^T(x_1,\mathrm{i}\omega)\,b \\ M^T(x_1,\mathrm{i}\omega) \end{pmatrix}^{\mathrm{c}}\begin{pmatrix} L^T(x_2,\mathrm{i}\omega)\,b \\ M^T(x_2,\mathrm{i}\omega) \end{pmatrix}^{\mathrm{T}}\right)\end{aligned} \tag{4.40}$$

It represents the statistical relations between the gust-force components at the two points x_1 and x_2 on the girder. The aerodynamic strip theory allows for connecting the spectral density matrix

of the forces with that of the fluctuating gust velocities $\mathbf{S}_{\boldsymbol{\alpha}^{\mathrm{g}}}$ by the aerodynamic transfer function of gust-induced aerodynamic forces along the imaginary frequency axis.

$$\begin{aligned}\mathbf{S}_{\mathbf{d}^{\mathrm{g}}_{\mathrm{ae}}} &= \begin{pmatrix} G^{\mathrm{g}}_{\mathrm{ae},Lw}(x_1,\mathrm{i}\omega) \\ G^{\mathrm{g}}_{\mathrm{ae},Mw}(x_1,\mathrm{i}\omega) \end{pmatrix}^{\mathrm{c}} \cdot \\ &\qquad \cdot \lim_{T\to\infty}\left(\frac{1}{T}\left(\frac{w^{\mathrm{g},T}(x_1,\mathrm{i}\omega)}{U}\right)^{\mathrm{c}}\left(\frac{w^{\mathrm{g},T}(x_2,\mathrm{i}\omega)}{U}\right)^{\mathrm{T}}\right)\begin{pmatrix} G^{\mathrm{g}}_{\mathrm{ae},Lw}(x_2,\mathrm{i}\omega) \\ G^{\mathrm{g}}_{\mathrm{ae},Mw}(x_2,\mathrm{i}\omega) \end{pmatrix}^{\mathrm{T}} \\ &= \left(\mathbf{G}^{\mathrm{g}}_{\mathrm{ae}}(x_1,\mathrm{i}\omega)\right)^{\mathrm{c}}\ \left(S_{w^{\mathrm{g}}}(x_1,x_2,\omega)\right)\ \left(\mathbf{G}^{\mathrm{g}}_{\mathrm{ae}}(x_2,\mathrm{i}\omega)\right)^{\mathrm{T}} \\ &= \left(\mathbf{G}^{\mathrm{g}}_{\mathrm{ae}}(x_1,\mathrm{i}\omega)\right)^{\mathrm{c}}\ \mathbf{S}_{\boldsymbol{\alpha}^{\mathrm{g}}}\ \left(\mathbf{G}^{\mathrm{g}}_{\mathrm{ae}}(x_2,\mathrm{i}\omega)\right)^{\mathrm{T}}\end{aligned} \tag{4.41}$$

For stable rational transfer functions, the variables in Eq. (2.1) can also be seen as Fourier transforms because the imaginary axis is included in the region of absolute convergence of the Laplace transforms. Since the Fourier transform takes inputs for negative times into account, the stochastic inputs, and consequently the outputs, can be non-zero prior to $t = 0$ in contrast to the restrictions made in Section 2.1. It has to be recalled that a transfer function can only provide the forced system response. Nevertheless, the use of the transfer function is sufficient in connection with Eq. (4.41) because the equation represents the transfer of the statistical properties of the input to those of the output.

With the help of the defined spectral matrices, the statistical properties of the modal lift L^{m}_j and the modal moment M^{m}_l of gust-induced aerodynamic forces according to Eq. (4.36) can be derived. By way of example, the derivation of the cross-spectral density function of the aerodynamic lifts of different modes j and l

$$S_{L^{\mathrm{m}}_j L^{\mathrm{m}}_l}(\omega) = \lim_{T\to\infty}\left(\frac{1}{T}\ (L^{\mathrm{m},T}_j(\mathrm{i}\omega)\,b)^{\mathrm{c}}\ \ L^{\mathrm{m},T}_l(\mathrm{i}\omega)\,b\right) \tag{4.42}$$

is demonstrated. With the definition of the modal aerodynamic lift and after regrouping the variables, the spectral density function takes the following form.

$$S_{L^{\mathrm{m}}_j L^{\mathrm{m}}_l}(\omega) = \frac{\displaystyle\int_{\mathrm{g}}\int_{\mathrm{g}} \breve{\Omega}_{h,j}(x_1)\breve{\Omega}_{h,l}(x_2)\ \overbrace{\lim_{T\to\infty}\left(\frac{1}{T}\ (L^{T}(x_1,\mathrm{i}\omega)\,b)^{\mathrm{c}}\ \ L^{T}(x_2,\mathrm{i}\omega)\,b\right)}^{=S_{LL}(x_1,x_2,\omega)}\ \mathrm{d}x_1\,\mathrm{d}x_2}{\displaystyle\int_{\mathrm{g}}\breve{\Omega}^2_{h,j}(x)\,\mathrm{d}x\ \int_{\mathrm{g}}\breve{\Omega}^2_{h,l}(x)\,\mathrm{d}x} \tag{4.43}$$

Using the spectral transfer information of Eq. (4.41), the cross-spectral density function of the modal aerodynamic lifts can be connected to the spectral density function of the fluctuating gust

velocities. When the admittance function of gust-induced forces is assumed to not vary with the girder coordinate x, the following equation is obtained.

$$S_{L_j^{\mathrm{m}} L_l^{\mathrm{m}}}(\omega) = (G^{\mathrm{g}}_{\mathrm{ae},Lw}(\mathrm{i}\omega))^{\mathrm{c}} G^{\mathrm{g}}_{\mathrm{ae},Lw}(\mathrm{i}\omega) \cdot \frac{\int_{\mathrm{g}}\int_{\mathrm{g}} \breve{\Omega}_{h,j}(x_1)\breve{\Omega}_{h,l}(x_2)\, S_{w^{\mathrm{g}}}(x_1,x_2,\omega)\, \mathrm{d}x_1\, \mathrm{d}x_2}{\int_{\mathrm{g}} \breve{\Omega}^2_{h,j}(x)\,\mathrm{d}x \int_{\mathrm{g}} \breve{\Omega}^2_{h,l}(x)\,\mathrm{d}x} \tag{4.44}$$

The phase of the complex cross-spectral density function $S_{w^{\mathrm{g}}}(x_1,x_2,\omega)$ is usually taken as zero, and the absolute value is expressed using the coherence function.

$$\mathrm{coh}_w(x_1,x_2,\omega) = \frac{|S_{w^{\mathrm{g}}}(x_1,x_2,\omega)|}{\sqrt{S_{w^{\mathrm{g}}}(x_1,\omega) S_{w^{\mathrm{g}}}(x_2,\omega)}} \tag{4.45}$$

Assuming the auto-spectral density functions $S_{w^{\mathrm{g}}}(x,\omega)$ to be constant along the horizontal bridge girder, $S_{L_j^{\mathrm{m}} L_l^{\mathrm{m}}}$ can be expressed as

$$S_{L_j^{\mathrm{m}} L_l^{\mathrm{m}}}(\omega) = (G^{\mathrm{g}}_{\mathrm{ae},Lw}(\mathrm{i}\omega))^{\mathrm{c}} G^{\mathrm{g}}_{\mathrm{ae},Lw}(\mathrm{i}\omega)\, S_{w^{\mathrm{g}}}(\omega)\, J^2_{\mathrm{m}}(\omega) \quad , \tag{4.46}$$

where

$$J^2_{\mathrm{m}}(\omega) = \frac{\int_{\mathrm{g}}\int_{\mathrm{g}} \breve{\Omega}_{h,j}(x_1)\breve{\Omega}_{h,l}(x_2)\, \mathrm{coh}_w(x_1,x_2,\omega)\, \mathrm{d}x_1\, \mathrm{d}x_2}{\int_{\mathrm{g}} \breve{\Omega}^2_{h,j}(x)\,\mathrm{d}x \int_{\mathrm{g}} \breve{\Omega}^2_{h,l}(x)\,\mathrm{d}x} \quad . \tag{4.47}$$

The joint acceptance function J^2_{m} accounts for a reduction of the transfer at a single girder point due to both the modal shapes and the decreasing coherence of gust speeds at two girder points with an increasing distance. Joint acceptance functions were introduced for wind engineering applications by Davenport (e. g. Davenport 1962).

For aerodynamic gust admittances of arbitrary cross sections, the fluctuating along-wind component u^{g} has to be additionally accounted for in Eq. (4.41). The cross-spectral densities S_{uw} and S_{wu} are usually neglected. Accordingly, Eq. (4.46) has to be extended by a second summand that can be obtained from the shown expression by just replacing the index w with the index u. Derivatives of the gust velocities can also appear in the input of the aerodynamic transfer equation, as is the case for the used rational function approximation (cp. Eq. (3.18)). With the help of Eq. (1.14), it can be shown that, again, additional summands appear in Eq. (4.46) which are similar to the shown expression.

A very favourable procedure can be derived for the special case of a bimodal approach with identical bending and torsional mode shapes $\breve{\Omega}_j(x)$ and identical coherence functions of the gust

velocities. The last requirement is fulfilled if the input only contains the vertical gust velocity and its derivatives. This is the case for the flat-plate gust admittance used here. Under these assumptions, the joint acceptance function

$$J_{\mathrm{m}}^2(\omega) = \frac{\int_{\mathrm{g}}\int_{\mathrm{g}} \breve{\Omega}_j(x_1)\breve{\Omega}_j(x_2)\,\mathrm{coh}_w(x_1,x_2,\omega)\;\mathrm{d}x_1\,\mathrm{d}x_2}{\left(\int_{\mathrm{g}} \breve{\Omega}_j^2(x)\,\mathrm{d}x\right)^2} \tag{4.48}$$

is identical for all transfer paths. Moreover, the transfer of the statistical properties takes the form of the two-dimensional transfer at a single girder point where the spectral density matrix of the input is just modified with J_{m}^2.

Parallel to the finite-element approach, the investigated bridge is modelled with a bimodal approach. The first bending and the first torsional mode of the results of Section 4.2 are used for this purpose. Though the modes do not show affine shapes and the pylon is modelled with a mass, the formulas derived here for identical shapes are applied. The modes are scaled so that their maximum values in the mid span equal one. For the selected modes, the correction factors of Eq. (4.39), which are not taken into account for most of the investigations in this work, have the following numerical values.

$$\frac{\int_{\mathrm{g}} \breve{\Omega}_h(x)\breve{\Omega}_\alpha(x)\,\mathrm{d}x}{\int_{\mathrm{g}} \breve{\Omega}_h^2(x)\,\mathrm{d}x} = 1.1339\,, \qquad \frac{\int_{\mathrm{g}} \breve{\Omega}_h(x)\breve{\Omega}_\alpha(x)\,\mathrm{d}x}{\int_{\mathrm{g}} \breve{\Omega}_\alpha^2(x)\,\mathrm{d}x} = 0.82020 \tag{4.49}$$

To evaluate the joint acceptance function, the coherence of the vertical gust velocity is assumed in the customary exponential form.

$$\mathrm{coh}_w(x_1,x_2,\omega) = \mathrm{e}^{-|\phi_{\mathrm{coh}}|\frac{|x_1-x_2|}{l_{\mathrm{b}}}}\,, \quad \phi_{\mathrm{coh}} = \frac{\omega}{2\pi}\frac{C_{\mathrm{coh}}l_{\mathrm{b}}}{U} \tag{4.50}$$

The non-dimensional frequency ϕ_{coh} uses the decay parameter C_{coh} and the length of the bridge girder l_{b}. With the mentioned modes and the girder length $l_{\mathrm{b}} = 645$ m, the joint acceptance function J_{m}^2 in Eq. (4.48) can be determined as a function of this non-dimensional frequency. The numerical results are displayed in Figure 4.4 for the bending and the torsional mode shape. Since both curves do not significantly differ from each other, it is judged to be acceptable for the objectives of the work presented here to take the arithmetic mean of both curves for the further investigations.

The derived formulas of the selected, special bimodal approach can be interpreted as a result of the mathematical description of the two-dimensional system shown in Figure 4.5 with a flat-plate cross section. The structural properties are given in Table 4.5.

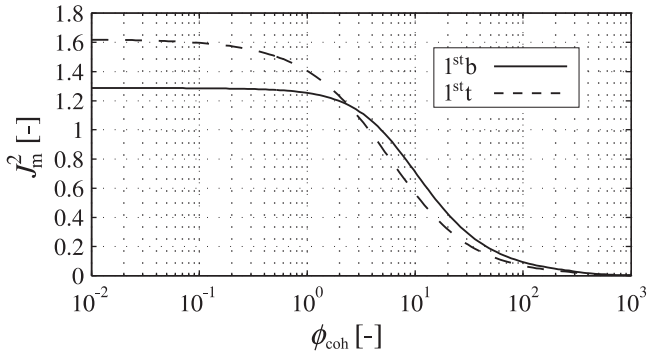

Figure 4.4: Joint acceptance functions for the first bending and the first torsional structural mode.

Table 4.5: Structural properties of the two-dimensional bridge model.

$m = 6.4\,\mathrm{t/m}$	$\omega_{s,h} = 2.4701\,1/\mathrm{s}$	$\delta_{s,h} = 0.015$
$I = 200\,\mathrm{tm^2/m}$	$\omega_{s,\alpha} = 3.0876\,1/\mathrm{s}$	$\delta_{s,\alpha} = 0.015$

Along with the finite-element model, which is referred to as the three-dimensional (3d) model, this two-dimensional (2d) model of the bridge is applied for the further investigations. Using the definitions of Eq. (2.19), the mass, the damping, and the stiffness matrix of the two-dimensional model take the following form.

$$\mathbf{M}_s = \begin{pmatrix} m\,b^2 & 0 \\ 0 & I \end{pmatrix}, \quad \mathbf{C}_s = \begin{pmatrix} 2\omega_{s,h} m \frac{\delta_{s,h}}{2\pi}\, b^2 & 0 \\ 0 & 2\omega_{s,\alpha} I \frac{\delta_{s,\alpha}}{2\pi} \end{pmatrix}$$
$$\mathbf{K}_s = \begin{pmatrix} \omega_{s,h}^2 m\, b^2 & 0 \\ 0 & \omega_{s,\alpha}^2 I \end{pmatrix} \tag{4.51}$$

Its displacements h and α are referred to as translation and rotation, respectively.

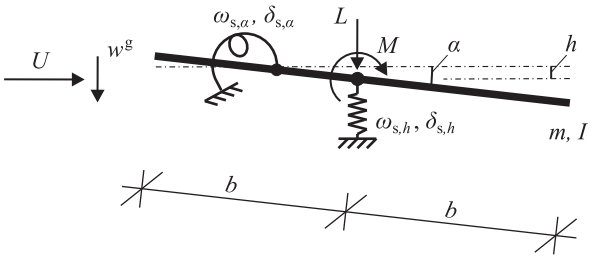

Figure 4.5: 2d system corresponding to the chosen bimodal approach.

4.5 State-Space Models of the Bridge

The displacements of the derived bridge models under the influence of arbitrary forces $\mathbf{f}(t)$ are described with the following equation of motion.

$$\mathbf{M}_\mathrm{s}\ddot{\boldsymbol{\xi}}_\mathrm{s}(t)+\mathbf{C}_\mathrm{s}\dot{\boldsymbol{\xi}}_\mathrm{s}(t)+\mathbf{K}_\mathrm{s}\boldsymbol{\xi}_\mathrm{s}(t)=\mathbf{f}(t) \tag{4.52}$$

So far, it has been assumed that Eq. (4.52) is a linearisation around the self-weight position of the bridge. Depending on the size of the acting forces $\mathbf{f}(t)$, non-linearities and occurring couplings have to be taken into account. Several further assumptions are made to facilitate the investigations. Besides wind loads, no other unavoidably impacting loads, like, for instance, those from road traffic or snow, which disturb the self-weight position of the bridge, are considered. The displacement of the girder under the static aerodynamic load $\mathbf{d}_\mathrm{ae}^\mathrm{s}$, due to the constant horizontal reference wind velocity U, is separated from $\boldsymbol{\xi}_\mathrm{s}$ and not addressed either. Hence, the position of the reference point S_a in thickness direction, which is mentioned in Section 2.3, is not relevant for the further investigations. The effect of an inclined zero position of the cross section on the aerodynamic forces is also excluded. Since the aerodynamic forces and, thus, the behaviour of the bridge within streaming air strongly depend on the way of linearisation, the simplifications made in Section 2.3 for real cross sections should be treated with caution. Moreover, the coupling of bending and torsion of the girder that arises due to a constant deflection is neglected, and the stiffness of the cables is not adjusted to the deflected position.

Under these assumptions, only the motion-induced aerodynamic forces $\mathbf{f}_\mathrm{ae}$ and the gust-induced aerodynamic forces $\mathbf{d}_\mathrm{ae}^\mathrm{g}$ occur on the right side of Eq. (4.52). The linearised equation of motion can be converted into the following state-space form

$$\dot{\mathbf{x}}_\mathrm{st}=\mathbf{A}_\mathrm{st}\mathbf{x}_\mathrm{st}+\mathbf{E}_\mathrm{st}\mathbf{f}_\mathrm{ae}+\mathbf{E}_\mathrm{st}\mathbf{d}_\mathrm{ae}^\mathrm{g} \tag{4.53a}$$

$$\mathbf{y}_\mathrm{st}=\mathbf{C}_\mathrm{st}\mathbf{x}_\mathrm{st} \quad , \tag{4.53b}$$

where

$$\mathbf{x}_\mathrm{st}=\begin{pmatrix}\dot{\boldsymbol{\xi}}_\mathrm{s}\\ \boldsymbol{\xi}_\mathrm{s}\end{pmatrix}, \quad \mathbf{A}_\mathrm{st}=\begin{pmatrix}-\mathbf{M}_\mathrm{s}^{-1}\mathbf{C}_\mathrm{s} & -\mathbf{M}_\mathrm{s}^{-1}\mathbf{K}_\mathrm{s}\\ \mathbf{I} & \mathbf{0}\end{pmatrix}, \quad \mathbf{E}_\mathrm{st}=\begin{pmatrix}\mathbf{M}_\mathrm{s}^{-1}\\ \mathbf{0}\end{pmatrix} \quad . \tag{4.54a}$$

The definition of the measured output $\mathbf{y}_\mathrm{st}$ and, consequently, the output matrix $\mathbf{C}_\mathrm{st}$ depends on the special purpose and is left open in this section. If accelerations are measured, the output in Eq. (4.53b) also depends on the inputs $\mathbf{f}_\mathrm{ae}$ and $\mathbf{d}_\mathrm{ae}^\mathrm{g}$. Additional linear feedthrough summands must then be introduced on the right side of the output equation. As explained in a later section, the measurement of certain elements of the structural state is sufficient for the studies presented here.

With the chosen linear approaches, both aerodynamic forces can be represented in the time domain using the convolution integrals of Section 2.1. The solution of the resulting integro-differential equation is mathematically cumbersome. However, if the transfer functions of the aerodynamic forces are described with rational functions, the state-space model of the structure and those of the aerodynamic forces can be favourably combined.

First, the motion-induced aerodynamic forces are considered in detail. The state-space model that is described with Eq. (3.18) and Eq. (3.10b) can be inserted into Eq. (4.53), and a new state-space model can be assembled

$$\dot{\mathbf{x}}_{\mathrm{as}} = \mathbf{A}_{\mathrm{as}}\mathbf{x}_{\mathrm{as}} + \mathbf{E}_{\mathrm{as}}\mathbf{d}_{\mathrm{ae}}^{\mathrm{g}} \tag{4.55a}$$

$$\mathbf{y}_{\mathrm{st}} = \mathbf{C}_{\mathrm{as}}\mathbf{x}_{\mathrm{as}} \quad , \tag{4.55b}$$

where

$$\mathbf{x}_{\mathrm{as}} = \begin{pmatrix} \mathbf{x}_{\mathrm{st}} \\ \boldsymbol{\xi}_{\mathrm{a}} \end{pmatrix} = \begin{pmatrix} \dot{\boldsymbol{\xi}}_{\mathrm{s}} \\ \boldsymbol{\xi}_{\mathrm{s}} \\ \boldsymbol{\xi}_{\mathrm{a}} \end{pmatrix} , \quad \mathbf{A}_{\mathrm{as}} = \begin{pmatrix} -\bar{\mathbf{M}}^{-1}\bar{\mathbf{C}} & -\bar{\mathbf{M}}^{-1}\bar{\mathbf{K}} & q_0\bar{\mathbf{M}}^{-1}\mathbf{D} \\ \mathbf{I} & \mathbf{0} & \mathbf{0} \\ \mathbf{E} & \mathbf{0} & (U/b)\mathbf{R} \end{pmatrix} \tag{4.56a}$$

$$\mathbf{E}_{\mathrm{as}} = \begin{pmatrix} \bar{\mathbf{M}}^{-1} \\ \mathbf{0} \\ \mathbf{0} \end{pmatrix} , \quad \mathbf{C}_{\mathrm{as}} = \begin{pmatrix} \mathbf{C}_{\mathrm{st}} & \mathbf{0} \end{pmatrix} \tag{4.56b}$$

and

$$\bar{\mathbf{M}} = \mathbf{M}_{\mathrm{s}} - \overbrace{q_0(b/U)^2}^{=\pi\rho b^4}\mathbf{A}_2 , \quad \bar{\mathbf{C}} = \mathbf{C}_{\mathrm{s}} - q_0(b/U)\mathbf{A}_1 , \quad \bar{\mathbf{K}} = \mathbf{K}_{\mathrm{s}} - q_0\mathbf{A}_0 \quad . \tag{4.57}$$

The state-space model in Eq. (4.55) describes the aeroelastic system, a term that is often used to stress the interaction between the structure and the air stream. Not only inertial, damping, and elastic forces depend on the displacements of the structure but also the motion-induced aerodynamic forces. The state vector $\mathbf{x}_{\mathrm{as}}$ of the aeroelastic system thus combines the structural state $\mathbf{x}_{\mathrm{st}}$ and the state $\boldsymbol{\xi}_{\mathrm{a}}$ of this aerodynamic force type. Consequently, the system matrix $\mathbf{A}_{\mathrm{as}}$ incorporates not only the structural parameters but also the parameters of the motion-induced aerodynamic forces. The aerodynamic system of the motion-induced forces is connected to the structural system in a feedback loop. For such an interconnection of systems, the structure of the system matrix $\mathbf{A}_{\mathrm{as}}$ is typical. The problem of the non-causal transfer of the motion-induced aerodynamic forces, which is mentioned in Section 2.2.2, does not exist in the state-space model of the aeroelastic system because the displacements are not a part of the system input. For a given bridge with a defined shape, the constant horizontal reference wind velocity U is the only varying parameter in the system matrix. Gust-induced aerodynamic forces act on the system

independently of the displacements. Hence, they appear in Eq. (4.55) as a disturbance. The output equation in Eq. (4.55b) cannot extract more than the entries of the structural state $\mathbf{x}_{\mathrm{st}}$ because the mathematically introduced lag states $\boldsymbol{\xi}_{\mathrm{a}}$ cannot be directly measured.

Sometimes it is argued that the modification of the structural mass with the $\mathbf{A}_2$ matrix is negligible and, thus, $\mathbf{A}_2$ can be omitted in Eq. (3.17) for the derivative approximation (Wilde & Fujino 1998). For the most cases, the first statement is correct. The second statement, however, leads to a poor approximation. For the flat plate, for instance, the $\mathbf{A}_2$ matrix is well-founded, as explained in Section 3.5.2, and if omitted, the other summands have to take over its role with all the occurring shortcomings described for the approximation of cross-section derivatives in real flow.

For the further investigations, it is also interesting to simplify Eq. (4.53a) for the case when the gust forces act as quasi-static forces.

$$\mathbf{0} = -\mathbf{K}_{\mathrm{s}}\boldsymbol{\xi}_{\mathrm{s}} + \mathbf{f}_{\mathrm{ae}} + \mathbf{d}_{\mathrm{ae}}^{\mathrm{g}} \tag{4.58}$$

The motion-induced aerodynamic forces can be introduced into this equation using the static version of Eq. (2.1a) and Eq. (2.8a) with $\mathbf{Q}(p=0)$. For the chosen rational function approximation given in Eq. (3.17), it is $\mathbf{Q}(p=0) = \mathbf{A}_0$, as already mentioned there, and thus

$$\mathbf{0} = -\bar{\mathbf{K}}\boldsymbol{\xi}_{\mathrm{s}} + \mathbf{d}_{\mathrm{ae}}^{\mathrm{g}} \quad . \tag{4.59}$$

A state-space representation of the system disturbance complies with Eq. (3.18) and Eq. (3.10b) adjusted to the gust-induced aerodynamic forces. Together with the state-space model of the aeroelastic system, the disturbance model can be combined to a single model

$$\dot{\mathbf{x}}_{\mathrm{asg}} = \mathbf{A}_{\mathrm{asg}}\mathbf{x}_{\mathrm{asg}} + \mathbf{E}_{\mathrm{asg}}\mathbf{a}^{\mathrm{g}} \tag{4.60a}$$

$$\mathbf{y}_{\mathrm{st}} = \mathbf{C}_{\mathrm{asg}}\mathbf{x}_{\mathrm{asg}} \quad , \tag{4.60b}$$

where

$$\mathbf{x}_{\mathrm{asg}} = \begin{pmatrix} \mathbf{x}_{\mathrm{as}} \\ \boldsymbol{\xi}_{\mathrm{a}} \end{pmatrix} , \quad \mathbf{A}_{\mathrm{asg}} = \begin{pmatrix} \mathbf{A}_{\mathrm{as}} & \mathbf{E}_{\mathrm{as}}\, q_0\mathbf{D} \\ \mathbf{0} & (U/b)\mathbf{R} \end{pmatrix} \tag{4.61a}$$

$$\mathbf{E}_{\mathrm{asg}} = \begin{pmatrix} \mathbf{0} & \mathbf{E}_{\mathrm{as}}\, q_0\mathbf{A}_0 \\ \mathbf{E} & \mathbf{0} \end{pmatrix} , \quad \mathbf{C}_{\mathrm{asg}} = \begin{pmatrix} \mathbf{C}_{\mathrm{as}} & \mathbf{0} \end{pmatrix} \tag{4.61b}$$

and

$$\mathbf{a}^{\mathrm{g}} = \begin{pmatrix} \dot{\boldsymbol{\alpha}}^{\mathrm{g}} \\ \boldsymbol{\alpha}^{\mathrm{g}} \end{pmatrix} \quad . \tag{4.62}$$

As already done in Section 3.2, the approximation matrices for the transfer function of gust-induced aerodynamic forces are denoted with the same variables that are used for the transfer of the motion-induced ones. The combination of both models has to be understood as a cascade connection. In contrast to the interaction between structural forces and motion-induced aerodynamic forces, there is no feedback of the structural behaviour on the disturbance. Additionally, the effect of the decreasing correlation of the wind velocities along the continuous structural elements must be taken into account, as mentioned in Section 4.1 and Section 4.4.

The vector $\boldsymbol{\alpha}^{\mathrm{g}}$ of the fluctuating wind velocity components as the input of the disturbance model can, moreover, be modelled with a linear time-invariant dynamic system. This system transfers a Gaussian white-noise input to the desired multicorrelated stochastic gust data. If the corresponding state-space model is combined with that of Eq. (4.60), the covariance matrix of the system response $\mathbf{y}_{\mathrm{st}}$ can be directly determined in a mathematically advantageous way by solving a bilinear matrix equation in the form of the Lyapunov equation (e. g. Arnold 1973, Schlitt 2005, Goßmann 1981, Chen & Kareem 2001a). Here, that model for the gust-velocities and this kind of determining the covariance matrix is not necessary and, thus, not dealt with further.

An alternative representation of the equation of motion can be derived based on the frequency-domain version of Eq. (4.53) when for the transfer function of the motion-induced aerodynamic forces, the notation of Eq. (2.10a) is employed.

$$s\,\mathbf{x}_{\mathrm{st}} = \tilde{\mathbf{A}}_{\mathrm{as}}(p)\,\mathbf{x}_{\mathrm{st}} + \tilde{\mathbf{E}}_{\mathrm{as}}(p)\,\mathbf{d}^{\mathrm{g}}_{\mathrm{ae}} \tag{4.63a}$$

$$\mathbf{y}_{\mathrm{st}} = \mathbf{C}_{\mathrm{st}}\,\mathbf{x}_{\mathrm{st}} \tag{4.63b}$$

For the derivation, the $\mathscr{L}_s$ transform is applied, keeping in mind that the transfer function approximation of the motion-induced aerodynamic forces enforces $\mathbf{x}_{\mathrm{st}}(t<0)=0$. The matrices in Eq. (4.63a) have the entries

$$\tilde{\mathbf{A}}_{\mathrm{as}}(p) = \begin{pmatrix} -(\bar{\bar{\mathbf{M}}}(p))^{-1}\mathbf{C}_{\mathrm{s}} & -(\bar{\bar{\mathbf{M}}}(p))^{-1}\mathbf{K}_{\mathrm{s}} \\ \mathbf{I} & \mathbf{0} \end{pmatrix}, \quad \tilde{\mathbf{E}}_{\mathrm{as}}(p) = \begin{pmatrix} (\bar{\bar{\mathbf{M}}}(p))^{-1} \\ \mathbf{0} \end{pmatrix} \quad , \tag{4.64}$$

where

$$\bar{\bar{\mathbf{M}}}(p) = \mathbf{M}_{\mathrm{s}} + \pi\rho b^4 \mathbf{C}_{\mathrm{ae}}(p) \quad . \tag{4.65}$$

Again, the model depends, for a given structure, only on the constant horizontal reference wind velocity U that is hidden in the reduced complex frequency p. Eq. (4.63) is not the frequency-domain version of the state-space model of a linear time-invariant system because the system matrix $\tilde{\mathbf{A}}_{\mathrm{as}}$ and the input matrix $\tilde{\mathbf{E}}_{\mathrm{as}}$ are functions of the reduced complex frequency p. Hence,

the chosen names for the matrices are misleading, and Eq. (4.63) cannot be converted into a time-domain version like Eq.(4.55) with the matrices $\tilde{\mathbf{A}}_{\mathrm{as}}$, $\mathbf{C}_{\mathrm{st}}$, and $\tilde{\mathbf{E}}_{\mathrm{as}}$. Anyway, a time-domain version is, of course, possible. For instance, when using the aeroelastic transfer function

$$\mathbf{G}_{\mathrm{as}}(s) = \mathbf{C}_{\mathrm{st}}(s\mathbf{I} - \tilde{\mathbf{A}}_{\mathrm{as}}(p))^{-1}\tilde{\mathbf{E}}_{\mathrm{as}}(p) \tag{4.66}$$

based on a consistent aerodynamic transfer functions $\mathbf{G}_{\mathrm{ae}}(s)$, the time-domain representation of the aeroelastic input-output transfer follows as a convolution of the corresponding impulse response $\mathbf{G}_{\mathrm{as}}(t)$ with the input $\mathbf{d}^{\mathrm{g}}_{\mathrm{ae}}(t)$.

$$\mathbf{y}_{\mathrm{st}}(t) = \mathbf{G}_{\mathrm{as}}(t) \overset{t}{*} \mathbf{d}^{\mathrm{g}}_{\mathrm{ae}}(t) \qquad \overset{t,s}{\circ\!\!-\!\!\bullet} \qquad \mathbf{y}_{\mathrm{st}}(s) = \mathbf{G}_{\mathrm{as}}(s)\, \mathbf{d}^{\mathrm{g}}_{\mathrm{ae}}(s) \tag{4.67}$$

When replacing Eq. (4.63a) with

$$s\,\mathbf{x}_{\mathrm{st}} = \tilde{\mathbf{A}}_{\mathrm{as}}(p)\,\mathbf{x}_{\mathrm{st}} + \tilde{\mathbf{E}}_{\mathrm{asg}}(s)\,\boldsymbol{\alpha}^{\mathrm{g}} \quad , \tag{4.68}$$

where

$$\tilde{\mathbf{E}}_{\mathrm{asg}}(s) = \begin{pmatrix} -(\bar{\bar{\mathbf{M}}}(p))^{-1}\pi\rho b^4 s^2 \mathbf{C}^{\mathrm{g}}_{\mathrm{ae}}(p) \\ \mathbf{0} \end{pmatrix} \quad , \tag{4.69}$$

the transfer from the fluctuating gust velocities to the gust-induced aerodynamic forces can be included in the model. Accordingly, the transfer function

$$\tilde{\mathbf{G}}_{\mathrm{asg}}(s) = \mathbf{C}_{\mathrm{st}}(s\mathbf{I} - \tilde{\mathbf{A}}_{\mathrm{as}}(p))^{-1}\tilde{\mathbf{E}}_{\mathrm{asg}}(s) \tag{4.70}$$

and the transfer equation

$$\mathbf{y}_{\mathrm{st}}(t) = \tilde{\mathbf{G}}_{\mathrm{asg}}(t) \overset{t}{*} \boldsymbol{\alpha}^{\mathrm{g}}(t) \qquad \overset{t,s}{\circ\!\!-\!\!\bullet} \qquad \mathbf{y}_{\mathrm{st}}(s) = \tilde{\mathbf{G}}_{\mathrm{asg}}(s)\, \boldsymbol{\alpha}^{\mathrm{g}}(s) \tag{4.71}$$

must be altered. In contrast to Eq. (4.60), the vector of the fluctuating gust velocities $\boldsymbol{\alpha}^{\mathrm{g}}$ and not $\mathbf{a}^{\mathrm{g}}$, which includes also the derivative of $\boldsymbol{\alpha}^{\mathrm{g}}$, represents the input vector in Eq. (4.71).

4.6 Stability Investigations

Stability is the basic characteristic that has to be studied for slender bridges in streaming air. In the work presented here, the term stability is used for the dynamic system in different ways. Unless otherwise specified, it is used in the sense of Lyapunov for the equilibrium state of the system. When starting from an arbitrary but limited initial state, the state of a stable system in

the natural response remains near the equilibrium state for all times. The system is moreover asymptotically stable if the state converges to the equilibrium state. For linear systems, this stability only depends on the location of the eigenvalues of the system matrix and stability is used with reference to both the system and the individual eigenvalues. In addition, there is the input-output stability. A system as a transfer element is stable in this sense if, for a zero initial state and an arbitrary bounded input, the output remains bounded for all times. For linear systems, input-output stability depends on the locations of the transfer function poles. In connection with rational transfer functions, this kind of stability is mentioned several times in the foregoing sections. Finally, a stability for static problems can be defined which does not refer to the state but to the displacements ξ_s.

The stability of the bridge in vacuum depends on the location of the eigenvalues s_{st} of the structural system matrix $\mathbf{A}_{st}$. All eigenvalues in this work are denoted with the variables of the complex frequency. An index points to the considered system. Based on Eq. (4.53), the linear eigenvalue problem

$$(s_{st}\mathbf{I} - \mathbf{A}_{st})\breve{\mathbf{x}}_{st} = \mathbf{0} \tag{4.72}$$

can be derived, where

$$\breve{\mathbf{x}}_{st} = \begin{pmatrix} s_{st}\breve{\xi}_s \\ \breve{\xi}_s \end{pmatrix} \quad . \tag{4.73}$$

In the following, the absolute value of the imaginary part of an eigenvalue is called eigenfrequency. Figure 4.6 shows one half of the eigenvalues of both the two- and the three-dimensional bridge model with structural damping. For brevity, the complex-conjugate eigenvalues in the lower frequency plane are not displayed. The first 14 bending and the first 14 torsional eigenvalues are shown for the three-dimensional model. All eigenvalues lie in the asymptotically stable left frequency half-plane because structural damping is assigned to each undamped eigenmode and all kinds of static structural instabilities are assumed to be inhibited, as explained in Section 4.2. Since structural damping is small, the eigenfrequencies ω_{st} almost equal those of Eq. (4.18). The subeigenvectors $\breve{\xi}_s$ of Eq. (4.72) and those of the undamped problem are identical because modal structural damping is used. Hence, bending and torsion is still uncoupled. Due to the symmetry of the bridge and the chosen values of the structural damping, some of the eigenvalues that are connected to different torsional eigenmodes are equal, as they are for the undamped structure.

For the evaluation of the bridge stability within streaming air, the eigenvalues s_{as} of the aeroelastic system matrix $\mathbf{A}_{as}$ must be determined. With reference to Eq. (4.55), the eigenvalue problem reads as follows.

$$(s_{as}\mathbf{I} - \mathbf{A}_{as})\breve{\mathbf{x}}_{as} = \mathbf{0} \tag{4.74}$$

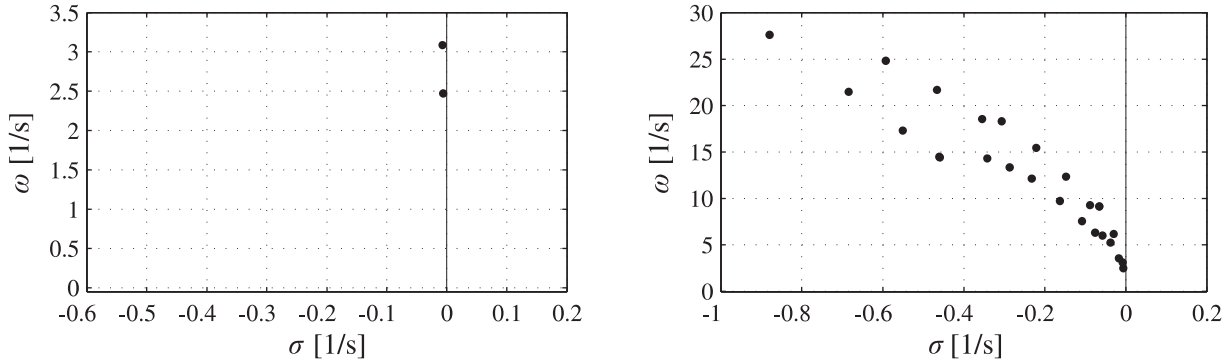

(a) 2d model. (b) 3d model.

Figure 4.6: Eigenvalues of the damped structural system in the upper complex frequency half-plane.

Again, the velocity and the displacement part in the structural subeigenvector depend on each other.

$$\breve{\mathbf{x}}_{\mathrm{as}} = \begin{pmatrix} s_{\mathrm{as}}\breve{\boldsymbol{\xi}}_{\mathrm{s}} \\ \breve{\boldsymbol{\xi}}_{\mathrm{s}} \\ \breve{\boldsymbol{\xi}}_{\mathrm{a}} \end{pmatrix} \tag{4.75}$$

The eigenvalues of the aeroelastic system differ from a simple combination of those of the structural system matrix $\mathbf{A}_{\mathrm{st}}$ and the ones of the system matrix $(U/b)\mathbf{R}$ of the motion-induced aerodynamic forces. This can be seen when considering $\mathbf{A}_{\mathrm{as}}$ in Eq. (4.56a). Due to the feedback interconnection, there is no block triangular form with the system matrices of both subsystems on the main diagonal.

Through the effect of the motion-induced aerodynamic forces, bending and torsion become coupled and both are additionally coupled with the aerodynamic degrees of freedom, in general. To see how the constant horizontal reference wind velocity U governs the stability, a parameter-dependent eigenvalue problem must be solved. Since the aeroelastic system matrix $\mathbf{A}_{\mathrm{as}}$ includes the matrices of the more or less artificial state-space realisation of only the transfer behaviour of the motion-induced aerodynamic forces, the meaning of stability is limited for the air flow to some extent. Moreover, the block triangular form of the system matrix in Eq. (4.61a) shows that the eigenvalues of the aeroelastic system are not altered if the transfer behaviour of gust-induced aerodynamic forces are additionally included in the model.

For the stability analysis, it is desirable to track the paths of the different eigenvalues for changing values of the parameter U. Zero crossings of the eigenvalue real parts can then be found by using numerical algorithms, like the regula falsi method. When the eigenvalue solver is applied, the eigenvalues are, however, not arranged in an appropriate way, in general. Especially predictor-corrector methods lend themselves to eigenvalue tracking. To find the correct permutation for

the eigenvalues at the step U_j, an estimation must be calculated by the predictor, based on the eigenvalues of the foregoing steps U_l, $(l < j)$, and compared with the exact ones. In the technical literature, mathematically sophisticated predictors can be found that are used, for instance, in current software packages of aerospace engineering (e. g. ZAERO 2004).

Here, it is not necessary to distinguish multiple eigenvalues for the path tracking. Hence, a simple eigenvalue extrapolation has been developed that has turned out to be sufficient and very efficient. It uses a quadratic polynomial with complex coefficients that is fitted to the eigenvalues of the three foregoing steps. The difference between the predicted and exactly calculated eigenvalues can be quantified, for instance, with a normalised squared error that is summed up over all pairs. Not all permutations of the eigenvalues can usually be evaluated and compared in an acceptable time because their total number equals the factorial of the width of the quadratic system matrix. The new eigenvalue arrangement for the step U_j is therefore found in another way. Successively, one of the predicted eigenvalues is combined with the one of the exactly calculated eigenvalues that has the lowest distance from it. For the remaining predicted eigenvalues, the assigned exact one is not accessible anymore. After finding all pairs in this way, the permutation is evaluated as described above. If the calculated error is higher than a certain bound, the calculated eigenvalues are rejected and the corrector refines the increment between U_j and U_{j-1} by locally introducing more steps, e. g. ten, before a new set of eigenvalues is determined. If eigenvalues appear near the origin of the frequency plane, the chosen error normalisation with reference to the modulus of the eigenvalue becomes problematic and the corrector is not applied. For starting the algorithm, a very small step size is used and the eigenvalues of the second and third step are not compared with predicted ones but with the eigenvalues of the foregoing step. The transition from the size of the starting steps to a higher one can be formed using the factorial function, for instance.

First, aeroelastic stability is addressed for the two-dimensional bridge model with a flat-plate cross section and theoretical aerodynamic derivatives. The aeroelastic eigenvalues are analysed and compared for three different rational function approximations of the derivatives. Figure 4.7 shows the results for the direct rational function approximation of the derivatives with the Roger approach and $n_\gamma = 5$ poles as given in Eq. (3.32a). The two upper subfigures depict the real and the imaginary part of the eigenvalues against the reference wind velocity U, and in the two lower subfigures, the eigenvalues are displayed in both the complex frequency plane and its reduced version.

For $U \to 0$, there are the two pairs of complex-conjugate eigenvalues. They are similar to the eigenvalues of the damped system in vacuum, as can be seen by comparing Figure 4.7(c) and Figure 4.6(a), because they are only slightly influenced by the air. For increasing wind speeds, the real and the imaginary part of these eigenvalues change. Numerous additional eigenvalues occur due to the simultaneous modelling of the motion-induced aerodynamic forces in the aeroelastic system matrix. Their exact number depends on the chosen approximation approach. Mostly, they

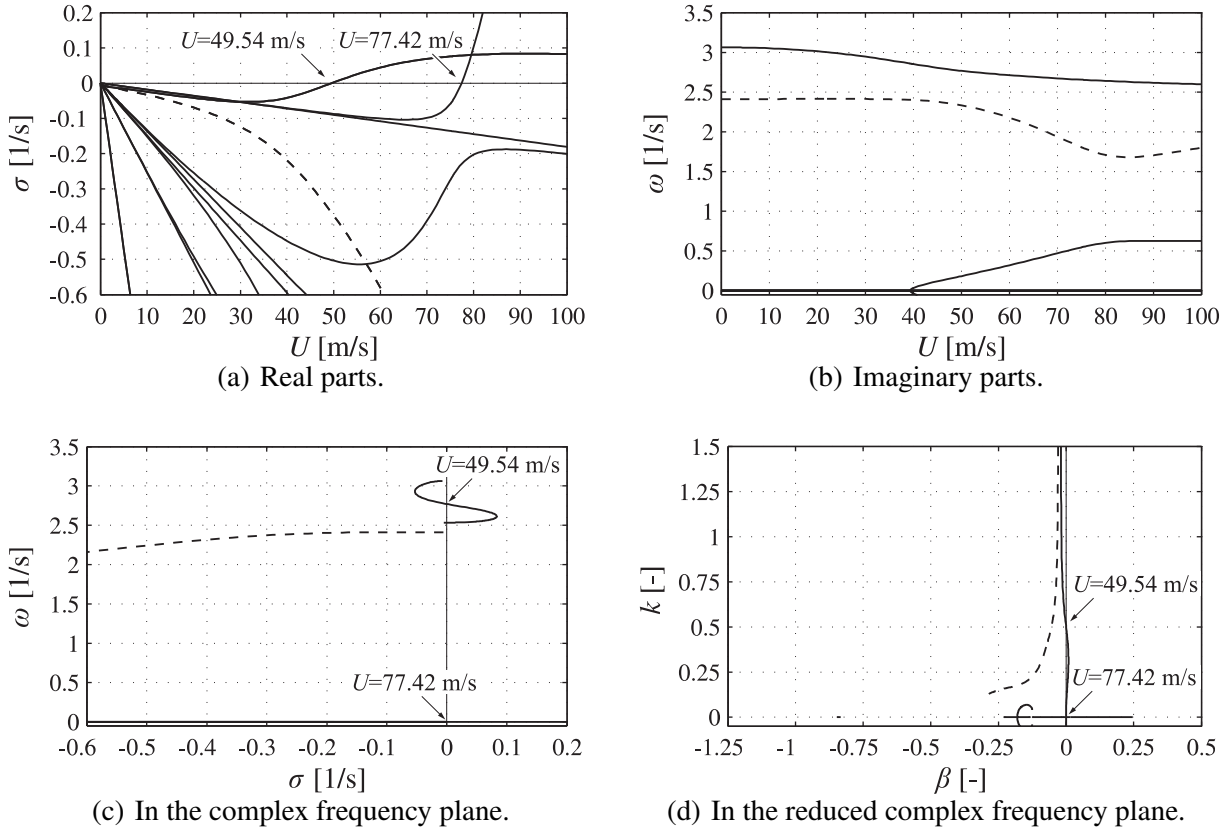

(a) Real parts.
(b) Imaginary parts.
(c) In the complex frequency plane.
(d) In the reduced complex frequency plane.

Figure 4.7: Eigenvalues of the 2d model of the aeroelastic system with the theoretical flat-plate derivatives. Rfa with the Roger approach and $n_\gamma = 5$ poles according to Eq. (3.32a).

are real-valued when they are based on the theoretical derivatives of the flat plate. They tend to the origin of the frequency plane for $U \to 0$. For increasing values of the reference wind velocity, they also change their size. Together with the first mentioned eigenvalues, they determine the total natural response of the aeroelastic system, also in the structural part of the state.

The statements in the last paragraph concerning the eigenvalues for $U \to 0$ can be proven with the structure of the aeroelastic system matrix.

$$\mathbf{A}_{\text{as}}(U=0) = \begin{pmatrix} \begin{pmatrix} -\bar{\mathbf{M}}^{-1}\mathbf{C}_{\text{s}} & -\bar{\mathbf{M}}^{-1}\mathbf{K}_{\text{s}} \\ \mathbf{I} & \mathbf{0} \end{pmatrix} & \begin{pmatrix} \mathbf{0} \\ \mathbf{0} \end{pmatrix} \\ \begin{pmatrix} \mathbf{E} & \mathbf{0} \end{pmatrix} & \begin{pmatrix} \mathbf{0} \end{pmatrix} \end{pmatrix} \tag{4.76}$$

Due to the occurring block triangular form, the mentioned sets of eigenvalues can be directly identified. The $\mathbf{A}_2$ matrix, which modifies the structural mass in Eq. (4.57), represents the only influence of the flow on the non-zero eigenvalues for $U \to 0$. According to Eq. (3.29) and Eq. (2.20), $\mathbf{A}_2$ includes the inertia effect of the non-circulatory flow around the flat plate. As $\mathbf{A}_2$ is a diagonal matrix for the two-dimensional flat-plate case, the structural subeigenvectors of

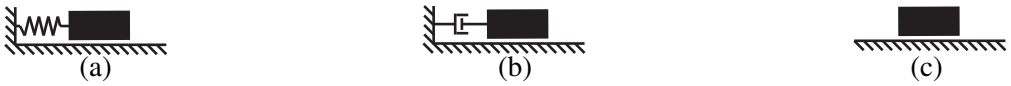

Figure 4.8: Simple structural systems to illustrate the natural responses that are connected with eigenvalues on the imaginary axis.

the complex-conjugate eigenvalues at $U \to 0$ equal those of the structural eigenvalue problem in Eq. (4.72).

At the transition between the stable and the unstable behaviour of single natural responses that are connected with the eigenvalues, two characteristic critical wind speeds can be identified in the figures. For these critical wind speeds, the behaviour of the single natural response is stable but not asymptotically stable.

The lower critical wind speed $U = 49.54\ \mathrm{m/s}$ is called flutter wind speed. It occurs with two complex-conjugate eigenvalues at the imaginary frequency axis. They are connected with two complex-conjugate eigenvectors. Both pairs of complex conjugates can be combined to describe the related part of the real-valued natural response. Using the degrees of freedom defined at the end of Section 4.4, the eigenvectors have complex non-zero entries in all elements of the aeroelastic state. For the eigenvalue in the upper frequency plane and the corresponding displacement part of the structural subeigenvector, the numerical details are as follows.

$$\omega_{\mathrm{as}} = 2.7705\ 1/\mathrm{s}\ , \quad k_{\mathrm{as}} = 0.50326 \tag{4.77a}$$

$$|\check{\xi}_{\mathrm{s}}| = \begin{pmatrix} 1 \\ 0.95604 \end{pmatrix}\ , \quad \arg(\check{\xi}_{\mathrm{s}}) = \begin{pmatrix} 0 \\ -50.109^{\circ} \end{pmatrix} \tag{4.77b}$$

The shown eigenvector is normalised with a complex scalar factor — that means rotated and stretched — so that the first entry in the given subvector has the value one. As is typical for aeroelastic systems with streamlined cross sections, bending and torsion are strongly coupled in the flutter eigenvector. The behaviour of the natural response that corresponds to the complex-conjugate eigenvalues on the imaginary axis is comparable to that of the simple undamped structural system shown in Figure 4.8(a). When the reference wind velocity reaches higher values, there is a second crossing of the imaginary axis by the addressed two complex-conjugate eigenvalues back into the stable half-plane, as can be seen in Figure 4.7(c). This behaviour is typical for two-dimensional flat-plate systems to which structural damping is assigned (Starossek 1992, Kirch 2010).

At $U = 77.42\ \mathrm{m/s}$, a single eigenvalue is located at the origin of the frequency plane. The value of the reference wind velocity is called the divergence wind speed. A zero eigenvalue indicates a static phenomenon. The associated eigenvector is thus real-valued and has not only zero entries

in the speed part of the structural subvector but also in the lag-states subvector. The remaining displacement part of the structural subvector takes the following numerical values.

$$\breve{\boldsymbol{\xi}}_{\mathrm{s}} = \begin{pmatrix} 1 \\ -0.82945 \end{pmatrix} \tag{4.78a}$$

Figure 4.8(b) shows a simple structural system to illustrate the natural aeroelastic response associated with a zero eigenvalue and a negative real one.

An alternative way to find the result at the divergence wind speed is provided by Eq. (4.59). The static eigenvalue problem

$$(\mathbf{K}_{\mathrm{s}} - q_0\, \mathbf{A}_0)\breve{\boldsymbol{\xi}}_{\mathrm{s}} = \mathbf{0} \tag{4.79}$$

can be derived, which yields the divergence wind speed from the eigenvalue q_0. Eq. (4.79) especially shows the importance of a good approximation of the original steady coefficients of motion-induced aerodynamic forces with the $\mathbf{A}_0$ matrix. Therefore, the $\mathbf{A}_0$ matrix is always constrained in this work. For the numerical example, the divergence wind speed is higher than the flutter wind speed, as in the majority of such aeroelastic systems. The total natural response of the aeroelastic system is dominated by the eigenvalues with the highest real part. Since the real part of the addressed single eigenvalue monotonically increases with growing values of the reference wind velocity, the unstable natural response of the aeroelastic system is more or less non-oscillating for higher wind speeds.

The terms flutter and divergence are also used for the system characteristics caused by the unstable branches of the eigenvalues mentioned so far. However, the two terms should especially denote the phenomena connected with eigenvalues on the imaginary axis, unless otherwise specified.

For comparison purposes, Figure 4.9 and Figure 4.10 show the eigenvalues that are obtained when other rational function approximations are employed. The first figure is based on the aerodynamic derivatives given in Eq. (3.30a) that are derived from the approximation of the consistent Theodorsen function. For the second figure, a direct derivative approximation with the Karpel approach is carried out using the same original values and settings that are described for the approximation in Eq. (3.32a).

When comparing all results, it turns out that some eigenvalue branches, or parts of them, are almost identical for all employed rational function approximations. Taking also the illustration of the derivative approximation in Figure 3.7(a) into account and comparing it with the eigenvalue paths in the reduced complex frequency plane, an explanation can be found. All eigenvalues that are not located within the vicinity of the approximation poles on the negative real frequency

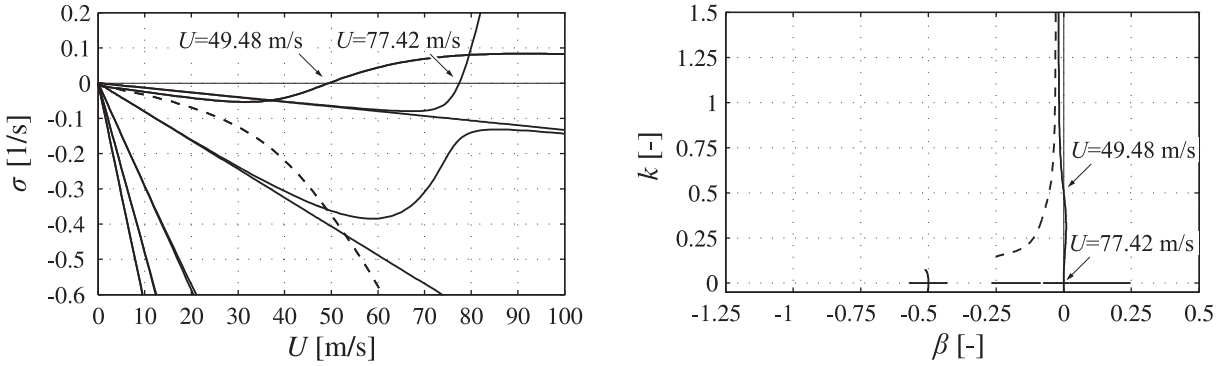

(a) Real parts. (b) In the reduced complex frequency plane.

Figure 4.9: Eigenvalues of the 2d model of the aeroelastic system with the theoretical flat-plate derivatives. Rfa with the Roger approach and $n_\gamma = 5$ poles according to Eq. (3.30a).

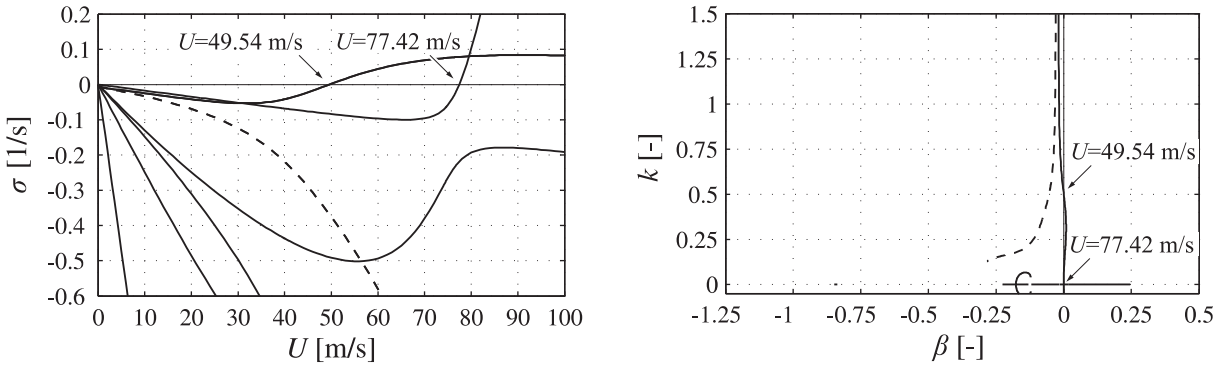

(a) Real parts. (b) In the reduced complex frequency plane.

Figure 4.10: Eigenvalues of the 2d model of the aeroelastic system with the theoretical flat-plate derivatives. Rfa with the Karpel approach and $n_\gamma = 5$ poles as addressed in Section 3.5.2.

axis, where the approximation of the aerodynamic forces is very bad, are nearly congruent for all approximations. Hence, both pairs of complex-conjugate eigenvalue branches that almost originate in the vacuum values for $U \to 0$ are well founded, at least if the reference wind velocity is not too high. The branch of the single real eigenvalue that crosses the origin at the divergence wind speed takes almost identical values in all figures if it is non-negative. All other branches depend on the chosen rational function approximation. As long as their real values are much smaller than those of the well-founded ones, they do not noticeably affect the total natural response.

Up to $U \approx 37$ m/s, one or more of the negative real-valued eigenvalues are located furthest to the right in the complex frequency plane. In Figure 4.7(a) and Figure 4.9(a), they are only visible as a single line due to the low resolution. The reason for their occurrence is the approximation pole with the lowest absolute value, which is located very close to the origin of the frequency plane. For the direct derivative approximations with the Roger and the Karpel approach, this pole has a slightly higher absolute value than that of the approximation of the consistent Theodorsen

function, as can be seen in Eq. (3.32a) and Eq. (3.30a). Therefore, the described phenomenon is a little bit smaller in Figure 4.7(a) and Figure 4.10(a) than in Figure 4.9(a). Though the mentioned eigenvalues are to the right of all others, they do not dominate the natural response in its displacement part in terms of a slowly vanishing non-oscillating motion because the corresponding eigenvectors have dominant entries only in the lag states.

Concerning the critical wind speeds, all rational function approximations addressed so far give almost identical results due to the similar approximation quality. The divergence wind speeds in all figures have exactly the same values because they only depend on the constrained $\mathbf{A}_0$ matrix.

Eq. (4.63) is also connected to an eigenvalue problem

$$(s_{\mathrm{as}}\mathbf{I} - \tilde{\mathbf{A}}_{\mathrm{as}}(p_{\mathrm{as}}))\check{\mathbf{x}}_{\mathrm{st}} = \mathbf{0} \tag{4.80}$$

where Eq. (4.73) holds. Due to the dependence of the matrix $\tilde{\mathbf{A}}_{\mathrm{as}}$ on the reduced complex frequency, the eigenvalue problem is non-linear. Again, it has the reference wind velocity U as a parameter. The solution of the non-linear eigenvalue problem is very sophisticated. Theorems and algorithms known from linear eigenvalue problems cannot be applied in general. However, it can be used for an alternative and favourable procedure to determine the critical wind speeds.

For those speeds, it is known that the real part of an eigenvalue vanishes. Hence, the focus can be laid on purely imaginary values $p_{\mathrm{as}} = \mathrm{i}k_{\mathrm{as}}$ of the reduced eigenvalues. For this restriction, Eq. (4.80) can be interpreted as a linear eigenvalue problem with the real parameter k_{as}. The eigenvalues s_{as} can then be determined for a sufficiently wide range of the parameter. For positive (negative) values of the parameter, only the eigenvalues of the resulting complex matrix $\tilde{\mathbf{A}}_{\mathrm{as}}$ that have positive (negative) imaginary parts are suited for a deeper analysis. The contradiction between a purely imaginary assumption for p_{as} and an arbitrarily complex solution vanishes for purely imaginary eigenvalues $s_{\mathrm{as}} = \mathrm{i}\omega_{\mathrm{as}}$. The assumption $\mathrm{i}k_{\mathrm{as}}$ and the solution $\mathrm{i}\omega_{\mathrm{as}}$ can then be converted into each other using a proper value of the reference wind velocity U, which equals a critical wind speed. To summarize, zero crossing of eigenvalue real parts must again be determined. For the path tracking, the already described predictor-corrector algorithm can be employed. There are some advantages to this procedure compared to the one described first. The matrix $\tilde{\mathbf{A}}_{\mathrm{as}}$ is much smaller than the system matrix $\mathbf{A}_{\mathrm{as}}$. Hence, the calculation time for the eigenvalues is significantly reduced. Additionally, the aerodynamic derivatives do not have to be Laplace transforms because only their discrete complex value must be known for the reduced imaginary frequency that occurs with a critical wind speed. Measured derivatives can thus be approximated with simpler functions that approximate their real and imaginary values more precisely. Moreover, for the flat plate, the original derivatives can be employed. The transfer functions of other forces are also less restricted than before. For instance, the imaginary stiffness

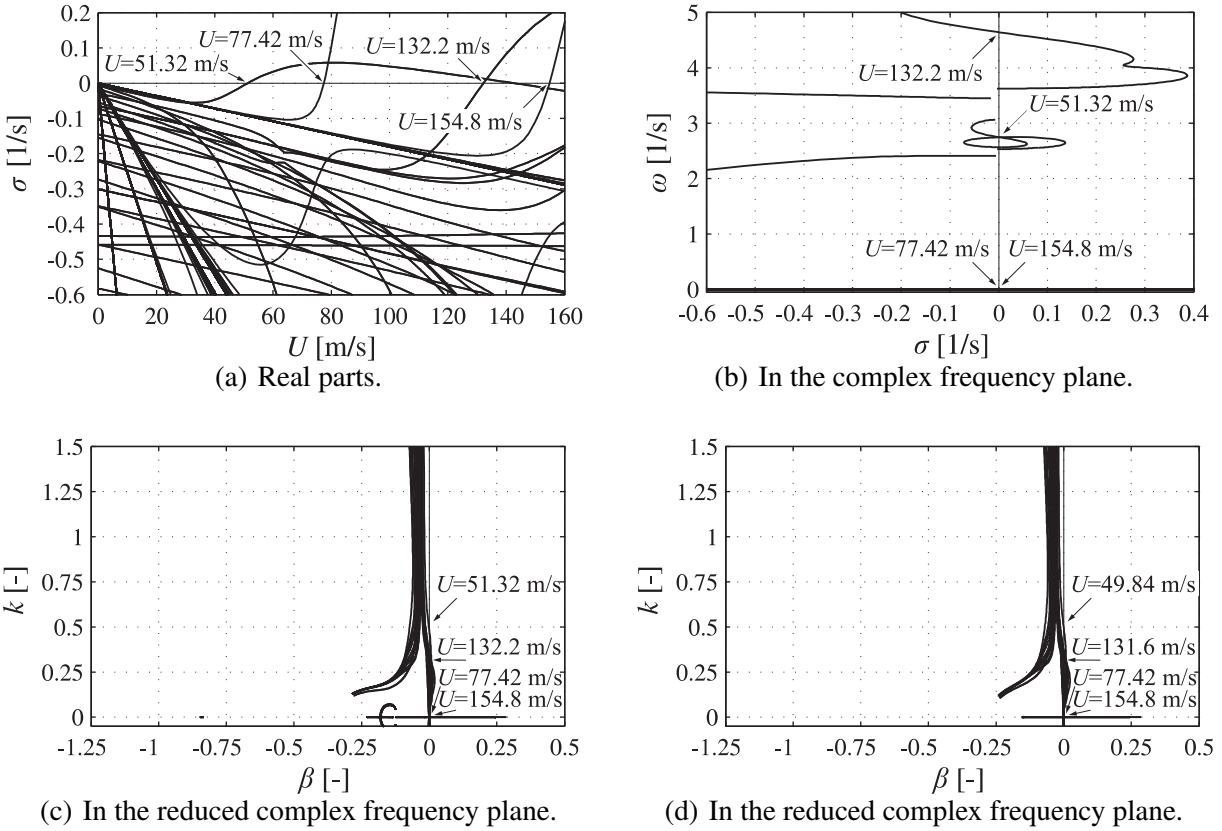

(a) Real parts.

(b) In the complex frequency plane.

(c) In the reduced complex frequency plane.

(d) In the reduced complex frequency plane.

Figure 4.11: Eigenvalues of the 3d model of the aeroelastic system with the theoretical flat-plate derivatives. a)-c): Rfa of the 2d derivatives with the Roger approach and $n_\gamma = 5$ poles according to Eq. (3.32a). d): Rfa of the 3d derivatives with the Karpel approach and $n_\gamma = 15$ poles according to the second block of Table 4.4

can be applied for the damping force. More details on this alternative procedure to determine the critical wind speeds are given in Kirch (2010).

For the two-dimensional bridge model and the original derivatives, the following result is obtained for the flutter wind speed.

$$U = 49.508\ \mathrm{m/s}\,, \quad \omega_{\mathrm{as}} = 2.7707\ 1/\mathrm{s}\,, \quad k_{\mathrm{as}} = 0.50367 \tag{4.81a}$$

$$|\breve{\xi}_{\mathrm{s}}| = \begin{pmatrix} 1 \\ 0.95722 \end{pmatrix}\,, \quad \arg(\breve{\xi}_{\mathrm{s}}) = \begin{pmatrix} 0 \\ -50.108^\circ \end{pmatrix} \tag{4.81b}$$

Again, the associated eigenvalue in the upper frequency plane and the corresponding subeigenvector are given. The quality of the rational function approximations of the flat-plate derivatives for the critical wind speeds is, thus, confirmed.

The stability of the three-dimensional bridge model can be analysed in the same manner as shown for the two-dimensional one. Eigenvalues are displayed in Figure 4.11 for the finite-element model which includes the 14 lowest bending and the 14 lowest torsional modes of the

undamped structure. As explained in Section 4.2, the approximation matrices of the cross-section derivatives in terms of the Roger approach given in Eq. (3.32a) can be used to assemble the global approximation matrices of the investigated bridge. With these global approximation matrices, whose modal versions are reduced to the 28 investigated modes, the first three subfigures are obtained.

Motion-induced aerodynamic forces lead to a coupling among the structural eigenmodes. The only exception is that symmetric and antimetric modes do not get coupled. In addition to the critical wind speeds that are known from the two-dimensional model, several others are obtained for higher wind speeds. Though they are not of interest for practical purposes and the aerodynamic models are not valid for this wind-speed range, the second flutter wind speed and the second divergence wind speed are marked in the figures. In contrast to the two-dimensional model, the eigenvalue branch that causes the first instability crosses the imaginary axis more often. For $U \to 0$, the structural subeigenvectors of the complex-conjugate eigenvalues do not equal those of the structural eigenvalue problem in Eq. (4.72) because the $\mathbf{A}_2$ matrix is not diagonalisable with $\mathbf{\Phi}_\mathrm{s}$. All other phenomena that are described above can also be found in the results of the three-dimensional model. Figure 4.12 shows the aeroelastic modes based on the eigenvectors of the mentioned four critical wind speeds. For the flutter wind speeds, the eigenmodes are displayed that correspond to the eigenvalue in the upper frequency plane. As stated in Starossek (1992), the flutter eigenvectors cannot be normalised so that either the bending or the torsional mode shape is purely real-valued. The divergence modes, however, are real-valued as it has to be for real eigenvalues. In the side spans, the torsional rotations of the flutter modes are low but non-zero. In contrast, the divergence modes have no torsion there. An explanation for the latter fact can be given as follows. In contrast to bending, there is no structural coupling of the torsion in the three spans because warping torsion is not modelled. The torsion of the main span induces not only an aerodynamic torque but also a lift force there. Along the whole bridge girder, bending occurs, which does not generate steady aerodynamic forces and, thus, no steady torsion in the side spans.

The question of how the eigenmodes of the undamped structure participate in the aeroelastic modes is answered in Figure 4.13. All eigenvectors in the truncated modal matrix $\mathbf{\Phi}_\mathrm{s}$ are normalised so that the maxima of their element moduli take the value one for this figure. With the chosen finite-element discretisation, a normalisation of the selected continuous eigenmodes to the maximum modulus one is achieved in a sufficiently accurate way. The value 100 % corresponds to the sum of the absolute values of the eigenvector elements in the displacement part of the structural subvector in modal degrees of freedom for either bending or torsional elements. The first flutter mode is almost only determined by the first bending and the first torsional mode. The second flutter mode, however, is to some small extent more influenced by higher modes. For the

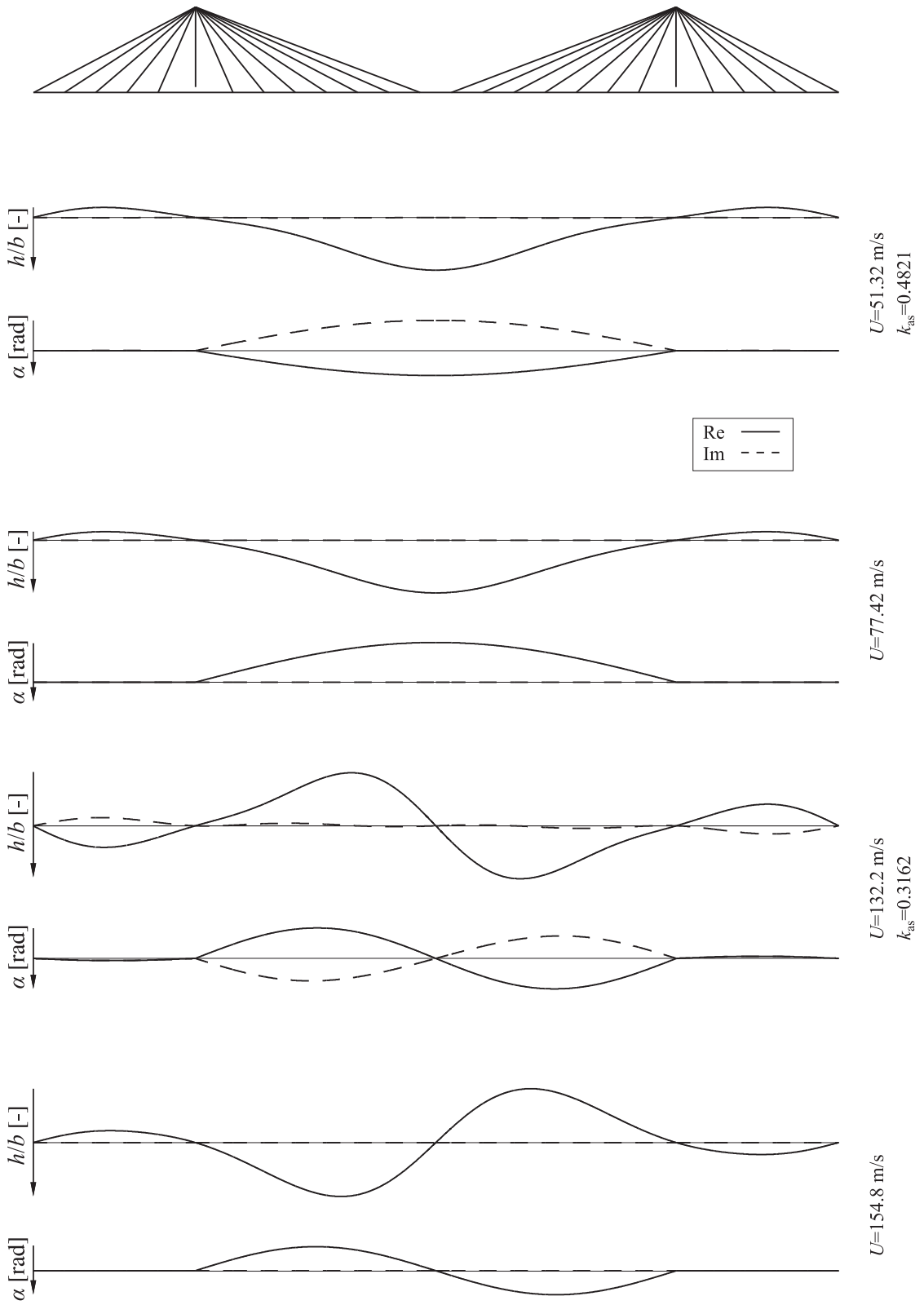

Figure 4.12: Critical aeroelastic modes for the first four critical values of the constant horizontal reference wind velocity U with respect to the results given in Figure 4.11(a)-Figure 4.11(c).

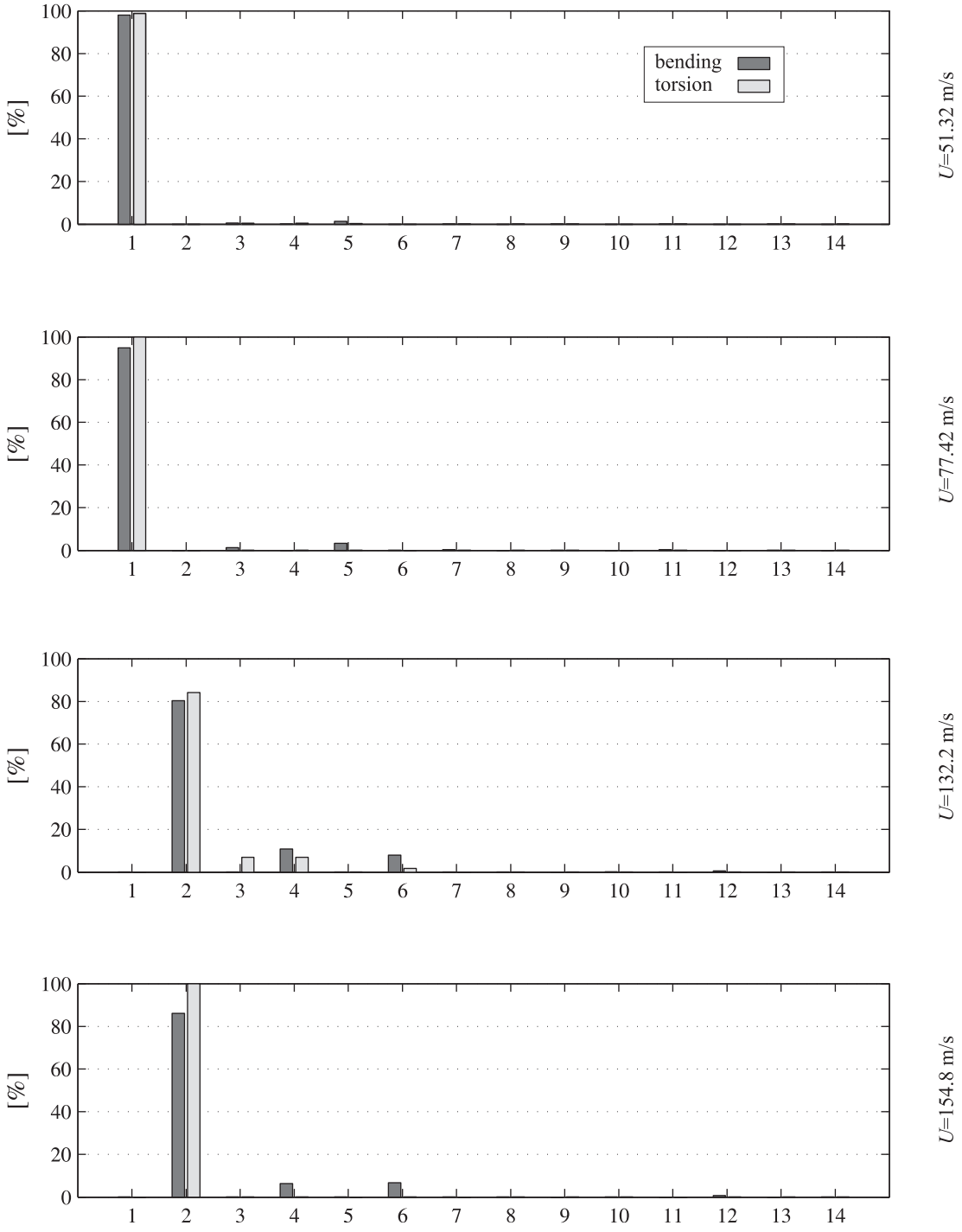

Figure 4.13: Participation of the structural modes in the critical aeroelastic modes with respect to the results given in Figure 4.11(a)-Figure 4.11(c).

torsional part of the first and the second divergence mode, the first and the second torsional mode are the total basis, respectively.

The latter remarkable fact is a consequence of the decoupling of bending and torsion in the undamped structure. It can be proved with the help of the static eigenvalue problem in Eq. (4.79). First, the problem is transferred to the following special linear form.

$$(\frac{1}{q_0}\,\mathbf{I}-\mathbf{K}_{\mathrm{s}}^{-1}\mathbf{A}_0)\check{\boldsymbol{\xi}}_{\mathrm{s}}=\mathbf{0} \tag{4.82}$$

Due to the assumptions made for the structure in the foregoing sections, the inverse of the structural stiffness matrix exists in contrast to the inverse of the $\mathbf{A}_0$ matrix. The $\mathbf{A}_0$ matrix is singular due to the zero columns, which are in connection with the bending degrees of freedom. If modal degrees of freedom are used and grouped in bending and torsional ones, the matrix $(\mathbf{K}_{\mathrm{s}}^{-1}\mathbf{A}_0)$ takes a special triangular form of four block matrices. The four blocks are defined by the two groups of torsional and bending degrees of freedom. On the diagonal, the bending block matrix is a zero matrix and the torsional block matrix has non-zero entries only on the main diagonal. Each of the latter entries is influenced by the stiffness of the respective torsional mode only. The eigenvalue problem is now easy to solve due to the triangular form. As a consequence, there is a first group of infinitely high divergence wind speeds that are in connection with bending modes. Each divergence wind speed of the second group is determined by the stiffness of only one respective torsional mode. The corresponding aeroelastic eigenmode is made up of the special torsional mode and a mixture of weighted bending modes. A detailed verification of this proof is left to the reader.

To conclude, the first flutter wind speed can be determined in a sufficiently precise manner and the first divergence wind speed in an exact manner on the basis of the lowest bending and the lowest torsional mode of the undamped structure. The decision to take only the addressed 28 modes into account for the rational function approximation of the motion-induced aerodynamic forces is justified by Figure 4.13 for determining the first four critical wind speeds. Constraining the $\mathbf{A}_0$ matrix to the reduced modal version of the original steady aerodynamic admittance, which is explained in Section 4.3, thus does not noticeably affect the divergence wind speed either.

The effect of some of the derivative approximations explained in Section 4.3 on the critical wind speeds can be observed with the help of the numerical results given in Table 4.6. Since the divergence wind speeds are governed by the always constrained $\mathbf{A}_0$ matrix, they take the same value for all approximations. Hence, only the flutter wind speeds and the corresponding eigenfrequencies are displayed. Solutions with two different truncations of the modal matrix $\boldsymbol{\Phi}_{\mathrm{s}}$ are shown. The solutions that are obtained with all structural modes do not noticeably differ from those with 28 modes in the first five digits and are thus not additionally displayed. As a reference, the solutions determined with the alternative procedure based on Eq. (4.80)

Table 4.6: Lowest flutter wind speeds and corresponding eigenfrequencies calculated with the 3d model. Results in the left half are obtained with a truncation of the modal matrix $\mathbf{\Phi}_s$ to the 14 lowest bending and the 14 lowest torsional modes and those in the right half with a truncation to the first bending and the first torsional mode.

U [m/s]	ω_{as} [1/s]	k_{as} [−]	U [m/s]	ω_{as} [1/s]	k_{as} [−]
original derivatives, Eq. (4.80)					
51.280	2.7495	0.48255	51.088	2.7509	0.48461
132.17	4.6467	0.31641			
rfa of the 2d derivatives according to the Roger approach in Eq. (3.32a)					
51.322	2.7492	0.48211	51.130	2.7506	0.48417
132.21	4.6448	0.31620			
rfa of the 3d derivatives with $n_\gamma = 5$ poles according to the Roger approach in the first block of Table 4.4					
51.310	2.7494	0.48225	51.118	2.7508	0.48431
132.23	4.6447	0.31613			
rfa of the 3d derivatives with $n_\gamma = 16$ poles according to the Karpel approach in the first block of Table 4.4					
50.604	2.7295	0.48544	50.453	2.7307	0.48710
138.69	4.4506	0.28881			
rfa of the 3d derivatives with $n_\gamma = 5$ poles according to the Roger approach in the second block of Table 4.4					
51.322	2.7494	0.48214	51.129	2.7508	0.48421
132.29	4.6438	0.31592			
rfa of the 3d derivatives with $n_\gamma = 15$ poles according to the Karpel approach in the second block of Table 4.4					
49.848	2.7581	0.49797	49.698	2.7593	0.49969
131.59	4.6317	0.31678			

and the original derivatives are given in the first block. The second block again shows the solutions with the approximated derivatives that are explained in the foregoing paragraphs. As foreseeable, the flat-plate derivatives and consequently the critical wind speeds are very well approximated due to the special suitability of the rational functions with real poles. The same holds true when the derivatives of the three-dimensional system are directly approximated with the Roger approach and $n_\gamma = 5$ poles as addressed in Table 4.4. The respective solutions are given in the third and the fifth block of Table 4.6. Interestingly, the direct approximation of the three-dimensional derivatives with the Karpel approach whose quality is comparable to the Roger approach with $n_\gamma = 1$ pole leads to good results for the investigated critical wind speeds, as can be seen in the fourth and sixth block. Anyway, if the critical wind speeds occur with other reduced eigenfrequencies, for instance due to a modification of the structural parameters of the bridge, the quality of the latter solution can be distinctly worse. Remarkable advantages of the different data weightings used for the approximations in Table 4.4 cannot be observed here. Figure 4.11(d) depicts the eigenvalues for the Karpel approach of the second block of Table 4.4 in the reduced frequency plane. Due to a higher distortion of the derivative approximation around

the negative real frequency axis, the eigenvalue branches somewhat differ there from those shown in Figure 4.11(c).

It remains to be explained why the results in the right half of Table 4.6 differ from those of the two-dimensional model. The reasons for the differences are the simplifications that are described in Section 4.4. The most important of these is ignoring the correction factors of Eq. (4.49). Adjusting the two-dimensional model with these factors and determining the flutter wind speed with the alternative procedure and the original derivatives leads to a much better result.

$$U = 51.049\ \mathrm{m/s}\ , \quad \omega_{\mathrm{as}} = 2.7520\ 1/\mathrm{s}\ , \quad k_{\mathrm{as}} = 0.48517 \tag{4.83}$$

The divergence wind speed is not affected by the correction factors because it depends only on the main diagonal element $Q_{\alpha\alpha}(p=0)$. Nonetheless, the error that occurs for the flutter wind speed when the corrections are not taken into account is judged to be acceptable for further investigations. Due to the very good agreement between the solutions of the two-dimensional and the three-dimensional aeroelastic model, the convergence of the finite-element solution with an increasing amount of aeroelastic elements is not studied. Concerning this topic, reference is also made to the small examples presented in Starossek (1992). The convergence of the finite-element solution for the structural elements is taken for granted.

For an additional verification of the implemented three-dimensional model, the first two flutter wind speeds are determined with the structural parameters that are employed in Starossek (1992). Using the alternative procedure and the original flat-plate derivatives leads to the results given in Table 4.7. The italic values taken from Starossek (1992) are in a very good agreement.

Table 4.7: Verification of the 3d aeroelastic bridge model using the first two flutter wind speeds. Italic values are taken from Starossek (1992).

U [m/s]	ω_{as} [1/s]	k_{as} [−]	U [m/s]	ω_{as} [1/s]	k_{as} [−]
44.466	2.5917	0.52456	111.82	4.3782	0.35237
44.4	*2.591*	*0.525*	*112*	*4.377*	*0.352*

In the last part of this section, the effect of the rational function approximation of the aerodynamic derivatives of cross sections in real flow on the eigenvalues of the aeroelastic system and its theoretical stability is studied. Concerning the cross sections addressed in Section 3.6, the approximation characteristics of the TaS cross-section derivatives differ most significantly from those of the theoretical flat-plate ones. The following investigations are, thus, carried out with the TaS derivatives to show some shortcomings that can occur with a poor approximation. For this purpose, the use of the two-dimensional bridge model is considered to be sufficient.

As mentioned before, the algorithm that is explained in connection with Eq. (4.80) to determine the critical wind speeds does not necessitate a derivative approximation in terms of a consistent

transfer function. Independent of the rational function approximation, a solution can be found that is used as a reference. The real and the imaginary part of the measured derivatives can, for instance, be approximated with real-valued polynomials in the least-squares sense. Using polynomials of degree five whose constant coefficients are constrained to the original steady derivatives leads within the interval of Table 2.1 to the following flutter wind speed.

$$U = 30.584\ \mathrm{m/s}\,, \quad \omega_{\mathrm{as}} = 2.8599\ 1/\mathrm{s}\,, \quad k_{\mathrm{as}} = 0.84159 \tag{4.84a}$$

$$|\breve{\boldsymbol{\xi}}_{\mathrm{s}}| = \begin{pmatrix} 1 \\ 19.083 \end{pmatrix}\,, \quad \arg(\breve{\boldsymbol{\xi}}_{\mathrm{s}}) = \begin{pmatrix} 0 \\ -71.083^{\circ} \end{pmatrix} \tag{4.84b}$$

The associated eigenvalue in the upper frequency plane and the related subeigenvector are additionally given. As is typical for structures with such a section shape, flutter occurs with a dominant torsional component. Aeroelastic divergence is impossible for this cross section and the used derivatives because a quasi-static small rotation of the cross section generates a counteracting quasi-static aerodynamic moment.

Using the rational function approximation given in Eq. (3.34a) with $n_\gamma = 5$ poles and solving the parameter-dependent eigenvalue problem in Eq. (4.74) leads to the curves depicted in Figure 4.14. The flutter wind speed described in Eq. (4.84) can again be identified with the following details.

$$U = 30.112\ \mathrm{m/s}\,, \quad \omega_{\mathrm{as}} = 2.8577\ 1/\mathrm{s}\,, \quad k_{\mathrm{as}} = 0.85409 \tag{4.85a}$$

$$|\breve{\boldsymbol{\xi}}_{\mathrm{s}}| = \begin{pmatrix} 1 \\ 25.168 \end{pmatrix}\,, \quad \arg(\breve{\boldsymbol{\xi}}_{\mathrm{s}}) = \begin{pmatrix} 0 \\ -3.5912^{\circ} \end{pmatrix} \tag{4.85b}$$

The good agreement of the flutter wind speed and the eigenfrequencies in Eq. (4.84) and Eq. (4.85) indicates a comparable quality of both approximations for the most relevant derivatives at the reduced flutter eigenfrequency. For the TaS cross section, flutter is mainly driven by the torsional mode. The approximation of the derivatives that influence the bending part differs, as can be seen when comparing the subeigenvectors.

Several differences exist compared to the results of the flat plate. Some are caused by the matrix coefficients $\mathbf{A}_1$ and $\mathbf{A}_2$. As explained in Section 3.6, the two matrices strongly depend on the settings of the identification procedure. In contrast to the flat-plate case, their entries are not physically justified in general.

For $U \to 0$, there are two pairs of complex-conjugate eigenvalues of the aeroelastic system, which noticeably differ from the purely structural ones in Figure 4.6(a). The corresponding eigenvectors, which are not given here, show a strong coupling of the bending and torsional degree of freedom. The physically not comprehensible result is a consequence of the mathematically determined

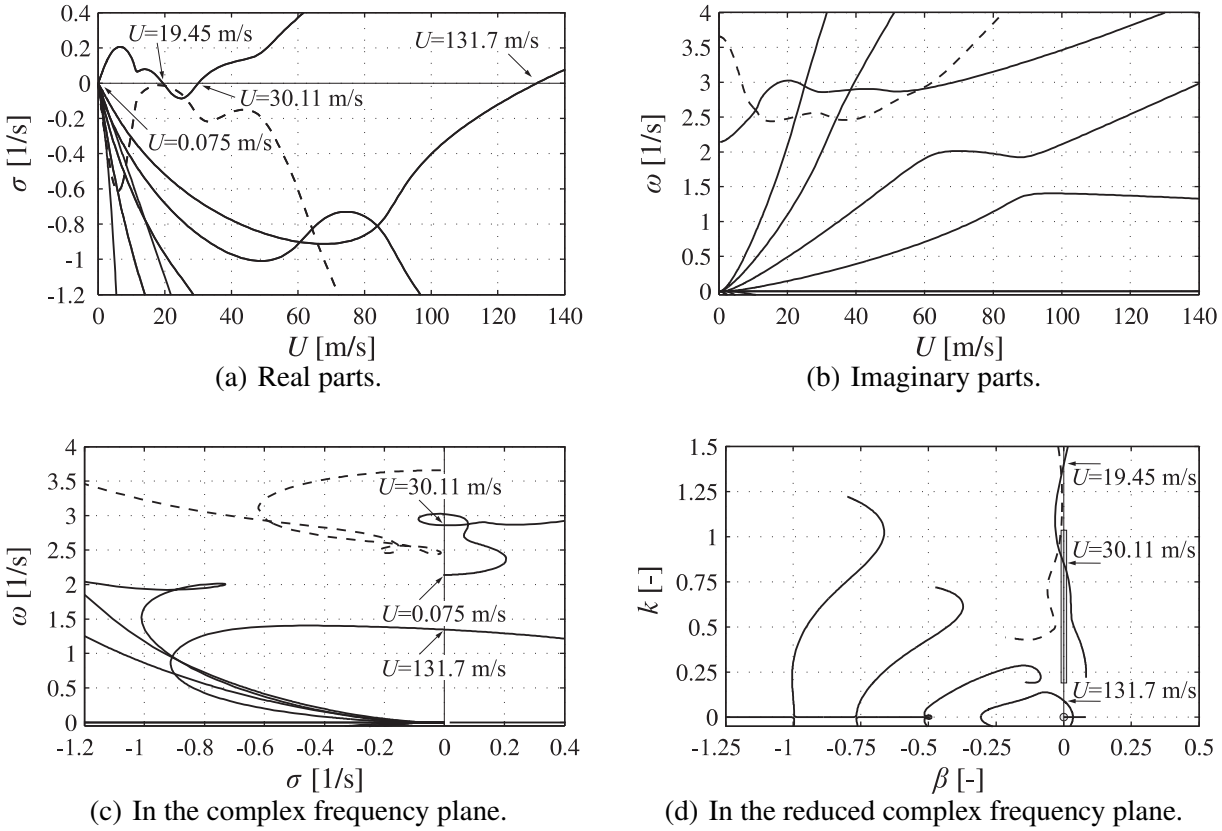

(a) Real parts. (b) Imaginary parts.

(c) In the complex frequency plane. (d) In the reduced complex frequency plane.

Figure 4.14: Eigenvalues of the 2d model of the aeroelastic system with the TaS derivatives. Rfa with the Roger approach and $n_\gamma = 5$ poles according to Eq. (3.34a).

$\mathbf{A}_2$ matrix, which is, according to Eq. (4.76), the only aerodynamic influence on the non-zero eigenvalues.

Astonishingly, there is an unstable interval between $U = 0.075$ m/s and $U = 19.45$ m/s that is contrary to the physical experience. It is obviously caused by the rational function approximation. The exact source of the strange results is the $\mathbf{A}_1$ matrix. Since an explanation can be restricted to the critical wind speeds, only the imaginary frequency axis must be considered in the frequency domain. For large absolute values of the imaginary reduced frequency, the imaginary part of the derivatives are dominated by the $\mathbf{A}_1$ summand, as can be seen in Eq. (3.26b) and in Figure 3.2(b). The imaginary parts of the elements on the main diagonal of the derivative matrix can be interpreted as aerodynamic damping coefficients. A positive imaginary part of these derivatives for positive imaginary frequencies corresponds to a negative aerodynamic damping, which can generate uncoupled flutter. For the flat plate, the theoretical derivatives on the main diagonal do not show this sign. In the case of the TaS cross section, however, such a negative damping is responsible for the torsional flutter addressed in Eq. (4.84) and Eq. (4.85). Additionally, the positive $A_{1,\alpha\alpha}$ element in the approximation of Eq. (3.34a) generates negative damping for the torsional degree of freedom at high absolute values of the imaginary reduced frequency. When

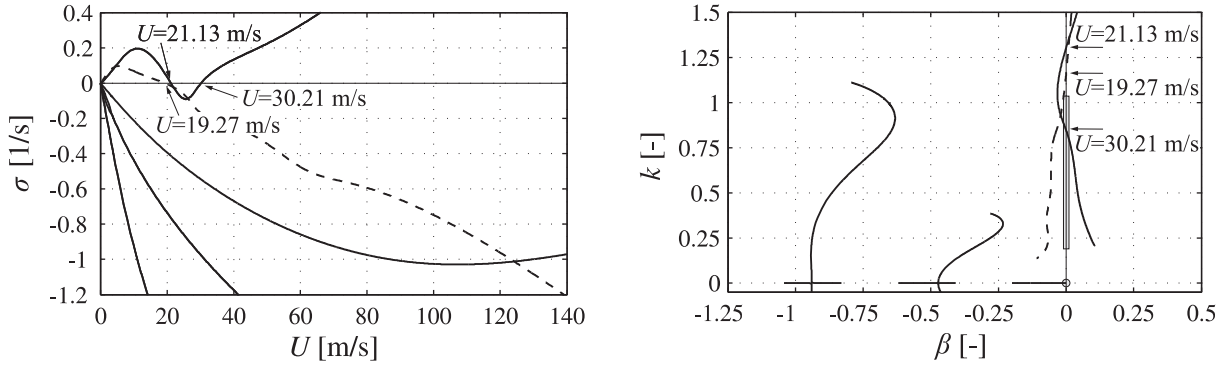

(a) Real parts. (b) In the reduced complex frequency plane.

Figure 4.15: Eigenvalues of the 2d model of the aeroelastic system with the TaS derivatives. Rfa with the Karpel approach and $n_\gamma = 5$ poles as addressed in Table 3.6.

comparing Figure 4.14(a) and Figure 4.14(d), it can be confirmed that the low unstable speed range is in connection with high absolute values of the imaginary part of the eigenvalues outside the grey-coloured identification range and thus caused by the positive $A_{1,\alpha\alpha}$ element.

A similar effect can also be observed by comparing Figure 3.10(a) and Figure 4.14(d). The imaginary part of the Q_{hh} derivative becomes positive for a bounded interval above $k \approx 1.1$. This negative aerodynamic damping causes very slightly damped eigenvalues of the dashed branch around $U \approx 19\,\mathrm{m/s}$. Additional structural and aerodynamic damping prevent a zero crossing. Further investigations, which are not given here in detail, have revealed that these effects outside the identification interval can also appear for the approximated derivatives of streamlined cross sections in real flow. It remains to be examined whether these effects can be prohibited with more constraints in the identification procedure without considerably reducing the approximation quality.

To judge the dependence of the eigenvalues in the frequency plane from the special rational function approximation, Figure 4.15 shows the eigenvalues based on an alternative approximation. The Karpel approach with $n_\gamma = 5$ poles that is addressed in Table 3.6 is employed. The flutter wind speed of Eq. (4.84) has the following details for the selected approximation approach.

$$U = 30.212\,\mathrm{m/s}\,, \quad \omega_{\mathrm{as}} = 2.8468\,1/\mathrm{s}\,, \quad k_{\mathrm{as}} = 0.84804 \tag{4.86a}$$

$$|\breve{\boldsymbol{\xi}}_{\mathrm{s}}| = \begin{pmatrix} 1 \\ 11.484 \end{pmatrix}\,, \quad \arg(\breve{\boldsymbol{\xi}}_{\mathrm{s}}) = \begin{pmatrix} 0 \\ -0.14698^\circ \end{pmatrix} \tag{4.86b}$$

The comments to the results in Eq. (4.85) also apply here. Since both entries on the main diagonal of the $\mathbf{A}_1$ matrix are positive for this approximation, two eigenvalue branches drift into the unstable frequency half-plane for low reference wind speeds. The very low critical wind speeds are not labelled in Figure 4.15(a). From the negative real frequency axis, complex

eigenvalue branches originate, which are evidently a consequence of the distorted approximation values, as can be seen when comparing Figure 3.10(b) with Figure 4.14(d) and Figure 4.15(b). The flutter wind speed that occurs in Figure 4.14(d) with eigenvalues between the identification interval and the origin cannot be found in Figure 4.15(b).

Obviously, all eigenvalues that are located outside the grey-coloured identification interval on the imaginary frequency axis differ in both approximations. Due to the approximation with highly weighted lag terms, the eigenvalues are not reliable in most areas of the frequency plane.

4.7 Transfer Behaviour Concerning Gust Input

In the foregoing section, the stability of the dynamic system is defined by means of its natural response to a non-zero arbitrary initial state. The initial state of the modelled aeroelastic system, however, is constrained to be zero for a simulation because the state in the state-space realisation of the identified transfer behaviour of the motion-induced aerodynamic forces is not based on a physical background, as already explained in Section 3.2. As a consequence of the zero condition, the state of the aeroelastic system and its time history are only determined by the input history.

Due to the chosen linear approach for the motion-induced and the gust-induced aerodynamic forces, the aerodynamic admittances generally depend on the defined zero position of the degrees of freedom, as mentioned in Section 2.1. In Chen & Kareem (2001b), for instance, a procedure is proposed to account for this dependence in a time-domain simulation by continuously updating the aerodynamic admittances according to the size of a low frequency component of the displacements. For each type of aerodynamic forces, thus, different sets of identified black-box transfer functions are used in a single time-domain model in order to achieve a non-linear simulation. Such an attempt has to fail in general, regardless of whether the time-domain simulation is carried out with a convolution integral or a state-space model of the aerodynamic forces. If, for instance, the forces are calculated with a convolution, an update of the aerodynamic admittances changes the aerodynamic impulse response. Since the impulse response accounts for the history of the system input, the influence of this history is continuously changed in a curious way. Moreover, the convolution, as a linear operation, necessitates a linear system. If the time-domain calculation is carried out with a state-space model, an update of the aerodynamic admittances changes the state-space model. The numerical entries in the aerodynamic state, however, are only justified by the mathematically realised aerodynamic transfer function and the time history of that aerodynamic state, which begins with a zero initial state. The state variables of the black-box state-space realisations of different aerodynamic transfer functions can have the same length, but they do not have the same meaning, in general. Hence, numerical entries cannot be simply handed over from one state to the other. The aeroelastic response on an arbitrary input that is calculated

with such simulations may have a nice shape, but it is usually based on an inconsistent model. Critical wind speeds, however, can be correctly identified with such non-linear time-domain simulations because these wind speeds are connected with a single set of derivatives.

Although the total behaviour of the aeroelastic system investigated here only contains the forced response and no natural response due to the zero initial condition, the results of the last section concerning stability still have a meaning. The time behaviour of the impulse response, for instance, is determined by the same functions that appear in the natural response of the system. Hence, each eigenvalue of the system matrix also influences the forced response. The last statement requires that the canonical system states which are connected with the eigenvalues are accessible from the input and the output. If the system is asymptotically stable, it is also input-output stable. The system is not stable in the last sense when a critical wind speed is reached.

The transfer characteristics, or equivalently expressed the filter characteristics, of a linear system can be comprehensively described especially in the frequency domain using the transfer function. All eigenvalues that are accessible in the sense of the last paragraph appear as poles in the transfer functions of the state-space models derived in Section 4.5. For the following explanations, the two-dimensional bridge model is used for the sake of clarity. The results can be easily transferred to the three-dimensional model.

Based on Eq. (4.53), the structural transfer function can be derived as

$$\mathbf{G}_{\mathrm{st}}(s) = \mathbf{C}_{\mathrm{st}}(s\mathbf{I} - \mathbf{A}_{\mathrm{st}})^{-1}\mathbf{E}_{\mathrm{st}} \quad , \tag{4.87}$$

where

$$\mathbf{C}_{\mathrm{st}} = \begin{pmatrix} \mathbf{0} & \begin{pmatrix} 1 & 0 \\ 0 & 1 \end{pmatrix} \end{pmatrix} \tag{4.88}$$

if $\mathbf{d}_{\mathrm{ae}}^{\mathrm{g}}$ and $\boldsymbol{\xi}_{\mathrm{s}}$ are chosen as input and output, respectively. Since rotation and translation are decoupled in the structural model, the transfer function matrix of the two-dimensional system only has non-zero entries on the main diagonal. Figure 4.16(a) illustrates the absolute value of the transfer function element $G_{\mathrm{st},hh}(s)$ in the complex frequency plane. The decoupling leads to pole-zero cancellations in the transfer elements, and, thus, one pair of respective poles change to removable singularities. Only the complex-conjugate poles are visible that are connected with a translational vibration. Since the full transfer information is incorporated in every infinite straight line parallel to the imaginary axis that lies in the region of absolute convergence of the transfer function, the transfer behaviour does not have to be analysed in the full frequency plane. Hence, it is sufficient to consider the frequency response $\mathbf{G}_{\mathrm{st}}(\mathrm{i}\omega)$, that means the transfer function along the imaginary axis, because all eigenvalues of the structural model lie in the left plane. The

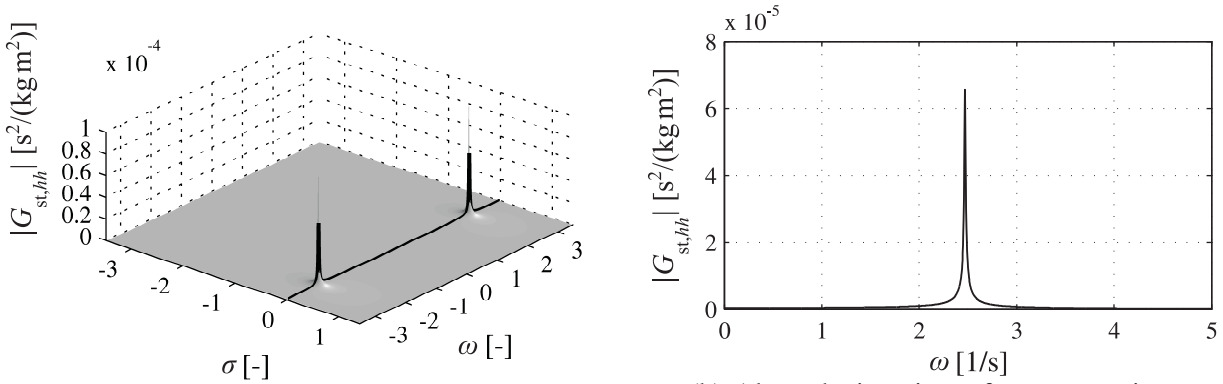

(a) Above the complex frequency plane. (b) Along the imaginary frequency axis.

Figure 4.16: Transfer-function element $G_{\mathrm{st},hh}$ of the structural system.

frequency response particularly lends itself for an analysis because its absolute value and its phase can be directly identified in the steady-state response to an input in terms of a sine signal. Additionally, it is used for the transfer of the spectral density matrices of ergodic processes, as already applied in Section 4.4. One half of the frequency response is shown in Figure 4.16(b) with its absolute value, and it is, moreover, accentuated with a black line in Figure 4.16(a). The function starts at the origin with the steady transfer value. Due to the low structural damping, the poles of the transfer function are located close to the imaginary axis. As a result, the frequency response has a high resonance peak. For high values of the imaginary frequency, $\mathbf{G}_{\mathrm{st}}(\mathrm{i}\omega)$ tends to zero.

The aeroelastic transfer function follows from the state-space model in Eq. (4.55).

$$\mathbf{G}_{\mathrm{as}}(s) = \mathbf{C}_{\mathrm{as}}(s\mathbf{I} - \mathbf{A}_{\mathrm{as}})^{-1}\mathbf{E}_{\mathrm{as}} \tag{4.89}$$

Input and output are defined in the same way as for the structural transfer. Due to the coupling effect of the motion-induced aerodynamic forces, the aeroelastic transfer function matrix in general has non-zero entries everywhere.

As for the eigenvalues in the foregoing section, the aeroelastic transfer is analysed in the first step for the bridge model with a flat-plate cross section and theoretical aerodynamic derivatives. The absolute value of the element $G_{\mathrm{as},h\alpha}(s)$, which transfers the moment to the translational displacement, is displayed in Figure 4.17(a) above the reduced complex frequency plane for a reference wind velocity $U = 25$ m/s. For the motion-induced aerodynamic forces, the rational function approximation of the flat-plate derivatives with $n_\gamma = 5$ poles according to Eq. (3.32a) is employed. The pole locations of the aeroelastic transfer function correspond to those of the eigenvalues in Figure 4.7(d) for $U = 25$ m/s. Since all poles of the asymptotically stable system are located to the left of the imaginary axis, it is again sufficient to investigate the frequency response. All four matrix elements of the frequency response are depicted in Figure 4.18. The

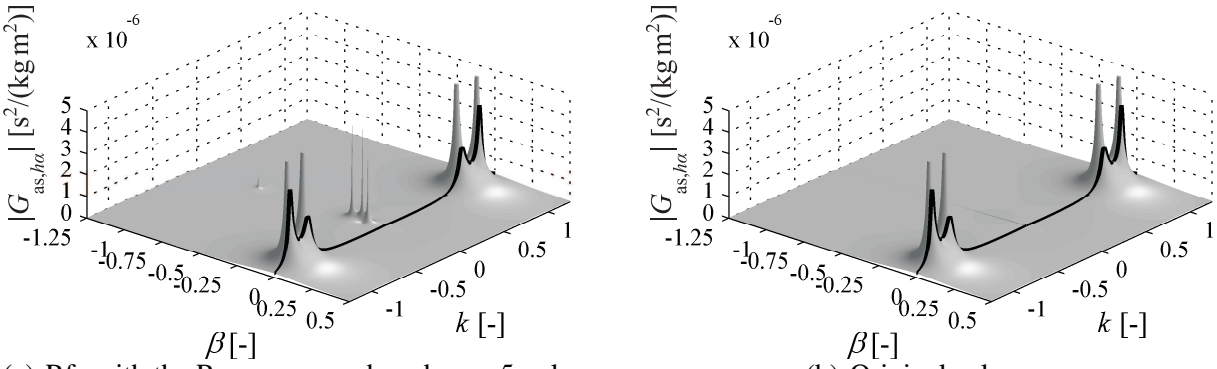

(a) Rfa with the Roger approach and $n_\gamma = 5$ poles according to Eq. (3.32a).

(b) Original values.

Figure 4.17: Transfer-function element $G_{\mathrm{as},h\alpha}$ of the aeroelastic system with the theoretical flat-plate derivatives above the complex frequency plane for $U = 25$ m/s.

motion-induced aerodynamic forces have a damping effect on the transfer behaviour, as can be seen when comparing the ordinates of the resonance peaks in Figure 4.18 and Figure 4.16(b). Due to the aerodynamic coupling, both pairs of complex-conjugate eigenvalues shown in Figure 4.7 for $U = 25$ m/s appear as poles in every element of the transfer function matrix and, thus, as a more or less distinct resonance peak in the elements of the frequency response matrix.

By imagining the aeroelastic transfer function in its partial-fraction form, it becomes clear that the heights of the peaks depend on the distance between the poles and the imaginary axis and a weighting factor. The individual weighting factors that are connected with a special pole differ in each transfer path. Figure 4.19 gives an idea how the heights of the resonance peaks vary with the reference wind velocity. In contrast to Figure 4.18, the ordinates are logarithmically scaled. At $U \to 0$, the eigenmodes are decoupled for the theoretical flat-plate derivatives, as explained in the preceding section. Due to the mentioned pole-zero cancellations, the elements on the main diagonal of the frequency response matrix only have one resonance peak, whose respective location corresponds to the imaginary part of the eigenvalues shown in Figure 4.7(b). All coupling elements have zero entries. For increasing wind speeds, both pairs of poles influence every matrix element. The locations of the peaks change according to the imaginary parts of the eigenvalues. Close to the flutter wind speed, one pair of eigenvalues, and, hence, the corresponding poles, are near the imaginary axis. In all elements of the frequency response, a corresponding distinct resonance peak is visible. At the same wind speed, the other eigenvalue, which is shown in Figure 4.7 with a dashed line, is far away from the imaginary axis, and its influence cannot be seen in terms of a distinct peak.

To derive the aeroelastic transfer function $\mathbf{G}_{\mathrm{as}}(s)$, the flat-plate derivatives do not have to be approximated because the original ones are known for almost every complex frequency. With Eq. (4.66), the original aeroelastic transfer function values can be determined. The element

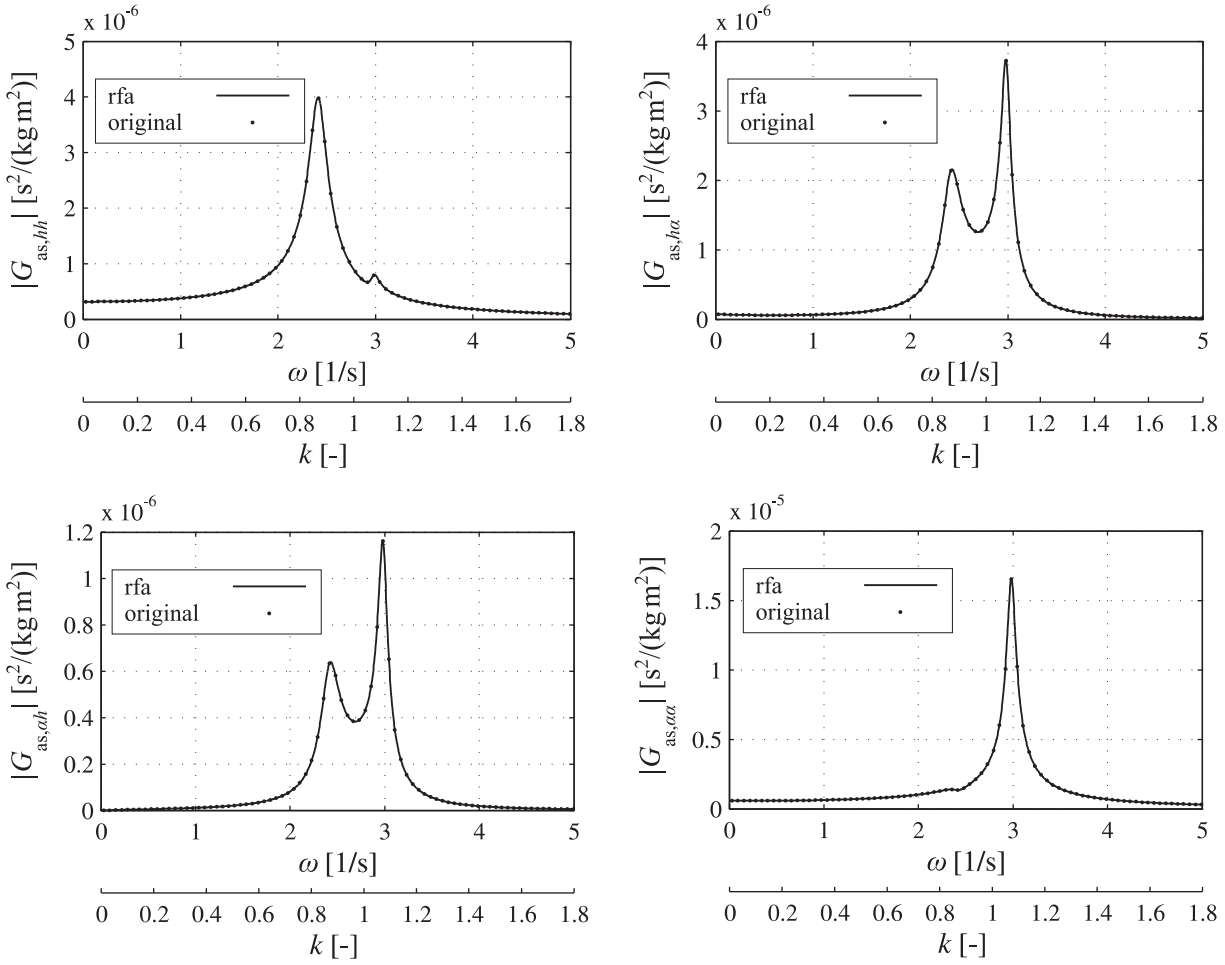

Figure 4.18: Transfer function $\mathbf{G}_{\text{as}}$ of the aeroelastic system with the theoretical flat-plate derivatives along the imaginary frequency axis for $U = 25$ m/s.

$G_{\text{as},h\alpha}(s)$ is displayed in Figure 4.17(b). Compared to the neighbouring figure, the transfer function based on original derivatives does not have the poles along the negative real axis, but it is not defined for non-positive real frequencies. Since the transfer function of the motion-induced aerodynamic forces has a removable singularity at the origin, as can be seen when considering Eq. (2.20) and the explanations of Section 2.2.1, the aeroelastic frequency response $\mathbf{G}_{\text{as}}(\mathrm{i}\omega)$ can again be analysed instead of the aeroelastic transfer function. In all curves of Figure 4.18 and Figure 4.19, the results based on original derivatives are added as small dots. All these values almost exactly lie on the curves that are based on the rational function approximation of the derivatives. The real eigenvalues that are located furthest to the right in the frequency plane for low values of U, which are mentioned in the foregoing section, do not worsen the approximation of the frequency response around the origin, as can be seen in Figure 4.18. Again, the special suitability of the chosen rational functions for approximating the flat-plate derivatives is demonstrated.

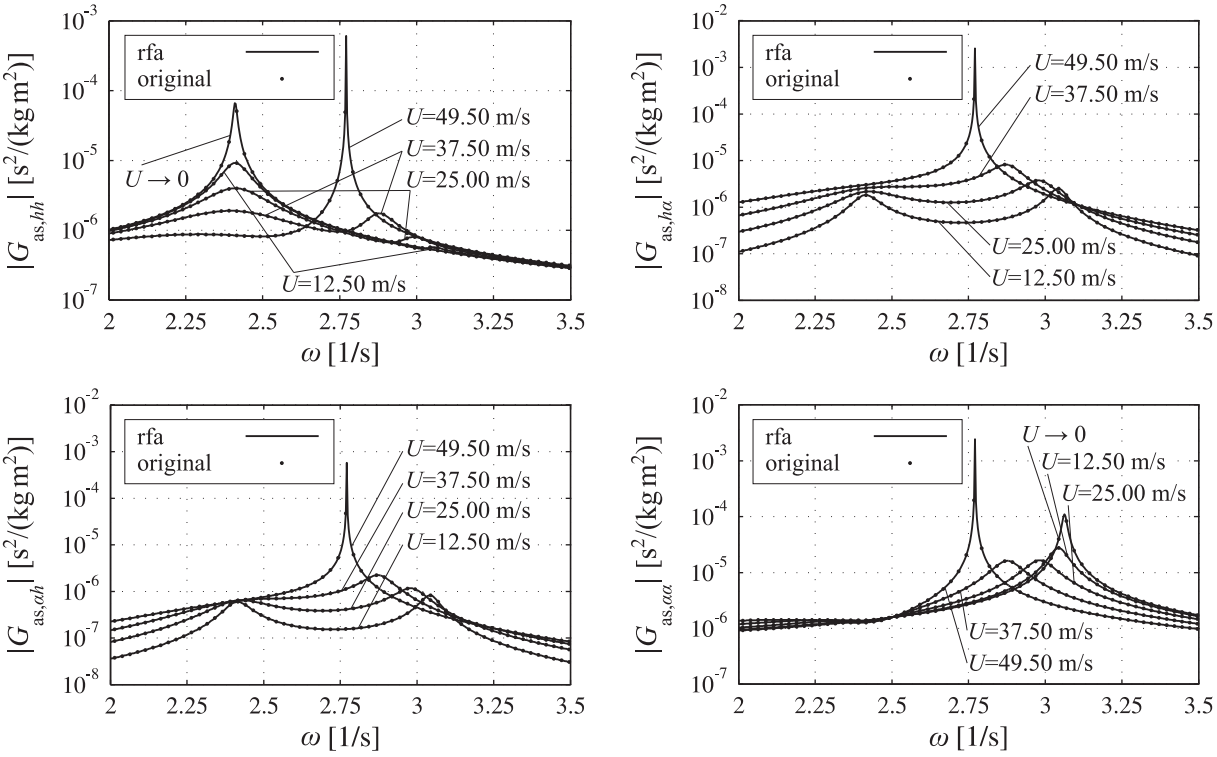

Figure 4.19: Transfer function $\mathbf{G}_{\text{as}}$ of the aeroelastic system with the theoretical flat-plate derivatives along the imaginary frequency axis for several values of the reference wind velocity U.

The stochastic response of the aeroelastic system to the fluctuating gust velocity in the natural wind field can be analysed based on Eq. (4.60) for different values of the reference wind velocity U. Since the investigated aeroelastic system is linear, the solution can be found with the transfer of the statistical parameters in the frequency domain. The equation that transfers the spectral density function of the gusts speeds to that of the displacements reads as

$$\mathbf{S}_{\mathbf{y}_{\text{st}}}(\omega) = \mathbf{G}^{\text{c}}_{\text{asg}}(\text{i}\omega)\, \mathbf{S}_{\mathbf{a}^{\text{g}}}(\omega)\, \mathbf{G}^{\text{T}}_{\text{asg}}(\text{i}\omega) \quad , \tag{4.90}$$

where

$$\mathbf{G}_{\text{asg}}(s) = \mathbf{C}_{\text{asg}}(s\mathbf{I} - \mathbf{A}_{\text{asg}})^{-1}\mathbf{E}_{\text{asg}} \quad , \tag{4.91}$$

with the matrices of Eq. (4.61). According to the displacement definition in Eq. (2.19a), the spectral density matrix of the output $\mathbf{y}_{\text{st}}$ has the following entries.

$$\mathbf{S}_{\mathbf{y}_{\text{st}}}(\omega) = \begin{pmatrix} S_{hh}(\omega) & S_{h\alpha}(\omega) \\ S_{\alpha h}(\omega) & S_{\alpha\alpha}(\omega) \end{pmatrix} \tag{4.92}$$

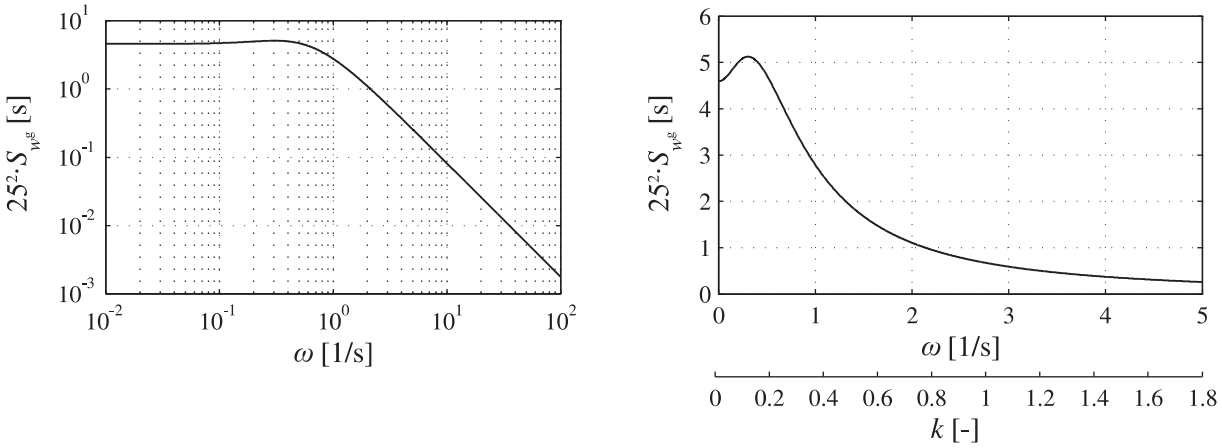

(a) Logarithmic scaling. (b) Linear scaling.

Figure 4.20: Spectral density function $S_{w^g}(\omega)$ of the vertical gust velocity at a constant horizontal reference wind velocity $U = 25$ m/s.

The submatrices in the spectral density matrix of the input $\mathbf{a}^g$ are determined with the help of Eq. (1.14).

$$\mathbf{S}_{\mathbf{a}^g}(\omega) = \begin{pmatrix} \mathbf{S}_{\dot{\boldsymbol{\alpha}}^g \dot{\boldsymbol{\alpha}}^g}(\omega) & \mathbf{S}_{\dot{\boldsymbol{\alpha}}^g \boldsymbol{\alpha}^g}(\omega) \\ \mathbf{S}_{\boldsymbol{\alpha}^g \dot{\boldsymbol{\alpha}}^g}(\omega) & \mathbf{S}_{\boldsymbol{\alpha}^g \boldsymbol{\alpha}^g}(\omega) \end{pmatrix} = \begin{pmatrix} \omega^2 & -\mathrm{i}\omega \\ \mathrm{i}\omega & 1 \end{pmatrix} S_{w^g}(\omega) \tag{4.93}$$

Due to the definition in Eq. (2.19b), all submatrices depend on the auto-spectral density function $S_{w^g}(\omega)$. To account for the decreasing correlation of the gusts along the girder length, the spectral density matrix of the input must, moreover, be multiplied by the joint acceptance function J_{m}^2, as derived in Section 4.4.

For the auto-spectral density function $S_{w^g}(\omega)$ of the vertical gust component w^g/U, the two-sided von Kármán spectrum is chosen.

$$S_{w^g} = \pi \frac{\sigma_{w^g}^2}{|\omega|} 4 \left(\frac{L_{wx}|\omega|}{2\pi U} \right) \left(1 + 755.2 \left(\frac{L_{wx}|\omega|}{2\pi U} \right)^2 \right) \left(1 + 283.2 \left(\frac{L_{wx}|\omega|}{2\pi U} \right)^2 \right)^{-\frac{11}{6}} \tag{4.94}$$

It appears to be sufficient for the objectives of this work to define the standard deviation σ_{w^g} and the integral length scale L_{wx} of the vertical gusts with respect to a constant turbulence intensity and a constant integral time scale, respectively. The following numerical values are selected.

$$\sigma_{w^g} = 0.07\,, \quad L_{wx} = 0.75 \text{ s } U \tag{4.95}$$

Figure 4.20 shows the auto-spectral density function against positive values of ω for $U = 25$ m/s with differently scaled axes. The variance $\sigma_{w^g}^2$ of the input w^g/U equals the integral of the spectral density function over all frequencies $\omega/(2\pi)$. It is a measure of the power of the wind

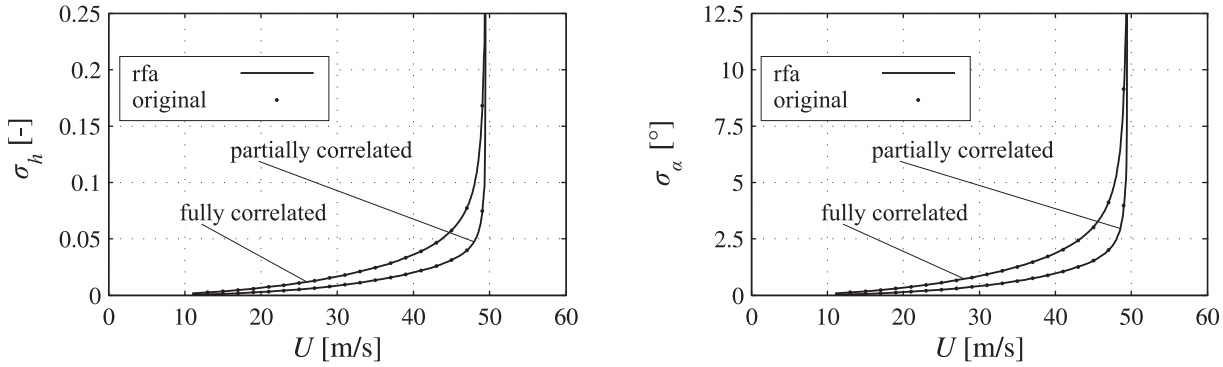

Figure 4.21: Standard deviations of the displacements of the aeroelastic system under the influence of vertical gusts.

fluctuations. For the assumed spectral density function and integral length scale, 96.2 % of the theoretical power is incorporated in the interval $|\omega| < 2\pi \cdot 10.0\ 1/\mathrm{s}$, independent of the reference wind velocity.

The integral of a spectral density matrix over all frequencies equals the covariance matrix. Hence, the covariance matrix of the stochastic aeroelastic system output can be calculated from the results of Eq. (4.90). The standard deviations of the output elements follow as square roots of the diagonal elements of the covariance matrix. To numerically solve the integral by summing up the areas of rectangles, the frequency spacing is set to $\Delta\omega = 2\pi \cdot 5 \cdot 10^{-4}\ 1/\mathrm{s}$, which seems to be sufficient to adequately cover the resonance peaks in the aeroelastic transfer function. The integration is carried out in the mentioned interval $|\omega| < 2\pi \cdot 10\ 1/\mathrm{s}$. Due to the filter effect of the aeroelastic transfer, most of the output power is assumed to be captured, much more than the captured percentage of the wind-field power.

Figure 4.21 displays the standard deviations σ_h and σ_α of the output vector elements h/b and α, respectively, against the reference wind speed U. The results are carried out for both fully and partially correlated gusts. For the latter case, the joint acceptance function is used that is derived at the end of Section 4.4. The decay parameter is assumed to be $C_{\mathrm{coh}} = 8$. For the admittance of gust-induced aerodynamic forces, the approximation of the consistent Sears function with $n_\gamma = 5$ poles is employed that is given in the third block of Table 3.3. The elements of the state-space model of the gust-induced aerodynamic forces are chosen according to Eq. (3.19) because the length of the input vector is shorter than that of the output vector. As to be expected, the magnitudes of the stochastic output drastically increase when the value of the reference wind velocity approaches the flutter wind speed. Taking the decaying correlation of the gusts along the girder into account roughly halves the calculated response of the aeroelastic system for the chosen numerical example.

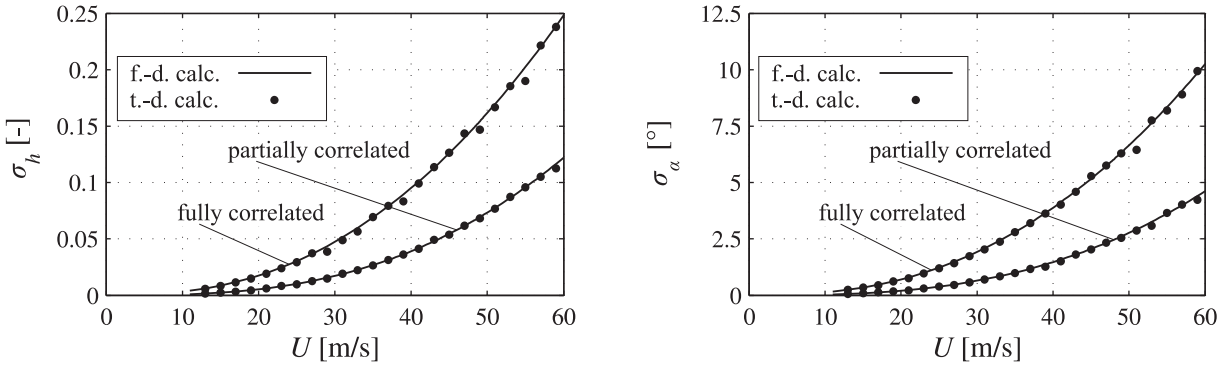

Figure 4.22: Standard deviations of the displacements of the structural system under the influence of vertical gusts (f.- / t.-d. calc.: frequency- / time-domain calculation).

The standard deviations can alternatively be determined with the original admittances of both the motion-induced and the gust-induced aerodynamic forces of the theoretically described flow around the flat plate if the transfer function $\tilde{\mathbf{G}}_{\mathrm{asg}}$ given in Eq. (4.70) is employed.

$$\mathbf{S}_{\mathbf{y}_{\mathrm{st}}}(\omega) = \tilde{\mathbf{G}}^{\mathrm{c}}_{\mathrm{asg}}(\mathrm{i}\omega)\, \mathbf{S}_{\boldsymbol{\alpha}^{\mathrm{g}}}(\omega)\, \tilde{\mathbf{G}}^{\mathrm{T}}_{\mathrm{asg}}(\mathrm{i}\omega) \tag{4.96}$$

Here, the spectral density matrix of the input $\boldsymbol{\alpha}^{\mathrm{g}}$ only has one element

$$\mathbf{S}_{\boldsymbol{\alpha}^{\mathrm{g}}}(\omega) = S_{w^{\mathrm{g}}}(\omega) \tag{4.97}$$

according to the definition given in Eq. (2.19b). Again, the results that are based on original admittances are added as small dots in Figure 4.21. After examining the transfer functions in the foregoing paragraphs and remembering the good suitability of the chosen rational function for approximating the consistent Sears function, it is not astonishing that all these dots almost exactly lie on the approximation-based curves.

To demonstrate the influence of the motion-induced aerodynamic forces on the calculated standard deviations, these forces can be cancelled from the state-space model in Eq. (4.60) by replacing the matrices and vectors of Eq. (4.55) with those of Eq. (4.53), that means simply changing the index from $(\ )_{\mathrm{as}}$ to $(\ )_{\mathrm{st}}$. Accordingly, the transfer of the statistical properties given in Eq. (4.90) must be modified. Repeating the calculations for the modified model leads to the curves displayed in Figure 4.22. Although the structural system does not become unstable, the standard deviations of this model are distinctly higher than those of the aeroelastic model until the flutter wind speed is almost reached. Hence, if the reference wind speed is not in the direct vicinity of the critical wind speed, the motion-induced aerodynamic forces have a strong damping effect on the structure.

For the sake of completeness, it should be described how the shown results can be verified with those of an alternative time-domain calculation based on the state-space model in Eq. (4.60).

The sample record $w^{\mathrm{g}}(t)$ of the gust speed at a single bridge girder point can be generated as a stochastic process with an inverse discrete Fourier transform of the square root of the auto-spectral density function. The latter must be discretised at uniformly spaced frequencies within a limited bandwidth. Due to the finite frequency spacing, the limit $S_{w^{\mathrm{g}}}(\omega = 0)$ must be set to zero to obtain a zero-mean time-domain signal. The missing phase information is added by a random signal with values in the interval $[0; 2\pi)$. To avoid preferring individual phase intervals, a constant shape of the underlying probability distribution is chosen. The inverse transform leads to a zero-mean discrete-time signal with a Gaussian probability density function due to the central limit theorem. The time axis is uniformly spaced and the signal values jump so strongly that a linear interpolation would lead to sharp kinks. In general, a smooth interpolation to get signal values at a higher number of time points is necessary for both the time-domain simulation of the model response and the generation of the differentiated signal $\dot{w}^{\mathrm{g}}(t)$ that is needed for the input vector $\mathbf{a}^{\mathrm{g}}$. Interpolation and differentiation in the time domain is equivalent to padding the discrete Fourier transform of the generated signal with zeros and multiplying the Fourier transform with $(\mathrm{i}\omega)$, respectively. When carrying out both operations in the frequency domain, the desired exact spectral density function of the signal is guaranteed. Having generated the input signal, the system response can be numerically calculated with respect to the continuous-time state-space model. A very fast and precise solution method for a linear system is to convert the continuous-time to a discrete-time state-space model, which can be directly solved. For this purpose, the function `lsim` of MATLAB (2007) is used. The standard deviation of the discrete time response can be determined with the usual unbiased estimator.

Figure 4.22 additionally shows the results gained with such a time-domain simulation. For calculating the statistical parameters, the first seconds are not considered, to avoid including a relevant transient response. In the numerical example, the frequency spacing of the wind spectrum is set to $\Delta\omega = 2\pi \cdot 5 \cdot 10^{-4}\ 1/\mathrm{s}$, and $\omega = 2\pi \cdot 10\ 1/\mathrm{s}$ is chosen as the Nyquist frequency corresponding to the values of the frequency-domain calculation. The resulting duration $t = 2000\ \mathrm{s}$ of the stationary wind event is not unrealistic because the wind-speed fluctuations within such a time period are usually caused by the modelled turbulence of the neutral atmospheric boundary layer (Van der Hoven 1957). For the interpolation, the spacing of the time axis is reduced with the factor $1/10$. Hence, the signal part with the Nyquist frequency is sufficiently sampled. Frequency- and time-domain results are in a good agreement.

As carried out for the eigenvalues in the last section, the TaS cross-section derivatives are employed to describe the problems that can occur when the aeroelastic transfer of the two-dimensional bridge model with a cross section in real flow is modelled. The investigations are carried out with the same rational function approximations that are used for the eigenvalues displayed in Figure 4.14 and Figure 4.15. With respect to the eigenvalues in these figures, it only makes sense to consider the small intervals of the reference wind speed inside which the

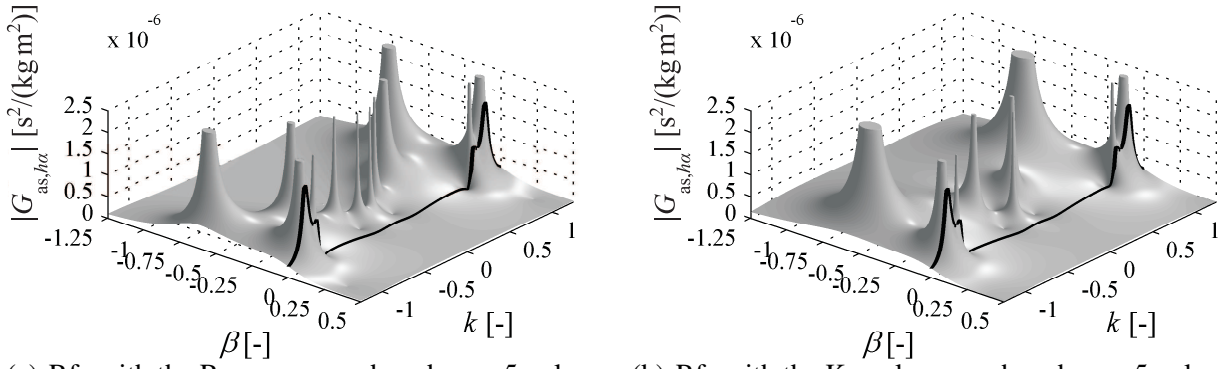

(a) Rfa with the Roger approach and $n_\gamma = 5$ poles according to Eq. (3.34a).

(b) Rfa with the Karpel approach and $n_\gamma = 5$ poles as addressed in Table 3.6.

Figure 4.23: Transfer-function element $G_{\text{as},h\alpha}$ of the aeroelastic system with the TaS derivatives above the complex frequency plane for $U = 25$ m/s.

system is stable. The reference wind speed $U = 25$ m/s is again taken for this purpose because it is located approximately in the middle of this interval.

Figure 4.23 shows the aeroelastic transfer function element $G_{\text{as},h\alpha}$ for the Roger and the Karpel approximation approach above the reduced complex frequency plane. Corresponding to the eigenvalues in Figure 4.14(d) and Figure 4.15(b), the rational function approximations cause poles not only near the negative real axis. The investigation of the transfer function of the stable system can again be limited to the frequency response given in Figure 4.24. In addition to the curves that base on the derivative approximation, the discrete values are given that follow from the measured derivatives. Due to the aerodynamic coupling of the translational and rotational degrees of freedom, two distinct resonance peaks appear in each transfer element. Within the grey-shaded approximation interval, both approximations lead to very similar values. Unfortunately, the aeroelastic transfer function has non-negligible values outside the identification interval. As mentioned in Section 3.6, the intervals in Table 2.1 are set to capture the frequencies that are connected with the flutter wind speeds. Inside the interval, the approximation of the minor diagonal elements is poor, especially at the resonance peaks. The gust-induced aerodynamic forces for frequencies outside the identification interval are not fully negligible. This can be seen with the help of Figure 4.20(b) and assuming that the gust admittance is somewhat comparable to that of the flat plate which is based on the consistent Sears function as given in Figure 2.2. Hence, to sufficiently ensure a measured basis for the aeroelastic admittance, a larger approximation interval is desirable for the derivatives. A larger approximation interval, however, increases the problem of an approximation with highly weighted derivatives.

In a three-dimensional model of the bridge, vibrations of higher modes are also excited as long as the wind field contains enough power at the relevant frequencies. Close to the first flutter wind speed, the response of the spatial model is dominated for the investigated bridge by the

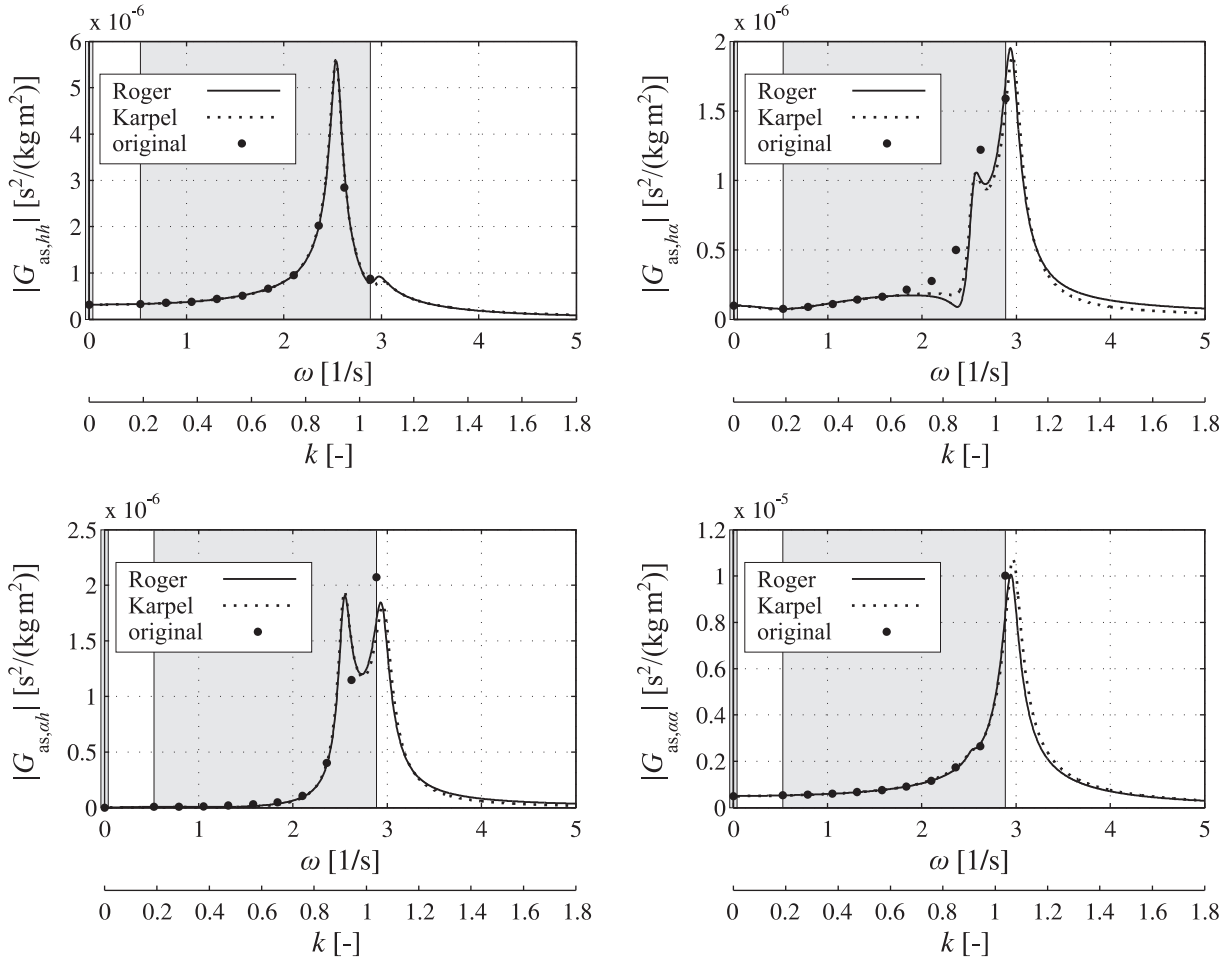

Figure 4.24: Transfer function $\mathbf{G}_{\text{as}}$ of the aeroelastic system with the TaS derivatives along the imaginary frequency axis for $U = 25$ m/s.

first two structural modes which mainly determine the flutter mode. For those wind speeds, the displacements of the two-dimensional model represent a large part of the total displacements.

As shown, different kinds of problems can occur when rational functions with negative real poles are applied for the approximation of aerodynamic admittances of cross sections in real flow. These problems normally remain veiled if only some simple investigations are made in the time domain. To facilitate the investigations in the following chapter, the aeroelastic system is only modelled with the theoretical admittances of the flat plate. At least for streamlined bridge cross sections, the aerodynamic admittances show similar values. Misinterpreted numerical artefacts can be avoided in this way. For admittances of cross sections in real flow, the results in the following chapter must be adapted.

5 Bridge Characteristics under the Influence of Controlled Actuators

5.1 Employed Actuators

In order to change the described dynamic characteristics of the bridge, one or more of the terms that occur in Eq. (4.52) must be altered. A modification of the basic structural bridge design that leads to other structural forces in the left part of the equation is excluded in the following investigations. Adding fixed supports or modifying the mass properties, the stiffness, and the structural damping of the bridge is, thus, not considered. Various possibilities of streamlining the shape of the girder cross section in order to favourably change the motion-induced and gust-induced aerodynamic forces on the right side of Eq. (4.52) have been analysed since the 1950s, which are also excluded. The focus is rather on controlled actuators that generate additional time-varying forces which act on the bridge girder. To be effective, these forces should preferably act at points along the girder length where they can create large energetically corresponding displacements within a beneficial deflection shape. Three different types of actuators are introduced in this section. Actuators that connect the bridge girder to the ground are not considered because they are expected to undermine the basic structural design of the bridge. Elements like hydraulic rams that can induce relative displacements between the ends of neighbouring structural components of the bridge (e. g. Yang & Giannopolous 1979) are not investigated either. Apart from the subsequently described actuating elements, no further actuator or sensor dynamics are accounted for in the system model. Other elements are assumed to be fast compared to the modelled components of the actuator-equipped bridge.

A reaction wheel, which is mounted to the bridge girder, is the actuator type investigated first. When the wheel rotation is accelerated with a torque between the wheel and the bridge girder, the magnitude of its angular momentum is changed. Simultaneously, a torque acts as a reaction on the bridge. The reaction wheel is rotated around its centre of gravity. In contrast to a free mass that is moved in the vertical direction, for instance, no mechanical work due to gravity must be done that is impossible to be regained without dissipation. Reaction wheels have been used for the attitude control of satellites and space vehicles for a long time (Horri & al. 2010).

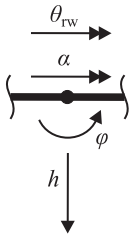

Figure 5.1: Degree of freedom θ_{rw} of a reaction wheel in addition to those of the girder at one node.

The application of reaction wheels for increasing the flutter wind speed of bridges is proposed in Miyata & al. (1994). Experimental investigations of this idea conducted in a wind tunnel are described in Körlin & Starossek (2007).

The semidiscrete equation of motion of the finite-element model of the bridge can be easily adjusted to include a model of the reaction wheels. In the following, the procedure is explained for a reaction wheel that is positioned at one node of the girder. Figure 5.1 shows that node with the global girder degrees of freedom of the girder. Moreover, the angle θ_{rw}, which is defined relative to the bridge deck, symbolises the wheel rotation around the torsional axis of the girder. The centre of gravity of the reaction wheel is identical to that of the bridge girder. This simplification is necessary to further avoid the modelling of the horizontal girder displacement. The wheel of the mass m_{rw} is assumed to be a solid of revolution with respect to the axis of the wheel rotation θ_{rw}. It has an oblate shape, so that the principal moment of inertia $I_{\mathrm{rw,h}}$ around the symmetry axis is higher than the two others, which have equal values $I_{\mathrm{rw,l}}$. To reduce the number of parameters, the masses of bearings, linkages, and similar actuator components are not modelled, although they can have a significant total value. A vector ξ_{c} of the actuator degrees of freedom is introduced in addition to the structural degrees of freedom ξ_{s} of the bridge.

$$\begin{pmatrix} \xi_{\mathrm{s}} \\ \xi_{\mathrm{c}} \end{pmatrix}, \quad \xi_{\mathrm{s}} = \begin{pmatrix} h & \varphi & \alpha \end{pmatrix}^{\mathrm{T}}, \quad \xi_{\mathrm{c}} = \begin{pmatrix} \theta_{\mathrm{rw}} \end{pmatrix} \tag{5.1}$$

To account for the reaction wheel, the assembled global matrices and vectors of the bridge model must be expanded with zeros in accordance with the dimension of the augmented vector in Eq. (5.1). Additionally, the mass matrix

$$\mathbf{M}_{\mathrm{c}} = \begin{pmatrix} m_{\mathrm{rw}} & 0 & 0 & 0 \\ 0 & I_{\mathrm{rw,l}} & 0 & 0 \\ 0 & 0 & I_{\mathrm{rw,h}} & I_{\mathrm{rw,h}} \\ 0 & 0 & I_{\mathrm{rw,h}} & I_{\mathrm{rw,h}} \end{pmatrix} \tag{5.2}$$

and the force vector

$$\begin{pmatrix} \mathbf{0} \\ \mathbf{f}_c \end{pmatrix}, \quad \mathbf{f}_c = \begin{pmatrix} M_{rw} \end{pmatrix} \tag{5.3}$$

are added. There is only an inertia coupling between the rotation of the actuator and the torsion of the bridge. The moment M_{rw}, which is the input force of the actuator, acts between the bridge and the reaction wheel. Gyroscopic effects due to a simultaneous rotation of the wheel with the bending angle φ of the bridge girder are not taken into account. The entries in Eq. (5.2) and Eq. (5.3) become comprehensible when the equations of motion are considered that are derived in Appendix A.2.

The second actuator type is a control moment gyroscope, which is attached to the bridge girder. It consists of a spinning rotor that is mounted in a gimbal. When tilting the spin axis of the rotor around the gimbal axis, a torque perpendicular to both the spin and the gimbal axis is generated as a reaction on the bridge due to the changing direction of the angular momentum. Depending on the tilting rate and the angular momentum of the spinning rotor, large moments can be created. If the centre of gravity lies on the gimbal axis, again, no work due to gravity must be done. Control moment gyroscopes are effective mechanical devices not only for the attitude control of satellites (e. g. Jacot & Liska 1966, Horri & al. 2010). They have also been used since the beginning of the last century to counteract the rolling of ships (e. g. Ferry 1932). In Yamada & al. (1997) and Higashiyama & al. (1998), the application of gyroscopes to attenuate the amplitudes of wind-induced vibrations of tower-like structures is presented. The idea of stabilising an aerofoil with control moment gyroscopes is described in Buchek (1974). Some publications are available dealing with theoretical and experimental investigations of increasing the flutter wind speed of bridges by means of these devices (Murata & Ito 1971, Fujisawa 1995, Okada & al. 2001, Okada & al. 2003).

Adjusting the equation of motion of the finite-element bridge model is again explained for an actuator that is positioned at one node of the girder, as displayed in Figure 5.2. Here, a twin control moment gyroscope is employed. For an application in naval engineering, for instance, this special device is commercially available (e. g. www.shipdynamics.com). A twin type features the possibility of creating resulting torques around a fixed axis. For this purpose, two identical rotors that spin in opposite directions with the same constant spin speed Ω_{gy} are simultaneously tilted around equal but opposite gimbal angles θ_{gy}. The gimbal angles are again defined relative to the bridge deck. Other orientations of the gimbal and the spin axis are also possible to generate a torque around the torsional axis of the girder than those shown in Figure 5.2. Again, the centre of gravity of the gyroscope is assumed to be identical to that of the bridge girder, for the same reason that is explained for the reaction wheel. To further simplify the analysis, only the masses

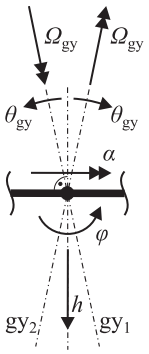

Figure 5.2: Degree of freedom θ_{gy} of a double control moment gyroscope in addition to those of the girder at one node. The gimbal axes of both gyroscopes gy_1 and gy_2 are perpendicular to the drawing plane.

of the rotors are taken into account. Concerning the shape and the inertia properties of the rotors, the assumptions that are made for the reaction wheel still hold true. After defining

$$\boldsymbol{\xi}_c = \begin{pmatrix} \theta_{gy} \end{pmatrix} \quad , \tag{5.4}$$

the matrices

$$\mathbf{M}_c = \begin{pmatrix} m_{gy} & 0 & 0 & 0 \\ 0 & I_{gy,l} & 0 & 0 \\ 0 & 0 & I_{gy,l} & 0 \\ 0 & 0 & 0 & I_{gy,l} \end{pmatrix} , \quad \mathbf{C}_c = \begin{pmatrix} 0 & 0 & 0 & 0 \\ 0 & 0 & 0 & 0 \\ 0 & 0 & 0 & I_{gy,h}\Omega_{gy} \\ 0 & 0 & -I_{gy,h}\Omega_{gy} & 0 \end{pmatrix} \tag{5.5}$$

and the vector

$$\begin{pmatrix} \mathbf{0} \\ \mathbf{f}_c \end{pmatrix} , \quad \mathbf{f}_c = \begin{pmatrix} M_{gy} \end{pmatrix} \tag{5.6}$$

are added to those of the bridge model, as already explained for the reaction wheel in Eq. (5.2) and Eq. (5.3). The inertia values m_{gy}, $I_{gy,l}$, $I_{gy,h}$ are twice those of one rotor. For the derivation of the entries with principles of mechanics, a sufficiently high angular momentum $I_{gy,h}\Omega_{gy}$ of the rotor and small gimbal angles θ_{gy} are assumed. Linearisations are made as they are usual for gyroscope models in technical applications (Magnus 1971). To model the gyroscope, the gyroscopic matrix $\mathbf{C}_c$ is introduced. There is only a gyroscopic coupling between the degree of freedom of the actuator and the torsion of the bridge. Contrary to the symmetric structural damping matrix, the gyroscopic matrix has no dissipative effect on the structure due to its antimetric form. The reason is that the gyroscopic forces, whose magnitudes are those of the entries in $\mathbf{C}_c(\ \dot{\boldsymbol{\xi}}_s^T \quad \dot{\boldsymbol{\xi}}_c^T\ )^T$, act perpendicular to their initiating rotations. Energy is rather directly added to, or subtracted from, the dynamic system with the actuator input force $\mathbf{f}_c$ and the corresponding displacements. That

holds for both actuators described so far. The actuator input variable M_{gy} signifies the resulting input torque that acts between the kinematically coupled gimbals and the bridge girder around an axis perpendicular to the drawing plane in Figure 5.2. This torque energetically corresponds to the tilting angle θ_{gy}. For the special kinematic coupling of the gimbals, the input torque $M_{\mathrm{gy}}/2$ can alternatively act between both gimbals energetically corresponding to the angle $2\theta_{\mathrm{gy}}$. As can be seen in the fourth rows of $\mathbf{M}_{\mathrm{c}}$ and $\mathbf{C}_{\mathrm{c}}$, the torque M_{gy} is necessary to accelerate the rotors around the gimbals and to modify the effect of the gyroscopic forces. The latter kind of gyroscopic forces occurs as soon as the bridge rotates with $\dot{\alpha}$ around its longitudinal axis. Again, the entries in Eq. (5.5) and Eq. (5.6) become understandable when the equations of motion in Appendix A.2 are considered.

One disadvantage of reaction wheels and gyroscopes is that they need a certain minimum mass to generate a sufficient torque on the girder. Hence, those actuators increase the self-weight of the bridge with all negative consequences. By contrast, aerodynamically effective, movable control surfaces, or alternatively called control shields, the third actuator type, do not need inertia properties. The additional forces are generated by the air flow. Assuming a proper design of the girder-shield configuration, it can be expected that considerably lower forces and less power is necessary for the shield motion than for the motions of the other two actuators.

Aerodynamically effective, movable control surfaces have been used for many years to suppress the influences of disturbances on aircraft wings (e. g. Edwards 1977, Chambers 2005). Depending on their purpose, different terms like flap, slat, or aileron are used in aerospace engineering. For simplicity's sake, only the word flap is used here for a control surface which is directly attached to the side of a rigid girder cross section. The application of control surfaces to bridge decks is proposed for instance in Klein & al. (1972). First investigations are presented in Kobayashi & Nagaoka (1992) and Ostenfeld & Larsen (1992). In aerospace engineering, the primary task of a wing is to produce a lift force. Flaps as integrated parts of the aerofoil modify its surface in order to evoke positive effects without increasing the disturbing impact of gusts. With respect to bridges, however, control surfaces are extra components that augment the area exposed to the wind. They cannot bear any significant live load and can hence not directly fulfil the inherent task of a bridge. In addition to motion-induced aerodynamic forces, new gust-induced ones usually arise simultaneously, which also need to be suppressed. Therefore, aerodynamically effective control surfaces are generally less effective for bridges than for aircraft wings. Moreover, control surfaces need a minimum wind speed to work. They are not suited for damping oscillations in still air. This shortcoming is similar to that of fin stabilisers, also called hydrofoils, which are used to counteract the rolling of ships (Den Hartog 1985). For aircraft wings, this disadvantage does not exist either.

A number of investigations of bridge-like systems with control surfaces are available in addition to the papers mentioned in the last paragraph (e. g. Kobayashi & Nita 1996, Ostenfeld & Larsen

1997, Preidikman & Mook 1997, Hansen 1998, Kobayashi & al. 1998, Preidikman & Mook 1998, Wilde & Fujino 1998, Cobo del Arco & Aparicio 1999, Piésold & Corney 1999, Wilde & al. 1999, Hansen & al. 2000, Huynh 2000, Kwon & Chang 2000, Omenzetter & al. 2000a, Omenzetter & al. 2000b, Hansen & Thoft-Christensen 2001, Huynh & Thoft-Christensen 2001, Wilde & al. 2001, Omenzetter & al. 2002a, Omenzetter & al. 2002b, Larsen & Walther 2003, Nissen & al. 2004, Starossek & Aslan 2007, Aslan & Starossek 2008, Phan & Kobayashi 2011, Graham & al. 2011, Limebeer & al. 2011). As introduced in Section 2.2.3, the focus of the work presented here is on finding new insights into bridge models with a girder cross section that is equipped with aerodynamically balanced flaps on both sides. In contrast to control surfaces that are located far away from the bridge girder, adjacent flaps can modify the flow around the girder effectively and favourably.

To account for the flaps in the finite-element model of the bridge, the element described in Section 4.1 can be extended. Nodal rotations of the flaps are defined in addition to those of Eq. (4.1).

$$\mathbf{v}^{\mathrm{e}} = \begin{pmatrix} \mathbf{v}^{\mathrm{e}}_{h} \\ \mathbf{v}^{\mathrm{e}}_{\alpha} \\ \mathbf{v}^{\mathrm{e}}_{\theta_{\mathrm{fl,win}}} \\ \mathbf{v}^{\mathrm{e}}_{\theta_{\mathrm{fl,lee}}} \end{pmatrix}, \quad \mathbf{v}^{\mathrm{e}}_{\theta_{\mathrm{fl,win}}} = \begin{pmatrix} \theta_{\mathrm{fl,win,le}} \\ \theta_{\mathrm{fl,win,mi}} \\ \theta_{\mathrm{fl,win,ri}} \end{pmatrix}, \quad \mathbf{v}^{\mathrm{e}}_{\theta_{\mathrm{fl,lee}}} = \begin{pmatrix} \theta_{\mathrm{fl,lee,le}} \\ \theta_{\mathrm{fl,lee,mi}} \\ \theta_{\mathrm{fl,lee,ri}} \end{pmatrix} \tag{5.7}$$

Figure 5.3 illustrates the nodal degrees of freedom of the flaps. The vector $\mathbf{s}^{\mathrm{e}}$ in Eq. (4.2) is extended with energetically corresponding nodal forces.

$$\mathbf{s}^{\mathrm{e}} = \begin{pmatrix} \mathbf{s}^{\mathrm{e}}_{h} \\ \mathbf{s}^{\mathrm{e}}_{\alpha} \\ \mathbf{s}^{\mathrm{e}}_{\theta_{\mathrm{fl,win}}} \\ \mathbf{s}^{\mathrm{e}}_{\theta_{\mathrm{fl,lee}}} \end{pmatrix} \tag{5.8}$$

To approximate the continuous flap torsions $\theta_{\mathrm{fl,win}}$ and $\theta_{\mathrm{fl,lee}}$, new entries are also incorporated in the vectors and matrices of Eq. (4.3).

$$\mathbf{u}^{\mathrm{e}} = \begin{pmatrix} h \\ \alpha \\ \theta_{\mathrm{fl,win}} \\ \theta_{\mathrm{fl,lee}} \end{pmatrix}, \quad \mathbf{\Omega}^{\mathrm{e}} = \begin{pmatrix} \mathbf{\Omega}^{\mathrm{e}}_{h} & \mathbf{0} & \mathbf{0} & \mathbf{0} \\ \mathbf{0} & \mathbf{\Omega}^{\mathrm{e}}_{\alpha} & \mathbf{0} & \mathbf{0} \\ \mathbf{0} & \mathbf{0} & \mathbf{\Omega}^{\mathrm{e}}_{\alpha} & \mathbf{0} \\ \mathbf{0} & \mathbf{0} & \mathbf{0} & \mathbf{\Omega}^{\mathrm{e}}_{\alpha} \end{pmatrix} \tag{5.9}$$

Using the same approximation functions for the girder torsion and the torsion of a flap facilitates the following derivation of the element matrices $\mathbf{M}^{\mathrm{e}}$ and $\mathbf{Q}^{\mathrm{e}}$.

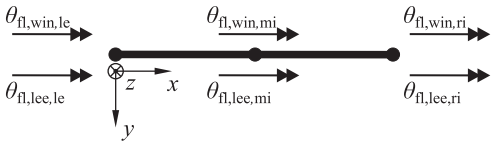

Figure 5.3: Element nodal displacements of the flaps in addition to those of the girder shown in Fig. 4.1.

According to the expansion of the vector $\mathbf{u}^{\mathrm{e}}$, the continuous stiffness matrix $\mathbf{E}^{\mathrm{e,c}}$ and the continuous mass matrix $\mathbf{M}^{\mathrm{e,c}}$ of the girder are enlarged. The flaps are modelled without a torsional stiffness. Hence, $\mathbf{E}^{\mathrm{e,c}}$ gets only new zero elements. However, when a flap mass is accounted for, the matrix $\mathbf{M}_{\mathrm{c}}^{\mathrm{e,c}}$ must be employed in addition to the continuous mass matrix $\mathbf{M}^{\mathrm{e,c}}$.

$$\mathbf{M}_{\mathrm{c}}^{\mathrm{e,c}} = \begin{pmatrix} m_{\mathrm{fl}} & 0 & \frac{m_{\mathrm{fl}}}{2} d_{\mathrm{h,win}} & \frac{m_{\mathrm{fl}}}{2} d_{\mathrm{h,lee}} \\ & I_{\mathrm{fl}} + m_{\mathrm{fl}}(b+b_{\mathrm{fl}})^2 & \frac{I_{\mathrm{fl}}}{2} - \frac{m_{\mathrm{fl}}}{2}(b+b_{\mathrm{fl}}) d_{\mathrm{h,win}} & \frac{I_{\mathrm{fl}}}{2} + \frac{m_{\mathrm{fl}}}{2}(b+b_{\mathrm{fl}}) d_{\mathrm{h,lee}} \\ & & \frac{I_{\mathrm{fl}}}{2} + \frac{m_{\mathrm{fl}}}{2} d_{\mathrm{h,win}}^2 & 0 \\ \text{symm.} & & & \frac{I_{\mathrm{fl}}}{2} + \frac{m_{\mathrm{fl}}}{2} d_{\mathrm{h,lee}}^2 \end{pmatrix} \tag{5.10}$$

The mass centre of a flap is assumed to be in its middle. One flap has the mass $m_{\mathrm{fl}}/2$ and the moment of inertia $I_{\mathrm{fl}}/2$ with respect to its centre of gravity. The entries in $\mathbf{M}_{\mathrm{c}}^{\mathrm{e,c}}$ can be derived from the equations of motion of the problem in Appendix A.2. Whereas the element stiffness matrix $\mathbf{K}^{\mathrm{e}}$ consequently gets new zero entries only, the element mass matrix $\mathbf{M}^{\mathrm{e}}$ has to be modified and enlarged with non-zero elements. Hence, the matrix

$$\mathbf{M}_{\mathrm{c}}^{\mathrm{e}} = \int_0^{l_{\mathrm{e}}} \mathbf{\Omega}^{\mathrm{e}\mathrm{T}} \mathbf{M}_{\mathrm{c}}^{\mathrm{e,c}} \mathbf{\Omega}^{\mathrm{e}} \,\mathrm{d}x \tag{5.11}$$

$$= l_{\mathrm{e}} \begin{pmatrix} M_{\mathrm{c},hh}^{\mathrm{e,c}} \mathbf{\Psi}_{hh} & M_{\mathrm{c},h\alpha}^{\mathrm{e,c}} \mathbf{\Psi}_{h\alpha} & M_{\mathrm{c},h\alpha_{\mathrm{fl,win}}}^{\mathrm{e,c}} \mathbf{\Psi}_{h\alpha} & M_{\mathrm{c},h\alpha_{\mathrm{fl,lee}}}^{\mathrm{e,c}} \mathbf{\Psi}_{h\alpha} \\ & M_{\mathrm{c},\alpha\alpha}^{\mathrm{e,c}} \mathbf{\Psi}_{\alpha\alpha} & M_{\mathrm{c},\alpha\theta_{\mathrm{fl,win}}}^{\mathrm{e,c}} \mathbf{\Psi}_{\alpha\alpha} & M_{\mathrm{c},\alpha\theta_{\mathrm{fl,lee}}}^{\mathrm{e,c}} \mathbf{\Psi}_{\alpha\alpha} \\ & & M_{\mathrm{c},\theta_{\mathrm{fl,win}}\theta_{\mathrm{fl,win}}}^{\mathrm{e,c}} \mathbf{\Psi}_{\alpha\alpha} & M_{\mathrm{c},\theta_{\mathrm{fl,win}}\theta_{\mathrm{fl,lee}}}^{\mathrm{e,c}} \mathbf{\Psi}_{\alpha\alpha} \\ \text{symm.} & & & M_{\mathrm{c},\theta_{\mathrm{fl,lee}}\theta_{\mathrm{fl,lee}}}^{\mathrm{e,c}} \mathbf{\Psi}_{\alpha\alpha} \end{pmatrix} \tag{5.12}$$

is added to the pumped-up version of that in Eq. (4.6a). Constant flap properties along the element length are assumed.

Concerning the motion-induced aerodynamic forces, the element derivative matrix $\mathbf{Q}^{\mathrm{e}}$ according to Eq. (4.9) must be replaced with

$$\mathbf{Q}^{\mathrm{e}} = \int_0^{l_{\mathrm{e}}} \mathbf{\Omega}^{\mathrm{e}\mathrm{T}} \begin{pmatrix} \frac{1}{b} & \mathbf{0} \\ \mathbf{0} & \mathbf{I} \end{pmatrix} \mathbf{Q} \begin{pmatrix} \frac{1}{b} & \mathbf{0} \\ \mathbf{0} & \mathbf{I} \end{pmatrix} \mathbf{\Omega}^{\mathrm{e}} \,\mathrm{d}x \tag{5.13a}$$

$$= l_\mathrm{e} \begin{pmatrix} Q_{hh}\frac{1}{b^2}\Psi_{hh} & Q_{h\alpha}\frac{1}{b}\Psi_{h\alpha} & Q_{h\theta_{\mathrm{fl,win}}}\frac{1}{b}\Psi_{h\alpha} & Q_{h\theta_{\mathrm{fl,lee}}}\frac{1}{b}\Psi_{h\alpha} \\ Q_{\alpha h}\frac{1}{b}\Psi_{\alpha h} & Q_{\alpha\alpha}\Psi_{\alpha\alpha} & Q_{\alpha\theta_{\mathrm{fl,win}}}\Psi_{\alpha\alpha} & Q_{\alpha\theta_{\mathrm{fl,lee}}}\Psi_{\alpha\alpha} \\ Q_{\theta_{\mathrm{fl,win}}h}\frac{1}{b}\Psi_{\alpha h} & Q_{\theta_{\mathrm{fl,win}}\alpha}\Psi_{\alpha\alpha} & Q_{\theta_{\mathrm{fl,win}}\theta_{\mathrm{fl,win}}}\Psi_{\alpha\alpha} & Q_{\theta_{\mathrm{fl,win}}\theta_{\mathrm{fl,lee}}}\Psi_{\alpha\alpha} \\ Q_{\theta_{\mathrm{fl,lee}}h}\frac{1}{b}\Psi_{\alpha h} & Q_{\theta_{\mathrm{fl,lee}}\alpha}\Psi_{\alpha\alpha} & Q_{\theta_{\mathrm{fl,lee}}\theta_{\mathrm{fl,win}}}\Psi_{\alpha\alpha} & Q_{\theta_{\mathrm{fl,lee}}\theta_{\mathrm{fl,lee}}}\Psi_{\alpha\alpha} \end{pmatrix}, \tag{5.13b}$$

where the derivatives $\mathbf{Q}$ are those from Section 2.2.3. Due to the chosen approximation functions, all matrices Ψ_j in Eq. (5.11) and Eq. (5.13) are already given in Section 4.1.

With the help of Eq. (4.6c), a continuous actuator input

$$\begin{pmatrix} 0 \\ 0 \\ M_{\mathrm{fl,win}} \\ M_{\mathrm{fl,lee}} \end{pmatrix}, \tag{5.14}$$

whose non-zero entries energetically correspond to the respective torsions of the flaps, can be discretised. The actuator input in the nodal force vector of the finite element is thus as follows.

$$\begin{pmatrix} \mathbf{0} \\ \mathbf{0} \\ \mathbf{f}^\mathrm{e}_{\mathrm{c,win}} \\ \mathbf{f}^\mathrm{e}_{\mathrm{c,lee}} \end{pmatrix}, \quad \mathbf{f}^\mathrm{e}_{\mathrm{c,win}} = \begin{pmatrix} M_{\mathrm{fl,win,le}} \\ M_{\mathrm{fl,win,mi}} \\ M_{\mathrm{fl,win,ri}} \end{pmatrix}, \quad \mathbf{f}^\mathrm{e}_{\mathrm{c,lee}} = \begin{pmatrix} M_{\mathrm{fl,lee,le}} \\ M_{\mathrm{fl,lee,mi}} \\ M_{\mathrm{fl,lee,ri}} \end{pmatrix} \tag{5.15}$$

The variables $M_{\mathrm{fl},j}$ $M_{\mathrm{fl},j,l}$ represent the hinge moments between the girder and a flap. If the connections between girder and flaps are not continuous but discrete and they are not located at the element nodes, the nodal force vector can also be derived in the sense of Eq. (4.6c). Considering the last equations shows that the degrees of freedom of the flaps are coupled to those of the bridge with inertia elements in the mass matrix and aerodynamic elements in the derivative matrix.

After describing how to incorporate the actuators into the finite-element model, the global degrees of freedom of the actuator-equipped structure are now assumed to be separated as follows.

$$\begin{pmatrix} \xi_\mathrm{s} \\ \xi_\mathrm{c} \end{pmatrix} \tag{5.16}$$

If the global degrees of freedom are not directly assembled in this way, they must be rearranged with a proper permutation matrix. A reduction of the number of degrees of freedom is possible again. The degrees of freedom ξ_s of the original structure can still be transformed to modal coordinates according to Eq. (4.19) with the eigenvectors of Section 4.2. A truncation of the

modal matrix $\mathbf{\Phi}_\mathrm{s}$ has to be applied with care. All experiences gained in the last chapter concerning a reduction of the number of degrees of freedom are linked to the question of the critical wind speeds. They cannot be directly transferred to other problems, especially if actuators are applied. Moreover, the actuator degrees of freedom can be coupled. For the coupling matrix $\mathbf{a}_\chi$, the values of selected bending or torsional mode shapes at the actuator nodes are useful, for instance. Employing modal versions of the structural degrees of freedom of the bridge and couplings of the actuator degrees of freedom can significantly reduce the size of the displacement vector. The transformation takes the following form.

$$\begin{pmatrix} \xi_\mathrm{s} \\ \xi_\mathrm{c} \end{pmatrix} = \begin{pmatrix} \mathbf{\Phi}_\mathrm{s} & \mathbf{0} \\ \mathbf{0} & \mathbf{a}_\chi \end{pmatrix} \begin{pmatrix} \xi_\mathrm{s}^\mathrm{m} \\ \xi_\mathrm{c}^\mathrm{red} \end{pmatrix} \tag{5.17}$$

All other vectors and matrices in the equation of motion must be transformed with $\mathrm{diag}(\begin{array}{cc} \mathbf{\Phi}_\mathrm{s} & \mathbf{a}_\chi \end{array})$ as shown for the modal transformation in Eq. (4.21). The actuator input forces that energetically correspond to the reduced degrees of freedom $\xi_\mathrm{c}^\mathrm{red}$ are the resulting input forces that act between the coupled actuators and the bridge girder. Along with the total number of degrees of freedom, the number of aerodynamically effective degrees of freedom of the bridge and the flaps are reduced. If a rational function approximation of the aerodynamic forces with the Roger approach is applied, the explanations given in Section 4.3 can be transferred to the transformation used above in order to diminish the number of aerodynamic states.

Again, continuous mode shapes of the whole girder can alternatively be used for a discretisation of the structure that is equipped with single actuators. Unfortunately, the differential equations of different mode shapes get coupled in general because orthogonality conditions cannot be applied if actuators are placed at a small number of positions. A bimodal approach can hardly be justified with simple statements as done for the bridge so far. Additionally, one new equation per actuator has to be introduced. From the mathematical point of view, however, there is one interesting special case if the preconditions for Eq. (4.38) are complied with. Though this system is not directly suited to a real implementation, fundamental characteristics can be simply investigated with its help. Lots of identical actuators all along the girder are necessary. In the case of discrete actuators, they must be equidistantly distributed. The actuator degrees of freedom are continuously described as

$$\xi_\mathrm{c}(x,t) = \sum_{j=1}^{\infty} \breve{\Omega}_j(x)\xi_{\mathrm{c},j}(t) \tag{5.18}$$

in the sense of a kinematic coupling in the form of the mode $\breve{\Omega}_j(x)$. This kinematic constraint is restrictive because the actuator degrees of freedom are, in general, not limited by the constraints

of the structural system. The continuous actuator input force is described in a similar restrictive way.

$$\mathbf{f}_{\mathrm{c}}(x,t) = \sum_{j=1}^{\infty} \breve{\Omega}_j(x)\mathbf{f}_{\mathrm{c},j}(t) \tag{5.19}$$

The modal variables $\xi_{\mathrm{c},j}$ and $\mathbf{f}_{\mathrm{c},j}$ in both series energetically correspond with each other. As already done for the bridge girder itself, the inertia effect due to the bending rotation φ of the actuator is neglected. Without giving all the details here, the actuator-equipped structure can then be described with a few ordinary differential equations for each mode j. No couplings between the modes occur.

For one mode shape $\breve{\Omega}_j(x)$, the equations can again be interpreted as the result of the mathematical description of two-dimensional models. These models are a combination of that in Figure 4.5 with those of Appendix A.2. Due to the later described objective of the controller design, the first mode shape is again considered. The inertia properties of the reaction wheel and the control moment gyroscope, as well as their input force, are now considered as physical quantities per unit length. These variables are thus marked with a superscript $(\ )^{\mathrm{pl}}$ in the following. Similar to the finite-element model of the bridge, the degrees of freedom defined in Eq. (2.19) are extended and the equations of motion are adjusted.

The reaction wheel leads to an extension of the degrees of freedom with $\xi_{\mathrm{c}} = (\ \theta_{\mathrm{rw}}\ )$. After suitably expanding the matrices of the two-dimensional bridge model in Eq. (4.51) with zeros, the actuator mass matrix

$$\mathbf{M}_{\mathrm{c}} = \begin{pmatrix} m_{\mathrm{rw}}^{\mathrm{pl}} b^2 & 0 & 0 \\ 0 & I_{\mathrm{rw,h}}^{\mathrm{pl}} & I_{\mathrm{rw,h}}^{\mathrm{pl}} \\ 0 & I_{\mathrm{rw,h}}^{\mathrm{pl}} & I_{\mathrm{rw,h}}^{\mathrm{pl}} \end{pmatrix} \tag{5.20}$$

and the force vector with the actuator input

$$\begin{pmatrix} \mathbf{0} \\ \mathbf{f}_{\mathrm{c}} \end{pmatrix}, \quad \mathbf{f}_{\mathrm{c}} = \begin{pmatrix}\ M_{\mathrm{rw}}^{\mathrm{pl}}\ \end{pmatrix} \tag{5.21}$$

are added.

Together with the additional degree of freedom $\xi_{\mathrm{c}} = (\ \theta_{\mathrm{gy}}\ )$, the control moment gyroscope necessitates adding the matrices

$$\mathbf{M}_{\mathrm{c}} = \begin{pmatrix} m_{\mathrm{gy}}^{\mathrm{pl}} b^2 & 0 & 0 \\ 0 & I_{\mathrm{gy,l}}^{\mathrm{pl}} & 0 \\ 0 & 0 & I_{\mathrm{gy,l}}^{\mathrm{pl}} \end{pmatrix}, \quad \mathbf{C}_{\mathrm{c}} = \begin{pmatrix} 0 & 0 & 0 \\ 0 & 0 & I_{\mathrm{gy,h}}^{\mathrm{pl}} \Omega_{\mathrm{gy}} \\ 0 & -I_{\mathrm{gy,h}}^{\mathrm{pl}} \Omega_{\mathrm{gy}} & 0 \end{pmatrix} \tag{5.22}$$

and the vector

$$\begin{pmatrix} \mathbf{0} \\ \mathbf{f}_\mathrm{c} \end{pmatrix}, \quad \mathbf{f}_\mathrm{c} = \begin{pmatrix} M_\mathrm{gy}^\mathrm{pl} \end{pmatrix} \quad . \tag{5.23}$$

Finally, the degrees of freedom of the flaps are represented with $\boldsymbol{\xi}_\mathrm{c} = \begin{pmatrix} \theta_\mathrm{fl,win} & \theta_\mathrm{fl,lee} \end{pmatrix}^\mathrm{T}$. The details of the additional mass matrix are

$$\mathbf{M}_\mathrm{c} = \begin{pmatrix} b & \mathbf{0} \\ \mathbf{0} & \mathbf{I} \end{pmatrix} \mathbf{M}_\mathrm{c}^\mathrm{e,c} \begin{pmatrix} b & \mathbf{0} \\ \mathbf{0} & \mathbf{I} \end{pmatrix} \quad , \tag{5.24}$$

where $\mathbf{M}_\mathrm{c}^\mathrm{e,c}$ is that of Eq. (5.10). Instead of the derivatives of the bridge cross section, those of Section 2.2.3 must be employed. The actuator input in the force vector has the following detailed entries.

$$\begin{pmatrix} \mathbf{0} \\ \mathbf{f}_\mathrm{c,win} \\ \mathbf{f}_\mathrm{c,lee} \end{pmatrix}, \quad \mathbf{f}_\mathrm{c,win} = \begin{pmatrix} M_\mathrm{fl,win} \end{pmatrix}, \quad \mathbf{f}_\mathrm{c,lee} = \begin{pmatrix} M_\mathrm{fl,lee} \end{pmatrix} \tag{5.25}$$

Kinematic couplings between the wind- and leeward flap rotations can be modelled as explained in connection with Eq. (5.17).

5.2 State-Space Models of the Actuator-Extended System

With the matrices and vectors derived in the last section, the equation of motion of the actuator-equipped bridge takes the following form.

$$\mathbf{M}_\mathrm{s} \begin{pmatrix} \ddot{\boldsymbol{\xi}}_\mathrm{s} \\ \ddot{\boldsymbol{\xi}}_\mathrm{c} \end{pmatrix} + \mathbf{C}_\mathrm{s} \begin{pmatrix} \dot{\boldsymbol{\xi}}_\mathrm{s} \\ \dot{\boldsymbol{\xi}}_\mathrm{c} \end{pmatrix} + \mathbf{K}_\mathrm{s} \begin{pmatrix} \boldsymbol{\xi}_\mathrm{s} \\ \boldsymbol{\xi}_\mathrm{c} \end{pmatrix} = \mathbf{f}_\mathrm{ae} + \mathbf{d}_\mathrm{ae}^\mathrm{g} + \begin{pmatrix} \mathbf{0} \\ \mathbf{f}_\mathrm{c} \end{pmatrix} \tag{5.26}$$

The mass matrix $\mathbf{M}_\mathrm{s}$ and the damping matrix $\mathbf{C}_\mathrm{s}$ include the additional elements of the actuators. If reaction wheels or control moment gyroscopes are used, the actuator displacements do not induce aerodynamic forces, and aerodynamic forces do not act on the actuators. The aerodynamic admittance functions of the bridge can thus be simply pumped up.

$$\begin{pmatrix} \mathbf{I} \\ \mathbf{0} \end{pmatrix} \mathbf{Q} \begin{pmatrix} \mathbf{I} & \mathbf{0} \end{pmatrix}, \quad \begin{pmatrix} \mathbf{I} \\ \mathbf{0} \end{pmatrix} \mathbf{Q}^\mathrm{g} \tag{5.27}$$

Accordingly, the matrices of the rational function approximation determined for the bridge are modified. Whereas the matrices $\mathbf{A}_j$ are treated as shown for the admittances, $\begin{pmatrix}\mathbf{I} & \mathbf{0}\end{pmatrix}^{\mathrm{T}}\mathbf{D}$ for both admittances and $\mathbf{E}\begin{pmatrix}\mathbf{I} & \mathbf{0}\end{pmatrix}$ for the motion-induced aerodynamic forces must be performed. The matrix $\mathbf{R}$ and, thus, the number of aerodynamic states, remain unchanged. If, in contrast, flaps are employed as actuators, the admittance matrices change significantly. The rational function approximation must then be carried out as explained in the chapters before.

In terms of a state-space model, Eq. (5.26) reads as

$$\dot{\mathbf{x}}_{\mathrm{as}} = \mathbf{A}_{\mathrm{as}}\mathbf{x}_{\mathrm{as}} + \mathbf{E}_{\mathrm{as}}\mathbf{d}_{\mathrm{ae}}^{\mathrm{g}} + \mathbf{B}_{\mathrm{as}}\mathbf{f}_{\mathrm{c}} \tag{5.28a}$$

$$\mathbf{y}_{\mathrm{st}} = \mathbf{C}_{\mathrm{as}}\mathbf{x}_{\mathrm{as}} \quad . \tag{5.28b}$$

The entries of the matrices in both equations are similar to those in Eq. (4.56) and Eq. (4.57). However, in the state vector $\mathbf{x}_{\mathrm{as}}$, the structural degrees of freedom ξ_{s} must be replaced with the extended ones of Eq. (5.16), and the structural output matrix $\mathbf{C}_{\mathrm{st}}$ within the output matrix $\mathbf{C}_{\mathrm{as}}$ must be adjusted to the measured quantities. The input matrix of the actuator input $\mathbf{f}_{\mathrm{c}}$ is determined as follows.

$$\mathbf{B}_{\mathrm{as}} = \begin{pmatrix} \bar{\mathbf{M}}^{-1} \\ \mathbf{0} \\ \mathbf{0} \end{pmatrix} \begin{pmatrix} \mathbf{0} \\ \mathbf{I} \end{pmatrix} \tag{5.29}$$

As shown in Eq. (4.60) and the associated ones, the state-space representation of the gust-induced aerodynamic forces can be combined with that of the actuator equipped aeroelastic system. The alternative representation of the equation of motion in the sense of Eq. (4.63) is not pursued in the following because a mathematically consistent state-space model is necessary to apply customary methods of control theory later on.

The state in Eq. (5.28) contains both the actuator displacements ξ_{c} and the corresponding speeds $\dot{\xi}_{\mathrm{c}}$. As described in the following sections, the motions of the actuators are controlled so that the actuator-equipped system is asymptotically stable and, thus, input-output stable. For actuators in the form of flaps and gyroscopes, it makes sense to drive their displacements ξ_{c} back to zero if no disturbances act on the bridge. For reaction wheels, however, it does not matter at which angle the wheel finally stops. Asymptotic stability is only necessary for the rotational speed, not for the rotation. If it is desired to exclude the wheel rotation from the state vector, the actuator displacements ξ_{c} and, consequently, the forces that directly depend on them must be cancelled from Eq. (5.26). Actuator speeds $\dot{\xi}_{\mathrm{c}}$, actuator accelerations $\ddot{\xi}_{\mathrm{c}}$, and the corresponding forces

remain untouched. The modified equation of motion can now be converted to a state-space model in the form of Eq. (5.28). The state has the following entries in the structural part.

$$\mathbf{x}_{\mathrm{st}} = \begin{pmatrix} \dot{\xi}_{\mathrm{s}} \\ \dot{\xi}_{\mathrm{c}} \\ \xi_{\mathrm{s}} \end{pmatrix} \tag{5.30}$$

All columns and rows of the matrices $\mathbf{A}_{\mathrm{as}}$, $\mathbf{E}_{\mathrm{as}}$, $\mathbf{B}_{\mathrm{as}}$, and $\mathbf{C}_{\mathrm{as}}$ that directly correspond to the actuator displacements are deleted.

Eq. (5.28) yields the degrees of freedom of the actuator-equipped bridge under the effect of disturbing gusts and actuator input forces $\mathbf{f}_{\mathrm{c}}$. To alternatively allow an input in terms of the actuator displacements ξ_{c}, the model can be rearranged based on Eq. (5.26). According to the separation of the degrees of freedom in Eq. (5.16), the admittance matrix of the gust-induced aerodynamic forces is separated into an upper and lower part. The matrices of all other terms are separable into four submatrices due to their dependency on the displacements. All these submatrices are appropriately tagged with the indices s and c or combinations of them.

Since the actuator displacements ξ_{c} are now specified as input terms, only the structural displacements ξ_{s} are unknown degrees of freedom, which have to be determined with the help of the differential equation. Multiplying Eq. (5.26) by $\begin{pmatrix} \mathbf{I} & \mathbf{0} \end{pmatrix}$ from the left side gives the necessary equations.

$$\begin{aligned} &\begin{pmatrix} \mathbf{M}_{\mathrm{s,ss}} & \mathbf{M}_{\mathrm{s,sc}} \end{pmatrix} \begin{pmatrix} \ddot{\xi}_{\mathrm{s}} \\ \ddot{\xi}_{\mathrm{c}} \end{pmatrix} + \begin{pmatrix} \mathbf{C}_{\mathrm{s,ss}} & \mathbf{C}_{\mathrm{s,sc}} \end{pmatrix} \begin{pmatrix} \dot{\xi}_{\mathrm{s}} \\ \dot{\xi}_{\mathrm{c}} \end{pmatrix} + \begin{pmatrix} \mathbf{K}_{\mathrm{s,ss}} & \mathbf{K}_{\mathrm{s,sc}} \end{pmatrix} \begin{pmatrix} \xi_{\mathrm{s}} \\ \xi_{\mathrm{c}} \end{pmatrix} \\ &\quad = \begin{pmatrix} \mathbf{I} & \mathbf{0} \end{pmatrix} \mathbf{f}_{\mathrm{ae}} + \begin{pmatrix} \mathbf{I} & \mathbf{0} \end{pmatrix} \mathbf{d}_{\mathrm{ae}}^{\mathrm{g}} \end{aligned} \tag{5.31}$$

The lower block of Eq. (5.26), separable from Eq. (5.26) with a multiplication by $\begin{pmatrix} \mathbf{0} & \mathbf{I} \end{pmatrix}$ from the left, can be used to determine the actuator input forces $\mathbf{f}_{\mathrm{c}}$ that correspond to ξ_{c}.

If reaction wheels or control moment gyroscopes are employed, the motion-induced aerodynamic forces are not influenced by the actuator displacements. With the matrices of the rational function approximation of the bridge derivatives used in Section 4.5, a state-space model can be derived.

$$\dot{\mathbf{x}}_{\mathrm{as}} = \mathbf{A}_{\mathrm{as}} \mathbf{x}_{\mathrm{as}} + \mathbf{E}_{\mathrm{as}} \mathbf{d}_{\mathrm{ae}}^{\mathrm{g}} + \mathbf{B}_{\mathrm{as}} \mathbf{x}_{\mathrm{c}} \tag{5.32a}$$

$$\mathbf{y}_{\mathrm{st}} = \mathbf{C}_{\mathrm{as}} \mathbf{x}_{\mathrm{as}} \tag{5.32b}$$

The elements of the matrices and vectors almost comply with those of Eq. (4.56). Only the modified mass, damping, and stiffness matrices are altered.

$$\bar{\mathbf{M}} = \mathbf{M}_{\mathrm{s,ss}} - q_0 (b/U)^2 \mathbf{A}_2 \,, \quad \bar{\mathbf{C}} = \mathbf{C}_{\mathrm{s,ss}} - q_0 (b/U) \mathbf{A}_1 \,, \quad \bar{\mathbf{K}} = \mathbf{K}_{\mathrm{s,ss}} - q_0 \mathbf{A}_0 \tag{5.33}$$

The input matrix and the actuator input in the additional term of the state equation take the following form.

$$\mathbf{B}_{\mathrm{as}} = -\begin{pmatrix} \bar{\mathbf{M}}^{-1} \\ \mathbf{0} \\ \mathbf{0} \end{pmatrix} \begin{pmatrix} \mathbf{M}_{\mathrm{s,sc}} & \mathbf{C}_{\mathrm{s,sc}} & \mathbf{K}_{\mathrm{s,sc}} \end{pmatrix}, \quad \mathbf{x}_{\mathrm{c}} = \begin{pmatrix} \ddot{\xi}_{\mathrm{c}} \\ \dot{\xi}_{\mathrm{c}} \\ \xi_{\mathrm{c}} \end{pmatrix} \tag{5.34}$$

Gust-induced aerodynamic forces can, moreover, be handled in exactly the same way as described in Eq. (4.60) and the associated ones.

In the case of the reaction wheel, it is again an interesting alternative to exclude the actuator displacements, but not their derivatives, from the model. For this purpose, the variable ξ_{c}, but not its derivatives, must be cancelled in Eq. (5.31) and Eq. (5.34). Correspondingly, the matrix $\mathbf{K}_{\mathrm{s,sc}}$, which is a zero matrix, is deleted from the input matrix $\mathbf{B}_{\mathrm{as}}$.

If the actuator displacements generate aerodynamic forces, as is the case when flaps are attached to the girder, the derivation of a state-space model is a bit more complicated. First, the matrices of the rational function approximation of the motion-induced aerodynamic forces are separated.

$$\mathbf{A}_j = \begin{pmatrix} \mathbf{A}_{j,\mathrm{s}} \\ \mathbf{A}_{j,\mathrm{c}} \end{pmatrix} = \begin{pmatrix} \mathbf{A}_{j,\mathrm{ss}} & \mathbf{A}_{j,\mathrm{sc}} \\ \mathbf{A}_{j,\mathrm{cs}} & \mathbf{A}_{j,\mathrm{cc}} \end{pmatrix}, \quad \mathbf{D} = \begin{pmatrix} \mathbf{D}_{\mathrm{s}} \\ \mathbf{D}_{\mathrm{c}} \end{pmatrix}, \quad \mathbf{E} = \begin{pmatrix} \mathbf{E}_{\mathrm{s}} & \mathbf{E}_{\mathrm{c}} \end{pmatrix} \tag{5.35}$$

The matrices $\mathbf{A}_0$ and $\mathbf{D}$ of the admittance approximation of gust-induced aerodynamic forces are split up in the same way. With this kind of separation, the state-space model of the motion-induced aerodynamic forces that act corresponding to the structural degrees of freedom follows from Eq. (3.18) and Eq. (3.10b).

$$\xi_{\mathrm{a}}' = \mathbf{R}\xi_{\mathrm{a}} + \begin{pmatrix} \mathbf{0} & \begin{pmatrix} \mathbf{E}_{\mathrm{s}} & \mathbf{E}_{\mathrm{c}} \end{pmatrix} & \mathbf{0} \end{pmatrix} \begin{pmatrix} \begin{pmatrix} \xi_{\mathrm{s}}'' \\ \xi_{\mathrm{c}}'' \end{pmatrix} \\ \begin{pmatrix} \xi_{\mathrm{s}}' \\ \xi_{\mathrm{c}}' \end{pmatrix} \\ \begin{pmatrix} \xi_{\mathrm{s}} \\ \xi_{\mathrm{c}} \end{pmatrix} \end{pmatrix} \tag{5.36a}$$

$$\begin{aligned} \begin{pmatrix} \mathbf{I} & \mathbf{0} \end{pmatrix} \mathbf{f}_{\mathrm{ae}} &= q_0 \mathbf{D}_{\mathrm{s}} \xi_{\mathrm{a}} + \\ &+ q_0 \begin{pmatrix} \begin{pmatrix} \mathbf{A}_{2,\mathrm{ss}} & \mathbf{A}_{2,\mathrm{sc}} \end{pmatrix} & \begin{pmatrix} \mathbf{A}_{1,\mathrm{ss}} & \mathbf{A}_{1,\mathrm{sc}} \end{pmatrix} & \begin{pmatrix} \mathbf{A}_{0,\mathrm{ss}} & \mathbf{A}_{0,\mathrm{sc}} \end{pmatrix} \end{pmatrix} \begin{pmatrix} \begin{pmatrix} \xi_{\mathrm{s}}'' \\ \xi_{\mathrm{c}}'' \end{pmatrix} \\ \begin{pmatrix} \xi_{\mathrm{s}}' \\ \xi_{\mathrm{c}}' \end{pmatrix} \\ \begin{pmatrix} \xi_{\mathrm{s}} \\ \xi_{\mathrm{c}} \end{pmatrix} \end{pmatrix} \end{aligned} \tag{5.36b}$$

Inserting this model into Eq. (5.31) again leads to a state-space model in the form of Eq. (5.32). The entries in the system matrix $\mathbf{A}_{\mathrm{as}}$ are slightly changed, and the input matrix $\mathbf{B}_{\mathrm{as}}$ gets more summands.

$$\mathbf{A}_{\mathrm{as}} = \begin{pmatrix} -\bar{\mathbf{M}}^{-1}\bar{\mathbf{C}} & -\bar{\mathbf{M}}^{-1}\bar{\mathbf{K}} & q_0\bar{\mathbf{M}}^{-1}\mathbf{D}_{\mathrm{s}} \\ \mathbf{I} & \mathbf{0} & \mathbf{0} \\ \mathbf{E}_{\mathrm{s}} & \mathbf{0} & (U/b)\mathbf{R} \end{pmatrix} \tag{5.37a}$$

$$\begin{aligned} \mathbf{B}_{\mathrm{as}} = &- \begin{pmatrix} \bar{\mathbf{M}}^{-1} \\ \mathbf{0} \\ \mathbf{0} \end{pmatrix} \begin{pmatrix} \mathbf{M}_{\mathrm{s,sc}} & \mathbf{C}_{\mathrm{s,sc}} & \mathbf{K}_{\mathrm{s,sc}} \end{pmatrix} + \begin{pmatrix} \mathbf{0} \\ \mathbf{0} \\ \begin{pmatrix} \mathbf{0} & \mathbf{E}_{\mathrm{c}} & \mathbf{0} \end{pmatrix} \end{pmatrix} + \\ &+ \begin{pmatrix} \bar{\mathbf{M}}^{-1} \\ \mathbf{0} \\ \mathbf{0} \end{pmatrix} q_0 \begin{pmatrix} (b/U)^2\mathbf{A}_{2,\mathrm{sc}} & (b/U)\mathbf{A}_{1,\mathrm{sc}} & \mathbf{A}_{0,\mathrm{sc}} \end{pmatrix} \end{aligned} \tag{5.37b}$$

For this case, the following modified matrices are defined.

$$\bar{\mathbf{M}} = \mathbf{M}_{\mathrm{s,ss}} - q_0(b/U)^2\mathbf{A}_{2,\mathrm{ss}}\,, \quad \bar{\mathbf{C}} = \mathbf{C}_{\mathrm{s,ss}} - q_0(b/U)\mathbf{A}_{1,\mathrm{ss}}\,, \quad \bar{\mathbf{K}} = \mathbf{K}_{\mathrm{s,ss}} - q_0\mathbf{A}_{0,\mathrm{ss}} \tag{5.38}$$

In the appended model of the gust-induced aerodynamic forces, the upper matrices $\mathbf{D}_{\mathrm{s}}$ and $\mathbf{A}_{0,\mathrm{s}}$ must be employed.

In Eq. (5.36), the length of the output vector is shorter than that of the input vector. If the rational function approximation is carried out with the Roger approach, the number of aerodynamic states can thus be minimised with an arrangement in the form of Eq. (3.20). This minimisation requires two modifications. The first concerns the coefficient matrices $\mathbf{A}_j$, $(j > 2)$ in the matrix $\mathbf{E}$. From these matrices, the rows must be deleted that are connected with the forces which correspond to ξ_{c}. This can be simply done by the multiplication $\begin{pmatrix} \mathbf{I} & \mathbf{0} \end{pmatrix}\mathbf{A}_j$, $(j > 2)$. Cancelling the corresponding zero columns in the matrix $\mathbf{D}_{\mathrm{s}}$ is the second modification. To apply the procedure, the matrix $\mathbf{D}$ must not have been transformed with the modal matrix in a preceding step as explained in connection with Eq. (4.32) and Eq. (4.33).

If, moreover, it is desired to know the actuator input forces $\mathbf{f}_\mathrm{c}$, which correspond to the actuator displacements $\boldsymbol{\xi}_\mathrm{c}$, they follow from Eq. (5.26) as mentioned before.

$$\begin{aligned}\mathbf{f}_\mathrm{c} = &-\begin{pmatrix}\mathbf{0} & \mathbf{I}\end{pmatrix}\mathbf{f}_\mathrm{ae} - \begin{pmatrix}\mathbf{0} & \mathbf{I}\end{pmatrix}\mathbf{d}_\mathrm{ae}^\mathrm{g} + \\ &+\begin{pmatrix}\begin{pmatrix}\mathbf{M}_\mathrm{s,cs} & \mathbf{M}_\mathrm{s,cc}\end{pmatrix} & \begin{pmatrix}\mathbf{C}_\mathrm{s,cs} & \mathbf{C}_\mathrm{s,cc}\end{pmatrix} & \begin{pmatrix}\mathbf{K}_\mathrm{s,cs} & \mathbf{K}_\mathrm{s,cc}\end{pmatrix}\end{pmatrix}\begin{pmatrix}\begin{pmatrix}\ddot{\boldsymbol{\xi}}_\mathrm{s}\\ \ddot{\boldsymbol{\xi}}_\mathrm{c}\end{pmatrix}\\ \begin{pmatrix}\dot{\boldsymbol{\xi}}_\mathrm{s}\\ \dot{\boldsymbol{\xi}}_\mathrm{c}\end{pmatrix}\\ \begin{pmatrix}\boldsymbol{\xi}_\mathrm{s}\\ \boldsymbol{\xi}_\mathrm{c}\end{pmatrix}\end{pmatrix}\end{aligned} \tag{5.39}$$

In the case of reaction wheels and control moment gyroscopes, no aerodynamic forces act on the actuators. Both summands in the first line of Eq. (5.39) thus vanish. The remaining non-zero terms can be transformed into a simple output equation of the state-space model in Eq. (5.32).

$$\begin{aligned}\mathbf{f}_\mathrm{c} = &\begin{pmatrix}(\mathbf{C}_\mathrm{s,cs} - \mathbf{M}_\mathrm{s,cs}\bar{\mathbf{M}}^{-1}\bar{\mathbf{C}}) & (\mathbf{K}_\mathrm{s,cs} - \mathbf{M}_\mathrm{s,cs}\bar{\mathbf{M}}^{-1}\bar{\mathbf{K}}) & (\mathbf{M}_\mathrm{s,cs}\,q_0\bar{\mathbf{M}}^{-1}\mathbf{D})\end{pmatrix}\mathbf{x}_\mathrm{as} + \\ &+\left(\mathbf{M}_\mathrm{s,cs}\bar{\mathbf{M}}^{-1}\right)\mathbf{d}_\mathrm{ae}^\mathrm{g} + \\ &+\begin{pmatrix}(\mathbf{M}_\mathrm{s,cc} - \mathbf{M}_\mathrm{s,cs}\bar{\mathbf{M}}^{-1}\mathbf{M}_\mathrm{s,sc}) & (\mathbf{C}_\mathrm{s,cc} - \mathbf{M}_\mathrm{s,cs}\bar{\mathbf{M}}^{-1}\mathbf{C}_\mathrm{s,sc}) \\ & (\mathbf{K}_\mathrm{s,cc} - \mathbf{M}_\mathrm{s,cs}\bar{\mathbf{M}}^{-1}\mathbf{K}_\mathrm{s,sc})\end{pmatrix}\mathbf{x}_\mathrm{c}\end{aligned} \tag{5.40}$$

In contrast to Eq. (5.32b), this output equation, in general, has additional linear feedthrough summands that directly pass the disturbance and the displacement input to the output.

More effort is necessary to determine the forces $\mathbf{f}_\mathrm{c}$ when flaps are applied. If the Roger approach is used for the rational function approximation of the motion-induced aerodynamic forces and the number of aerodynamic states is minimised as described above, a solution cannot be found in terms of an additional output equation. In the latter case, the aerodynamic states in Eq. (5.32a) that are necessary for a calculation of the forces $\mathbf{f}_\mathrm{c}$ are cancelled. One way to get the forces for all kinds of the rational function approximation is to convert Eq. (5.39) into the following state-space model.

$$\dot{\boldsymbol{\xi}}_\mathrm{a} = (U/b\mathbf{R})\,\boldsymbol{\xi}_\mathrm{a} + \mathbf{0}\mathbf{d}_\mathrm{ae}^\mathrm{g} + \begin{pmatrix}\mathbf{0} & \begin{pmatrix}\mathbf{E}_\mathrm{s} & \mathbf{E}_\mathrm{c}\end{pmatrix} & \mathbf{0}\end{pmatrix}\begin{pmatrix}\begin{pmatrix}\dddot{\boldsymbol{\xi}}_\mathrm{s}\\ \dddot{\boldsymbol{\xi}}_\mathrm{c}\end{pmatrix}\\ \begin{pmatrix}\ddot{\boldsymbol{\xi}}_\mathrm{s}\\ \ddot{\boldsymbol{\xi}}_\mathrm{c}\end{pmatrix}\\ \begin{pmatrix}\dot{\boldsymbol{\xi}}_\mathrm{s}\\ \dot{\boldsymbol{\xi}}_\mathrm{c}\end{pmatrix}\end{pmatrix} \tag{5.41a}$$

$$\begin{aligned}\mathbf{f}_\mathrm{c} = &-q_0\mathbf{D}_\mathrm{c}\boldsymbol{\xi}_\mathrm{a} - \begin{pmatrix}\mathbf{0} & \mathbf{I}\end{pmatrix}\mathbf{d}_\mathrm{ae}^\mathrm{g} + \\ &+\left(\begin{pmatrix}\mathbf{M}_\mathrm{s,cs} & \mathbf{M}_\mathrm{s,cc}\end{pmatrix} - q_0(b/U)^2\begin{pmatrix}\mathbf{A}_\mathrm{2,cs} & \mathbf{A}_\mathrm{2,cc}\end{pmatrix}\right)\left(\begin{pmatrix}\ddot{\boldsymbol{\xi}}_\mathrm{s}\\ \ddot{\boldsymbol{\xi}}_\mathrm{c}\end{pmatrix}\right) \\ &\quad+\left(\begin{pmatrix}\mathbf{C}_\mathrm{s,cs} & \mathbf{C}_\mathrm{s,cc}\end{pmatrix} - q_0(b/U)\begin{pmatrix}\mathbf{A}_\mathrm{1,cs} & \mathbf{A}_\mathrm{1,cc}\end{pmatrix}\right)\left(\begin{pmatrix}\dot{\boldsymbol{\xi}}_\mathrm{s}\\ \dot{\boldsymbol{\xi}}_\mathrm{c}\end{pmatrix}\right) \\ &\quad\quad+\left(\begin{pmatrix}\mathbf{K}_\mathrm{s,cs} & \mathbf{K}_\mathrm{s,cc}\end{pmatrix} - q_0\begin{pmatrix}\mathbf{A}_\mathrm{0,cs} & \mathbf{A}_\mathrm{0,cc}\end{pmatrix}\right)\left(\begin{pmatrix}\boldsymbol{\xi}_\mathrm{s}\\ \boldsymbol{\xi}_\mathrm{c}\end{pmatrix}\right)\end{aligned} \tag{5.41b}$$

Having determined the structural states $\mathbf{x}_\mathrm{st}$ and $\dot{\mathbf{x}}_\mathrm{st}$ with Eq. (5.32), they can be inserted as the input into Eq. (5.41). A state minimisation in Eq. (5.41) is possible if the Roger approach is applied for the rational function approximation of the motion-induced aerodynamic forces. Similar to the minimisation procedure described for Eq. (5.32), rows in the submatrices of the matrix $\mathbf{E}$ must be deleted by multiplying $\begin{pmatrix}\mathbf{0} & \mathbf{I}\end{pmatrix}\mathbf{A}_j$, $(j>2)$ and the zero columns in $\mathbf{D}_\mathrm{c}$ must be cancelled.

From Eq. (5.40) and Eq. (5.41), it can be directly seen that the differentiability of the displacement input must fulfil some requirements. The one-sided second derivatives of $\boldsymbol{\xi}_\mathrm{c}$ and thus finite values of $\ddot{\boldsymbol{\xi}}_\mathrm{c}$ must exist to be connected to finite forces.

The vector $\mathbf{x}_\mathrm{c}$ does not only contain the displacement input $\boldsymbol{\xi}_\mathrm{c}$ but also its derivatives. As these subvectors are not independent of one another, the state-space model in Eq. (5.32) does not lend itself to be applied for investigations with the usual methods of control theory. Hence, the vector $\mathbf{x}_\mathrm{c}$ must be determined from one of its subvectors to get an independent input. In the studies presented here, the displacements $\boldsymbol{\xi}_\mathrm{c}$ themselves are usually chosen for this purpose. A simple state-space model for the transfer from $\boldsymbol{\xi}_\mathrm{c}$ to its derivatives, however, cannot be established and appended to that in Eq. (5.32). A pure differentiation without delay is not causal and not technically realisable.

One way to provide an input that almost exactly equals the actuator displacements $\boldsymbol{\xi}_\mathrm{c}$ is to use a special third-order system. In terms of a differential equation it has the following form.

$$\dddot{\boldsymbol{\xi}}_\mathrm{c} + \mathbf{C}_2^\mathrm{uc}\ddot{\boldsymbol{\xi}}_\mathrm{c} + \mathbf{C}_1^\mathrm{uc}\dot{\boldsymbol{\xi}}_\mathrm{c} + \mathbf{C}_0^\mathrm{uc}\boldsymbol{\xi}_\mathrm{c} = \mathbf{C}_0^\mathrm{uc}\mathbf{u}_\mathrm{c} \tag{5.42}$$

When setting $\mathbf{C}_j^\mathrm{uc} = C_j^\mathrm{uc}\mathbf{I}$, all the rows of this system of equations are decoupled and have the same dynamics. The equation can be interpreted as a description of the transfer from the elements of $\mathbf{u}_\mathrm{c}$ to the corresponding ones in $\boldsymbol{\xi}_\mathrm{c}$. It is equivalent to the state equation

$$\dot{\mathbf{x}}_\mathrm{c} = \mathbf{A}_\mathrm{uc}\mathbf{x}_\mathrm{c} + \mathbf{B}_\mathrm{uc}\mathbf{u}_\mathrm{c} \tag{5.43}$$

of a state-space model with the output $\boldsymbol{\xi}_\mathrm{c}$ where

$$\mathbf{A}_\mathrm{uc} = \begin{pmatrix} -\mathbf{C}_2^\mathrm{uc} & -\mathbf{C}_1^\mathrm{uc} & -\mathbf{C}_0^\mathrm{uc} \\ \mathbf{I} & \mathbf{0} & \mathbf{0} \\ \mathbf{0} & \mathbf{I} & \mathbf{0} \end{pmatrix}, \quad \mathbf{B}_\mathrm{uc} = \begin{pmatrix} \mathbf{C}_0^\mathrm{uc} \\ \mathbf{0} \\ \mathbf{0} \end{pmatrix} \quad . \tag{5.44}$$

Since identical parallel systems are used, the transfer equation takes the following form in the frequency domain

$$\boldsymbol{\xi}_\mathrm{c} = \mathbf{G}_\mathrm{uc}\, \mathbf{u}_\mathrm{c} = G_\mathrm{uc}\mathbf{I}\, \mathbf{u}_\mathrm{c} \quad , \tag{5.45}$$

where

$$G_\mathrm{uc} = \frac{C_0^\mathrm{uc}}{s^3 + C_2^\mathrm{uc} s^2 + C_1^\mathrm{uc} s + C_0^\mathrm{uc}} = \frac{C_0^\mathrm{uc}}{(s-s_1)(s-s_2)(s-s_3)} \quad . \tag{5.46}$$

The coefficients C_j^uc of this rational transfer function can be derived from its poles s_j.

$$C_0^\mathrm{uc} = -s_1 s_2 s_3 \,, \quad C_1^\mathrm{uc} = s_1 s_2 + s_1 s_3 + s_2 s_3 \,, \quad C_2^\mathrm{uc} = -(s_1 + s_2 + s_3) \tag{5.47}$$

Identical poles for the different signal paths are not problematic because the corresponding identical eigenvalues in the system matrix $\mathbf{A}_\mathrm{uc}$ are connected to different eigenvectors. Due to the selected coefficients, the zero-frequency gain is constrained to having the value one. If negative real poles are applied, the step response has no overshot. Placing one pole, e. g. s_1, far to the right of the others leads to a behaviour which is similar to that of a first order system. Hence, the step response reaches about 95 % of its final value at $t = 3 \cdot 1/|s_1|$. If sufficiently high absolute values are chosen for s_1, the transfer from $\mathbf{u}_\mathrm{c}$ to $\boldsymbol{\xi}_\mathrm{c}$ is very fast and both vectors are almost identical. To distinguish the elements of both displacement vectors, those of $\mathbf{u}_\mathrm{c}$ are marked with the superscript $(\,)^\mathrm{uc}$. Due to the lagging character of this dynamic system, the transfer has a low-pass behaviour. In order to allow a signal to pass with almost no changes in magnitude and phase at all frequencies that can occur in the actuator input, the poles must be appropriately placed. The transfer function along the positive part of the imaginary frequency axis for $s_1 = -1000\ 1/\mathrm{s}$, $s_2 = 10 s_1$, and $s_3 = 20 s_1$ is shown in Figure 5.4 in terms of a Bode plot. There are no resonance peaks because only real poles are used. The break frequencies of such a special rational transfer function equal the absolute values of its poles. In addition to the exact curves, the straight line approximations are displayed in Figure 5.4. The highest frequency of the actuator displacements is assumed to equal that of the gust disturbance, which is $\omega = 2\pi \cdot 10\ 1/\mathrm{s}$ according to Section 4.7. Up to this frequency, the transfer element shows no relevant changes in magnitude and phase. If the dynamics of further actuator parts need to be considered, they can

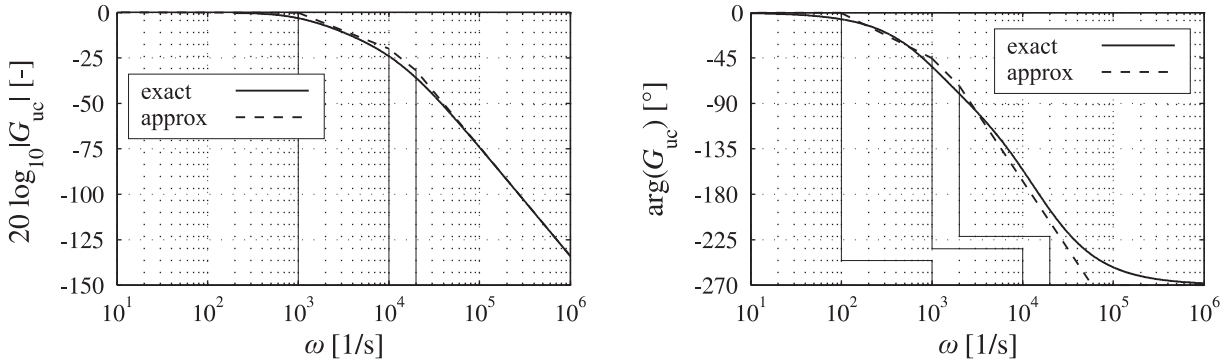

(a) Magnitude plot. (b) Phase plot.

Figure 5.4: Bode plots of the chosen third oder system.

also be modelled with this transfer element and appropriate pole locations. In ZAERO (2004), for instance, such a third-order system is, thus, denoted as an actuator model.

Finally, Eq. (5.43) can be combined with the state-space model in Eq. (5.32)

$$\dot{\mathbf{x}}_{\text{asu}} = \mathbf{A}_{\text{asu}}\mathbf{x}_{\text{asu}} + \mathbf{E}_{\text{asu}}\mathbf{d}_{\text{ae}}^{\text{g}} + \mathbf{B}_{\text{asu}}\mathbf{u}_{\text{c}} \tag{5.48a}$$

$$\mathbf{y}_{\text{st}} = \mathbf{C}_{\text{asu}}\mathbf{x}_{\text{asu}} \quad , \tag{5.48b}$$

where

$$\mathbf{x}_{\text{asu}} = \begin{pmatrix} \mathbf{x}_{\text{as}} \\ \mathbf{x}_{\text{c}} \end{pmatrix} , \quad \mathbf{A}_{\text{asu}} = \begin{pmatrix} \mathbf{A}_{\text{as}} & \mathbf{B}_{\text{as}} \\ \mathbf{0} & \mathbf{A}_{\text{uc}} \end{pmatrix} \tag{5.49a}$$

$$\mathbf{E}_{\text{asu}} = \begin{pmatrix} \mathbf{E}_{\text{as}} \\ \mathbf{0} \end{pmatrix} , \quad \mathbf{B}_{\text{asu}} = \begin{pmatrix} \mathbf{0} \\ \mathbf{B}_{\text{uc}} \end{pmatrix} , \quad \mathbf{C}_{\text{asu}} = \begin{pmatrix} \mathbf{C}_{\text{as}} & \mathbf{0} \end{pmatrix} \quad . \tag{5.49b}$$

The block triangular form of the system matrix $\mathbf{A}_{\text{asu}}$ shows that the eigenvalues of the actuator-extended aeroelastic system are not influenced by the eigenvalues of the third-order system. As parts of the state $\mathbf{x}_{\text{c}}$, the actuator displacements and their derivatives are again included in the state of the actuator-equipped system. The model of the gust-induced aerodynamic forces can be appended as explained before.

If it is desired to not include the actuator displacements ξ_{c} in the state of the actuator-equipped system, the vector $\mathbf{x}_{\text{c}}$ only contains the actuator speeds $\dot{\xi}_{\text{c}}$ and the actuator accelerations $\ddot{\xi}_{\text{c}}$. For this case, the speeds are chosen as the independent input. With a fast second order system, a transfer from an input $\mathbf{u}_{\text{c}}$ that almost exactly equals the actuator speeds can be modelled. The

state-space model takes the form of Eq. (5.43). Eq. (5.44), Eq. (5.46), and Eq. (5.47) must be replaced with

$$\mathbf{A}_{\mathrm{uc}} = \begin{pmatrix} -\mathbf{C}_2^{\mathrm{uc}} & -\mathbf{C}_1^{\mathrm{uc}} \\ \mathbf{I} & \mathbf{0} \end{pmatrix}, \quad \mathbf{B}_{\mathrm{uc}} = \begin{pmatrix} \mathbf{C}_1^{\mathrm{uc}} \\ \mathbf{0} \end{pmatrix} \quad , \tag{5.50}$$

$$G_{\mathrm{uc}} = \frac{C_1^{\mathrm{uc}}}{s^2 + C_2^{\mathrm{uc}} s + C_1^{\mathrm{uc}}} = \frac{C_1^{\mathrm{uc}}}{(s-s_1)(s-s_2)} \quad , \tag{5.51}$$

and

$$C_1^{\mathrm{uc}} = s_1 s_2 \, , \quad C_2^{\mathrm{uc}} = -(s_1 + s_2) \quad , \tag{5.52}$$

respectively. Choosing s_1 and s_2 as carried out for the third-order system again leads to a transfer element with an almost ideal low pass behaviour within a sufficiently wide frequency range.

The state-space model in Eq. (5.28) for the force input and that in Eq. (5.48) for the displacement input are the basis for the investigations in the following sections. The question of how to realise the theoretical force or displacement input and the kinematic coupling of the actuators in a sufficiently precise manner is not dealt with here.

5.3 Controllability and Observability

Controllability and observability are basic characteristics of a dynamic system which crucially influence the feasibility of a later applied feedback control. With such a control, only the part of the system can be manipulated that is both controllable and observable. A system is called completely controllable if it can be transferred from an arbitrary initial state to any other state within a finite time interval by an appropriate system input. It is said to be completely observable if the initial state can be determined from the system input and output of a finite time interval that begins at time $t = 0$.

Before examining these properties for the actuator-extended systems, they are checked for the employed state-space model of the motion-induced aerodynamic forces, which is given in Eq. (3.18) and Eq. (3.10b) together with the entries either in Eq. (3.19), Eq. (3.20), or Eq. (3.22). This force model is connected to the structural system in a feedback loop, as already mentioned in Section 4.5. If parts of the aerodynamic system are uncontrollable or unobservable, they do not change these properties in the model of the aeroelastic system. The diagonal canonical form of the system matrix $\mathbf{R}$ of the aerodynamic state-space model is favourable for an investigation. Provided that the n_γ poles have different values, only the state variables in $\xi_{\mathrm{a},\mu}$, which belong to

one pole $(-\gamma_\mu)$, together with the associated system matrix $\mathbf{R}_\mu$, the input matrix $\mathbf{E}_\mu$, and the output matrix $\mathbf{D}_\mu$ must be considered. Moreover, the Gilbert criteria (Gilbert 1963) can be used to check controllability and observability. These criteria read as follows.
Provided that the state-space model has a diagonal canonical form, a system is completely controllable (observable) if and only if the input (output) matrix has no zero rows (columns) and the rows (columns) of the input (output) matrix that belong to the state variables with identical eigenvalues are linearly independent.
A derivative matrix of an aerodynamic transfer equation where all elements of the input vector are linearly independent and aerodynamically effective is the basis of the following investigations. Both the elements of the input and the output vector are assumed to be defined in an energetically corresponding manner without redundancies. From such a derivative matrix, several rows or columns can have been deleted. Cases with other derivative matrices are not addressed here, but they can be studied in a similar way.

The following statements hold true for all types of the addressed derivative matrix. If the Karpel approach is used for the approximation, the system $\mathbf{R}_\mu$ has just a single element. As the input matrix $\mathbf{E}_\mu$ is a non-zero row vector, the aerodynamic model is completely controllable. Complete observability is ensured because the output matrix $\mathbf{D}_\mu$ is a non-zero column vector. If the Roger approach is applied, two interesting cases can be discussed. First, the length of the input vector is shorter than that of the output vector. For the version in Eq. (3.19), the number of diagonal elements of $\mathbf{R}_\mu$ equals the length of the input vector. The input matrix $\mathbf{E}_\mu$ is an identity matrix whose rows are linearly independent. Hence, the system is completely controllable. The number of columns in the output matrix $\mathbf{D}_\mu$ is lower than the number of rows. In general, these columns are linearly independent and the system is, thus, completely observable. In contrast, for the version given in Eq. (3.20), the number of diagonal elements of $\mathbf{R}_\mu$ equals the length of the output vector. The output matrix $\mathbf{D}_\mu$ is an identity matrix with linearly independent rows. Complete system observability is thus given. However, the number of rows of the input matrix $\mathbf{E}_\mu$ is greater than the number of columns. In general, the number of linearly dependent rows equals the difference of the dimensions. Hence, this model version is not completely controllable. With the help of a Kalman decomposition, a subsystem of this Roger approach version can be found that is both controllable and observable. Such a subsystem, however, always has the same transfer behaviour as the total system. It is called the minimal realisation of the transfer function. Interestingly, the model with the matrices of Eq. (3.19) is such a subsystem. In the second case, the length of the input vector is longer than that of the output vector. Similar as argued before, the Gilbert criteria can be used to show that the aerodynamic system with the matrices in Eq. (3.20) is now completely observable and, in general, completely controllable. With the matrices in Eq. (3.19), however, the model is completely controllable but not completely observable. A Kalman decomposition can again be applied to show that now the model version based on Eq. (3.20) can be identified as a controllable and observable subsystem of the model

version with the matrices in Eq. (3.19). After considering the two cases, it is also clear that for systems with a single input or a single output, the Karpel approach is a controllable and observable subsystem of the Roger approach.

Based on the foregoing statements, a special case is explained below for quadratic derivative matrices. The matrices $\mathbf{D}_\mu$ in the version of Eq. (3.19) and $\mathbf{E}_\mu$ in the version of Eq. (3.20) are also quadratic in this case. As a consequence of the explanations in the last paragraph, complete controllability and complete observability is given for the Roger approach in general. Despite that, if the theoretical derivatives of flat plates in two-dimensional flow, which are introduced in Section 2.2.2 and Section 2.2.3, are well approximated with the Roger approach, parts of the aerodynamic system become either unobservable or uncontrollable. All columns and all rows of the $\mathbf{A}_{\mu+2}$ matrix $(1 < \mu < n_\gamma)$ linearly depend on each other for the theoretical flat-plate case, as already mentioned in Section 3.5.2. Hence, according to the Gilbert criteria, the aerodynamic model based on Eq. (3.19) is not completely observable and the model with the version of Eq. (3.20) is not completely controllable. There is a parallel interconnection of subsystems whose relevant dynamic properties are identical. A Kalman decomposition shows that the Karpel approach is an observable and controllable subsystem of a Roger approach. This is an additional explanation why the Karpel approach can be derived from a Roger approach for the theoretical flat-plate case.

In the model of the actuator-extended aeroelastic system, the dimensions of the uncontrollable and unobservable system parts that originate from the model of motion-induced aerodynamic forces remain the same although the numerical values of the eigenvalues change. However, these lacks of controllability and observability are a consequence of the mathematical description of the transfer behaviour of the motion-induced aerodynamic forces. To which extent the total flow can be influenced and ascertained, is not the question here. As explained before, the lacks can be avoided if a minimal realisation of the aerodynamic transfer function is chosen. If not otherwise specified, such a minimal realisation is assumed for the following explanations. Controllability and observability of the actuator-extended aeroelastic system are first discussed for the two-dimensional system, before the investigations are extended to the three-dimensional one.

For the two-dimensional system, the explanations starts with the state-space model given in Eq. (5.28), where the force $\mathbf{f}_\mathrm{c}$ is the system input. Complete controllability is given in general for all types of actuators. Although the input forces are connected to the actuator degrees of freedom, the actuator-typical couplings, which are described in Section 5.1, ensure the signal transfer to the bridge. The selection of the introduced actuators would not make sense if complete controllability was not given. However, exceptions exist at singular wind speeds. They are decisive for the actuator application and are addressed in the next sections.

Observability depends on the entries of the output vector. One or more entries of the structural state vector $\mathbf{x}_{\mathrm{st}}$, or combinations of them, can be measured. Questions concerning their measurement or the choice of suitable sensors are excluded from the investigations presented here. For several cases of possible outputs, the actuator-typical couplings are not sufficient to make the complete system observable. For instance, if control moment gyroscopes are employed, measuring the gimbal angle θ_{gy} is, in general, sufficient for a complete observation of the aeroelastic system, whereas only the knowledge of the bridge rotation α or the vertical translation h is not.

To circumvent this problem, an additional coupling between the bridge and the actuator can be introduced in terms of a weak spring-damper connection.

$$M_{\mathrm{rw}} = K_{\mathrm{s},\theta}\,\theta_{\mathrm{rw}} + C_{\mathrm{s},\theta}\,\dot{\theta}_{\mathrm{rw}} \tag{5.53a}$$

$$M_{\mathrm{gy}} = K_{\mathrm{s},\theta}\,\theta_{\mathrm{gy}} + C_{\mathrm{s},\theta}\,\dot{\theta}_{\mathrm{gy}} \tag{5.53b}$$

$$M_{\mathrm{fl,win}} = K_{\mathrm{s},\theta}\,\theta_{\mathrm{fl,win}} + C_{\mathrm{s},\theta}\,\dot{\theta}_{\mathrm{fl,win}}\,, \quad M_{\mathrm{fl,lee}} = K_{\mathrm{s},\theta}\,\theta_{\mathrm{fl,lee}} + C_{\mathrm{s},\theta}\,\dot{\theta}_{\mathrm{fl,lee}} \tag{5.53c}$$

Further arbitrary force inputs into the actuator-extended system are still possible. If a reaction wheel is applied and the displacement θ_{rw} is cancelled from the state, only a damper connection makes sense. In this case, the first summand must be deleted in Eq. (5.53a), and in the aeroelastic model, it is not possible to take it into account. The constants $K_{\mathrm{s},\theta}$ and $C_{\mathrm{s},\theta}$ can be included in damping and stiffness matrices of the respective actuators in the way shown for the actuator properties in Section 5.1. As a consequence of the additional coupling, the measurement of only one entry of the structural state $\mathbf{x}_{\mathrm{st}}$ is adequate for complete observability of the aeroelastic state $\mathbf{x}_{\mathrm{as}}$, in general. Depending on the output, exceptions can occur at the mentioned singular wind speeds where the aeroelastic system is not completely controllable. The lack of observability is connected to the same system part that is also not controllable. Since the absence of only one of these characteristics is enough to make a system part inaccessible for a closed-loop control, observability problems are usually not further addressed here.

In order to choose the numerical parameters of the spring-damper connection, the isolated actuators are considered and their vibration frequency is related to the first structural bending frequency of the bridge.

$$K_{\mathrm{s},\theta} = (0.1\omega_{\mathrm{s},h})^2 I_{\mathrm{rw},h}\,, \qquad C_{\mathrm{s},\theta} = 0.5\left(2I_{\mathrm{rw},h}(0.1\omega_{\mathrm{s},h})\right) \tag{5.54a}$$

$$K_{\mathrm{s},\theta} = (0.1\omega_{\mathrm{s},h})^2 I_{\mathrm{gy},l}\,, \qquad C_{\mathrm{s},\theta} = 0.5\left(2I_{\mathrm{gy},l}(0.1\omega_{\mathrm{s},h})\right) \tag{5.54b}$$

$$K_{\mathrm{s},\theta} = (0.1\omega_{\mathrm{s},h})^2 (I_{\mathrm{fl}}/2)\,, \quad C_{\mathrm{s},\theta} = 0.5\left(2(I_{\mathrm{fl}}/2)(0.1\omega_{\mathrm{s},h})\right) \tag{5.54c}$$

In the case of the flaps, a hinge position in their midpoint is assumed for this purpose, independent of their real position. Apart from the observability problem, spring-damper connections, which are fixed and unvarying devices, have the advantage of smoothly limiting the rotation and the

angular speed of the actuators. Without them, free motions of the actuators are possible, which are presumably difficult to handle from a technical point of view. The term free motion, or alternatively rigid body motion, is used here if double eigenvalues of the system matrix at the origin of the frequency plane occur that are connected to identical eigenvectors. A dynamic system which includes parts that have a free motion is unstable in the sense of Lyapunov. Figure 4.8(c) shows a simple example for a system with a free motion. A free motion of an actuator goes along with an eigenvector that only has non-zero entries in the degrees of freedom of the actuator. In the cases of the reaction wheel and the control moment gyroscope, respectively, the inertia and the gyroscopic couplings of the degrees of freedom alone cannot avoid such kinds of actuator motions. If flaps are employed, only the motion-induced aerodynamic forces can have a limiting effect on their rotations. The chosen numerical values of the weak spring-damper parameters are similar to those proposed in Preumont & Seto (2008) and Preumont (2011) for active mass dampers. Transferred to the reaction wheel, for instance, these values ensure that the total moment which is created by the spring, the damper, and the input $M_{\mathrm{rw}}(0+\mathrm{i}\omega)$ almost equals the input $M_{\mathrm{rw}}(0+\mathrm{i}\omega)$ in the range of the first structural eigenfrequency $\omega_{\mathrm{s},h}$ and higher frequencies. This statement is correct only if the angular acceleration of the bridge $\ddot{\alpha}$ is much smaller than the relative one $\ddot{\theta}_{\mathrm{rw}}$ of the reaction wheel.

If the two-dimensional system is described with Eq. (5.48), the actuator-displacements are not only included in the aeroelastic state vector $\mathbf{x}_{\mathrm{asu}}$ but also as $\mathbf{u}_{\mathrm{c}}$ in the input vector. The state $\mathbf{x}_{\mathrm{c}}$ of the low-pass third-order system should not be affected with a closed-loop control and is excluded after a system decomposition, which is described at the end of this section. Questions concerning controllability and observability of this state are superfluous. Again, the remaining structural state $\mathbf{x}_{\mathrm{st}}$ and the aerodynamic states in ξ_{a} are completely controllable, in general. Measuring only one entry of the structural state vector is, in general, sufficient to completely observe these aeroelastic states. A spring-damper connection between the actuator and the bridge is not necessary because the actuator displacements are not free motions. The aforementioned exceptions of complete controllability and observability that occur for the system with a force input at singular wind speeds also exist for the system with a displacement input. They are excluded from the discussion in this section.

Concerning the three-dimensional system, the forgoing statements must be extended. Uncontrollable or unobservable parts of the model of the motion-induced aerodynamic forces due to similar rows and columns in approximation matrices do usually not occur. One discrete actuator or flaps along a finite girder length are generally sufficient to control all structural and aerodynamic degrees of freedom. Using modal variables facilitates the understanding of the phenomenon. Even if a discrete actuator is positioned at a nodal point of a structural mode, controllability of this mode is given due to the aerodynamic coupling with other structural modes that have no nodal point there. As exceptions, two examples are mentioned in the following. A single reaction

wheel in the midpoint of the bridge is not able to control the antimetric structural modes. All these modes have a nodal point there, and they are not coupled with the symmetric structural modes. Moreover, identical reaction wheels that are arranged symmetrically around the middle of the bridge and that are kinematically coupled in terms of symmetric shapes cannot control antimetric structural modes. Further exceptions are addressed in the following sections. Observability of the three-dimensional system, with respect to physical or modal outputs, can be assessed in a similar way.

All foregoing statements concerning the properties of the actuator-extended aeroelastic systems can be confirmed numerically after defining numerical parameters. Especially the Hautus criteria (Hautus 1970) lend themselves for such a numerical investigation. They read as follows.
A system with the state matrix $\mathbf{A}_{\mathrm{sys}}$*, the input matrix* $\mathbf{B}_{\mathrm{sys}}$ *and the output matrix* $\mathbf{C}_{\mathrm{sys}}$ *is completely controllable (observable) if and only if the rank of the matrix*

$$\begin{pmatrix} (s_{\mathrm{sys},i}\mathbf{I}-\mathbf{A}_{\mathrm{sys}}) & \mathbf{B}_{\mathrm{sys}} \end{pmatrix} \qquad \left(\begin{pmatrix} (s_{\mathrm{sys},i}\mathbf{I}-\mathbf{A}_{\mathrm{sys}}) \\ \mathbf{C}_{\mathrm{sys}} \end{pmatrix} \right) \tag{5.55}$$

equals the number of rows of the system matrix $\mathbf{A}_{\mathrm{sys}}$ *for all of its eigenvalues* $s_{\mathrm{sys},i}$*.*
As long as eigenvalues are not multiple, controllability and observability can be related without problems to the single eigenvalues and the corresponding canonical state variables. Under this condition, the Hautus criteria can be applied to check the properties for every eigenvalue. If eigenvalues are multiple and connected to controllable and uncontrollable state variables, the criterion only says that at least one of the multiple eigenvalues is not controllable. The same holds for the observability problem.

To determine the rank of a matrix, the function `rank` of MATLAB (2007) is employed. This function utilises a singular value decomposition because the rank of the matrix equals the number of its singular values. According to the software help, it is said to be the most reliable method. Numerically, if for instance rows are almost, but not exactly, identical, the number of singular values is higher than the expected rank. Therefore, only the singular values that are larger than a tolerance are counted. Especially if the model with the displacement input in Eq. (5.48) is used, the singular values can considerably differ in their size due to the large absolute values of the low-pass filter eigenvalues. Hence, the tolerance must be set with care, and it depends on the particular system. The range of singular values should always be checked.

As already carried out in Chapter 4 for the analysis of the bridge, the minimal realisation of the transfer function of the motion-induced aerodynamic forces is not always chosen a priori in the work presented here. The Roger approach, for instance, is often used, though it can always be converted in the Karpel form for the theoretical two-dimensional flat-plate problems. The later

addressed controller-design algorithms, however, finally take the system part into account that can be influenced with a closed-loop control. As explained in the last paragraph, state variables of the system can be erroneously considered as controllable and observable due to small numerical variations of the entries in the state-space model. Working with these state variables can lead to absurd controller gains. Therefore, separating the system part that is both controllable and observable should not be blindly left to black-box functions of the used software.

The following algorithm is recommendable if the Roger approach leads to uncontrollable or unobservable eigenvalues or if the low-pass filter eigenvalues of a system with a displacement input must be separated. The system matrix is assumed to be diagonalisable and multiple eigenvalues should not occur. Usually, these preconditions are fulfilled for the investigated aeroelastic systems if free motions of the actuators are avoided and the eigenvalues of the low-pass filter are treated separately. Exceptions are addressed in the next sections. First, an eigenvalue analysis of the aeroelastic system is performed. Using the matrix $\mathbf{\Phi}$ of the eigenvectors for the transform

$$\mathbf{x}_{\mathrm{as}} = \mathbf{\Phi}\mathbf{x}^{\mathrm{m}}_{\mathrm{as}} \,, \quad \mathbf{x}_{\mathrm{asu}} = \mathbf{\Phi}\mathbf{x}^{\mathrm{m}}_{\mathrm{asu}} \tag{5.56}$$

leads to the state-space models in their diagonal canonical form. Taking for instance the model of Eq.(5.28), the result is

$$\dot{\mathbf{x}}^{\mathrm{m}}_{\mathrm{as}} = \mathbf{A}^{\mathrm{m}}_{\mathrm{as}}\mathbf{x}^{\mathrm{m}}_{\mathrm{as}} + \mathbf{E}^{\mathrm{m}}_{\mathrm{as}}\mathbf{d}^{\mathrm{g}}_{\mathrm{ae}} + \mathbf{B}^{\mathrm{m}}_{\mathrm{as}}\mathbf{f}_{\mathrm{c}} \tag{5.57a}$$

$$\mathbf{y}_{\mathrm{st}} = \mathbf{C}^{\mathrm{m}}_{\mathrm{as}}\mathbf{x}^{\mathrm{m}}_{\mathrm{as}} \quad , \tag{5.57b}$$

where

$$\mathbf{A}^{\mathrm{m}}_{\mathrm{as}} = \mathbf{\Phi}^{-1}\mathbf{A}_{\mathrm{as}}\mathbf{\Phi} \,, \quad \mathbf{E}^{\mathrm{m}}_{\mathrm{as}} = \mathbf{\Phi}^{-1}\mathbf{E}_{\mathrm{as}} \,, \quad \mathbf{B}^{\mathrm{m}}_{\mathrm{as}} = \mathbf{\Phi}^{-1}\mathbf{B}_{\mathrm{as}} \,, \quad \mathbf{C}^{\mathrm{m}}_{\mathrm{as}} = \mathbf{C}_{\mathrm{as}}\mathbf{\Phi} \quad . \tag{5.58}$$

The transformed system matrix $\mathbf{A}^{\mathrm{m}}_{\mathrm{as}}$ is a diagonal matrix with the eigenvalues on its main diagonal, as intended. In the next step, every eigenvalue of the system, apart from those of the low-pass filter in Eq. (5.48), is checked for controllability and observability with the Hautus criteria. The eigenvectors of all eigenvalues that are detected as uncontrollable or unobservable are removed from the modal matrix. In the same way, the eigenvectors of the low-pass filter are cancelled. From the inverse modal matrix, the rows corresponding to all cancelled columns of the modal matrix are also deleted. Again conducting the transformation shown above with the reduced matrices yields the part of the system that is fully accessible for a feedback control.

The disadvantage of the explained procedure is that the transformed state-space model has complex entries in the matrices and consequently complex entries in the state. They occur because some of the eigenvalues and eigenvectors are complex. Often, controller design algorithms only accept real models. The usual way to get a real model is not to use the complex eigenvector and

its always appearing complex-conjugate in the modal matrix but its real and imaginary part. For the model of Eq.(5.28), this means

$$\boldsymbol{\Phi} = \begin{pmatrix} \cdots & \begin{pmatrix} \breve{\mathbf{x}}_{\mathrm{as}} & \breve{\mathbf{x}}^{\mathrm{c}}_{\mathrm{as}} \end{pmatrix} \cdots \end{pmatrix} \rightarrow \boldsymbol{\Phi} = \begin{pmatrix} \cdots & (\ \mathrm{Re}(\breve{\mathbf{x}}_{\mathrm{as}}) & \mathrm{Im}(\breve{\mathbf{x}}_{\mathrm{as}}) \ ) \cdots \end{pmatrix} \quad . \tag{5.59}$$

As a consequence, the system matrix takes a block diagonal form.

$$\mathbf{A}^{\mathrm{m}}_{\mathrm{as}} = \begin{pmatrix} \ddots & & 0 \\ & \begin{pmatrix} s_{\mathrm{as}} & 0 \\ 0 & s^{\mathrm{c}}_{\mathrm{as}} \end{pmatrix} & \\ 0 & & \ddots \end{pmatrix} \rightarrow \mathbf{A}^{\mathrm{m}}_{\mathrm{as}} = \begin{pmatrix} \ddots & & 0 \\ & \begin{pmatrix} \sigma_{\mathrm{as}} & \omega_{\mathrm{as}} \\ -\omega_{\mathrm{as}} & \sigma_{\mathrm{as}} \end{pmatrix} & \\ 0 & & \ddots \end{pmatrix} \tag{5.60}$$

5.4 Numerical Actuator Parameters and Open-Loop Characteristics

Knowledge about the dynamic characteristics of the uncontrolled actuator-equipped aeroelastic systems is necessary for a thorough controller design and a sound investigation of the controlled systems. Since the systems described so far are later extended with a feedback control, which is also called closed-loop control, they are not only denoted as uncontrolled systems but also as open-loop systems. The detailed controller design is presented in the next section for the two-dimensional systems with the actuator parameters given in Table 5.1. These parameters have been chosen also with respect to technical feasibility.

Small actuator masses are desirable to avoid an unnecessary increase of the bridge self-weight. To be effective under tolerable actuator displacements, however, a certain inertia is indispensable for the reaction wheels and the control moment gyroscopes. As the flaps do not need a mass to be effective, their mass is roughly estimated with respect to a sufficiently capable design. All the moments of inertia are determined with an adequate accuracy. Due to the additional weight of the actuators, the stiffness of the cables slightly increases. This effect is assumed to be small and not taken into account. If flaps are employed, their hinge positions are assumed to be fixed and not shiftable. Normally, two mean directions of the approaching flow are possible. Hence, only symmetric hinge positions are investigated. If not otherwise specified, $b_{\mathrm{fl}} = 0.1\,b$, the hinge position C, and aerodynamic forces of the type Kü oga are assumed to limit the number of investigated cases. Both separately driven and kinematically coupled flaps are considered. If the direction of the horizontal reference wind velocity changes, the terms windward and leeward flap change their positions.

For the single flat plate, the rational function approximation of the aerodynamic derivatives with the Roger approach according to Eq. (3.32a) is used in the following sections. The aerodynamic

Table 5.1: Actuator properties in the 2d model.

reaction wheel	
wheel shape	circular ring
radius	$r_{\mathrm{rw}} = \frac{1}{9}b$
actuator distance	25 m
mass	$m_{\mathrm{rw}}^{\mathrm{pl}} = 0.05\,m$
mass moment of inertia	$I_{\mathrm{rw,h}}^{\mathrm{pl}} = m_{\mathrm{rw}}^{\mathrm{pl}} r_{\mathrm{rw}}^2$
control moment gyroscope	
rotor shape	circular ring
radius	$r_{\mathrm{gy}} = \frac{1}{9}b$
actuator distance	25 m
mass	$m_{\mathrm{gy}}^{\mathrm{pl}} = 0.05\,m$
mass moment of inertia	$I_{\mathrm{gy,h}}^{\mathrm{pl}} = m_{\mathrm{gy}}^{\mathrm{pl}} r_{\mathrm{gy}}^2$ $I_{\mathrm{gy,l}}^{\mathrm{pl}} = \frac{1}{2} m_{\mathrm{gy}}^{\mathrm{pl}} r_{\mathrm{gy}}^2$
spin speed of a rotor	$\Omega_{\mathrm{gy}} = 5\,C_{\mathrm{s},\alpha} / I_{\mathrm{gy,h}}^{\mathrm{pl}}$
flaps	
mass	$m_{\mathrm{fl}} = 0.1\,m\,b_{\mathrm{fl}}/b$
mass moment of inertia	$I_{\mathrm{fl}} = \frac{1}{3} m_{\mathrm{fl}} b_{\mathrm{fl}}^2$
hinge positions	(A) $d_{\mathrm{h,win}} = 1\,b_{\mathrm{fl}}$, $d_{\mathrm{h,lee}} = -1\,b_{\mathrm{fl}}$ (B) $d_{\mathrm{h,win}} = 0.5\,b_{\mathrm{fl}}$, $d_{\mathrm{h,lee}} = -0.5\,b_{\mathrm{fl}}$ (C) $d_{\mathrm{h,win}} = 0\,b_{\mathrm{fl}}$, $d_{\mathrm{h,lee}} = 0\,b_{\mathrm{fl}}$ (D) $d_{\mathrm{h,win}} = -0.5\,b_{\mathrm{fl}}$, $d_{\mathrm{h,lee}} = 0.5\,b_{\mathrm{fl}}$ (E) $d_{\mathrm{h,win}} = -1\,b_{\mathrm{fl}}$, $d_{\mathrm{h,lee}} = 1\,b_{\mathrm{fl}}$
kinematic couplings	(sd) same direction $\begin{pmatrix} \theta_{\mathrm{fl,win}} \\ \theta_{\mathrm{fl,lee}} \end{pmatrix} = \begin{pmatrix} 1 \\ 1 \end{pmatrix} \theta_{\mathrm{fl}}$ (od) opposite directions $\begin{pmatrix} \theta_{\mathrm{fl,win}} \\ \theta_{\mathrm{fl,lee}} \end{pmatrix} = \begin{pmatrix} 1 \\ -1 \end{pmatrix} \theta_{\mathrm{fl}}$
aerodynamic forces	(Kü) according to Küssner & Göllnitz (1964) (Th) according to Theodorsen & Garrick (1941)
gap between bridge and flaps	(oga) open gap (sga) sealed gap

derivatives of the plate with flaps are directly approximated with the Roger approach for the different hinge positions and several flap widths. When using the same settings that are described for the addressed single-plate approximation, a problem arises. Especially for small flaps, double poles with large coefficients are not unlikely to occur. Employing the poles of the C approximation given in the third block of Table 3.2 as initial pole locations is one method to avoid them. In the case of kinematically coupled flaps, a reduction of the number of aerodynamic states as mentioned in connection with Eq. (5.17) is not performed.

Figure 5.5, Figure 5.6, and Figure 5.7 show the eigenvalues of the actuator-equipped systems with a displacement input according to Eq. (5.48). With respect to the bridge, the actuators are

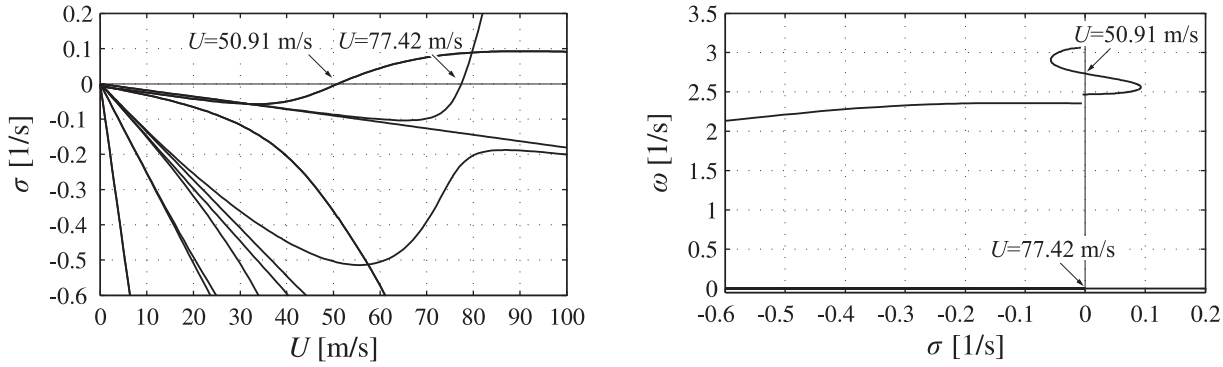

Figure 5.5: Eigenvalues of the 2d model of the aeroelastic system extended with reaction wheels. Displacement input.

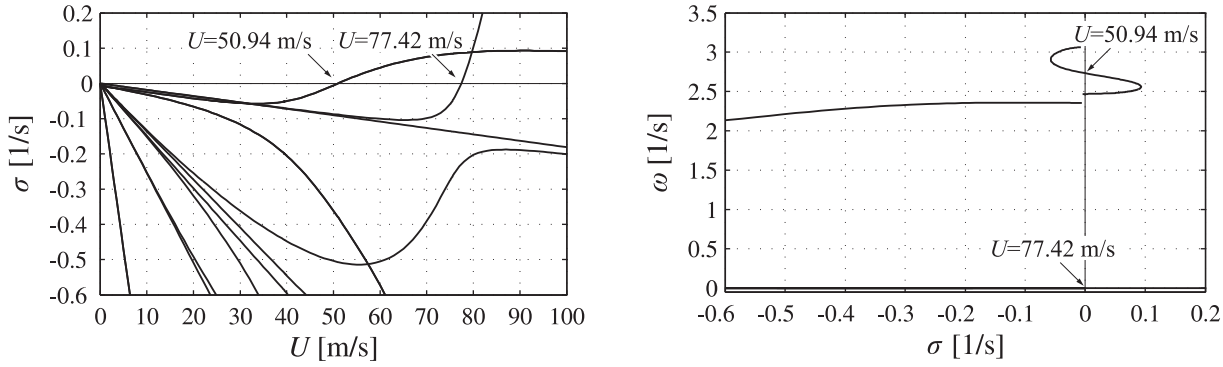

Figure 5.6: Eigenvalues of the 2d model of the aeroelastic system extended with control moment gyroscopes. Displacement input.

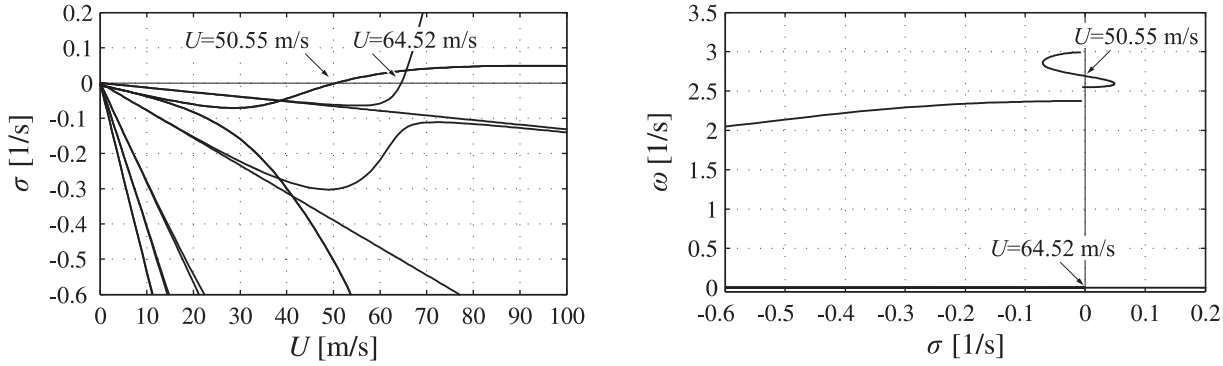

Figure 5.7: Eigenvalues of the 2d model of the aeroelastic system extended with flaps. Displacement input.

unmoved. When using a reaction wheel, the eigenvalues for both kinds of displacement inputs just differ in those of the low pass filter, which are far outside the displayed areas. Reaction wheels and control moment gyroscopes only marginally modify the inertia properties of the bridge. Hence, the flutter wind speeds almost equal that in Figure 4.7. The divergence wind speed, however, remains unchanged for both types of actuators. It only depends on the steady

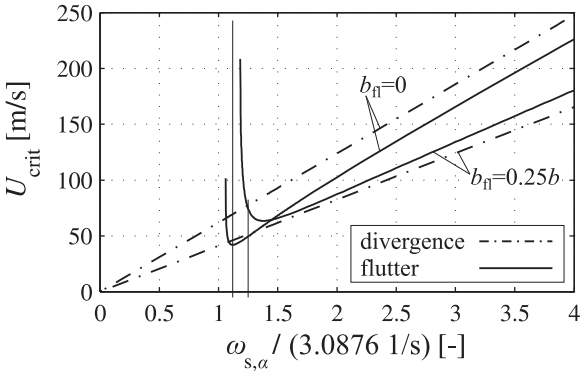

Figure 5.8: Influence of the varied torsional stiffness on the critical wind speeds.

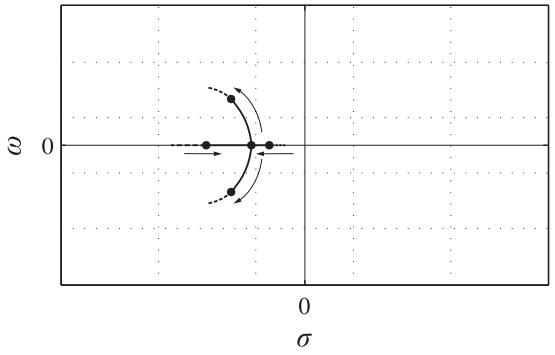

Figure 5.9: Sketch of a branching point.

aerodynamics of the bridge and the corresponding structural stiffness. Both properties are not modified with these actuators. That does not hold for attached flaps. They modify the admittance $\mathbf{G}_{\text{ae}}$ of motion-induced aerodynamic forces due to the broadened plate. Higher steady motion-induced aerodynamic forces lead to a lower divergence wind speed, as can be observed in Figure 5.7. As the flaps are unmoved, it does not matter if the flaps are kinematically coupled or not. The flutter wind speed is merely changed for the chosen numerical parameters. In general, this speed can be noticeably lower, higher, or a flutter instability can even not occur at all. Avoiding the flutter instability by means of a pure increase of the bridge width, however, is not desirable. Simultaneous to the change of the flutter wind speed, the divergence wind speed drastically decreases, the aeroelastic admittances become more unfavourable, and the gust-induced aerodynamic forces get higher.

In the work presented here, the effect of controlled actuator motions especially on aeroelastic instabilities is shown. Therefore, the numerical parameters of the bridge have been selected so that both kinds of aeroelastic instabilities occur for the uncontrolled actuator-extended systems. Figure 5.8 shows the critical wind speeds of the two-dimensional system for a varied torsional stiffness. The torsional moment of inertia I_{t} in Table 4.1 is adjusted to obtain a frequency ratio $\omega_{\text{s},\alpha}/\omega_{\text{s},h} = 1.25$. As can be seen, flutter occurs even if $b_{\text{fl}} = 0.25\,b$. For such a flap width, there is no flutter if $\omega_{\text{s},\alpha}/\omega_{\text{s},h} = 1.12$, which corresponds to the standard value of I_{t} in Starossek (1992).

Beginning with Figure 5.10, the eigenvalues of the actuator-equipped systems with a force input according to Eq. (5.28) are illustrated. The actuator motions are now degrees of freedom and occur as state variables in the state-space model. Figure 5.10 and Figure 5.11 show the eigenvalues of the bridge that is equipped with reaction wheels. The first pair of figures belongs to the model where θ_{rw} is included in the state vector. Due to the high ratio between the bridge and the actuator mass and due to the weak spring connection, there are two complex-conjugate

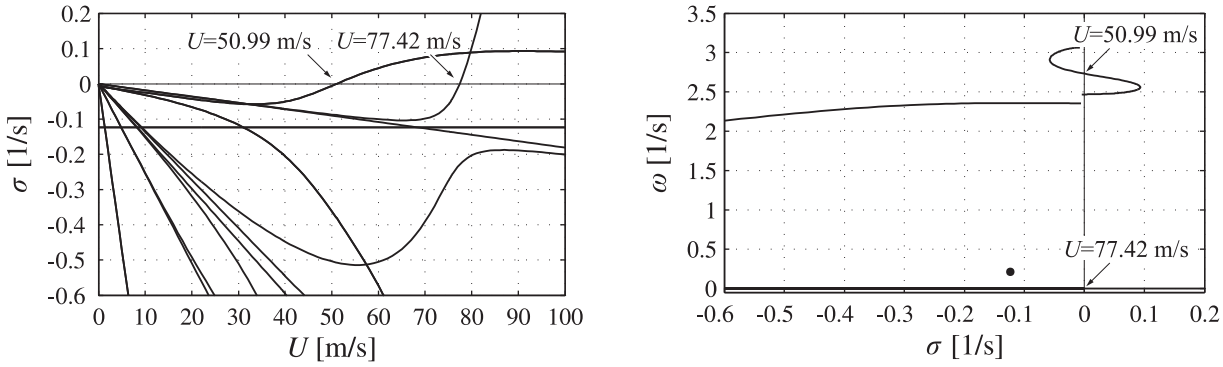

Figure 5.10: Eigenvalues of the 2d model of the aeroelastic system extended with reaction wheels. State includes θ_{rw}. Force input.

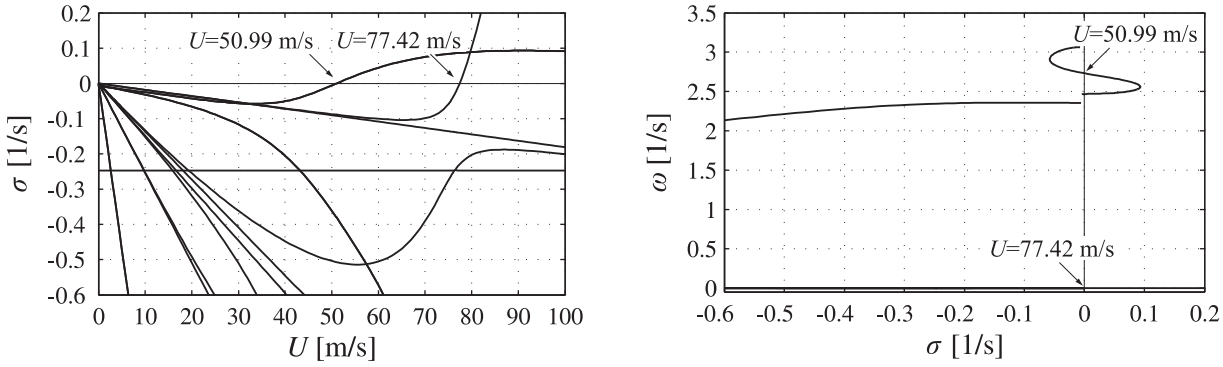

Figure 5.11: Eigenvalues of the 2d model of the aeroelastic system extended with reaction wheels. State does not include θ_{rw}. Force input.

eigenvalues whose eigenvectors have very dominant entries in the state variables of the wheel. These eigenvalues almost equal those of the isolated actuators and are almost not influenced by the reference wind speed U. All other eigenvalues are very similar to those of the bridge given in Figure 4.7. As explained for the displacement input, the divergence wind speed is not affected by the reaction wheel. The divergence eigenvector has zero entries in the state variables of the wheel. Because of the soft spring, the flutter wind speed is only marginally altered. As expectable, the relative wheel rotation appears in the flutter eigenvector with similar values as the bridge rotation, but with a phase shift of around π. The bridge motion with the flutter frequency excites the reaction wheel only a little. Figure 5.11 illustrates the eigenvalues when $\dot{\theta}_{\text{rw}}$, but not θ_{rw}, is included in the state vector. Compared to the first case, the main difference is that there is only one real eigenvalue and not a complex-conjugate pair as a consequence of the wheel. The numerical value is twice that of the real part of the complex conjugates, as it has to be. This statement can be confirmed when considering a simple isolated actuator, for instance.

If the bridge is equipped with control moment gyroscopes, the eigenvalues drastically change due to the gyroscopic couplings between the bridge and the gimbal rotation. The eigenvalues are displayed in Figure 5.12. In contrast to those of the reaction wheel, they cannot be approximately

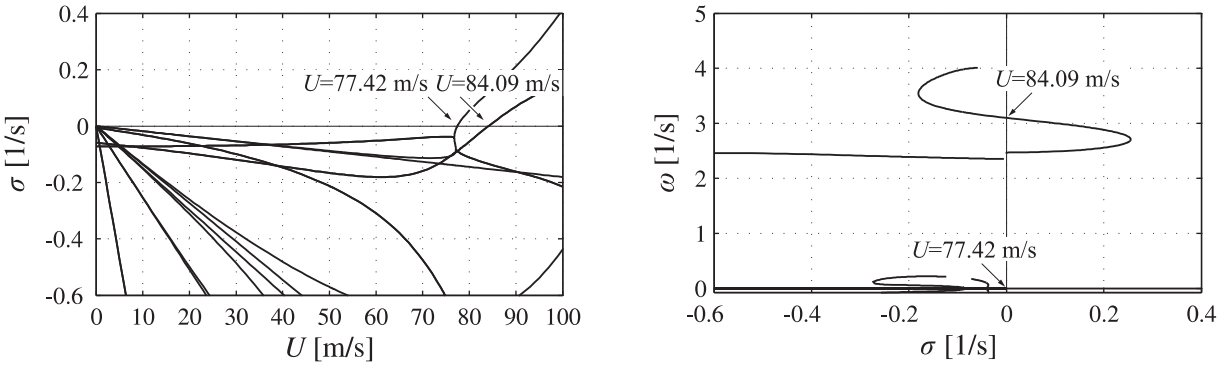

Figure 5.12: Eigenvalues of the 2d model of the aeroelastic system extended with control moment gyroscopes. Force input.

determined when considering the isolated systems. Only the divergence wind speed is not altered for the same reason that is given for the reaction wheel, and the corresponding eigenvector is again pumped up with zeros. The flutter wind speed is shifted to a value higher than that of the divergence wind speed. The flutter eigenvector is dominated by the state variables of the actuator. To conclude that such an actuator, whose degree of freedom is connected with a weak spring-damper connection to the bridge, is capable of improving the dynamic behaviour of the aeroelastic system, is wrong. A gust-input, for instance, is transferred to huge gimbal rotations that are contradictory to the model assumptions.

The eigenvalues of the flap-extended systems are shown in Figure 5.13, Figure 5.14, and Figure 5.15. Due to the small stiffness of the bridge-flap connection, there are transitions to instabilities that occur at very low wind speeds. The low critical speeds are not marked with their numerical values in the figures. If the flaps are separately driven, two crossings of the imaginary axis show the form of a divergence whose eigenvectors have dominant entries in the state variables of the flaps. Because of the distinctly higher elastic properties of the bridge, its rotation and translation are very small. The critical wind speeds at which the bridge state variables are involved in divergence and flutter eigenvectors have values in the range of those of the broadened bridge in Figure 5.7. They deviate due to the influence of the additional flap motions, whose size is in the range of the bridge motion. A similar behaviour can be observed when the flap angles are kinematically coupled. For sd-coupled flaps, the low critical wind speed is in connection with a flap divergence and for od-coupled flaps with a flap flutter. Remarkably, in the case of od-coupled flaps, the divergence wind speed has exactly the same value as that of the broadened bridge. The reason can be found in the theoretical aerodynamic forces. For the special coupling and the symmetry of the flap hinges, only a total steady lift L, but no steady moment M, can be generated with a rotation of the flaps. This holds true not only for Kü oga forces but also for Kü sga and Th sga ones.

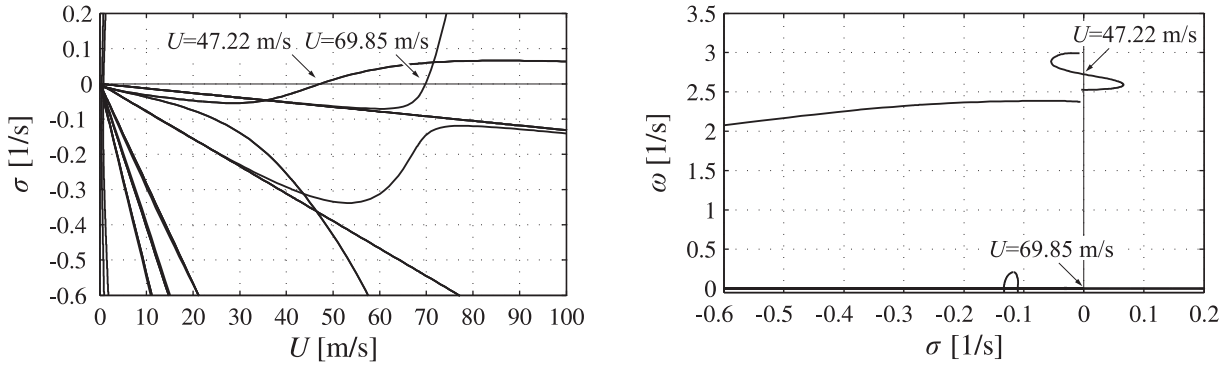

Figure 5.13: Eigenvalues of the 2d model of the aeroelastic system extended with separately driven flaps. Force input.

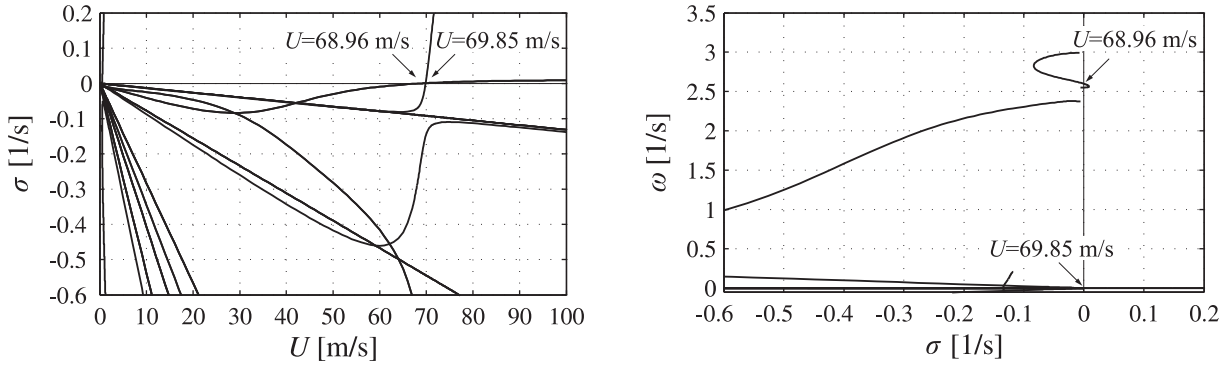

Figure 5.14: Eigenvalues of the 2d model of the aeroelastic system extended with sd-coupled flaps. Force input.

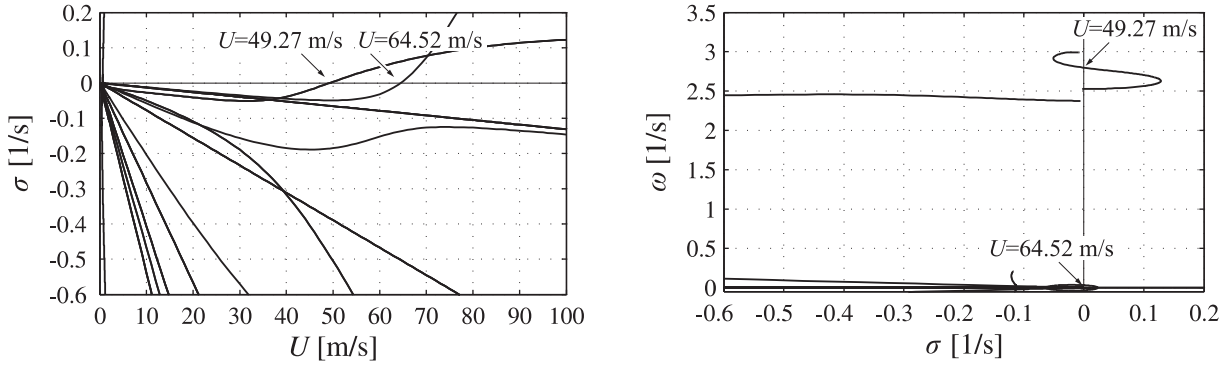

Figure 5.15: Eigenvalues of the 2d model of the aeroelastic system extended with od-coupled flaps. Force input.

The transfer characteristics of the uncontrolled actuator-equipped aeroelastic systems are not investigated beyond the statements given so far. For the fixed reaction wheel, for instance, it is similar to the bridge. For flaps with a force input, however, an uncontrolled system cannot be employed due to the unstable behaviour of the flaps.

There are interesting characteristics of the uncontrolled systems that have to be known when applying the algorithm described at the end of the last section. The first one concerns the occurrence of multiple eigenvalues that are in connection with identical eigenvectors. For the chosen mathematical description of aeroelastic systems, branching points of the eigenvalues at the real axis can arise. A sketch of such a point is given in Figure 5.9. Two complex-conjugate eigenvalues merge before they branch into two different real eigenvalues or vice versa. At the branching point, the eigenvectors must also be identical. Another transition from complex-conjugate to real eigenvectors is not possible. For the bridge in Figure 4.7, for instance, this behaviour can be observed at $U \approx 40\ \mathrm{m/s}$. The eigenvalue paths of the actuator-extended aeroelastic systems also have branching points. For the wind speeds that correspond to these points, the algorithm introduced at the end of Section 5.3 fails if at least one of the eigenvalues is controllable or observable. Either the Hautus criteria misinterpret eigenvalues to be uncontrollable or unobservable, or the system matrix of the minimal realisation is not diagonalisable. Especially if a diagonalisation is not possible, numerical problems can occur within a small speed range around these points.

Another phenomenon arises if several preconditions are fulfilled. A Roger approach according to Eq. (3.19) or Eq. (3.20) must be applied for the rational function approximation of the motion-induced aerodynamic forces, and the $\mathbf{A}_{\mu+2}$ matrices $(1 < \mu < n_\gamma)$ must have the rank one. As already mentioned, this happens for the two-dimensional aeroelastic systems whose aerodynamic forces are described with the theoretical flat-plate forces. Then, the system matrix $\mathbf{A}_{\mathrm{as}}$ of Eq. (5.28) for systems with a force input has n_γ groups of multiple eigenvalues at all wind speeds. The number of eigenvalues in each group equals the number of rows in $\mathbf{A}_{\mu+2}$ minus one if this matrix is quadratic. More than one eigenvalue in each group thus occurs for the two-dimensional flap-extended aeroelastic systems with a force input. Since all canonical states of the multiple eigenvalues are uncontrollable and unobservable, the Hautus criteria can be applied without problems. The number of different eigenvectors within a group of identical eigenvalues is irrelevant because the complete group is separated from the minimal realisation of the system with the described algorithm.

A separation does not work if, for instance, another eigenvalue of the system which belongs to the controllable and observable part crosses such a group of eigenvalues and simultaneously shares its eigenvector with them. At the crossing point, the Hautus criteria misinterpret the characteristic of the eigenvalue, and a diagonalisation of the system matrix of the minimal realisation is not possible. Due to the diagonalisation problem, the separation algorithm does not work properly within a speed range around the crossing point. The speed range can have a remarkable size if the eigenvalue curves cross each other at a very small angle.

If the two-dimensional system is extended with flaps and a force input is chosen, the latter phenomenon can be observed. To avoid it, the motion-induced aerodynamic forces are approximated with the Karpel approach in this case. When using this minimal realisation combined with a

force input, a system separation is not necessary at all. The settings of a derivative approximation with the Roger approach described in this section are also applied for an approximation with the Karpel approach. An illustration of the open-loop eigenvalues that result with a Karpel approach is not additionally given. Provided that the approximation poles are nearly identical, only the curves that belong to uncontrollable and unobservable eigenvalues have to be removed from Figure 5.13, Figure 5.14, and Figure 5.15.

5.5 Controller Design

The objective for the control of bridges is to attenuate the effect of acting disturbances. The aeroelastic system has to be stabilised if necessary, and the transfer of the disturbances to the structural states must be minimised as far as possible. Additionally, the controller design must fulfil a set of requirements. For instance, technical feasibility, economic efficiency, durability, as well as the robustness against model uncertainties must be taken into account. With a closed-loop control, the part of a dynamic system that is both controllable and observable can be manipulated in order to perform in a desired manner. Unwanted effects of the structural forces and the motion-induced aerodynamic forces on the transfer behaviour can be compensated to some extent. Through the use of a feedback loop, the inputs of the actuator-extended systems are made dependent on the measured outputs of the system. Measuring the output, that means the actual effects of the control input, and using this information for the control input has additional fundamental advantages. Even if the model quality is low or disturbances act that are not taken into account, the design objectives can often be satisfied in a sufficient way. This section addresses the feedback of the full aeroelastic state. How to obtain the state from the measured output with state observers is dealt with in a later section. A simple continuous-time state feedback with a linear, proportional controller $\mathbf{K}$ is sufficient to substantially change the dynamic characteristics of the system.

$$\mathbf{f}_\mathrm{c} = -\mathbf{K}\,\mathbf{x}_\mathrm{as}\,, \quad \mathbf{u}_\mathrm{c} = -\mathbf{K}\,\mathbf{x}_\mathrm{asu} \tag{5.61}$$

Alternatively, the controller is called a regulator because the control objective for bridges is not the tracking of a varying reference signal. The elements of the controller matrix are also termed controller gains. If the full aeroelastic state is not accessible or made available for the closed-loop control, the feedback is designed for the reduced states $\mathbf{x}_\mathrm{as}^\mathrm{m}$ or $\mathbf{x}_\mathrm{asu}^\mathrm{m}$ according to Eq. (5.56). Afterwards, the controller matrix is pumped up to the full state.

$$\mathbf{K} = \mathbf{K}^\mathrm{m}\boldsymbol{\Phi}^{-1} \tag{5.62}$$

Since the feedback law is linear, the controller can be designed in the frequency domain and the closed-loop behaviour of the aeroelastic system can be analysed there. A main advantage of state feedback is that all controllable eigenvalues can be arbitrarily placed in the frequency plane. To achieve the intended objectives, the controller is designed as a function of the system parameter, the reference wind speed U. For a real application, the current reference wind speed must be continuously updated by averaging a suitable number of previous measurements. In the design process, the controller gains are calculated for very closely spaced discrete nodes of the wind speed and cubically interpolated afterwards. There is no restrictive assumption for the gains in terms of analytical functions. This gain scheduling can be considered as adaptive control with one drawback. As gain scheduling has no feedback of the actual system behaviour, an incorrect schedule cannot be compensated. For a flow approaching from the right, the signs of some controller gains must be changed. The controller elements that connect translational with rotational quantities are affected by the flow direction.

The controller design usually leads to active controllers if the signs of the controller gains are not constrained. These kinds of controllers allow for a direct energy input into the system and in combination with state feedback, they are most favourable especially for a system stabilisation. To explore the capability of the different actuators under best circumstances, active controllers with state feedback are employed in the work presented here. Safety aspects of active stabilisation in permanent operation are not contemplated. At least for temporary construction stages of bridges with undesirable aeroelastic characteristics, active controllers seem to be a useful option.

If only the output of the system is used in the feedback equation together with a linear, proportional controller, the design objectives are much more difficult to reach. There is no guarantee as to whether a stable system, for instance, can be achieved at all. Compared to state feedback, such an output feedback can never give better results concerning the dynamic system characteristics. If, additionally, the signs of the controller gains are suitably constrained, passive controllers are obtained. Energy can only be dissipated with them. The introduced spring-damper connections in Eq. (5.53) can be seen as passive controllers. To effectively change the transfer characteristics of the aeroelastic system, their numerical parameters, however, must be defined differently from Eq. (5.54). A design of passive controllers is not addressed in this work. The passive controller gains of the spring-damper connection and some gains of the state feedback controller are related to the same signal paths. If they have identical signs, the passive gains can lower the force input that has to be applied by the controller. The other, undesirable case of higher control forces due to the passive gains is, however, also possible. This is another reason, why only weak spring-damper connections are chosen. For flaps, certain passive spring connections are necessary, in general, to compensate gravity effects, as indicated at the end of Appendix A.2. In oder to the simplify the analyses, they are also not addressed in the following.

Two popular algorithms are applied for the controller design of the state feedback. Both algorithms consider the natural response of the controlled system. Concerning the state-space model of the open-loop system, only the system matrix and the matrix of the control input, hence, the pair $(\mathbf{A}_{\mathrm{as}}, \mathbf{B}_{\mathrm{as}})$ or $(\mathbf{A}_{\mathrm{asu}}, \mathbf{B}_{\mathrm{asu}})$, are taken into account for the design of the controller. The pole-placement algorithm determines an appropriate controller matrix so that the eigenvalues of the closed-loop system matrix are placed at desired locations. Different pole-placement design algorithms are available in the technical literature. For systems with a single input, there is only one solution for the controller gains. For multiple-input systems, however, the controller matrix is not unique. In the work presented here, the function `place` of MATLAB (2007) based on the algorithm described in Kautsky & al. (1985) is used. If there is more than one input, the algorithm leads to controller gains that cannot be interpolated for a varying reference wind speed. This is one reason why pole placement is not preferred in this work. To obtain a stable transfer behaviour of the system with respect to all possible signal paths, the system does not only have to be stable but it must also be asymptotically stable. Achieving an asymptotically stable aeroelastic system with the pole-placement design is simple from the mathematical point of view. All unstable eigenvalues must be placed in the stable, left frequency plane. However, the question of how to shape the transfer function if only the pole locations are known is difficult to answer. The transfer function is not only determined by the location of the poles, as already mentioned in Section 4.7. Placing eigenvalues too far to the left requires a large control input and technical feasibility becomes questionable. If eigenvalues are placed too close to the imaginary axis, the resonance peaks in the frequency response become unacceptably high. A pole-placement design should primarily affect the eigenvalues that are furthest to the right in the frequency plane. As poles, they dominate the transfer function. Finally, their correct position must be found by trial and error.

A pole-placement controller design is only demonstrated for the two-dimensional system with reaction wheels and a displacement input where the state includes the wheel rotation θ_{rw}. The main design objective is to stabilise the aeroelastic system and to restrict the transfer of the disturbances within the speed range where the aeroelastic instabilities occur for the actuator-free bridge. Therefore, all eigenvalues that are to the right of a selected bound $\sigma_{\max}$ in the complex frequency plane are shifted to this bound along lines parallel to the real axis. Their imaginary values are kept constant. For an asymptotically stable system, the bound must be placed in the left frequency half-plane. It seems to be reasonable to select the real value of one of the structural eigenvalues as this bound.

$$\sigma_{\max} = -\omega_{\mathrm{s},\alpha} \frac{\delta_{\mathrm{s},\alpha}}{2\pi} \tag{5.63}$$

The main properties of the controller gains are addressed in connection with the second design algorithm because they are very similar.

In this work, the preferred design algorithm for a state feedback controller is that of the linear-quadratic regulator (lqr). The controller matrix is derived with the help of the optimal control theory. Mathematically, the design problem is expressed as the minimisation of a quadratic cost functional. The infinite-horizon continuous-time version of such a controller is applied here. For the aeroelastic system with a force input, for instance, the value of the integral

$$\int_0^\infty \left(\mathbf{x}_{\mathrm{as}}^{\mathrm{T}}(t)\mathbf{Q}_{\mathrm{lqr}}\mathbf{x}_{\mathrm{as}}(t)+\mathbf{f}_{\mathrm{c}}^{\mathrm{T}}(t)\mathbf{R}_{\mathrm{lqr}}\mathbf{f}_{\mathrm{c}}(t)\right)\,\mathrm{d}t \tag{5.64}$$

must be minimised. The state $\mathbf{x}_{\mathrm{as}}$ is the natural response as a consequence of an arbitrary non-zero initial-state. The input $\mathbf{f}_{\mathrm{c}}$ is defined by the time-invariant state feedback of Eq. (5.61). Only diagonal weighting matrices $\mathbf{Q}_{\mathrm{lqr}}$ and $\mathbf{R}_{\mathrm{lqr}}$ with positive, non-zero elements are used in this work for the controller design, though more arbitrary matrices are allowed from the viewpoint of optimal control theory. If the full aeroelastic state is not accessible or made available for the control loop, the matrix $\mathbf{\Phi}^{\mathrm{T}}\mathbf{Q}_{\mathrm{lqr}}\mathbf{\Phi}$ must be used to weight the reduced state. The integral does not only quantify how fast the state tends to zero but also the effort that is necessary for this. Due to the similarities between the natural response and the impulse response, also the transfer behaviour is shaped with this minimisation problem. To minimise the integral, the optimal gains of the controller matrix $\mathbf{K}$ must be found. The minimisation problem can be converted into the solution of an algebraic matrix Riccati equation. The whole procedure to determine the controller matrix is implemented in the function `lqr` of MATLAB (2007). The closed-loop system with the so found optimal controller is asymptotically stable. To ensure that the eigenvalues of the closed-loop system have a minimum distance from the imaginary axis, the design algorithm can be modified. If all eigenvalues should lie to the left of the bound $\sigma_{\max}$, the matrix $(-\sigma_{\max}\mathbf{I})$ must be added to the open-loop system matrices for the design of the controller. The main design problem of the linear-quadratic regulator is to choose reasonable values for the elements of the weighting matrices. Usually, the weights are found by trial and error. Compared to the pole placement design, however, reasonable controllers are often much easier to find.

The linear-quadratic regulators are designed for the two-dimensional models. These models, based on the first mode shape of the three-dimensional undamped structural system, cover the aeroelastic instabilities in the most relevant wind-speed range. Afterwards, the three-dimensional models are only investigated with respect to the abilities of the actuators for stabilisation. As described for the pole-placement design, the main focus is on the speed range where aeroelastic instabilities occur for the actuator-free bridge. With the weights given in Table 5.2 and the bound of Eq. (5.63), the controllers are designed for the different types of actuators and inputs. To effectively improve the transfer behaviour for lower speed ranges, other values must be chosen.

Specific characteristics of the controller gains are first addressed for the actuator-extended aeroelastic systems with a displacement input. For the bridge with reaction wheels where θ_{rw} is

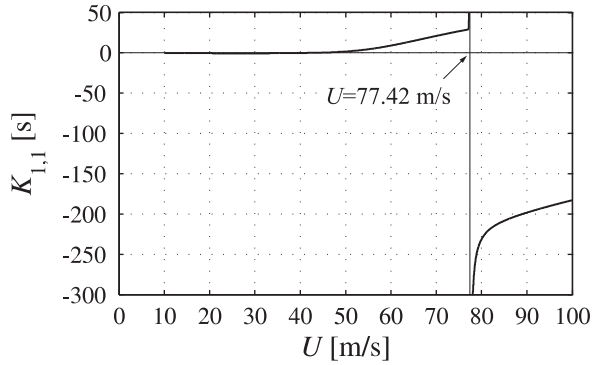

(a) Element of the controller matrix; lqr design.

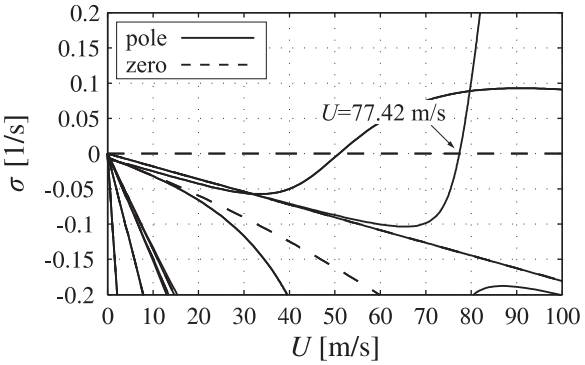

(b) Pole-zero plot ($\theta_{\mathrm{rw}}^{\mathrm{uc}} \rightsquigarrow \alpha$).

Figure 5.16: 2d model of the aeroelastic system extended with reaction wheels and a displacement input. State includes θ_{rw}.

Table 5.2: Diagonal weighting matrices $\mathbf{Q}_{\mathrm{lqr}}$ and $\mathbf{R}_{\mathrm{lqr}}$ of the controller design. All diagonal elements equal one unless otherwise specified in the table.

		force input	displacement input
rw	state includes θ_{rw}	$Q_{\dot{\theta}_{\mathrm{rw}}} = 10^6$, $Q_{\theta_{\mathrm{rw}}} = 10^6$	$R = 10^{-2}$
	state without θ_{rw}	$Q_{\dot{\theta}_{\mathrm{rw}}} = 10^6$	$R = 10^{-3}$
gy		$Q_{\dot{\theta}_{\mathrm{rw}}} = 10^7$, $Q_{\theta_{\mathrm{rw}}} = 10^7$	$R = 1$
fl	separately driven	$Q_{\dot{\theta}_{\mathrm{fl,win}}} = 5 \cdot 10^8$, $Q_{\theta_{\mathrm{fl,win}}} = 5 \cdot 10^8$, $Q_{\dot{\theta}_{\mathrm{fl,lee}}} = 5 \cdot 10^8$, $Q_{\theta_{\mathrm{fl,lee}}} = 5 \cdot 10^8$	$\mathbf{R} = 0.1\mathbf{I}$
	sd coupled	$Q_{\dot{\theta}_{\mathrm{fl}}} = 5 \cdot 10^8$, $Q_{\theta_{\mathrm{fl}}} = 5 \cdot 10^8$	$R = 0.1$
	od coupled	$Q_{\dot{\theta}_{\mathrm{fl}}} = 5 \cdot 10^8$, $Q_{\theta_{\mathrm{fl}}} = 5 \cdot 10^8$	$R = 0.1$

included in the state vector, Figure 5.16(a) shows a typical element of the controller matrix. The chosen weights obviously lead to a small gain in the low wind speed range.

For the theoretically described flow around the flat plate, translation and rotation become decoupled for $U \to 0$ because the $\mathbf{A}_2$ matrix is diagonal. As the wheel rotation is only coupled with the rotation of the bridge, the translation cannot be influenced at this zero speed. Complete controllability is thus not given there. Depending on the chosen output, complete observability can also vanish. At the transition from a non-zero to the zero speed, the coupling decreases. For the zero wind speed, it is interesting to consider the eigenvalue of the open-loop system whose eigenvector has in the structural part a non-zero entry only in the translational variables. This eigenvalue cannot be influenced with a control input. If the lower bound $\sigma_{\max}$ is to the left of this eigenvalue, as is the case for the numerical example, the design objectives cannot be reached for the zero speed. For slightly higher wind speeds, a high control input is necessary to compensate the decreasing coupling. At least some of the controller gains thus have a pole-like singularity at $U = 0$. The width of the high control gains depends on the distance between the uncontrollable

eigenvalue and the chosen bound. Since the controller design is not aimed at low reference wind speeds, the gain is not displayed there in Figure 5.16(a).

A further pole-like singularity is visible at the divergence wind speed $U = 77.42\ \mathrm{m/s}$. It appears in almost all elements of the controller matrix. The reason is an eigenvalue at the origin of the frequency plane that is not controllable. It cannot be stabilised with a closed-loop control. This eigenvalue is stable but not asymptotically stable. Input-output stability is thus not given for all possible signal paths. For a displacement in the divergence mode, there is no aeroelastic stiffness anymore. Asymptotic stability moreover necessitates a unique equilibrium state, which is not given there. At the divergence wind speed, a steady disturbing moment, for instance, could only be compensated with a steadily accelerated wheel rotation to avoid unbounded displacements of the bridge. A steady wheel acceleration is not acceptable from the technical point of view. Hence, it is necessary to include at least the angular speed in the state vector. Since the rotation and the angular speed are in the state vector, the system would not be asymptotically stable. The instability is only shifted from the bridge to the reaction wheel. A pole-zero plot of a signal path can be used to visualise the uncontrollability. Figure 5.16(b) shows the real parts of the poles and zeros for the transfer from the control input $\theta_{\mathrm{rw}}^{\mathrm{uc}}$ to the bridge rotation α. For all reference wind speeds, there is a transfer zero at the origin of the frequency plane. This transfer zero describes the inability of the reaction wheel to be effective if it has a steady rotation angle. At the divergence wind speed, there is the cancellation of the zero at the origin and the pole that is connected to the divergence eigenvalue. In a single signal path, which is identical to a single-input single-output system, a pole-zero cancellation is always related to an input-decoupling zero or an output-decoupling zero and thus an uncontrollable or an unobservable eigenvalue, respectively. As the gain of the state-feedback controller shows the singularity, the eigenvalue is at least uncontrollable. When approaching the divergence wind speed, the controllability of this eigenvalue decreases. The controller design algorithm tries to compensate this with increased controller gains. The gain thus tends to infinity when the eigenvalue becomes uncontrollable. The lower the chosen bound $\sigma_{\max}$, the wider is the pole area. Investigations that model the reaction wheel only with an arbitrary external force on the bridge or in an equivalent way (e. g. Körlin & Starossek 2004) are inappropriate. For such models, controllability is ensured for all wind speeds and the gain singularity at the divergence wind speed does not occur.

Below and above the divergence wind speed, where one eigenvalue crosses the imaginary axis, some of the controller gains considerably differ and, moreover, they have unequal signs. The gain displayed in Figure 5.16(a) is an example of that behaviour. The flutter wind speed of the actuator-extended aeroelastic system, where two complex-conjugate eigenvalues cross the imaginary axis, does not constitute such a significant point for the dimensioning of the controller. Related phenomena are known from other examples of system stabilisation (e. g. Magnus 1971, Ferry 1932).

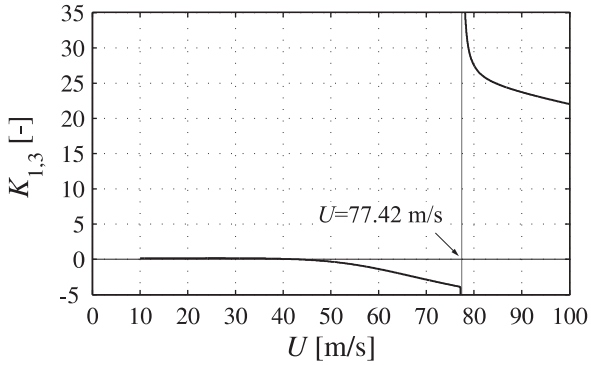

(a) Element of the controller matrix; lqr design.

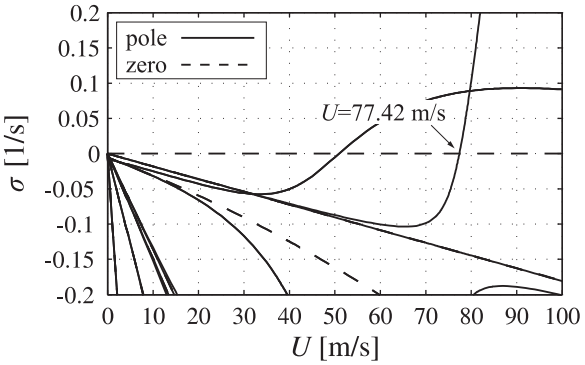

(b) Pole-zero plot ($\theta_{\mathrm{gy}}^{\mathrm{uc}} \rightsquigarrow \alpha$).

Figure 5.17: 2d model of the aeroelastic system extended with control moment gyroscopes. Displacement input.

For the application of reaction wheels where θ_{rw} is excluded from the state vector and the application of control moment gyroscopes, the same phenomena that are described for the case before appear in some of the controller gains. There is again the decoupling for $U \to 0$ if the theoretical flat-plate forces are used, and at the divergence wind speed, the eigenvalue at the origin of the frequency plane is uncontrollable. If reaction wheels are employed without θ_{rw} in the state vector, explanations can be found in the way given before. They are not listed in detail for the sake of brevity. For control moment gyroscopes, the situation is a bit different. According to Eq. (5.22), they can impose a constant moment on the bridge when the rotors are tilted with a constant angular speed around the gimbal axes. It has to be kept in mind, however, that the equation of motion is derived for small tilting angles. For larger angles, the imposed moment is not constant. It even changes its direction. Hence, including the tilting angle and the tilting rate in the state vector is necessary. For the application of the control moment gyroscopes, a striking gain and the pole-zero plot of a signal path is given in Figure 5.17.

If flaps are employed, their total effect on the aeroelastic system for $U = 0$ is not investigated. At this wind speed, their consequence on the aerodynamic forces due to the entries in the $\mathbf{A}_2$ matrix is very low. A possible generation of inertia forces by accelerating the flaps is not intended. Concerning the controller gains for non-zero wind speeds, it has to be distinguished whether the flaps are kinematically coupled or not. If separately driven flaps are used, the controller gains do not have any singularities for non-zero reference wind speeds. All the eigenvalues that are not asymptotically stable are controllable and can be shifted in the left frequency plane.

For sd-coupled flaps, most of the controller gains have a pole-like singularity at $U = 74.12\ \mathrm{m/s}$. Figure 5.18(a) is given as an example. With the help of the pole-zero plot in Figure 5.18(b), the reason can be found in terms of an uncontrollable eigenvalue at $s = 0.4810\ 1/\mathrm{s}$, this means an eigenvalue in the unstable frequency plane. When moving the flaps with the frequency of a transfer function zero, the steady-state effect of the generated aerodynamic and structural forces

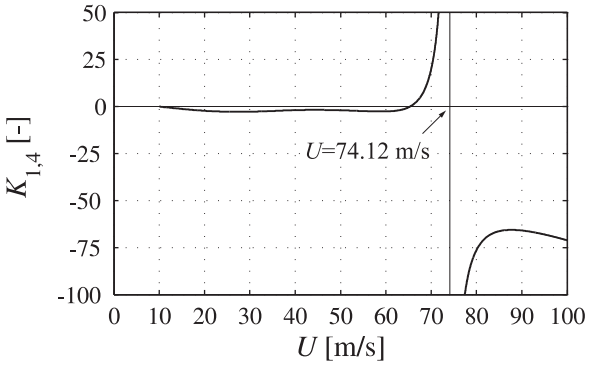

(a) Element of the controller matrix; lqr design.

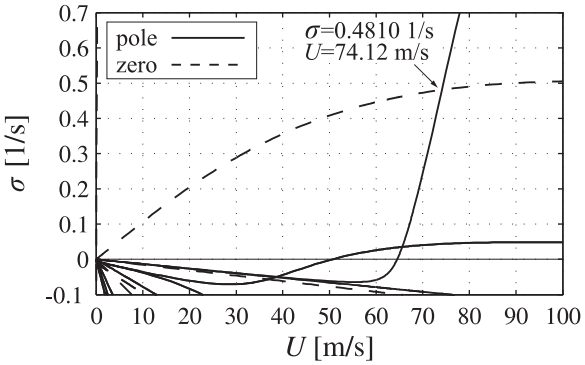

(b) Pole-zero plot ($\theta_{\mathrm{fl}}^{\mathrm{uc}} \rightsquigarrow \alpha$).

Figure 5.18: 2d model of the aeroelastic system extended with sd-coupled flaps. Displacement input.

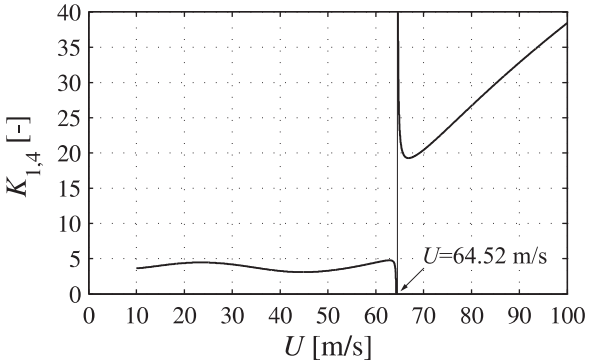

(a) Element of the controller matrix; lqr design.

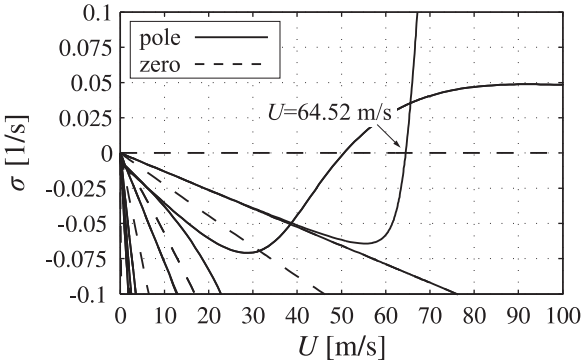

(b) Pole-zero plot ($\theta_{\mathrm{fl}}^{\mathrm{uc}} \rightsquigarrow \alpha$).

Figure 5.19: 2d model of the aeroelastic system extended with od-coupled flaps. Displacement input.

on the bridge rotation equals zero. If a natural response of the system has an eigenvalue of the same size, it cannot be sufficiently affected with the input. Similar controllability problems are mentioned in Edwards (1977) for force inputs on the leeward flap of an aircraft wing. The uncontrollable eigenvalue decisively depends on the aerodynamic forces. The reason for its occurrence is not a bad quality of the rational function approximation. At $p = 0.05841$, the highest relative deviation of an approximated element of the derivative matrix from its exact theoretical value is 0.62 %, the mean deviation of all elements is just 0.068 %. Table 5.3 gives the reference wind speeds U at which the gain singularities occur for different hinge positions and flap widths. For some of the investigated cases, there is no singularity at all. If the gaps between the flaps and the bridge girder are sealed, the results are identical for Th and Kü forces. The differences between both models of aerodynamic forces, which are addressed at the end of Appendix A.1, only concern derivatives that are not included in the flap-extended system with a displacement input. The results in Table 5.3 demonstrate the importance of the aerodynamic force model and of a sufficiently precise rational function approximation.

Table 5.3: Reference wind speed U [m/s] at which an unstabilisable eigenvalue occurs in the 2d model of the aeroelastic system extended with sd-coupled flaps and a displacement input.

			A	B	C	D	E
$b_{\mathrm{fl}} = 0.1\,b$	Kü	oga	74.21	74.17	74.12	74.07	74.03
	Kü, Th	sga	–	–	67.17	70.64	74.03
			$b_{\mathrm{fl}} = 0.05\,b$	$b_{\mathrm{fl}} = 0.1\,b$	$b_{\mathrm{fl}} = 0.15\,b$	$b_{\mathrm{fl}} = 0.2\,b$	$b_{\mathrm{fl}} = 0.25\,b$
C	Kü	oga	75.25	74.12	74.33	76.32	80.70
	Kü, Th	sga	71.89	67.17	63.11	59.55	56.42

Od-coupled flaps lead to pole-like singularities in some controller gains at $U = 64.52$ m/s, as shown in the example of Figure 5.19(a). This is the divergence wind speed of the open-loop system. The eigenvalue that is at the origin of the frequency plane at this wind speed is not controllable. The reason is given in the foregoing section. Based on the theoretical flat-plate forces and the investigated flap configurations, no steady moment M can be generated with a flap rotation. The ability to generate such a moment, however, is the precondition to modify the unfavourable eigenvalue. In Figure 5.19(b), the pole-zero-plot is given for the signal path from the flap rotation $\theta_{\mathrm{fl}}^{\mathrm{uc}}$ to the bridge rotation α. Apart from the pole-zero cancellation, the figure illustrates the inability of od-coupled flaps to excite a rotation of the bridge in the steady-state response to a steady flap rotation.

If the actuator extended systems have a force input, the uncontrollable eigenvalues and the wind speeds with pole-like singularities in the controller gains occur with the same numerical values as explained for the displacement input. The uncontrollable eigenvalues can again be illustrated with pole-zero plots, as given in Figure 5.20. Only the case where θ_{rw} is included in the state is shown for the reaction wheel. The results are similar if θ_{rw} is not included. For the selected signal paths, the output energetically corresponds to the input. These pole-zero plots are interesting because the zeros of the transfer function are the eigenvalues of the systems where the degree of the output is blocked (Preumont 2011). Due to an internal resonance, the state of the system, but not the special output, is excited by the input if it appears with the frequency of a zero. Hence, the poles are the eigenvalues that are displayed in Figure 5.10, Figure 5.12, Figure 5.14, and Figure 5.15. The zeros are the eigenvalues of Figure 5.5, Figure 5.6, and Figure 5.7. For the reaction wheel, most poles and zeros are almost, but not exactly, identical in contrast to the other displayed cases. Therefore, they cannot be optically distinguished with the chosen resolution of the figure. Only the poles that are connected to the wheel-dominated eigenvalues have no accompanying zeros. This means that the transfer function is merely affected by the actuator-free aeroelastic system. As a consequence, it can be expected that the transfer from the input to the bridge displacements is much lower compared to the transfer to the wheel rotation. It has to be kept in mind that for Figure 5.20(c) and Figure 5.20(d), the Karpel approach is now used in contrast to the Roger approach that is employed for the figures in Section 5.4. Poles and zeros

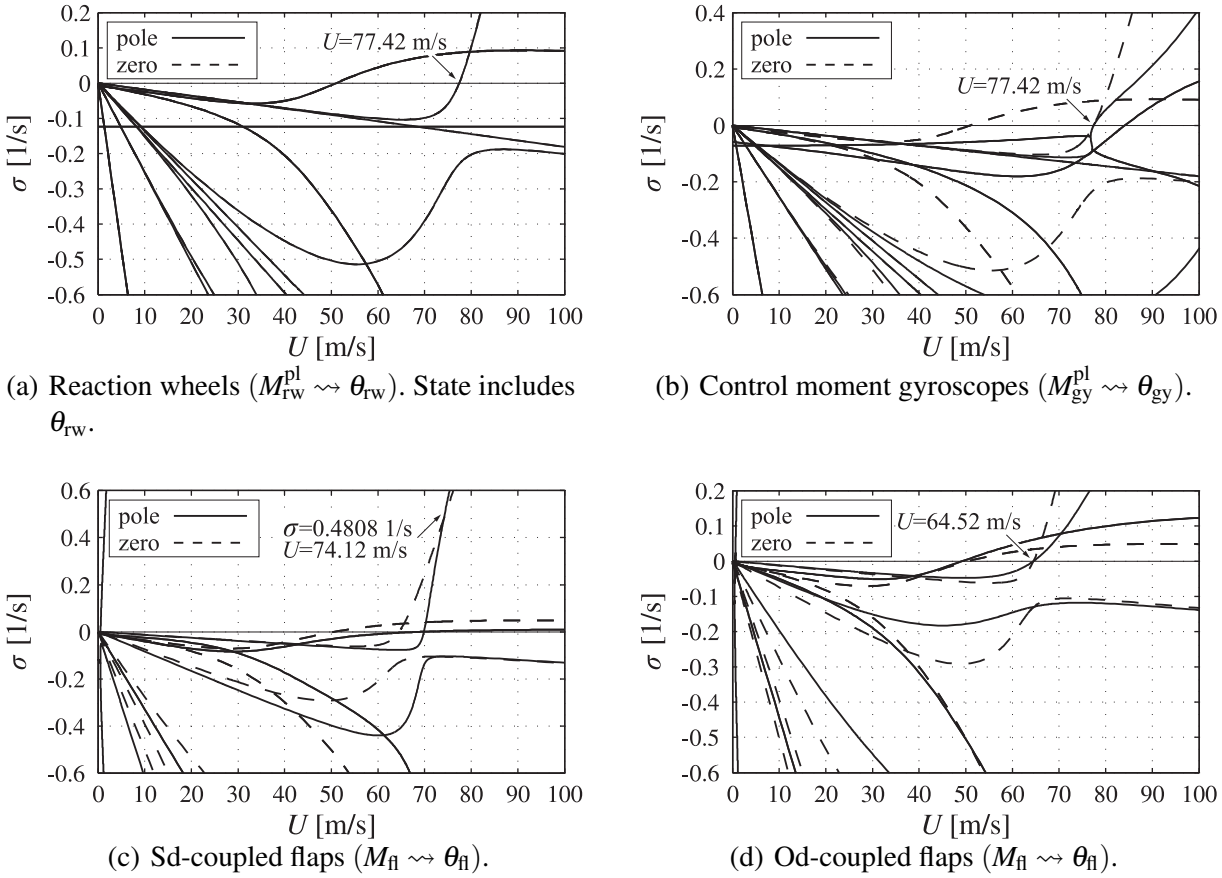

(a) Reaction wheels ($M_{\mathrm{rw}}^{\mathrm{pl}} \rightsquigarrow \theta_{\mathrm{rw}}$). State includes θ_{rw}.

(b) Control moment gyroscopes ($M_{\mathrm{gy}}^{\mathrm{pl}} \rightsquigarrow \theta_{\mathrm{gy}}$).

(c) Sd-coupled flaps ($M_{\mathrm{fl}} \rightsquigarrow \theta_{\mathrm{fl}}$).

(d) Od-coupled flaps ($M_{\mathrm{fl}} \rightsquigarrow \theta_{\mathrm{fl}}$).

Figure 5.20: Pole-zero plots of the 2d model of the actuator-extended systems. Force input.

that are identical at all wind speeds for the Roger approach do not exist for the Karpel approach. Compared to Figure 5.18(b), the numerical value of the uncontrollable eigenvalue that appears for sd-coupled flaps in the right frequency plane slightly differs due to the other rational function approximation.

In the next section, it is explained that a wind speed is a fundamental upper limit for the application of an actuator if there is an uncontrollable eigenvalue that is not asymptotically stable. Concerning reaction wheels and control moment gyroscopes, uncontrollable eigenvalues at the origin of the frequency plane also occur if three-dimensional models are used. Since there are more divergence wind speeds, theoretically derived controller gains show poles at several reference wind speeds. The physical background is the same as described for the two-dimensional models. The decisive lowest divergence wind speed equals that of the two-dimensional models. Concerning the upper application limit of both actuators, no new insights are gained from three-dimensional models.

The three-dimensional model gets more interesting when flaps are employed as actuators. Table 5.4 shows the reference wind speeds up to $U = 200\ \mathrm{m/s}$ for which uncontrollable eigenvalues occur that are not asymptotically stable. The model size of the flap-extended system is reduced

Table 5.4: Reference wind speeds U [m/s] in the interval $0 < U \leq 200$ m/s at which uncontrollable eigenvalues occur that are not asymptotically stable. Flaps are employed as actuators in the 3d model.

flap position	case no.	input shapes	separately driven	sd coupled	od coupled
	i	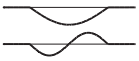	191.10	74.18 147.50 191.10	64.52 129.04 191.10 193.58
	ii	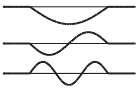	191.10	147.50 191.10	
	iii	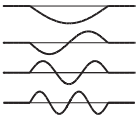	191.10	191.10	
	iv		–	74.83 149.06	
	v	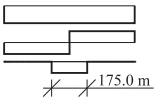	–	149.06	
	vi	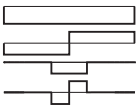	–	–	
	vii		191.10	74.83 149.06 191.10	
	viii		191.10	191.10	
	ix		191.10	74.53 147.50 191.10	
	x	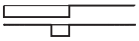	191.10	191.10	
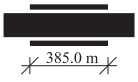	xi	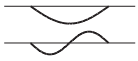	–	74.18 147.49	64.52 129.04 193.58
	xii	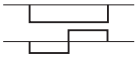	–	74.36 147.52	
	xiii	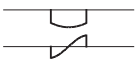	–	76.61 160.81	66.86 141.95
	xiv	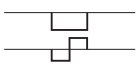	–	76.64 160.58	

according to Eq. (5.17) using the 14 lowest bending and the 14 lowest torsional modes of the undamped, actuator-free structure. The kinematic couplings that are applied for each row of flaps

are illustrated in the third column of the table. Three different arrangements of flaps along the bridge length are investigated. Flaps along the total bridge length, flaps in the main span, and flaps along 175 m around the centre of the main span. For each arrangement, different input shapes or combinations of them are analysed. As input shapes, the torsional mode shapes of the actuator-free undamped bridge or shapes with identical rotations of several flaps are applied. All results are determined for a flap half-width $b_{\mathrm{fl}} = 0.1\,b$, the hinge position C, and Kü oga forces. As long as flaps are installed all along the bridge girder, the rational function approximation of the derivative matrix is derived from the approximation of the two-dimensional case explained in Section 5.4. Otherwise the derivative matrix of the three-dimensional model with the reduced number of degrees of freedom is approximated in the same way as described in Section 4.3 using the Roger approach with $Q_{\min} = 0$ and $n_\gamma = 5$ poles. Again, the poles of the C approximation given in the third block of Table 3.2 are employed as initial values to avoid multiple poles. Searching singularities in the feedback gains of a state feedback leads to the results displayed in Table 5.4.

First, the results for flaps all along the girder are explained. As described for the two-dimensional model, od-coupled flaps cannot generate steady moments and thus not change the divergence wind speeds of the bridge with unmoved flaps. Four divergence wind speeds occur in the considered wind speed range. The third speed, $U = 191.10\,\mathrm{m/s}$, is related to a divergence mode with a torsional rotation of the side spans. The others occur with torsional rotations of the main span. As long as flaps are unmoved in at least one of the side spans, a divergence at $U = 191.10\,\mathrm{m/s}$ cannot be avoided with separately driven or sd-coupled flaps either. Hence, even if the flaps are separately driven, wind-speed limits for their application can exist. For sd-coupled flaps, the critical wind speed known from the two-dimensional model can also occur. This speed is connected to a symmetric mode shape. The similarity between the results of the two-dimensional and the three-dimensional model can be seen as a sign for a good convergence of the finite-element solution if flaps are modelled. Moreover, there can be another limit in the examined wind speed range at around $U \approx 150\,\mathrm{m/s}$ that is associated with an antimetric mode shape. In contrast to the two-dimensional model, both limits can be overcome if an additional independent symmetric or antimetric input shape is used, respectively. The latter findings are not restricted to input shapes in terms of structural eigenmodes, as can be seen from the results of the cases i–iii and the cases iv–vi. The number of input shapes can be halved if asymmetrical ones are used. For a demonstration of this statement, the cases vii, viii and the cases ix, x are displayed in the table. Whether such input shapes are suited to efficiently suppress the effect of disturbances is another question. For the second flap arrangement with flaps only in the main span, two cases are analysed. The divergence wind speed that is connected with a torsional rotation of the side spans is higher than before due to the lower total deck width, and it is above the upper limit of the investigated wind-speed interval. No flap motion can avoid this divergence because there are no flaps in the side spans. All other results are similar to those of case i and

case iv. For the third flap arrangement, flaps are only employed along a part around the centre of the main span. Although the wind speed limits that are connected with more than one antinode in the main span get higher values due to the partially lower total deck width, the decisive lowest wind-speed limits are merely changed. For the latter ones, the flaps are still positioned in the influential parts of the span.

5.6 Closed-Loop Characteristics

Inserting the feedback approaches of Eq. (5.61) into the state space models in Eq. (5.28) and Eq. (5.48) leads to the state equations of the closed loops

$$\dot{\mathbf{x}}_{\text{as}} = \mathbf{A}_{\text{as,cl}}\mathbf{x}_{\text{as}} + \mathbf{E}_{\text{as}}\mathbf{d}_{\text{ae}}^{\text{g}} \tag{5.65}$$

$$\dot{\mathbf{x}}_{\text{asu}} = \mathbf{A}_{\text{asu,cl}}\mathbf{x}_{\text{asu}} + \mathbf{E}_{\text{asu}}\mathbf{d}_{\text{ae}}^{\text{g}} \quad , \tag{5.66}$$

where

$$\mathbf{A}_{\text{as,cl}} = \mathbf{A}_{\text{as}} - \mathbf{B}_{\text{as}}\mathbf{K} \tag{5.67}$$

$$\mathbf{A}_{\text{asu,cl}} = \mathbf{A}_{\text{asu}} - \mathbf{B}_{\text{asu}}\mathbf{K} \quad . \tag{5.68}$$

The output equations in both models remain unchanged. In this section, the closed-loop characteristics are analysed for the two-dimensional models with the different actuators and controllers that are introduced in the foregoing sections.

Figure 5.21 shows the closed-loop eigenvalues of the controlled system that is chosen in the last section as an example for the pole-placement controller design. As described, the bridge is extended with reaction wheels, the system has a displacement input, and the state-space model

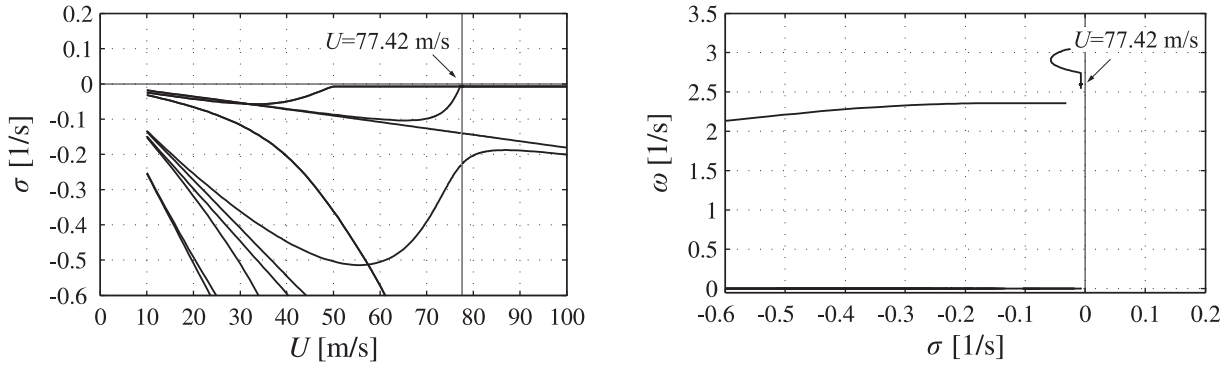

Figure 5.21: Closed-loop eigenvalues of the 2d model of the aeroelastic system extended with reaction wheels. State includes θ_{rw}. Displacement input. Pole-placement design.

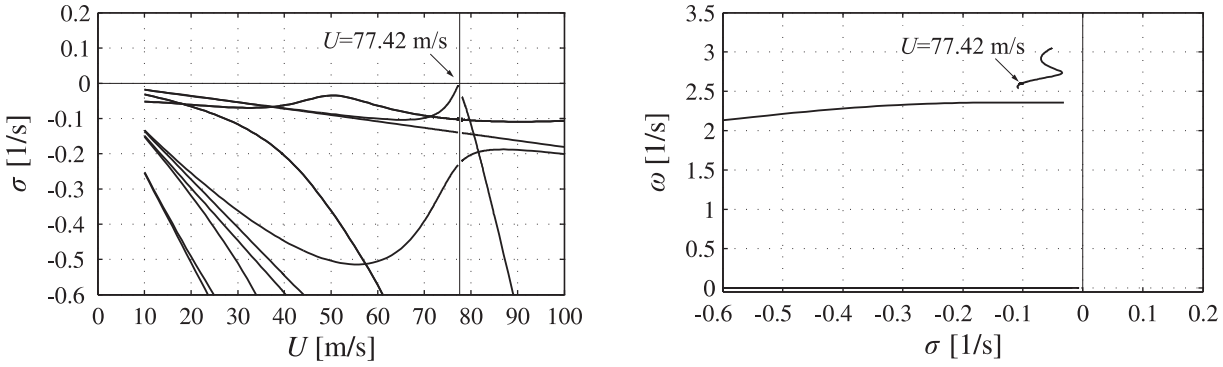

Figure 5.22: Closed-loop eigenvalues of the 2d model of the aeroelastic system extended with reaction wheels. State includes θ_{rw}. Displacement input. Lqr design.

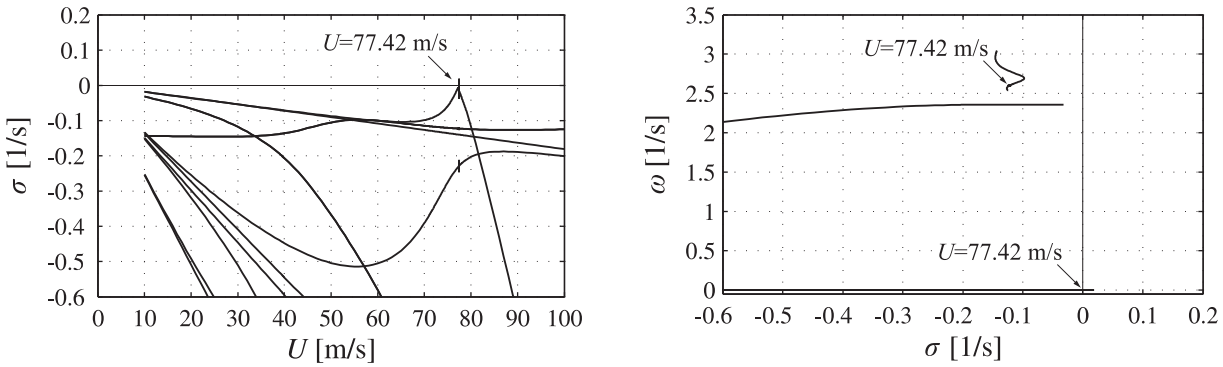

Figure 5.23: Closed-loop eigenvalues of the 2d model of the aeroelastic system extended with reaction wheels. State does not include θ_{rw}. Displacement input. Lqr design.

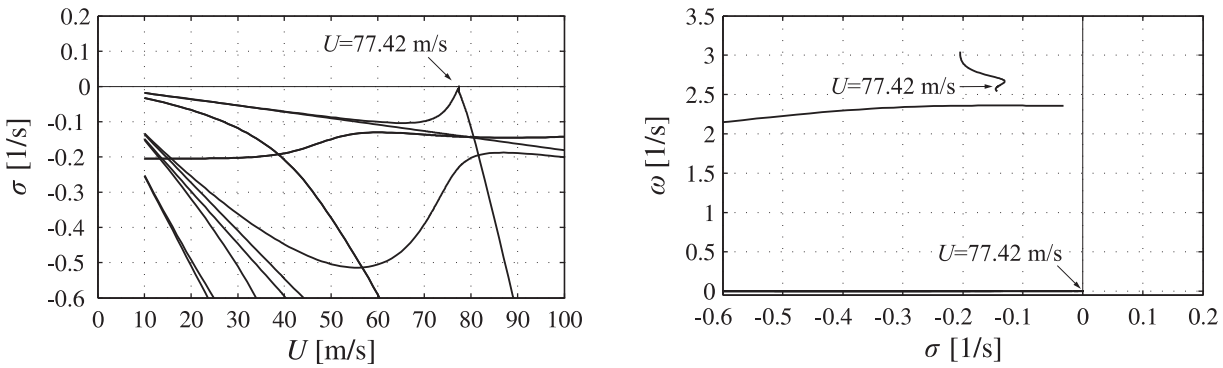

Figure 5.24: Closed-loop eigenvalues of the 2d model of the aeroelastic system extended with control moment gyroscopes. Displacement input. Lqr design.

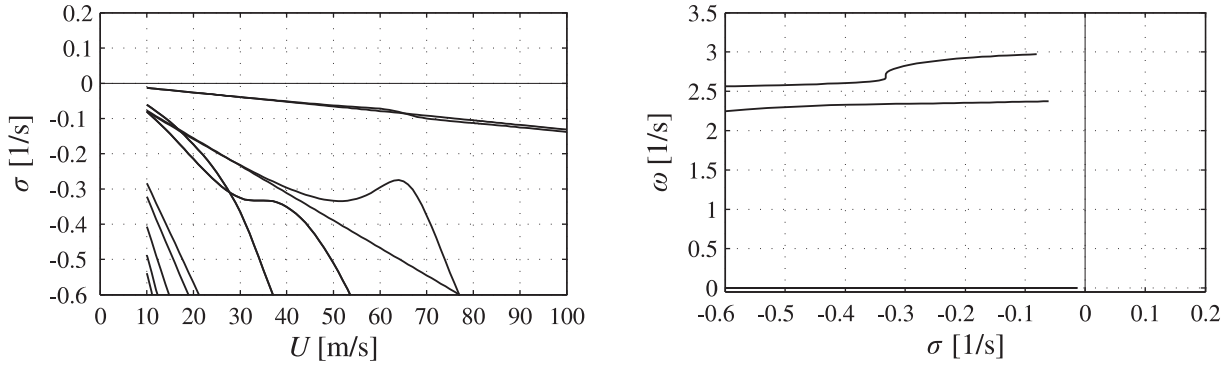

Figure 5.25: Closed-loop eigenvalues of the 2d model of the aeroelastic system extended with separately driven flaps. Displacement input. Lqr design.

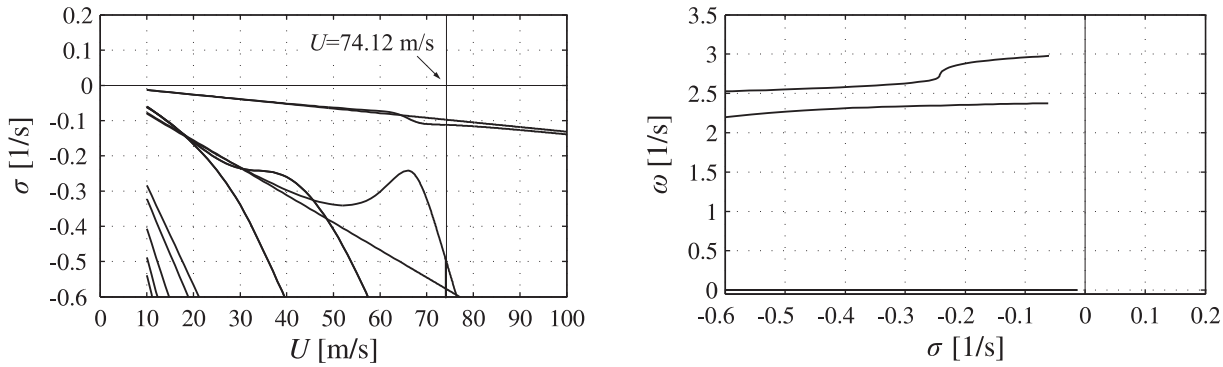

Figure 5.26: Closed-loop eigenvalues of the 2d model of the aeroelastic system extended with sd-coupled flaps. Displacement input. Lqr design.

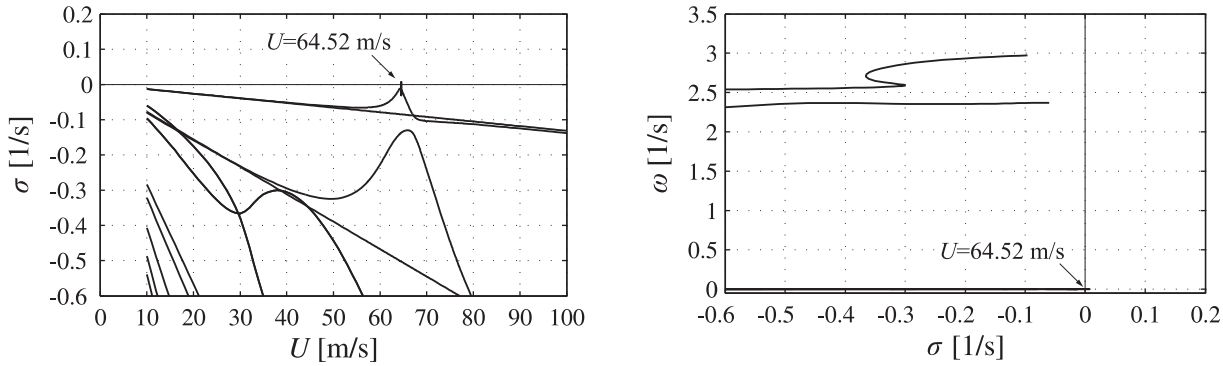

Figure 5.27: Closed-loop eigenvalues of the 2d model of the aeroelastic system extended with od-coupled flaps. Displacement input. Lqr design.

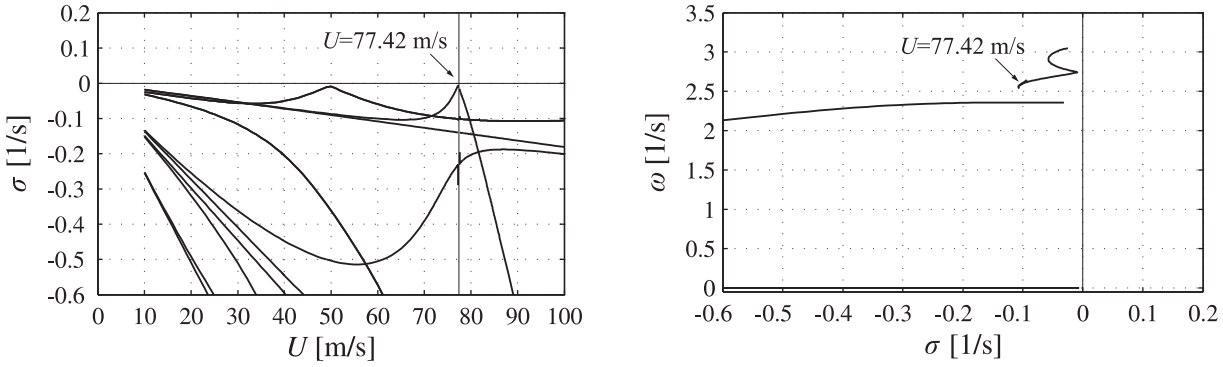

Figure 5.28: Closed-loop eigenvalues of the 2d model of the aeroelastic system extended with reaction wheels. State includes θ_{rw}. Force input. Lqr design.

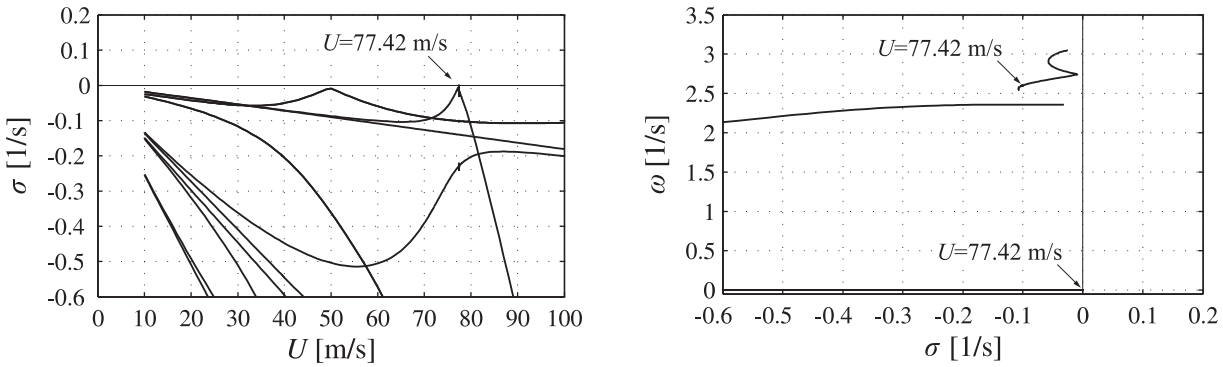

Figure 5.29: Closed-loop eigenvalues of the 2d model of the aeroelastic system extended with reaction wheels. State does not include θ_{rw}. Force input. Lqr design.

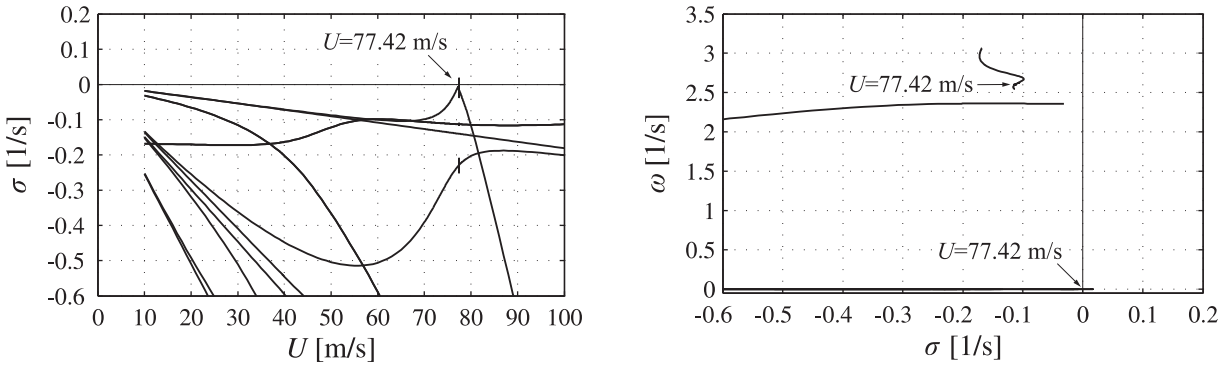

Figure 5.30: Closed-loop eigenvalues of the 2d model of the aeroelastic system extended with control moment gyroscopes. Force input. Lqr design.

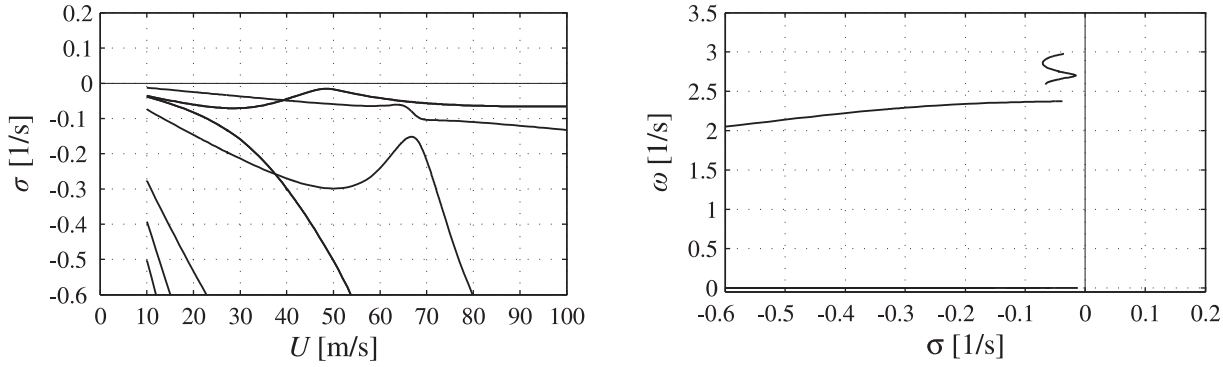

Figure 5.31: Closed-loop eigenvalues of the 2d model of the aeroelastic system extended with separately driven flaps. Force input. Lqr design.

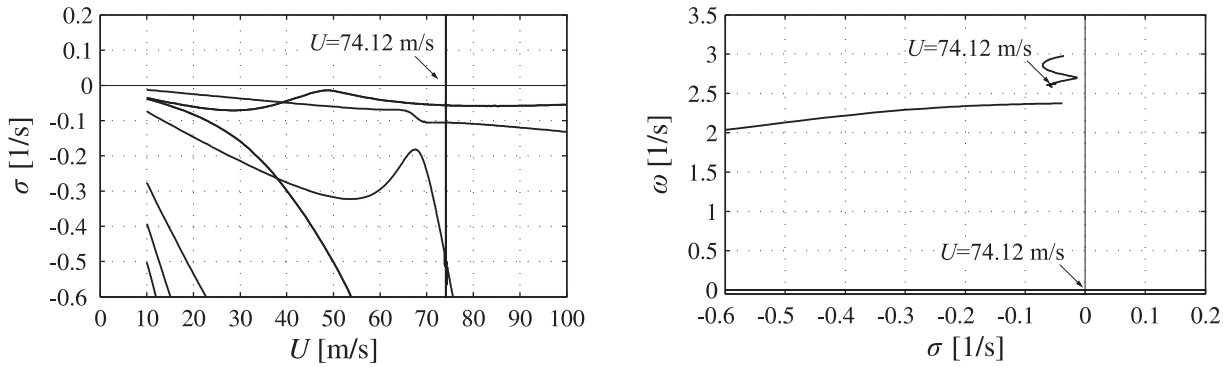

Figure 5.32: Closed-loop eigenvalues of the 2d model of the aeroelastic system extended with sd-coupled flaps. Force input. Lqr design.

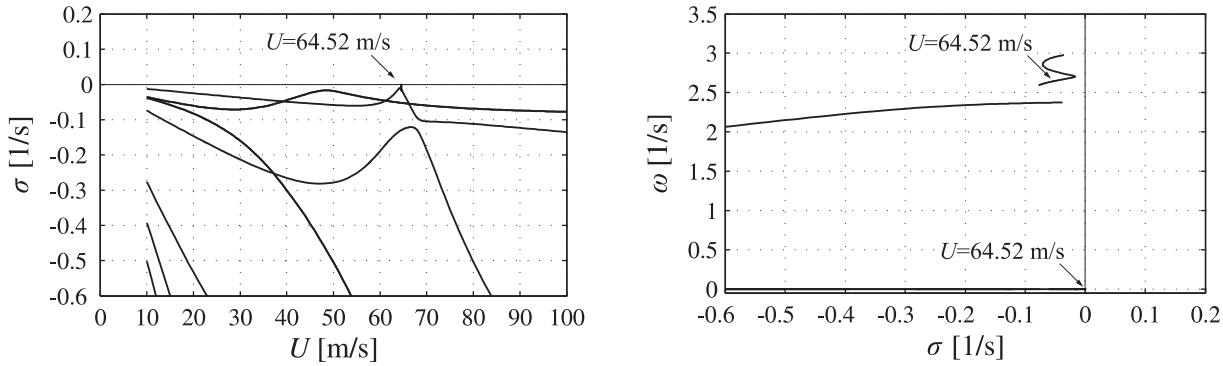

Figure 5.33: Closed-loop eigenvalues of the 2d model of the aeroelastic system extended with od-coupled flaps. Force input. Lqr design.

includes the wheel rotation. Whereas the $\omega(\sigma)$-plots shown so far illustrate the eigenvalues also for very low and very high wind speeds, the eigenvalues in this section are only displayed for reference wind speeds between $U = 10\,\mathrm{m/s}$ and $U = 100\,\mathrm{m/s}$. Most eigenvalues are placed as desired, as can be seen when comparing them with those of Figure 5.5. Since the controller gains are numerically determined with an interpolation of discrete nodes, the gain singularity is not fully captured. Hence, the eigenvalues in a small finite interval around the divergence wind speed cannot be placed as intended. In this example, the eigenvalues fluctuate so strongly there that they are not displayed in the figure. To mark the wind speed where the eigenvalue at the origin of the frequency plane cannot be shifted at all, a thin vertical line is additionally inserted in the $\sigma(U)$-plot.

Figure 5.22 up to Figure 5.33 illustrate the eigenvalues for all investigated kinds of actuator-extended systems with the designed linear-quadratic controllers. Unlike the results based on the pole-placement design, all eigenvalues are now affected by the controlled input. If the eigenvalues around the wind speed of the gain singularity fluctuate too strongly, they are again not displayed and a thin vertical line is added there. The eigenvalues of the systems with a displacement input, which are illustrated in the first half of the figures, differ from those where a force input is applied. Since the transfer function of a controlled system is not only governed by the position of its eigenvalues, conclusions on the transfer behaviour cannot be drawn from them. As intended, the systems are stabilised for all wind speeds unless a gain singularity occurs. Based on the chosen linear models, the system that is extended with separately driven flaps is the only one which a stabilisation without exceptions is possible for. All other actuator-extended systems are not asymptotically stable in a small interval around a single wind speed that is hardly visible in the figures. Assuming that the gain singularity is well captured with the interpolated discrete nodes, the transitions to instability appear in terms of a divergence because the problematic eigenvalues lie on the real frequency axis. To conclude that the small wind-speed intervals are not relevant in reality is wrong for several reasons. Depending on the system disturbance, for instance in terms of gusts, the high controller gains around the singularities lead to high control inputs that are contrary to the assumptions for the linear models or technically not realisable. Additionally, the theoretically derived wind speeds with a singularity of the controller gains are associated with uncertainties in the models. For an actuator with a controller-gain singularity, moreover, some of the controller gains a bit below and above the problematic wind speeds differ considerably from each other. This is visible in the displayed gains of the last section. The latter three facts indicate that the wind-speed intervals where the controlled systems are not asymptotically stable are not negligible. The wind speeds where uncontrollable eigenvalues occur that are not located in the left frequency half-plane rather constitute fundamental upper limits for the application of the actuators. As active actuators with state feedback are chosen, this statement with respect to the ability of the actuators for a system stabilisation holds true for all other kinds of possible controllers and closed-loop structures.

To judge the transfer behaviour of the controlled systems, their reactions to vertical gusts are analysed. The wind field defined in Section 4.7 is used for this purpose. For the following investigations, the linear-quadratic controllers are applied. The displacements of the controlled systems disturbed by gusts are decisive for the selection of the numerical parameters that are given in Table 5.2 for the controller design. All settings for frequency-domain and time-domain calculations are the same as described for the actuator-free bridge. The decaying correlation of the gusts along the girder is taken into account. For the admittance of the gust-induced aerodynamic forces, the approximated consistent Sears function is used as the basis for cross sections with attached flaps, as already explained for the flap-free plate.

On the next two double pages, the performance of the disturbed controlled systems is illustrated. For every actuator, four important quantities as functions of the reference wind speed U are shown in a row of figures. The results for a displacement input and a force input are given in every figure. In the first figure on the left side, the standard deviations of the bridge rotation are shown. For comparison, the associated result of the actuator-free bridge from Figure 4.21 is additionally included. The vertical displacements of the bridge are not illustrated. Due to the strong coupling of the structural degrees of freedom of the bridge by the motion-induced aerodynamic forces for wind speeds in the upper displayed range, the translational displacements are affected by the actuators in a similar way as shown for the rotation. Apart from the displacements of the bridge girder, it is very important to consider its internal forces. The distributions of the aerodynamic forces and the forces that are induced with the actuators on the girder differ. Even if the displacements are very low, the internal forces and, thus, the stresses can reach significant values. For the sake of simplicity, only displacements are analysed here. The second figure depicts the standard deviations of the elements of the actuator rotation $\boldsymbol{\xi}_\mathrm{c}$. If reaction wheels are applied, not the rotation but the angular speed $\dot{\theta}_\mathrm{rw}$ is given because it is the more important quantity for this actuator. The first figure on the right side displays the standard deviations of the elements of the actuator forces $\mathbf{f}_\mathrm{c}$. If a force input is chosen, they can be determined with Eq. (5.61), which is much simpler to use than Eq. (5.39) or related ones. For the discrete reaction wheel or the discrete control moment gyroscope with the highest actuator forces along the bridge length, the discrete forces can be determined with a sufficient accuracy by multiplying the displayed forces per length with the actuator distance. The quantities in the first three figures of a row can be seen as the output of a linear transfer where the vertical gust speeds are the input. Hence, the calculation can be carried out in the frequency domain. Since the gust input is assumed to have a Gaussian distribution, the output has this kind of distribution, too. For instance, statements like the following are possible. 98 % of the outputs have a smaller absolute value than 2.3 times the displayed standard deviations. A further interesting quantity to judge the performance of the controlled systems is the power demand

$$P = \mathbf{f}_\mathrm{c}^\mathrm{T} \dot{\boldsymbol{\xi}}_\mathrm{c} \tag{5.69}$$

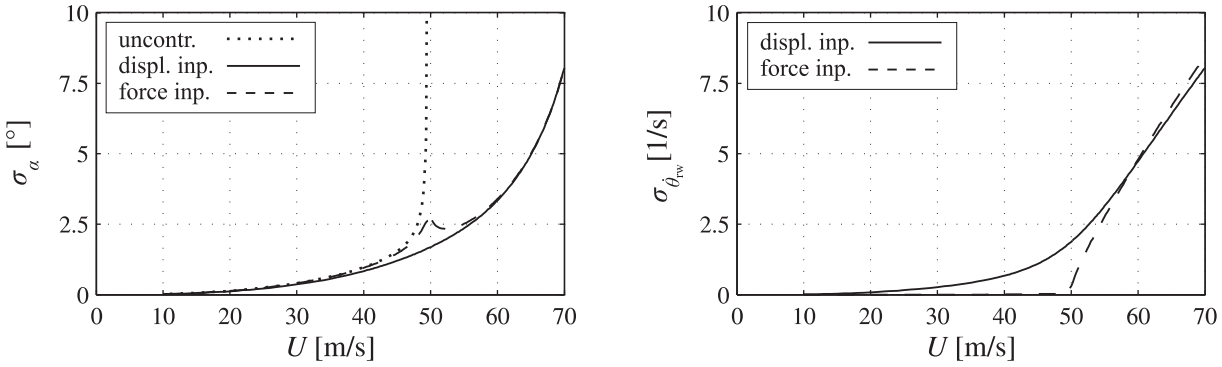

Figure 5.34: Standard deviations of the controlled bridge rotation and the angular speed of the reaction wheel due to vertical gusts. State includes θ_{rw}.

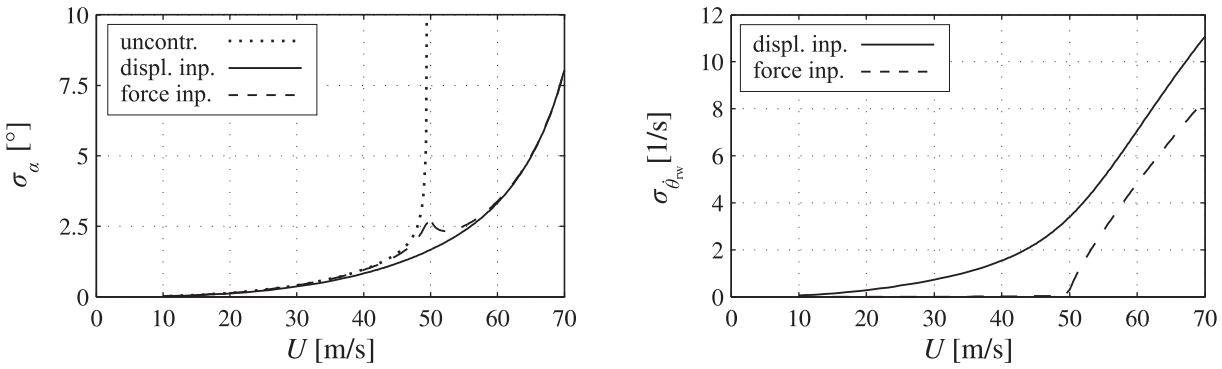

Figure 5.35: Standard deviations of the controlled bridge rotation and the angular speed of the reaction wheel due to vertical gusts. State does not include θ_{rw}.

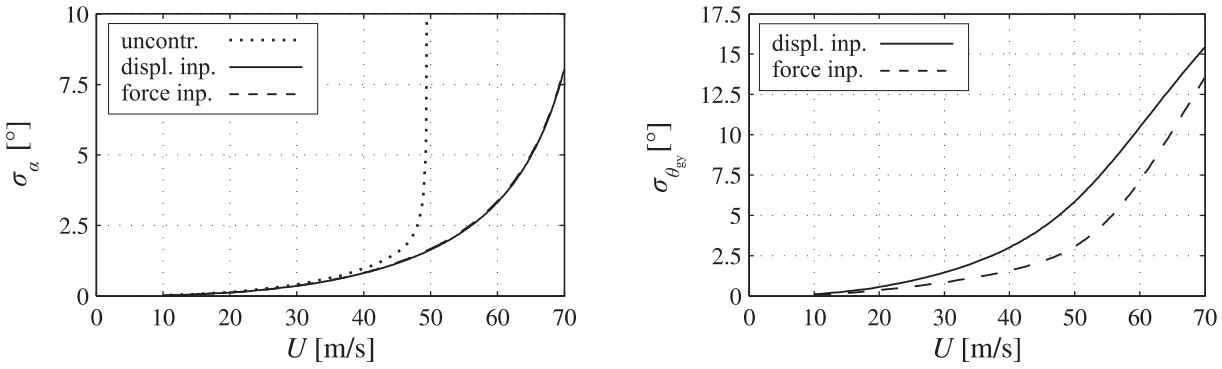

Figure 5.36: Standard deviations of the rotations of the controlled bridge and the control moment gyroscope due to vertical gusts.

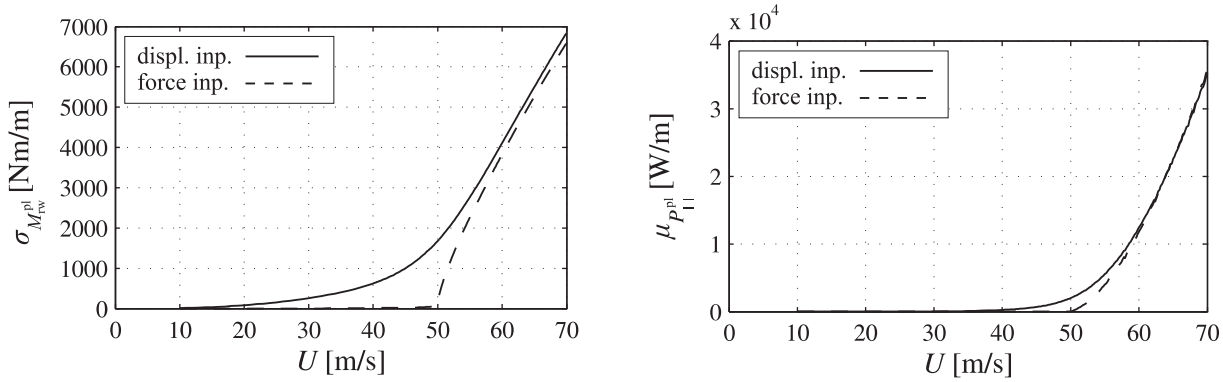

Figure 5.37: Standard deviation of the input moment of the reaction wheel and mean value of the actuator power. State includes θ_{rw}.

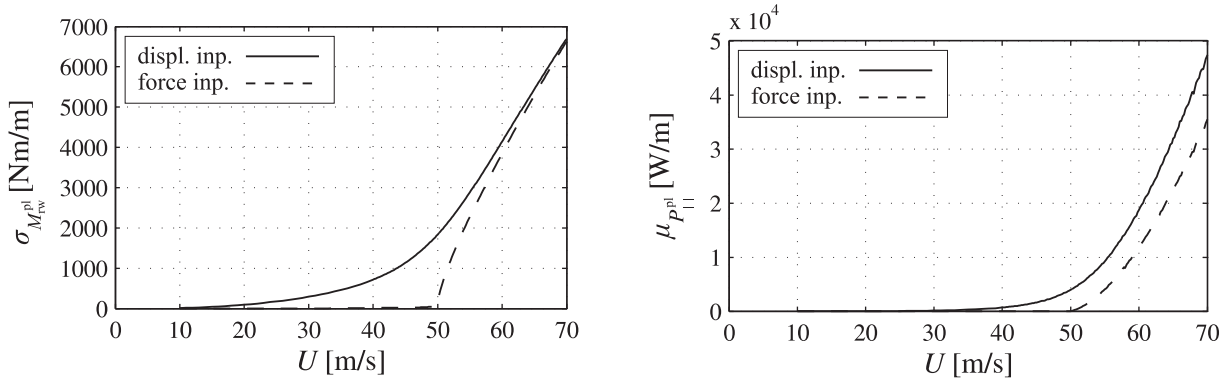

Figure 5.38: Standard deviation of the input moment of the reaction wheel and mean value of the actuator power. State does not include θ_{rw}.

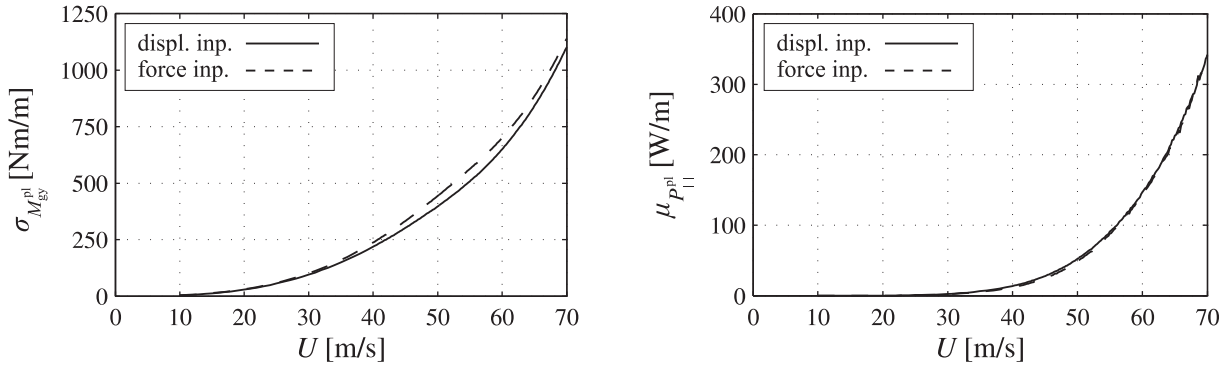

Figure 5.39: Standard deviation of the input moment of the control moment gyroscope and mean value of the actuator power.

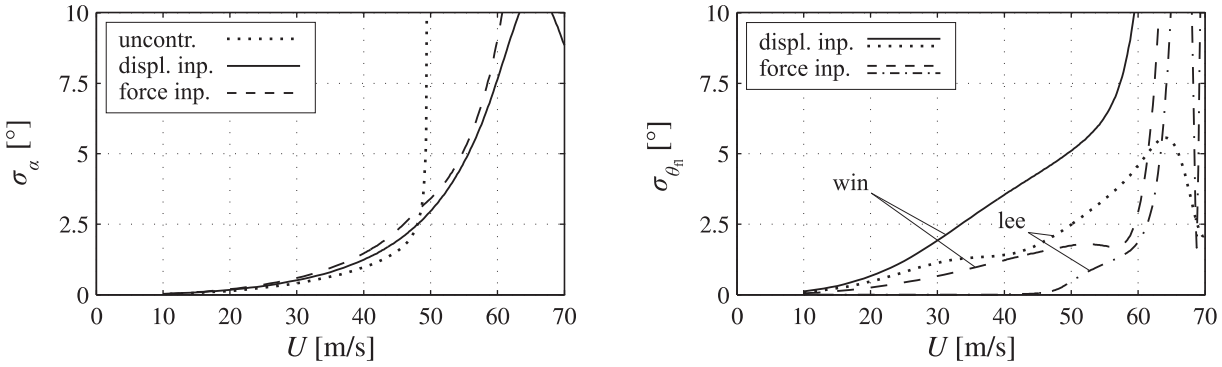

Figure 5.40: Standard deviations of the rotations of the controlled bridge and the separately driven flaps due to vertical gusts.

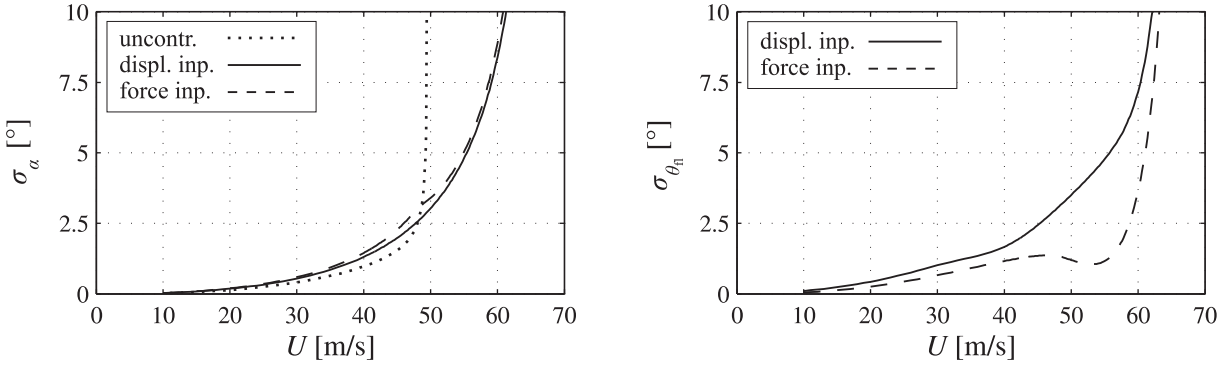

Figure 5.41: Standard deviations of the rotations of the controlled bridge and the sd-coupled flaps due to vertical gusts.

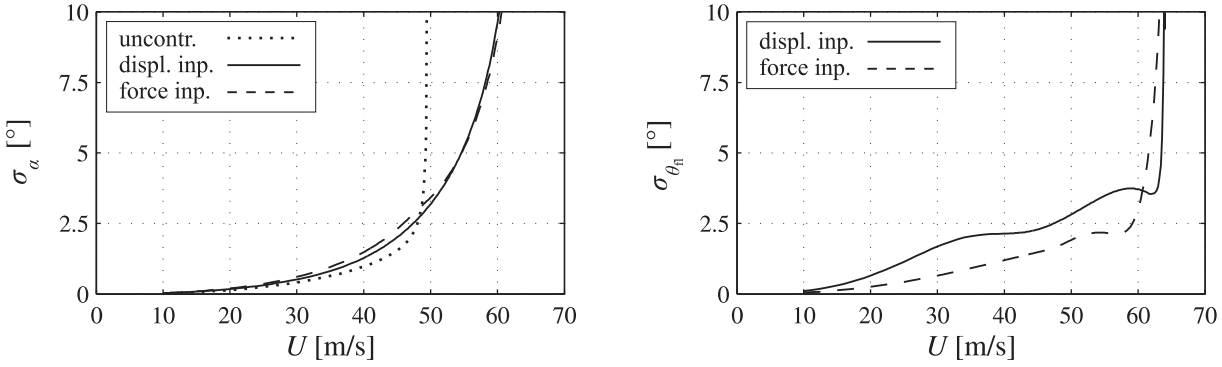

Figure 5.42: Standard deviations of the rotations of the controlled bridge and the od-coupled flaps due to vertical gusts.

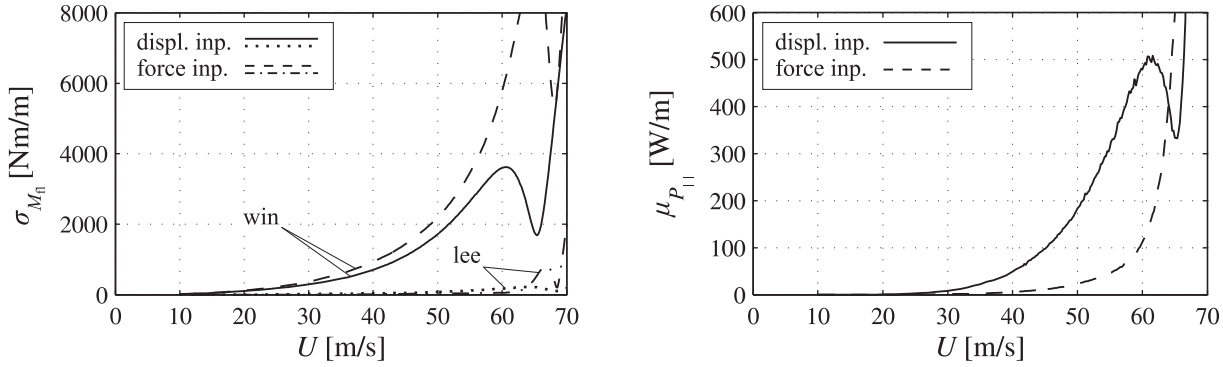

Figure 5.43: Standard deviations of the input moments of the separately driven flaps and mean value of the actuator power.

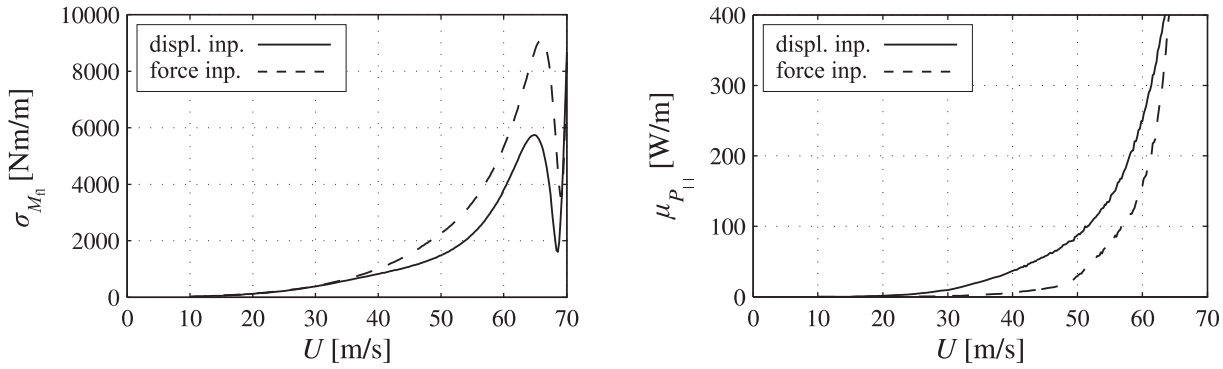

Figure 5.44: Standard deviation of the input moment of the sd-coupled flaps and mean value of the actuator power.

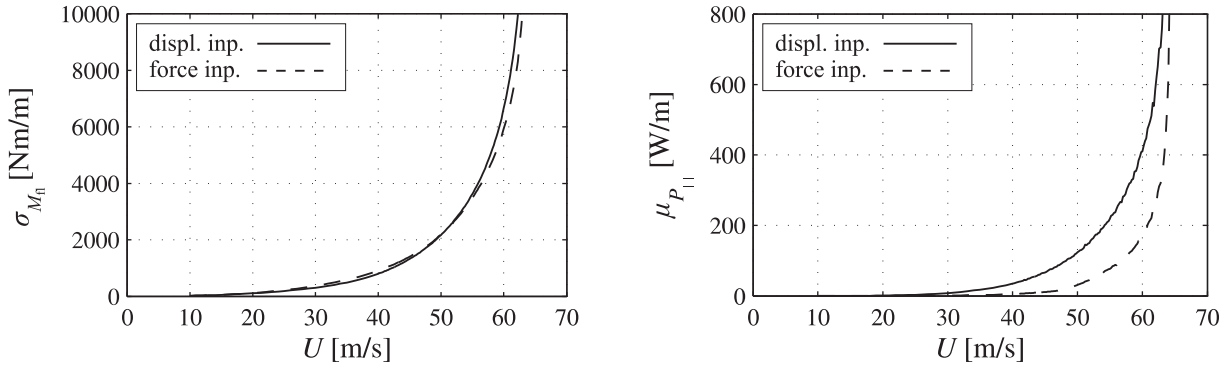

Figure 5.45: Standard deviation of the input moment of the od-coupled flaps and mean value of the actuator power.

of the actuators in the two-dimensional model. For the discrete reaction wheel or control moment gyroscope with the highest power demand along the bridge length, the discrete power is approximately the power per length times the actuator distance. The power of all actuators along the whole bridge in relation to the mode shape $\breve{\Omega}_j(x)$ is as follows.

$$\int_{\mathrm{g}} \mathbf{f}_{\mathrm{c}}^{\mathrm{T}}(x,t)\,\dot{\boldsymbol{\xi}}_{\mathrm{c}}(x,t)\,\mathrm{d}x = \mathbf{f}_{\mathrm{c},j}^{\mathrm{T}}(t)\,\dot{\boldsymbol{\xi}}_{\mathrm{c},j}(t) \int_{\mathrm{g}} \breve{\Omega}_j^2(x)\,\mathrm{d}x \tag{5.70}$$

Since the mode shapes are employed without dimensions, the integral over the squared mode shape is an effective length for the total power demand. As done for the joint acceptance function, this length is determined as the arithmetic mean of the integrals that are evaluated with respect to the first bending and the first torsional mode shape.

$$\frac{1}{2}\left(\int_{\mathrm{g}} \breve{\Omega}_h^2(x)\,\mathrm{d}x + \int_{\mathrm{g}} \breve{\Omega}_\alpha^2(x)\,\mathrm{d}x\right) = \frac{1}{2}\,(139.24\ \mathrm{m} + 192.50\ \mathrm{m}) = 165.87\ \mathrm{m} \tag{5.71}$$

The power is not a result of linear transfer of the gust input. It does not have a Gaussian distribution but a skewed one with a non-zero mean. For accelerating and braking, the power has positive and negative values, respectively. Regaining the energy for braking is assumed to be almost infeasible for the applied actuators from the technical point of view. Hence, the modulus of the power is considered in every summand of $\mathbf{f}_{\mathrm{c}}^{\mathrm{T}}\dot{\boldsymbol{\xi}}_{\mathrm{c}}$, which is indicated with the index $|\ |$. Because of the non-linear transfer from the gust speeds to the modulus of the power, a calculation must be carried out in the time domain. The mean $\mu_{P_{|\ |}}$ is estimated with the arithmetic mean of the discrete time history. For all investigated controlled systems, 98 % of the power $P_{|\ |}$ is less than roughly $5\mu_{P_{|\ |}}$. In the second figure on the right side, the mean of the power modulus per unit length is displayed.

Beginning with the reaction wheel, the displayed results are described. Including the wheel rotation in the state vector or not does not lead to significant differences between the shown quantities. If a force input is chosen, the chosen constant weighting matrices $\mathbf{Q}_{\mathrm{lqr}}$ and $\mathbf{R}_{\mathrm{lqr}}$ of the controller design entail controlled actuators below the flutter wind speed of the open-loop system that are almost unmoved and thus ineffective in contrast to those with a displacement input. It has to be kept in mind that the constant weighting matrices are selected with respect to the speed range where the actuator-free bridge is unstable. The differences between the bridge rotations for both kinds of actuator inputs, however, are not large. A bit below the flutter wind speed, all controlled bridge rotations are comparable to that of the actuator-free bridge. Theoretically, the system is stabilisable up to the divergence wind speed, which is the stabilisation limit for the reaction wheel, as described before. To what extent this limit can be reached at all under the effect of the selected disturbance depends on the technical feasibility of the actuator. The high controller gains that occur near the gain singularity necessitate high forces M_{rw}, fast angular speeds $\dot{\theta}_{\mathrm{rw}}$, and a high power $P_{|\ |}$. At $U = 60\ \mathrm{m/s}$, these quantities get so high that even very

powerful torque motors that are currently commercially available (e. g. www.oswald.de) can barely fulfil these requirements. For the numerical example, this wind speed seems to be the upper limit for an application of reaction wheels from the technical point of view. For a real application, other quantities like stresses in the bridge girder also limit the application range.

If a control moment gyroscope is employed, the designed controllers lead to a closed-loop behaviour where the difference between both variants of the actuator input is a bit lower than in the foregoing case. Below $U \approx 40\,\mathrm{m/s}$, the actuators are again ineffective. Above $U = 60\,\mathrm{m/s}$, the tilting angles of the gimbals become so large that they significantly contradict the model assumptions for the gyroscope. Concerning the non-linear behaviour, moreover, the pair of tilted rotors gets more and more ineffective for larger tilting angles. With respect to the model quality, the results of the numerical example for reference wind speeds greater than $U = 60\,\mathrm{m/s}$ are unreliable. The controlled rotations of the bridge under the effect of the control moment gyroscopes or the reaction wheels have a comparable low size. To think that a lower input can admit larger rotations of the bridge but can allow an actuator application for considerably higher wind speeds is questionable. The aeroelastic system is not only excited by the gust-induced but also by the motion-induced aerodynamic forces. At high wind speeds, the latter forces necessitate higher counteracting inputs for larger bridge rotations.

The application of attached flaps is limited by the model assumptions and the decreasing effectiveness of the flaps for large rotations, as explained for the control moment gyroscope. For all three kinds of flap motions, the controllers are designed so that the assumed rotation limit of $\sigma_j = 10^\circ$ is simultaneously reached for the flaps and the bridge at a certain reference wind speed. In the numerical example, this upper wind-speed limit is approximately $U = 60\,\mathrm{m/s}$, independent of the chosen flap motions. Hence, even under the effect of the gust disturbance with the chosen moderate turbulence intensity of $\sigma_{w^\mathrm{g}} = 0.07$, separately driven flaps cannot take the advantage of having no limiting singularity in the controller gains. The differences in the power demand between the force input and the displacement input indicate the potential to improve the controllers. For reference wind speeds a bit below the flutter wind speed of the actuator-free bridge, the bridge rotation is slightly increased compared to the flap-free case. One reason is that a larger area that is exposed to the gusts generates higher gust-induced aerodynamic forces. The other reason is that the constant weighting matrices for the controller design are not chosen for that low wind-speed range.

As explained, $U = 60\,\mathrm{m/s}$ marks a significant limit for the application of all actuators in the numerical example. The upper limit of the allowable reference wind speed is thus raised by about 20 % compared to the actuator-free bridge. For $U = 60\,\mathrm{m/s}$, Table 5.5 gives the numerical values of the quantities displayed in the figures for the different actuators in order to allow for a direct comparison. For the reaction wheels whose models include their rotation, the standard deviations $\sigma_{\theta_\mathrm{rw}}$ are additionally quoted. Without doubt, all controllers can still be optimised at this wind

Table 5.5: Closed-loop characteristics of the actuator-extended aeroelastic system under the influence of vertical gusts at $U = 60\,\mathrm{m/s}$.

displacement input	rw			σ_α [°]	$\sigma_{\theta_{\mathrm{rw}}}$ [°]	$\sigma_{\dot{\theta}_{\mathrm{rw}}}$ [1/s]	$\sigma_{M^{\mathrm{pl}}_{\mathrm{rw}}}$ [Nm/m]	$\mu_{P^{\mathrm{pl}}_{\mid\mid}}$ [W/m]
		state includes θ_{rw}		3.3428	121.23	4.7324	4111.1	12451
		state without θ_{rw}		3.3336		7.0767	4146.9	18732
	gy			σ_α [°]	$\sigma_{\theta_{\mathrm{gy}}}$ [°]		$\sigma_{M^{\mathrm{pl}}_{\mathrm{gy}}}$ [Nm/m]	$\mu_{P^{\mathrm{pl}}_{\mid\mid}}$ [W/m]
				3.3193	10.469		650.23	146.99
	fl			σ_α [°]	$\sigma_{\theta_{\mathrm{fl}}}$ [°]		$\sigma_{M_{\mathrm{fl}}}$ [Nm/m]	$\mu_{P_{\mid\mid}}$ [W/m]
		separately driven	win	7.6303	11.132		3600.7	478.88
			lee		4.5790		173.33	
		sd coupled		8.3734	7.1616		3799.5	248.99
		od coupled		9.6027	3.7135		6663.4	409.55
force input	rw			σ_α [°]	$\sigma_{\theta_{\mathrm{rw}}}$ [°]	$\sigma_{\dot{\theta}_{\mathrm{rw}}}$ [1/s]	$\sigma_{M^{\mathrm{pl}}_{\mathrm{rw}}}$ [Nm/m]	$\mu_{P^{\mathrm{pl}}_{\mid\mid}}$ [W/m]
		state includes θ_{rw}		3.3946	194.10	4.7936	3834.7	11826
		state without θ_{rw}		3.3882		4.8357	3854.3	11874
	gy			σ_α [°]	$\sigma_{\theta_{\mathrm{gy}}}$ [°]		$\sigma_{M^{\mathrm{pl}}_{\mathrm{gy}}}$ [Nm/m]	$\mu_{P^{\mathrm{pl}}_{\mid\mid}}$ [W/m]
				3.3637	7.1467		700.41	143.00
	fl			σ_α [°]	$\sigma_{\theta_{\mathrm{fl}}}$ [°]		$\sigma_{M_{\mathrm{fl}}}$ [Nm/m]	$\mu_{P_{\mid\mid}}$ [W/m]
		separately driven	win	9.0376	2.9201		5780.0	111.82
			lee		1.8587		59.418	
		sd coupled		8.8688	3.6305		5328.3	157.13
		od coupled		9.0909	3.0033		5932.6	168.53

speed. Hence, all the values should be considered only with respect to their order of magnitude. The reaction wheels have high rotation angles, as expected in the last section. They obviously not only necessitate large torque motors, as described above. The power demand is also extremely high compared to the other actuators. Taking into account that the motion of the flaps with a displacement input can still be improved, the power demand of the flaps is comparable to that of the control moment gyroscopes. The actuator input forces of the flaps, however, are in the order of magnitude of the reaction wheels. In contrast to the wheels, a higher number of weaker motors for the flaps can be installed with a shorter distance. The inertia effect of the flaps is negligible. Their accelerations are distinctly lower than those of the reaction wheels, as can be estimated when comparing their rotation angles with those of the reaction wheels. The lower rotation angles are also an explanation why, compared to the reaction wheels, the flaps need less power although the actuator input forces have similar values. The control moment gyroscope is the actuator with the lowest input forces. In addition to the low power demand, however, a high amount of energy is necessary for accelerating the rotors to the desired spin speed. According to

Table 5.6: Closed-loop characteristics of the aeroelastic system extended with separately driven flaps of the half-width $b_{\mathrm{fl}} = 0.1\,b$ under the influence of vertical gusts at $U = 60\,\mathrm{m/s}$. Displacement input.

		σ_{α} [°]	$\sigma_{\theta_{\mathrm{fl,win}}}$ [°]	$\sigma_{\theta_{\mathrm{fl,lee}}}$ [°]	$\sigma_{M_{\mathrm{fl,win}}}$ [Nm/m]	$\sigma_{M_{\mathrm{fl,lee}}}$ [Nm/m]	$\mu_{P_{\vert\,\vert}}$ [W/m]
Kü oga	A	7.5790	11.402	4.7413	9439.0	595.85	1283.7
	B	7.6051	11.258	4.7083	3090.5	384.19	427.80
	C	7.6303	11.132	4.5790	3600.7	173.33	489.89
	D	7.6579	10.989	4.5706	10136	70.428	1353.6
	E	7.6855	10.849	4.5700	16792	264.51	2244.3
Kü sga	A	9.2123	7.0994	4.9093	8386.0	2763.4	766.43
	B	9.7448	1.4068	5.9712	2530.8	1847.8	188.44
	C	9.4386	4.5982	6.1139	5091.4	748.71	279.80
	D	8.6291	8.6088	5.4455	11994	83.415	1158.9
	E	7.6855	10.849	4.5700	16792	264.51	2244.3
Th sga	A	9.2123	7.0994	4.9093	9265.1	1964.0	753.87
	B	9.7448	1.4068	5.9712	2620.4	1296.9	144.51
	C	9.4386	4.5982	6.1139	5244.2	496.85	267.52
	D	8.6291	8.6088	5.4460	12062	90.654	1165.8
	E	7.6855	10.849	4.5700	16792	264.51	2244.3

the model assumptions, all rotors along the bridge have the same spin speed. For the numerical example, the constant rotation energy has a large amount of $\frac{1}{2} I^{\mathrm{pl}}_{\mathrm{gy,h}} \Omega^2_{\mathrm{gy}} = 3.396 \cdot 10^5\ \mathrm{J/m}$. To make this value more transparent, the question can be asked how long a particular constant power has to be introduced into the gyroscopes to build up this energy. As the constant power, the arithmetic mean $145.00\ \mathrm{W/m}$ of the values given for the gyroscopes in Table 5.5 is chosen. The time follows from $3.396 \cdot 10^5\ \mathrm{J/m} \cdot 645\ \mathrm{m} = 145.00\ \mathrm{W/m} \cdot 165.87\ \mathrm{m} \cdot t$ as $t = 151.79$ min.

The flap hinges considered so far are located in the middle of a flap. To analyse the influence of the hinge position on the closed-loop behaviour, Table 5.6 gives the numerical results of a parameter study at $U = 60\,\mathrm{m/s}$. For different hinge positions of separately driven flaps, the controllers are designed and the closed-loop behaviour is determined. The results for the hinge position E are independent of the gap variant and the aerodynamic forces because the hinge is located between the flap edge and the bridge edge. There is no gap. For this case, the aerodynamic forces of the gap variants are identical. The power demand for the standard case Kü oga C differs a bit from the value shown in Table 5.5. Since two time histories of the input always differ due to the random phase used for their generation, the results are correct. As already described in the last section, the results for Kü sga and Th sga forces are identical concerning the first three columns. The input forces and consequently the power demand, however, differ. They also depend on the derivatives which are different for Kü and Th forces, according to Appendix A.1. The differences do not influence the conclusions of this paragraph and are accepted. The only very small difference of the leeward flap rotations originates from different rational function

approximations which are respectively carried out for the complete derivative matrices. In all three cases, the actuators with the hinge position B need the lowest power. With respect to the input forces, the motion of the windward flap seems to be more effective than that of the leeward one. If the windward flap is imagined as a single free flap in a flow, the position B is identical to the point where the aerodynamic lift force attacks under steady conditions. Hence, a relevant part of the aerodynamic forces is directly transferred to the bridge girder over the hinge. It does not affect the actuator control. The standard position C leads to the second lowest power demand. Although the parameter study is carried out for separately driven flaps, the results concerning the optimal hinge position are expected to hold true for kinematically coupled flaps. Based on the numerical examples, the expectation given in Section 5.1 that the flaps are the actuators with both the lowest input forces and the lowest power demand cannot be fulfilled.

5.7 State Observers

The controllers described until now imply the knowledge about the part of the full system state that are considered for the state feedback. State observers can be applied to reconstruct that part of the state from the time history of the measured output. As a precondition, the mentioned state part must be completely observable. The following equations are derived based on the state-space model of Eq. (5.48) for the actuator-extended system with a displacement input. For a force input, only the indices must be changed. In the sense of a Luenberger observer, the chosen observer has the state-space model

$$\dot{\mathbf{x}}_{\mathrm{asu}}^{\mathrm{ob}} = \mathbf{A}_{\mathrm{asu}}\mathbf{x}_{\mathrm{asu}}^{\mathrm{ob}} + \mathbf{B}_{\mathrm{asu}}\mathbf{u}_{\mathrm{c}} + \mathbf{u}_{\mathrm{ob}} \tag{5.72a}$$

$$\mathbf{y}_{\mathrm{st}}^{\mathrm{ob}} = \mathbf{C}_{\mathrm{asu}}\mathbf{x}_{\mathrm{asu}}^{\mathrm{ob}} \quad , \tag{5.72b}$$

where the observer state and output is marked with a superscript $(\ )^{\mathrm{ob}}$. Acting disturbances are assumed to be unknown for the observer. In addition to the terms of the aeroelastic system, the observer input $\mathbf{u}^{\mathrm{ob}}$ is introduced in the state equation. It is defined by the proportional feedback of the difference between the system and the observer output.

$$\mathbf{u}_{\mathrm{ob}} = \mathbf{L}(\mathbf{y}_{\mathrm{st}} - \mathbf{y}_{\mathrm{st}}^{\mathrm{ob}}) \tag{5.73}$$

The purpose of the observer input is to bring the observer state $\mathbf{x}_{\mathrm{asu}}^{\mathrm{ob}}$ in line with the system state $\mathbf{x}_{\mathrm{asu}}$. Inserting the feedback of Eq. (5.73) into the state equation of the observer leads to

$$\dot{\mathbf{x}}_{\mathrm{asu}}^{\mathrm{ob}} = (\mathbf{A}_{\mathrm{asu}} - \mathbf{L}\mathbf{C}_{\mathrm{asu}})\mathbf{x}_{\mathrm{asu}}^{\mathrm{ob}} + \mathbf{B}_{\mathrm{asu}}\mathbf{u}_{\mathrm{c}} + \mathbf{L}\mathbf{y}_{\mathrm{st}} \quad . \tag{5.74}$$

Instead of the system state, the observer state is now used in the feedback equation of the controlled actuator input.

$$\mathbf{u}_\mathrm{c} = -\mathbf{K}\,\mathbf{x}_\mathrm{asu}^\mathrm{ob} \tag{5.75}$$

After combining the two foregoing equations with the state-space model of Eq. (5.48), whose output equation is extended with an additive measurement noise $\mathbf{r}_\mathrm{st}$, the following state-space model of the observer-extended closed loop can be derived.

$$\begin{aligned}\begin{pmatrix} \dot{\mathbf{x}}_\mathrm{asu} \\ \dot{\mathbf{x}}_\mathrm{asu} - \dot{\mathbf{x}}_\mathrm{asu}^\mathrm{ob} \end{pmatrix} &= \begin{pmatrix} \mathbf{A}_\mathrm{asu} - \mathbf{B}_\mathrm{asu}\mathbf{K} & \mathbf{B}_\mathrm{asu}\mathbf{K} \\ \mathbf{0} & \mathbf{A}_\mathrm{asu} - \mathbf{L}\mathbf{C}_\mathrm{asu} \end{pmatrix} \begin{pmatrix} \mathbf{x}_\mathrm{asu} \\ \mathbf{x}_\mathrm{asu} - \mathbf{x}_\mathrm{asu}^\mathrm{ob} \end{pmatrix} + \\ &\quad + \begin{pmatrix} \mathbf{E}_\mathrm{asu} \\ \mathbf{E}_\mathrm{asu} \end{pmatrix} \mathbf{d}_\mathrm{ae}^\mathrm{g} + \begin{pmatrix} \mathbf{0} \\ -\mathbf{L} \end{pmatrix} \mathbf{r}_\mathrm{st} \end{aligned} \tag{5.76a}$$

$$\mathbf{y}_\mathrm{st} = \begin{pmatrix} \mathbf{C}_\mathrm{asu} & \mathbf{0} \end{pmatrix} \begin{pmatrix} \mathbf{x}_\mathrm{asu} \\ \mathbf{x}_\mathrm{asu} - \mathbf{x}_\mathrm{asu}^\mathrm{ob} \end{pmatrix} + \mathbf{r}_\mathrm{st} \tag{5.76b}$$

If a disturbance and a measurement noise is taken into account for the controlled system, the state observer is often also called a state estimator. The block triangular form of the system matrix shows that the eigenvalues of the closed-loop system matrix in Eq. (5.67) are not changed. Together with those of the observer system matrix in Eq. (5.74), they are the eigenvalues of the observer-extended system. The controller matrix $\mathbf{K}$ of the state feedback can thus be designed independently of the observer. The latter fact is known as the principle of separation of control and estimation. The block triangular form also allows the determination of the transfer equation in the frequency domain in a simple way.

$$\mathbf{y}_\mathrm{st} = \mathbf{C}_\mathrm{asu}\left(s\mathbf{I} - (\mathbf{A}_\mathrm{asu} - \mathbf{B}_\mathrm{asu}\mathbf{K})\right)^{-1} \mathbf{G}_{\mathrm{mod},\mathbf{d}_\mathrm{ae}^\mathrm{g}} \mathbf{E}_\mathrm{asu}\mathbf{d}_\mathrm{ae}^\mathrm{g} + \mathbf{G}_{\mathrm{mod},\mathbf{r}_\mathrm{st}}\mathbf{r}_\mathrm{st} \tag{5.77}$$

Due to the observer, the closed-loop transfer function is modified with the following matrices.

$$\mathbf{G}_{\mathrm{mod},\mathbf{d}_\mathrm{ae}^\mathrm{g}} = \mathbf{I} + \mathbf{B}_\mathrm{asu}\mathbf{K}\left(s\mathbf{I} - (\mathbf{A}_\mathrm{asu} - \mathbf{L}\mathbf{C}_\mathrm{asu})\right)^{-1} \tag{5.78a}$$

$$\mathbf{G}_{\mathrm{mod},\mathbf{r}_\mathrm{st}} = \mathbf{I} - \mathbf{C}_\mathrm{asu}\left(s\mathbf{I} - (\mathbf{A}_\mathrm{asu} - \mathbf{B}_\mathrm{asu}\mathbf{K})\right)^{-1} \mathbf{B}_\mathrm{asu}\mathbf{K}\left(s\mathbf{I} - (\mathbf{A}_\mathrm{asu} - \mathbf{L}\mathbf{C}_\mathrm{asu})\right)^{-1}\mathbf{L} \tag{5.78b}$$

There are two major design objectives for the observer feedback matrix $\mathbf{L}$. The natural responses of the observer error $(\mathbf{x}_\mathrm{asu} - \mathbf{x}_\mathrm{asu}^\mathrm{ob})$ in Eq. (5.76) should decay fast compared to the state-feedback part and the modification matrices of Eq. (5.78) should minimise the transfer of the inputs. It is known from the technical literature that both objectives conflict with each other to some extent.

As the eigenvalues of a matrix equal those of its transpose, the eigenvalues of

$$\mathbf{A}_{\mathrm{asu}}^{\mathrm{T}} - \mathbf{C}_{\mathrm{asu}}^{\mathrm{T}} \mathbf{L}^{\mathrm{T}} \tag{5.79}$$

can be considered instead of those of the observer system matrix. There is a similarity between the matrix in Eq. (5.79) and the closed-loop system matrix in Eq. (5.68). Hence, the eigenvalues of the observer system matrix and thus the natural response of the observer error can be influenced with the transpose $\mathbf{L}^{\mathrm{T}}$ of the observer feedback matrix as shown for the closed-loop system matrix with the controller matrix $\mathbf{K}$. Concerning the state-space model of the open-loop system, only the pair $(\mathbf{A}_{\mathrm{asu}}^{\mathrm{T}}, \mathbf{C}_{\mathrm{asu}}^{\mathrm{T}})$ is taken into account for the design of the observer feedback matrix. The feedback is determined for the reduced states $\mathbf{x}_{\mathrm{as}}^{\mathrm{m}}$ according to Eq. (5.56) if the full aeroelastic state is not accessible or made available for the closed-loop control. This is the case for a system with a displacement input. Subsequently, the solution is pumped up to the full state.

$$\mathbf{L} = \mathbf{\Phi} \mathbf{L}^{\mathrm{m}} \tag{5.80}$$

As described for the controller matrix, the observer feedback matrix is designed as a function of the reference wind speed U.

To primarily fulfil the first design objective, the pole-placement design algorithm is usually preferred. The eigenvalues of the observer system matrix are placed to the left of the closed-loop eigenvalues and sufficiently far away from them. As a consequence, the observer-extended closed loop is dominated by the closed-loop eigenvalues. A high ratio between the real parts of the observer eigenvalues and the closed-loop eigenvalues, however, is recommendable only if there is no relevant disturbance and the measurement noise is negligible. In the transfer functions of Eq. (5.77), a high ratio leads to undesired high gains, which are contrary to the second design objective.

By way of example, the state feedback of the bridge with control moment gyroscopes and a displacement input that is addressed in the foregoing section is extended with an observer. The bridge rotation α is measured. As described in Section 5.3, knowledge on the time history of this single quantity is sufficient to ensure complete observability of that part of the system that is considered for the state feedback. Since the output has only one element, there are no problems with interpolating the results of the function `place` of MATLAB (2007), which are mentioned in Section 5.5. A measurement noise is not taken into account. As eigenvalues of the observer system matrix, those of the closed-loop are chosen whose real parts are all multiplied by the same factor 1.2. In this way, the effect of the gust disturbance on the output is close to that of the state feedback. The time-domain simulation is carried out assuming the initial observer error $(\mathbf{x}_{\mathrm{asu}}(0) - \mathbf{x}_{\mathrm{asu}}^{\mathrm{ob}}(0))$ to be zero because the transfer behaviour of the system is focussed on. Figure 5.46 and Figure 5.48 show the behaviour of the observer-extended closed loop. Because

of the observer, the actuator input moments and the power demand slightly increase, whereas the actuator displacements are even lower.

These figures do not show what happens if the initial states of the observer and the system differ. They give only an impression of the input-output behaviour of the observer-extended closed loop. Due to the low difference between the observer eigenvalues and the closed loop eigenvalues, the natural response of the observer error can unfavourably dominate the system output during a non-negligible time. For a real application, appropriate measures must be taken to minimise the initial observer error before the actuators are released. The open-loop system can be observed before an actuator motion becomes necessary, for instance.

An interesting question is how the observer and the observer-extended closed loop would change if the disturbance $\mathbf{d}_{\mathrm{ae}}^{\mathrm{g}}$ is measurable. The state equation of the observer in Eq. (5.72a) would get the additional summand $\mathbf{E}_{\mathrm{asu}}\mathbf{d}_{\mathrm{ae}}^{\mathrm{g}}$, and, finally, $\mathbf{G}_{\mathrm{mod},\mathbf{d}_{\mathrm{ae}}^{\mathrm{g}}}$ in Eq. (5.77) would equal the identity matrix. Hence, the transfer of the gust disturbance would not be altered by the observer. In this case, the observer eigenvalues could be placed with a larger distance from the closed-loop eigenvalues depending on the size of the measurement noise. The problem of a slowly decaying initial error would get smaller.

A direct measurement of the gust-induced aerodynamic forces is not possible because they always occur together with the motion-induced ones. An indirect measurement, however, is possible. The gust-induced aerodynamic forces can, for instance, be derived from their transfer model and a measurement of the gust speeds. This kind of indirect measurement has a disadvantage. The determined disturbance strongly depends on a theoretical model. Therefore the feedback in the control-loop must be able to compensate the effect of model uncertainties to some degree.

Due to the analogy with the controller design, the observer feedback matrix can also be determined in the sense of a linear-quadratic regulator. If the system disturbance and the measurement noise meet certain requirements, their properties can be used to derive the weighting matrices. The observer is then identical to a continuous-time Kalman filter. The inputs $\mathbf{E}_{\mathrm{asu}}\mathbf{d}_{\mathrm{ae}}^{\mathrm{g}}$ and $\mathbf{r}_{\mathrm{st}}$ are required to be uncorrelated, zero-mean Gaussian white-noise processes. For a time shift Δt, their autocovariance matrices must be $\mathbf{Q}_{\mathrm{lqr}}\delta(\Delta t)$ and $\mathbf{R}_{\mathrm{lqr}}\delta(\Delta t)$, respectively. Passing the matrices $\mathbf{A}_{\mathrm{asu}}^{\mathrm{T}}$, $\mathbf{C}_{\mathrm{asu}}^{\mathrm{T}}$, $\mathbf{Q}_{\mathrm{lqr}}$, and $\mathbf{R}_{\mathrm{lqr}}$ to the linear-quadratic regulator design algorithm yields the transpose $\mathbf{L}^{\mathrm{T}}$ of the observer feedback matrix. This solution guarantees a minimisation of the sum of the mean quadratic observer errors of all state variables. If the full aeroelastic state is not accessible or made available for the control loop, as it is for a system with a displacement input, the matrix $\mathbf{\Phi}^{-1}\mathbf{Q}_{\mathrm{lqr}}(\mathbf{\Phi}^{-1})^{\mathrm{T}}$ must be used to weight the reduced state.

The input $\mathbf{E}_{\mathrm{asu}}\mathbf{d}_{\mathrm{ae}}^{\mathrm{g}}$ does not fulfil the requirements for the application of the described Kalman-filter design because it is not a white-noise process. Nevertheless, the covariance matrix of $\mathbf{E}_{\mathrm{asu}}\mathbf{d}_{\mathrm{ae}}^{\mathrm{g}}$ is used for an observer design with the linear-quadratic regulator algorithm. For the

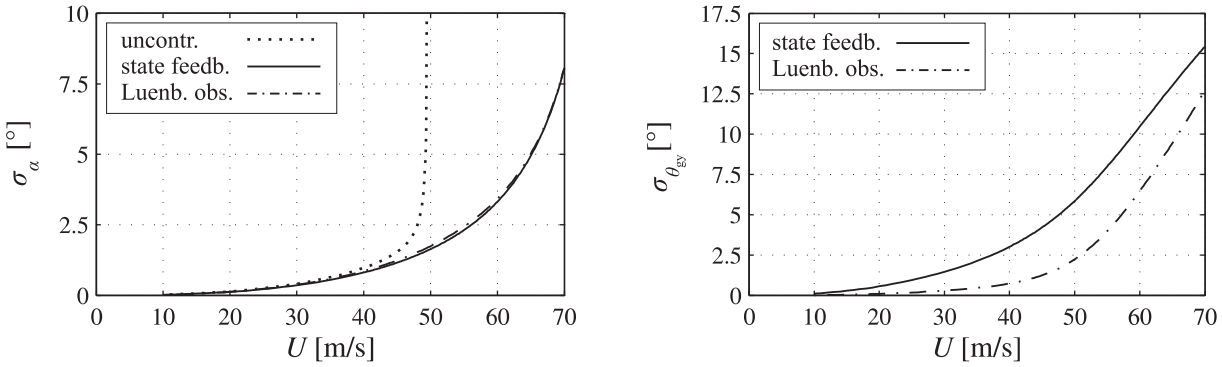

Figure 5.46: Standard deviations of the rotations of the controlled bridge and the control moment gyroscope due to vertical gusts. Displacement input.

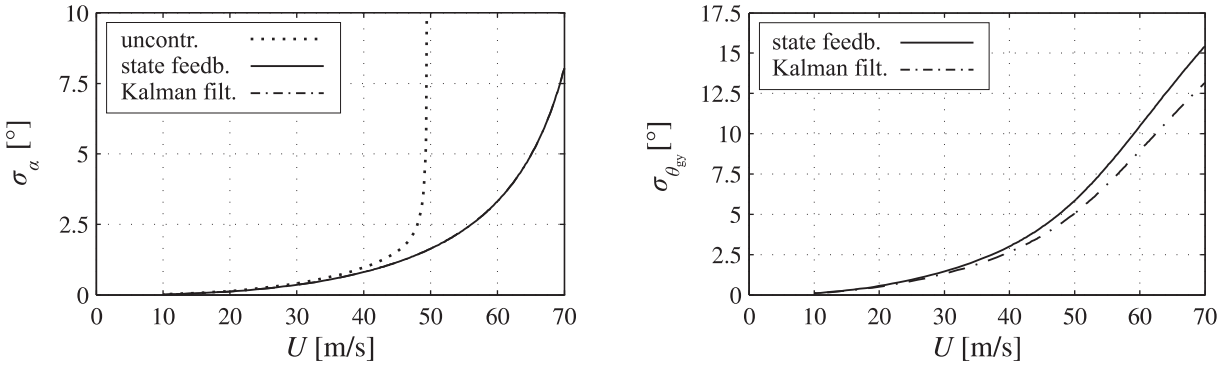

Figure 5.47: Standard deviations of the rotations of the controlled bridge and the control moment gyroscope due to vertical gusts. Displacement input.

two-dimensional models, it can be shown that the normalised version of this covariance matrix is identical for all reference wind speeds. The normalised covariance matrix equals the normalised version of the matrix $\mathbf{E}_{\text{asu}}\mathbf{A}_0\mathbf{A}_0^{\text{T}}\mathbf{E}_{\text{asu}}^{\text{T}}$. In the rational function approximation of Eq. (3.17) for the gust-induced aerodynamic forces, it is again important to constrain the $\mathbf{A}_0$ matrix to the original steady force coefficients. The normalisation is carried out so that the greatest absolute value of the matrix element equals a special value $r_{\mathbf{Q}_{\text{lqr}}}$ that is constant for all reference wind speeds U. The covariance matrix of the measurement noise, which is again not considered in the simulation, is assumed to be an identity matrix.

As a numerical example for the Kalman filter, the same system is chosen that is used for the pole-placement design of the observer. The quality of the transfer behaviour of the observer-extended closed-loop system depends on the normalisation of the matrix $\mathbf{Q}_{\text{lqr}}$. Since no measurement noise is accounted for, the disturbance transfer decreases if $r_{\mathbf{Q}_{\text{lqr}}}$ increases. Figure 5.47 and Figure 5.49 illustrate the results if $r_{\mathbf{Q}_{\text{lqr}}} = 10^4$. For higher values of $r_{\mathbf{Q}_{\text{lqr}}}$, the transfer behaviour is almost not improved. Though the disturbance is not a white noise, the bridge rotation, the actuator input forces, and the power demand of the observer-extended closed-loop system are lower than those obtained with the first observer. With the Kalman filter, the addressed results practically equal

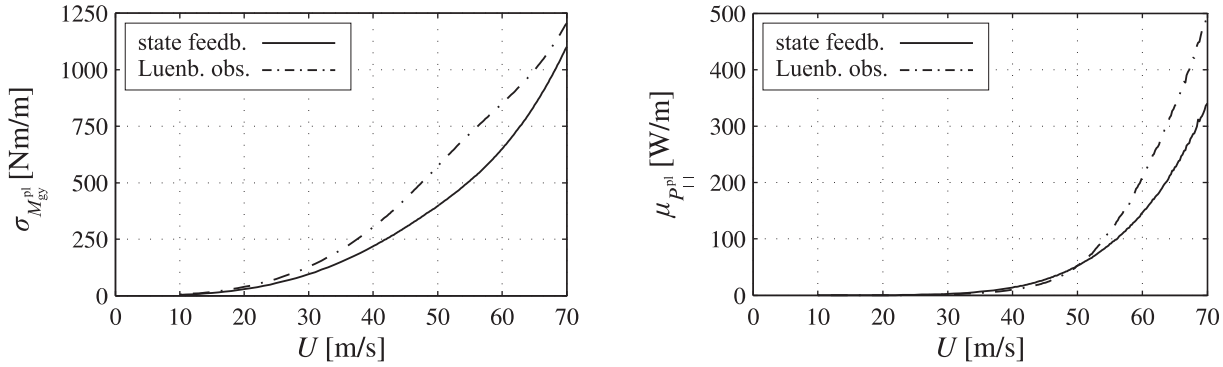

Figure 5.48: Standard deviation of the input moment of the control moment gyroscope and mean value of the actuator power. Displacement input.

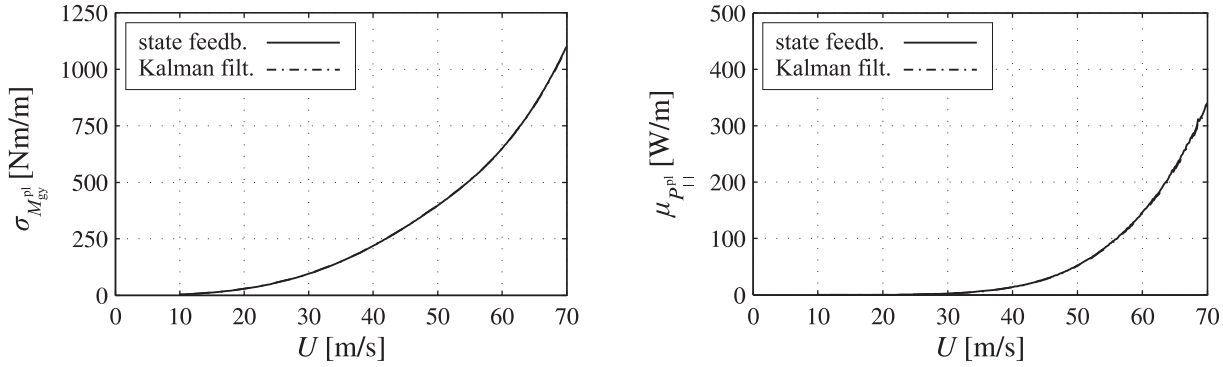

Figure 5.49: Standard deviation of the input moment of the control moment gyroscope and mean value of the actuator power. Displacement input.

those of the pure state feedback. Hence, information on the input of the aeroelastic system can be used to improve the state estimation.

5.8 Disturbance Feedforward

Up to this point, the actuator input is defined with the help of a feedback law in order to minimise the transfer of the disturbances. In the latter section, the idea of measuring the gust-induced aerodynamic forces $\mathbf{d}_{\mathrm{ae}}^{\mathrm{g}}$, which are the disturbance of the system, is introduced. Apart from the addressed improvement of an observer, the question of how this information can be taken advantage of is clarified in the following.

The idea is, as far as it is possible, to instantaneously compensate the disturbance with the actuator input before the system state is influenced. In the technical literature the term disturbance feedforward is used. First, actuator-extended systems with a force input are addressed. With Eq. (5.26), the potential of the different actuators can be revealed. To directly act against the disturbance, the actuator-input forces $\mathbf{f}_{\mathrm{c}}$ must be positioned in rows of the equation that also

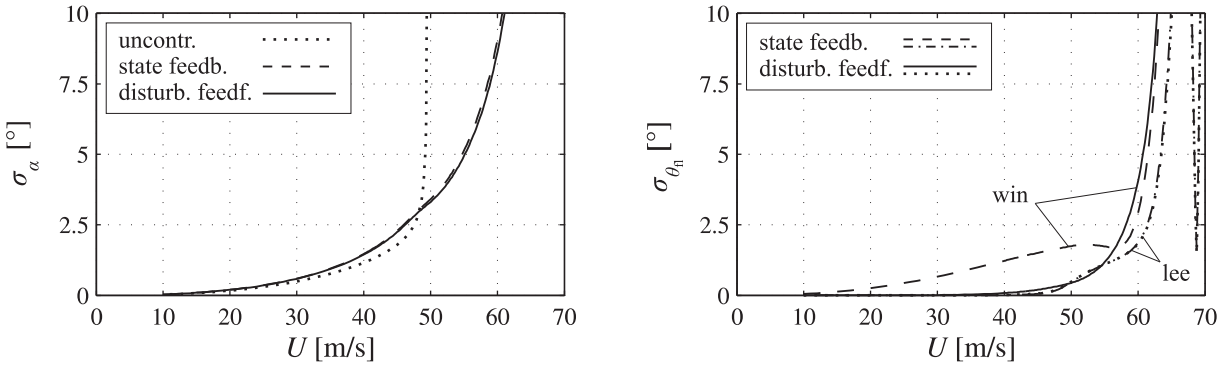

Figure 5.50: Standard deviations of the rotations of the controlled bridge and the separately driven flaps due to vertical gusts. Force input.

contain non-zero elements of the gust-force vector $\mathbf{d}_{ae}^{g}$. If reaction wheels or control moment gyroscopes are employed, disturbance forces act on the bridge but not directly on the actuators. Hence, the precondition for a direct counteraction is not given. Only flaps allow for a partial compensation because the gust-induced aerodynamic forces also act on the actuator elements.

Disturbance feedforward is modelled as follows.

$$\mathbf{f}_c = -\mathbf{K}_d \mathbf{d}_{ae}^{g} \tag{5.81}$$

The effect of a pure disturbance feedforward without a feedback of the actual system behaviour strongly depends on a theoretical model. Because of this disadvantage, disturbance feedforward must always be employed together with a closed-loop control to correct the effect of model uncertainties as far as necessary. After inserting Eq. (5.81) into Eq. (5.28), the matrix $\mathbf{K}_d$ must be determined so that the expression

$$(-\mathbf{B}_{as}\mathbf{K}_d + \mathbf{E}_{as})\mathbf{d}_{ae}^{g} \tag{5.82}$$

is minimised. As the matrix $\mathbf{B}_{as}$ is not invertible, a full compensation is not possible. A least-squares solution can be found with the Moore-Penrose pseudoinverse.

$$\mathbf{K}_d = (\mathbf{B}_{as}^{T}\mathbf{B}_{as})^{-1}\mathbf{B}_{as}^{T}\mathbf{E}_{as} \tag{5.83}$$

With this solution, Eq. (5.28a) reads as

$$\dot{\mathbf{x}}_{as} = \mathbf{A}_{as}\mathbf{x}_{as} + \left(\mathbf{I} - \mathbf{B}_{as}(\mathbf{B}_{as}^{T}\mathbf{B}_{as})^{-1}\mathbf{B}_{as}^{T}\right)\mathbf{E}_{as}\mathbf{d}_{ae}^{g} + \mathbf{B}_{as}\mathbf{f}_c \quad . \tag{5.84}$$

To determine the actuator-input forces, those of Eq. (5.81) have to be added to those of Eq. (5.61).

As a numerical example, the state-feedback of the bridge with separately driven flaps and a force input that is addressed as a standard case in Section 5.6 is extended with a disturbance

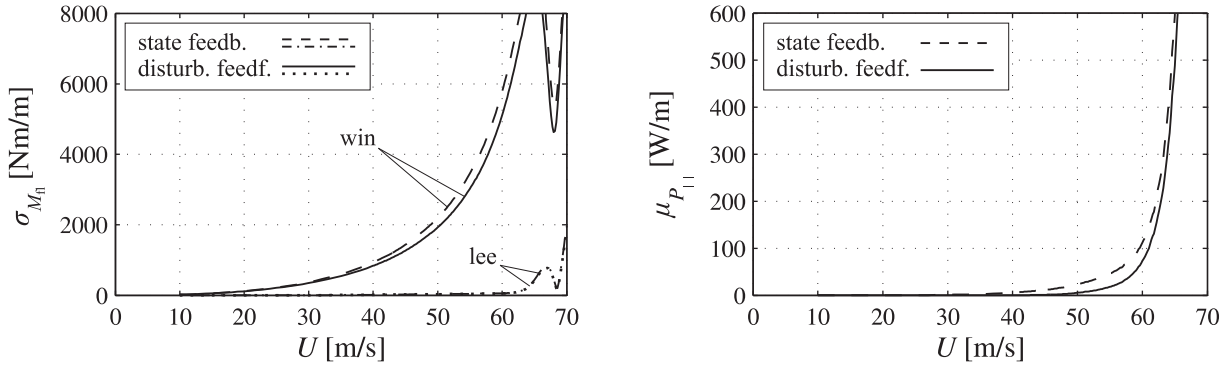

Figure 5.51: Standard deviation of the input moments of the separately driven flaps and mean value of the actuator power. Force input.

feedforward. Figure 5.50 and Figure 5.51 illustrate the results. Compared to the pure state feedback, the rotation of the bridge, the rotation of the leeward flap, and the actuator input force on the leeward flap are merely altered. The rotation of the windward flap, however, gets slightly higher values shortly before the reference wind speed reaches $U = 60\,\mathrm{m/s}$, but it is considerably attenuated for lower reference wind speeds. The actuator input forces on the windward flap and the power demand even have lower values for all displayed reference wind speeds. Based on these results, an additional disturbance feedforward should be added to an active control if the disturbances are measurable without much effort and they directly act on the actuator.

For actuator-extended systems with a displacement input, the situation is more complicated. Especially for the model with the third-order lag element used in this work, a direct compensation cannot be modelled as easily as demonstrated for the force input because there is the small time lag between the input $\mathbf{u}_\mathrm{c}$ and the actuator displacement $\boldsymbol{\xi}_\mathrm{c}$. Moreover, the actuator state $\mathbf{x}_\mathrm{c}$ is a part of the full system state. A compensation without influencing the system state is thus not possible with this model. In Eq. (5.48), non-zero elements of $\mathbf{E}_{\mathrm{asu}}\mathbf{d}_{\mathrm{ae}}^{\mathrm{g}}$ and $\mathbf{B}_{\mathrm{asu}}\mathbf{u}_\mathrm{c}$ are positioned in different rows as a consequence. In addition to the mathematical problems, a rotation of a flap, for instance, does not only have an instantaneous effect but also transient forces are generated. A direct compensation of the disturbance without influencing the system state is thus hardly possible. For systems with a displacement input, disturbance feedforward is not discussed further here.

Another interesting question is whether in Eq. (5.26) it makes sense to consider the motion-induced aerodynamic forces $\mathbf{f}_{\mathrm{ae}}$ as a disturbance on the structural system and to develop a disturbance feedforward for them. This kind of aerodynamic forces can also be indirectly measured, for instance, with their transfer model and a measurement of the structural displacements. Based on the foregoing results, a rough answer can be found. The disturbance feedforward is ineffective if reaction wheels and control moment gyroscopes are applied. Flaps can only compensate a part of the motion-induced aerodynamic forces. The compensated forces cannot be

used for a favourable damping of a structure. A feedback of the aeroelastic state of the model in Eq. (5.28), however, has access to most of the components of the motion-induced aerodynamic forces in Eq. (3.10b) and is much more flexible than a fixed disturbance feedforward.

So far, only the structural displacements and their first derivatives have been measured and used for the feedback control. A measurement of the acceleration of the structure has not been considered. In an output equation, a measurement of accelerations is identical with the first rows of the state-space model or combinations of them. The output thus not only depends on the system state but also directly on the system disturbance. For instance, a proportional feedback of accelerations in addition to the system state can be interpreted as an additional output feedback together with a special kind of disturbance feedforward. Additional or pure acceleration feedbacks are not analysed in the work presented here.

5.9 Proportional-Integral Control

In the foregoing sections, the performance of the controlled system under a zero-mean disturbance is analysed. The total system displacement with respect to the self-weight position of the bridge is, moreover, influenced by static loads. These loads originate, for instance, from road traffic or wind. For a simulation of the dynamic system behaviour, they are modelled with the help of a step function. As a consequence of the static loads, constant steady-state deviations of some state variables from their zero position occur. In the two-dimensional bridge model that is extended with control moment gyroscopes, for instance, a constant moment causes constant steady-state translational and rotational displacements of the bridge, as well as a constant steady-state actuator rotation θ_{gy}. The actuator rotation is a consequence of the state feedback. Constant steady-state deviations never occur for state variables that are derivatives of other state variables because this would be contradictory to the stability of the controlled system. Due to the linearity of the bridge model, the response to the gust disturbance superposes the system reaction on the static loads. Depending on the size of the static loads, the mean position of a control moment gyroscope deviates more or less from its zero position, although no favourable forces are generated. Since the behaviour of a control moment gyroscope is linearised around the zero position, the operation limit is reached for lower time-varying disturbances if there are static loads.

The application of integral controllers is the proper tool to avoid constant steady-state deviations of selected state variables from their zero position. The following derivations are carried out for the asymptotically stable closed-loop system that has a force input. For a system with a displacement input, only the indices have to be changed. In addition to the controlled input defined with the state feedback of Eq. (5.61), a further force input is possible.

$$\dot{\mathbf{x}}_{\mathrm{as}} = \mathbf{A}_{\mathrm{as,cl}}\mathbf{x}_{\mathrm{as}} + \mathbf{E}_{\mathrm{as}}\mathbf{d}_{\mathrm{ae}}^{\mathrm{g}} + \mathbf{B}_{\mathrm{as}}\mathbf{f}_{\mathrm{c}} \tag{5.85}$$

With

$$\dot{\mathbf{x}}_\mathrm{r} = \mathbf{C}_\mathrm{r}\mathbf{x}_\mathrm{as} \quad , \tag{5.86}$$

the integrator state $\mathbf{x}_\mathrm{r}$ is defined, whose variables equal the integrals of different measured state variables that are selected with the truncated permutation matrix $\mathbf{C}_\mathrm{r}$. The feedback

$$\mathbf{f}_\mathrm{c} = -\mathbf{K}_\mathrm{r}\mathbf{x}_\mathrm{r} \tag{5.87}$$

is necessary to obtain controlled state variables that are free of constant steady-state deviations from a zero position. This is not possible for all state variables. The precondition is that a static actuator input causes constant non-zero steady-state values of the integrated state variables. Hence, the final value $\mathbf{K}_\mathrm{as,cl}^\infty$ of the associated step response must be considered. It can be determined with the final value theorem of Laplace transforms

$$\begin{aligned} \mathbf{K}_\mathrm{as,cl}^\infty &= \lim_{t\to\infty} \int_0^t \mathbf{G}_\mathrm{as,cl}(\tau)\,\mathrm{d}\tau = \lim_{s\to 0}\left(s\left(\frac{1}{s}\mathbf{C}_\mathrm{r}(s\mathbf{I}-\mathbf{A}_\mathrm{as,cl})^{-1}\mathbf{B}_\mathrm{as}\right)\right) \\ &= -\mathbf{C}_\mathrm{r}\mathbf{A}_\mathrm{as,cl}^{-1}\mathbf{B}_\mathrm{as} \end{aligned} \tag{5.88}$$

and is called the zero frequency gain or the static gain. If more than one state variable is integrated, the input must be able to generate arbitrary constant steady-state values for them. Hence, there must be at least as many input variables as integrated state variables. The more precise condition is that the rank of $\mathbf{K}_\mathrm{as,cl}^\infty$ equals the number of integrated state variables, which is known from technical literature as the necessary and sufficient condition for the existence of integral control.

Table 5.7 gives some examples for the existence of an integral control with reference to the two-dimensional systems which proportional state-feedback controllers are designed for in the foregoing sections. The table can be easily compiled based on the insights into the system behaviour gained in this chapter. Concerning the possibility of integral control, it does not matter if a force or a displacement input is chosen. In contrast to the reaction wheel and the control moment gyroscope, the flaps can be used to force the steady-state values of bridge variables to a zero position. It depends on the size of the static loads, however, whether constant steady-state displacements of the bridge can be compensated with acceptable flap rotations.

Usually, the integral control is not designed in an additional step, as shown before, but together with the proportional feedback as a proportional-integral control. To allow for this, the open-loop state-space model of Eq. (5.28) is combined with Eq. (5.86).

$$\dot{\mathbf{x}}_\mathrm{as,I} = \mathbf{A}_\mathrm{as,I}\mathbf{x}_\mathrm{as,I} + \mathbf{E}_\mathrm{as,I}\mathbf{d}_\mathrm{ae}^\mathrm{g} + \mathbf{B}_\mathrm{as,I}\mathbf{f}_\mathrm{c} \tag{5.89a}$$

$$\mathbf{y}_\mathrm{st,I} = \mathbf{C}_\mathrm{as,I}\mathbf{x}_\mathrm{as,I} \quad , \tag{5.89b}$$

Table 5.7: Existence of asymptotically stable controlled 2d systems with a feedback of the integrator state.

		$\mathbf{f}_\mathrm{c}$	$\mathbf{u}_\mathrm{c}$	$\dot{\mathbf{x}}_\mathrm{r}$	$\mathrm{rank}(\mathbf{K}^{\infty}_{\mathrm{as,cl}})$	(yes / no)
rw	state includes θ_rw	$M^\mathrm{pl}_\mathrm{rw}$	$\theta^\mathrm{uc}_\mathrm{rw}$	h/b	0	n
				α	0	n
				θ_rw	1	y
	state without θ_rw	$M^\mathrm{pl}_\mathrm{rw}$	$\dot{\theta}^\mathrm{uc}_\mathrm{rw}$	h/b	0	n
				α	0	n
				$\dot{\theta}_\mathrm{rw}$	1	y
gy		$M^\mathrm{pl}_\mathrm{gy}$	$\theta^\mathrm{uc}_\mathrm{gy}$	h/b	0	n
				α	0	n
				θ_gy	1	y
fl	separately driven	$\begin{pmatrix} M_\mathrm{fl,win} \\ M_\mathrm{fl,lee} \end{pmatrix}$	$\begin{pmatrix} \theta^\mathrm{uc}_\mathrm{fl,win} \\ \theta^\mathrm{uc}_\mathrm{fl,lee} \end{pmatrix}$	$\begin{pmatrix} h/b \\ \alpha \end{pmatrix}$	2	y
				$\begin{pmatrix} \theta_\mathrm{fl,win} \\ \theta_\mathrm{fl,lee} \end{pmatrix}$	2	y
	sd coupled	M_fl	$\theta^\mathrm{uc}_\mathrm{fl}$	h/b	1	y
				α	1	y
				θ_fl	1	y
	od coupled	M_fl	$\theta^\mathrm{uc}_\mathrm{fl}$	h/b	1	y
				α	0	n
				θ_fl	1	y

where

$$\mathbf{x}_\mathrm{as,I} = \begin{pmatrix} \mathbf{x}_\mathrm{as} \\ \mathbf{x}_\mathrm{r} \end{pmatrix}, \quad \mathbf{A}_\mathrm{as,I} = \begin{pmatrix} \mathbf{A}_\mathrm{as} & \mathbf{0} \\ \mathbf{C}_\mathrm{r} & \mathbf{0} \end{pmatrix} \tag{5.90a}$$

$$\mathbf{E}_\mathrm{as,I} = \begin{pmatrix} \mathbf{E}_\mathrm{as} \\ \mathbf{0} \end{pmatrix}, \quad \mathbf{B}_\mathrm{as,I} = \begin{pmatrix} \mathbf{B}_\mathrm{as} \\ \mathbf{0} \end{pmatrix}, \quad \mathbf{C}_\mathrm{as,I} = \begin{pmatrix} \mathbf{C}_\mathrm{as} & \mathbf{0} \\ \mathbf{0} & \mathbf{I} \end{pmatrix} \quad . \tag{5.90b}$$

The output equation includes a readout of the integrator state to ensure its observability. The integrals are usually not measured but numerically determined based on the measured state variables that have to be integrated. It can be shown that the controllability of the integrator state is given if the rank criterion derived above is fulfilled. The block triangular shape of the system matrix indicates that new zero eigenvalues occur because of the integrator state. Due to different signal paths, these identical eigenvalues are connected to different eigenvectors. The proportional-integral controller $\mathbf{K}_\mathrm{I}$ of the feedback

$$\mathbf{f}_\mathrm{c} = -\mathbf{K}_\mathrm{I}\mathbf{x}_\mathrm{as,I} = -\begin{pmatrix} \mathbf{K} & \mathbf{K}_\mathrm{r} \end{pmatrix} \begin{pmatrix} \mathbf{x}_\mathrm{as} \\ \mathbf{x}_\mathrm{r} \end{pmatrix} \tag{5.91}$$

can now be designed as shown for the proportional controller.

If flaps are employed as actuators, the wind-speed limits for their application, which are derived in the foregoing sections, can be negatively influenced by integral control. In the case of sd-coupled flaps, for instance, the extension of the system state with the integrated flap rotation leads to a reduction of the upper limit of the application range to $U = 64.52\,\mathrm{m/s}$. This divergence wind speed of the flap-extended system with unmoved flaps cannot be changed because of the restriction of the steady-state behaviour of the motion of the flaps that is caused by the integration. In contrast, the wind speed limits for the application of reaction wheels and control moment gyroscopes remain unaffected by integral control. These limits equal the divergence wind speeds, which do not depend on the controlled motions of the latter actuator types.

To demonstrate a proportional-integral control, the two dimensional model of the bridge that is extended with reaction wheels is suited because the foregoing sections already contain a numerical example. The system where the wheel rotation θ_{rw} is not included in the state vector has a remarkable shortcoming. It responds to a static disturbance with a constant non-zero steady-state angular speed. Including the integral of the angular speed in the feedback equation equals the system where the wheel rotation is included in the state vector. In essence, the state-space model of the latter system has the form of Eq. (5.89). The integrator equation is not positioned below the aeroelastic state but at the end of the block of structural state variables.

As shown for the state feedback, the feedback of Eq. (5.91) can be combined with a state observer. Instead of the state $\mathbf{x}_{\mathrm{as}}$, the observed ones $\mathbf{x}_{\mathrm{as}}^{\mathrm{ob}}$ are used. The integrator states do not have to be observed because they can be obtained by integration.

6 Conclusion

6.1 Summary

Theoretical models of an actuator-equipped bridge within streaming air are derived. Moreover, the effectiveness of different controlled actuators for the improvement of the dynamic bridge characteristics is analysed. Throughout the work presented here, all investigated parts of the dynamic system, which are linearised around their operating point, are considered as linear time-invariant transfer elements. Much attention is paid to this interpretation because in this context, a lot of improper statements circulate through the technical literature of the last decades. Since the transfer functions of all dynamic systems are finally described with rational functions in the frequency domain, a standardised representation with state-space models of continuous-time time-invariant systems is made possible. All methods and theorems that are available from the theory of linear time-invariant systems can be used for the analyses. This applies to the air flow, the bridge structure, as well as their combination in terms of the aeroelastic system. Moreover, the controllers for the actuator-equipped bridge can be examined with the methods of control theory that exist for multivariable systems.

Motion-induced and gust-induced aerodynamic forces are defined as outputs of linear time-invariant transfer elements. As usual, the strip theory is applied. The theoretical forces due to an incompressible flow around one or three flat plates play a key role as reference values because they can be described with analytical functions. Additional measured values for motion-induced forces on idealised bridge cross sections are taken from the technical literature. For their description, the similarity characteristics of the theoretical flat-plate forces are assumed to be valid.

To approximate the transfer functions of the theoretical or measured aerodynamic forces with rational functions, a general approach for each force coefficient is introduced. General partial fraction expansions of the rational functions are used. In the time domain, they correspond to state-space models with system matrices in the Jordan normal form. Two commonly applied matrix-based approaches are derived as special cases. With comprehensive studies, it is shown that these special cases of rational functions are particularly suited to approximate the transfer behaviour of the theoretical flat-plate forces. However, the more the real flow around a bridge cross section deviates from this theoretical flow, the less appropriate is the rational function

approach. Increasing the number of partial fractions leads to an improved approximation of the transfer function within the identification interval but produces unacceptable numerical artefacts at other frequencies.

A long-span cable-stayed bridge is presented as a numerical example. Either element-wise or global shape functions are applied to discretise the spatial structure. Combining the structure and the aerodynamic forces leads to the aeroelastic system. Its stability and the transfer of the gust-induced forces to the displacements of the bridge are extensively analysed. Parameter-dependent eigenvalue problems are solved for investigating the system stability. An algorithm for tracking the eigenvalue paths is developed that especially allows a comprehensible illustration of the calculated results. For different cross sections, it is demonstrated how the approximation of the transfer behaviour of the aerodynamic forces determines the theoretical dynamic characteristics of the aeroelastic system.

Reaction wheels, control moment gyroscopes, and aerodynamically effective flaps are introduced as actuators, which seem to be especially suitable to improve the dynamic behaviour of a bridge under the effect of the streaming air. The models of the bridge are extended to incorporate these actuators. Two different kinds of inputs, forces and displacements, are chosen for their control. Controllability and observability are analysed as preconditions for a control in a feedback loop. Attention is paid to the effect of the rational function approximation. To investigate the capability of the actuators under best conditions, active controllers with state feedback are employed. The design algorithm of a linear-quadratic regulator is chosen for most of the numerical examples. For a system stabilisation with the help of the actuators, fundamental wind-speed limits are revealed. Reaction wheels and control moment gyroscopes cannot stabilise the bridge beyond the divergence wind speed. Based on the employed theoretical aerodynamic forces, separately driven flaps can stabilise the bridge for a wide range of the mean wind speed. If windward and leeward flap motions are kinematically coupled, there are usually upper bounds for a stabilisation of the system. Some of these bounds can be overcome if a higher number of independent proper shapes of flap rotations along the girder length are chosen as inputs. Depending on the size of the system disturbance, the upper limit for the application of the actuators can be distinctly lower. The performance of the controlled system is compared for the different types of actuators. To generate an effective motion of the reaction wheels, high forces and a lot of power are necessary. Flaps also need high input forces, whereas their power demand is considerably lower. For control moment gyroscopes, the power demand is comparably low. Moreover, they require only low input forces. A remarkable energy input, however, is needed to create an appreciable angular momentum of their rotors. In the final sections of the work presented here, state observers, disturbance feedforward, and integral control are explained with respect to the investigated bridge.

6.2 Outlook

Many of the presented theoretical investigations are carried out using simplifying assumptions. Further research activities should explore whether refined models change the results obtained so far. Especially the linearised descriptions of the different kinds of aerodynamic forces seem to be a weak point of the model. Concerning the aerodynamic forces on a bridge cross section in real flow, it should be investigated to what extent an approach with rational functions and more general pole locations is capable of improving the approximation quality of the transfer functions. If the actuators are employed for non-streamlined cross sections, additional vortex-induced aerodynamic forces must be taken into account when the quality of the designed controllers is tested. Moreover, at least for final controller tests, other flow models should be applied that are not restricted to small displacements of the structure and do not distinguish between the different kinds of aerodynamic forces.

The performance of the controlled bridge is analysed only for the two-dimensional model. A further study of a model is desirable that includes more structural degrees of freedom and an optimised arrangement of the actuators and sensors along the bridge girder. A comprehensive investigation of the effectiveness of the different actuators also necessitates a sufficient variation of all parameters of the controlled aeroelastic system. Such a parameter study, preferably based on a model representation with similarity parameters, is not given here and still needs to be carried out.

In this work, the design of the controllers is focussed on a special range of high reference wind speeds. To allow the controllers to be effective also for lower wind speeds, the linear-quadratic regulators must be designed with varying weighting matrices. State feedback in combination with a state observer is known to be often not sufficiently robust against model uncertainties. Model uncertainties arise, for instance, from a rough discretisation of the continuous system or the linearisation of the non-linear system behaviour. To ensure the stability or a special performance of the closed loop for defined system uncertainties, dynamic controllers with an output feedback can be designed (Zhou & al. 1996, Boyd & al. 1994). If active controllers are considered to be problematic, attention should be turned to passive controllers. Moreover, active gains can be replaced by passive elements in order to minimise the power demand. The effectiveness of a passive control, which is designed to fulfil some basic requirements, can be improved with an additional active control as well. Both latter combinations of active and passive controllers are known as hybrid control (Housner & al. 1997).

Finally, an experimental analysis is still necessary to confirm the theoretical findings of this work. For civil-engineering structures, these experiments can usually only be carried out with scaled models. The decisive similarity parameters of the structure and the flow should equal those of the full-scale aeroelastic system.

Appendix

A.1 Transformation from Aerofoil to Bridge-Flaps Derivatives

Aerofoil According to Theodorsen & Garrick (1941)

The geometry variables and the degrees of freedom of the wing-aileron-tab problem according to Theodorsen & Garrick (1941) are given in Figure A.1(a). All physical quantities of the aerofoil are marked with the index Th and are not included in the notation list. After adapting the lengths ratio of the aerofoil components to that of the bridge flaps problem, which is done in Figure A.1(b), the variables of this work in Figure 2.5 can be compared with the aerofoil variables.

With the following matrix equation, the geometry variables of the bridge problem are transformed to those of the aerofoil.

$$\begin{pmatrix} b \\ ab \\ cb \\ db \\ eb \\ fb \end{pmatrix}_{\mathrm{Th}} = \begin{pmatrix} 1 & 2 & 0 & 0 \\ 0 & 0 & 0 & 0 \\ -1 & 0 & 0 & 0 \\ 1 & 0 & 0 & 0 \\ -1 & -1 & -1 & 0 \\ 1 & 1 & 0 & -1 \end{pmatrix} \begin{pmatrix} b \\ b_{\mathrm{fl}} \\ d_{\mathrm{h,win}} \\ d_{\mathrm{h,lee}} \end{pmatrix} \tag{A.1}$$

The gaps at the wing-aileron and aileron-tab transitions are considered to be sealed. This seems to be appropriate to model the transitions of elements of finite thickness with obtuse neighbouring edges. The sealed gaps must be modelled with a finite length to avoid infinitely large values of special logarithmic terms in the analytic descriptions of the aerodynamic derivatives. The length is set to 10 % of the flap half-width b_{fl} according to recommendations given in Theodorsen & Garrick (1941).

Also based on a comparison of Figure A.1(b) with Figure 2.5, the degrees of freedom defined in Eq. (2.26a) can be transformed into those used for the aerofoil problem.

$$\begin{pmatrix} h/b & \alpha & \beta & \gamma \end{pmatrix}^{\mathrm{T}}_{\mathrm{Th}} = \mathbf{a}_{\mathrm{Th}} \boldsymbol{\xi}_{\mathrm{s}} \tag{A.2}$$

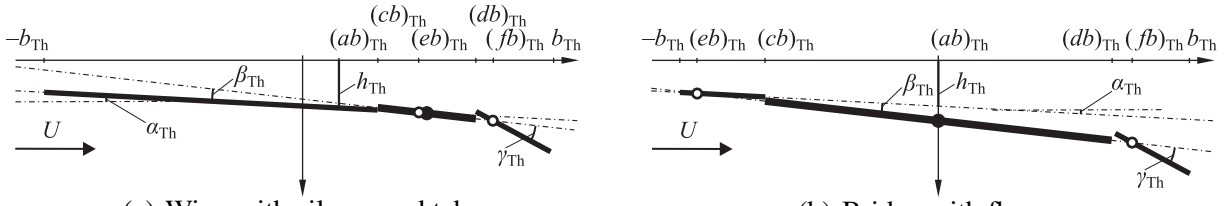

(a) Wing with aileron and tab. (b) Bridge with flaps.

Figure A.1: Flat-plate problems described with the variables used in Theodorsen & Garrick (1941).

The transformation matrix $\mathbf{a}_{\mathrm{Th}}$ has the following entries.

$$\mathbf{a}_{\mathrm{Th}} = \begin{pmatrix} b/b_{\mathrm{Th}} & 0 & -e_{\mathrm{Th}} & 0 \\ 0 & 1 & 1 & 0 \\ 0 & 0 & -1 & 0 \\ 0 & 0 & 0 & 1 \end{pmatrix} \tag{A.3}$$

The motion-induced aerodynamic forces and the degrees of freedom are defined for the aerofoil in an energetically corresponding way and without redundancies. As explained in Section 1.3, the transformation between the forces in Eq. (2.26a) and those defined for the aerofoil problem is thus as follows.

$$\mathbf{f}_{\mathrm{ae}} = \mathbf{a}_{\mathrm{Th}}^{\mathrm{T}} \begin{pmatrix} Pb & M_\alpha & M_\beta & M_\gamma \end{pmatrix}_{\mathrm{Th}}^{\mathrm{T}} \tag{A.4}$$

The reduced frequency used for the aerofoil problem is related to the aerofoil half length b_{Th}. Hence, the reduced frequency in Eq. (1.7) must be transformed.

$$p_{\mathrm{Th}} = p\, b_{\mathrm{Th}}/b \tag{A.5}$$

For the aerofoil problem, the transfer equation of motion-induced aerodynamic forces is given for purely imaginary frequencies

$$\begin{pmatrix} Pb & M_\alpha & M_\beta & M_\gamma \end{pmatrix}_{\mathrm{Th}}^{\mathrm{T}} = \mathbf{G}_{\mathrm{ae,Th}}(\mathrm{i}\omega) \begin{pmatrix} h/b & \alpha & \beta & \gamma \end{pmatrix}_{\mathrm{Th}}^{\mathrm{T}} \quad , \tag{A.6}$$

where the aerodynamic transfer function is defined as follows.

$$\mathbf{G}_{\mathrm{ae,Th}}(\mathrm{i}\omega) = \pi\rho b_{\mathrm{Th}}^4 \omega^2 \mathbf{C}_{\mathrm{ae,Th}}(\mathrm{i}k_{\mathrm{Th}}) \tag{A.7}$$

Similar to Eq. (2.8a), the following notation can be defined.

$$\mathbf{G}_{\mathrm{ae,Th}}(\mathrm{i}\omega) = \pi\rho b_{\mathrm{Th}}^2 U^2 \mathbf{Q}_{\mathrm{Th}}(\mathrm{i}k_{\mathrm{Th}}) \tag{A.8}$$

The aerofoil derivatives of both notations can be transformed into each other.

$$\mathbf{Q}_{\mathrm{Th}}(\mathrm{i}k_{\mathrm{Th}}) = k_{\mathrm{Th}}^2 \mathbf{C}_{\mathrm{ae,Th}}(\mathrm{i}k_{\mathrm{Th}}) \tag{A.9}$$

In contrast to the aerodynamic derivatives in $\mathbf{C}_{\mathrm{ae,Th}}$, those in $\mathbf{Q}_{\mathrm{Th}}$ can be evaluated for the steady case limit $\omega \to 0$. The application of the generalisation procedure described in Section 2.2.2 for the single flat plate means replacing ω^2 with $(-s^2)$ and $\mathrm{i}k_{\mathrm{Th}}$ with p_{Th}.

Combining the foregoing equations and comparing them with those of Section 2.1 leads to the formulas for the transformation from aerofoil to bridge-flaps derivatives.

$$\mathbf{C}_{\mathrm{ae}} = \mathbf{a}_{\mathrm{Th}}^{\mathrm{T}} \mathbf{C}_{\mathrm{ae,Th}} \mathbf{a}_{\mathrm{Th}} (b_{\mathrm{Th}}/b)^4 \tag{A.10a}$$

$$\mathbf{Q} = \mathbf{a}_{\mathrm{Th}}^{\mathrm{T}} \mathbf{Q}_{\mathrm{Th}} \mathbf{a}_{\mathrm{Th}} (b_{\mathrm{Th}}/b)^2 \tag{A.10b}$$

Aerofoil According to Küssner & Göllnitz (1964)

In a similar way as in the foregoing section, the aerofoil description according to Küssner & Göllnitz (1964) can be transformed to the bridge-flaps description used here. All physical quantities of the aerofoil are marked with the index Kü and are again not included in the list of notation.

The geometry variables of the aerofoil and the bridge show the following relationship.

$$\begin{pmatrix} l \\ x_0 \\ x_1 \\ x_2 \\ x_3 \\ x_4 \end{pmatrix}_{\mathrm{Kü}} = \begin{pmatrix} 1 & 2 & 0 & 0 \\ \frac{1}{2} & 1 & 0 & 0 \\ 1 & 0 & 0 & 0 \\ 1 & 1 & 1 & 0 \\ -1 & 0 & 0 & 0 \\ -1 & -1 & 0 & 1 \end{pmatrix} \begin{pmatrix} b \\ b_{\mathrm{fl}} \\ d_{\mathrm{h,win}} \\ d_{\mathrm{h,lee}} \end{pmatrix} \tag{A.11}$$

The gaps between the different flaps can be described either as open or as sealed to model the cases of acute and obtuse edges of neighbouring cross-section components, respectively. For the sealed case, the length of the gaps is again set to 10 % of the flap half-width b_{fl}.

Compared to Theodorsen & Garrick (1941), there are additional degrees of freedom in Küssner & Göllnitz (1964) because the aileron and tab motions are possible with independent rotations and translations. The transformation can be obtained based on a comparison between Figure A.2(b) and Figure 2.5.

$$\begin{pmatrix} A & B & C & D & E & F \end{pmatrix}_{\mathrm{Kü}}^{\mathrm{T}} = \mathbf{a}_{\mathrm{Kü}} \boldsymbol{\xi}_{\mathrm{s}} \tag{A.12}$$

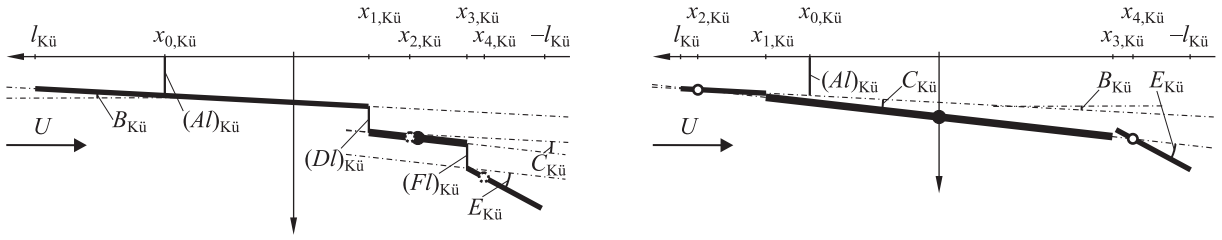

(a) Wing with aileron and tab.

(b) Bridge with flaps.

Figure A.2: Flat-plate problems described with the variables used in Küssner & Göllnitz (1964).

In the transformation matrix $\mathbf{a}_{\text{Kü}}$, the following entries appear.

$$\mathbf{a}_{\text{Kü}} = \begin{pmatrix} 1 & 0 & 0 & 0 \\ 0 & 1 & 0 & 0 \\ 0 & 0 & 1 & 0 \\ 0 & 0 & \dfrac{(x_2-x_1)_{\text{Kü}}}{l_{\text{Kü}}} & 0 \\ 0 & 0 & 0 & 1 \\ 0 & 0 & 0 & \dfrac{(x_4-x_3)_{\text{Kü}}}{l_{\text{Kü}}} \end{pmatrix} \begin{pmatrix} \dfrac{b}{l_{\text{Kü}}} & \dfrac{-x_{0,\text{Kü}}}{l_{\text{Kü}}} & \dfrac{(x_2-x_0)_{\text{Kü}}}{l_{\text{Kü}}} & 0 \\ 0 & 1 & 1 & 0 \\ 0 & 0 & -1 & 0 \\ 0 & 0 & 0 & 1 \end{pmatrix} \tag{A.13}$$

Contrary to Section A.1, the transformation must also couple the independent components of the aileron and tab motions shown in Figure A.2(a) to define a hinge position. This is done with the left part of $\mathbf{a}_{\text{Kü}}$. In Figure A.2(b), the translation variables $D_{\text{Kü}}$ and $F_{\text{Kü}}$ are thus not shown because they depend on the rotations $C_{\text{Kü}}$ and $E_{\text{Kü}}$ and the hinge locations.

Due to the appropriate definitions of the motion-induced aerodynamic forces and the degrees of freedom, the transformation is possible again, as shown below.

$$\mathbf{f}_{\text{ae}} = \mathbf{a}_{\text{Kü}}^{\text{T}} \begin{pmatrix} Kl & M_0 & N & Rl & Q & Pl \end{pmatrix}_{\text{Kü}}^{\text{T}} \tag{A.14}$$

The reduced frequency must also be adjusted.

$$p_{\text{Kü}} = p\, l_{\text{Kü}}/b \tag{A.15}$$

The variable $\omega^*_{\text{Kü}}$ denotes the imaginary part of the reduced frequency $p_{\text{Kü}}$ of the aerofoil problem.

For purely imaginary frequencies, the transfer equation of motion-induced aerodynamic forces for the aerofoil problem is given in Küssner & Göllnitz (1964).

$$\begin{pmatrix} Kl & M_0 & N & Rl & Q & Pl \end{pmatrix}_{\text{Kü}}^{\text{T}} = \mathbf{G}_{\text{ae,Kü}}(\mathrm{i}\omega) \begin{pmatrix} A & B & C & D & E & F \end{pmatrix}_{\text{Kü}}^{\text{T}} \tag{A.16}$$

The aerodynamic transfer function can be defined in two ways

$$\mathbf{G}_{\mathrm{ae,Kü}}(\mathrm{i}\omega) = \pi\rho l_{\mathrm{Kü}}^4 \omega^2 \mathbf{C}_{\mathrm{ae,Kü}}(\mathrm{i}\omega_{\mathrm{Kü}}^*) \tag{A.17a}$$

$$\mathbf{G}_{\mathrm{ae,Kü}}(\mathrm{i}\omega) = \pi\rho l_{\mathrm{Kü}}^2 U^2 \mathbf{Q}_{\mathrm{Kü}}(\mathrm{i}\omega_{\mathrm{Kü}}^*) \quad , \tag{A.17b}$$

where

$$\mathbf{Q}_{\mathrm{Kü}}(\mathrm{i}\omega_{\mathrm{Kü}}^*) = (\omega_{\mathrm{Kü}}^*)^2 \mathbf{C}_{\mathrm{ae,Kü}}(\mathrm{i}\omega_{\mathrm{Kü}}^*) \quad . \tag{A.18}$$

Replacing ω^2 with $(-s^2)$ and $\mathrm{i}\omega_{\mathrm{Kü}}^*$ with $p_{\mathrm{Kü}}$ is part of the generalisation procedure described in Section 2.2.2.

Finally, a combination of the foregoing equations and a comparison with those of Section 2.1 lead to the equations for the derivative transformation from the aerofoil to the bridge-flaps problem.

$$\mathbf{C}_{\mathrm{ae}} = \mathbf{a}_{\mathrm{Kü}}^{\mathrm{T}} \mathbf{C}_{\mathrm{ae,Kü}} \mathbf{a}_{\mathrm{Kü}} (l_{\mathrm{Kü}}/b)^4 \tag{A.19a}$$

$$\mathbf{Q} = \mathbf{a}_{\mathrm{Kü}}^{\mathrm{T}} \mathbf{Q}_{\mathrm{Kü}} \mathbf{a}_{\mathrm{Kü}} (l_{\mathrm{Kü}}/b)^2 \tag{A.19b}$$

When comparing the transformed results of Theodorsen & Garrick (1941) and Küssner & Göllnitz (1964) for the case of sealed gaps, it turns out that there are differences in the steady real parts of the elements Q_{33} and Q_{44}. The differences occur if sealed gaps exist, that means if hinges are not positioned at the end of neighbouring plates. Expressions that include the representation of the influence of the inclined sealed gaps cause the different results. In detail, the following terms do not comply with each other.

$$(T_{28}(c))_{\mathrm{Th}} \quad \neq \quad (\phi_{21}(\varphi) + 2\ln\tau_{\mathrm{SR}})_{\mathrm{Kü}} \tag{A.20a}$$

$$(T_{28}(d))_{\mathrm{Th}} \quad \neq \quad (\phi_{21}(\psi) + 2\ln\tau_{\mathrm{SH}})_{\mathrm{Kü}} \tag{A.20b}$$

One reason for the discrepancy is the unequal definition of the exact location of the beginning and the end of the inclined step. Adjusting the positions, however, does not lead to equal results. Further reasons could be different assumptions that were made for the derivation of the terms or, simply, errors in the publications. A more detailed investigation of the formulas has not been carried out. Since the values of the terms strongly depend on the length of the assumed gap, they should be brought in line with values that are experimentally determined in a steady flow if the theoretical aerodynamic derivatives are applied for real aerofoils. This recommendation is given in the original references. Considering the quality of the model for bridges with flaps, the discussion seems to be unnecessary as far as the results of this work are not significantly affected by the differences between the publications.

A.2 Equations of Motion of Actuator-Equipped Rigid Bodies

The linear equations of motion of the following rigid body problems are given to explain the detailed entries of the matrices used in Section 5.1. The rigid body has the arbitrary length dx perpendicular to the drawing plane. Its displacements are presupposed to be small and the elastic supports have a linear force-displacement behaviour. All assumptions made for the actuators in Section 5.1 still hold true for the following problems. The linearised equations are derived with the principle of virtual displacements for dynamic systems. As in the derivation of the equations of motion of the bridge with element-wise or global shape functions, the virtual displacements are assumed in terms of the virtual versions of the defined degrees of freedom. Symmetric mass, viscous damping, and stiffness matrices, as well as an antimetric gyroscopic damping matrix are achieved in this way for the investigated systems. For the application of the equations of motion to the model of the actuator-equipped bridge, the bending rotation φ of the girder must be additionally considered and the length dx is assumed to be infinitesimal.

Reaction Wheel as Actuator

(a) Kinematic variables and spring constants.

(b) Forces and mass properties.

Figure A.3: Rigid body equipped with a reaction wheel.

From a virtual displacement of the whole system in vertical direction it follows that

$$(m\,\mathrm{d}x)\ddot{h} + m_{\mathrm{rw}}\ddot{h} = -(K_{\mathrm{s},h}\,\mathrm{d}x)h + (L\,\mathrm{d}x) \quad . \tag{A.21}$$

A virtual rotation of the whole system around the centre of gravity leads to

$$(I\,\mathrm{d}x)\ddot{\alpha} + I_{\mathrm{rw,h}}(\ddot{\alpha} + \ddot{\theta}_{\mathrm{rw}}) = -(K_{\mathrm{s},\alpha}\,\mathrm{d}x)\alpha + (M\,\mathrm{d}x) \quad , \tag{A.22}$$

and a virtual rotation of the reaction wheel around its hinge results in

$$I_{\mathrm{rw,h}}(\ddot{\alpha} + \ddot{\theta}_{\mathrm{rw}}) = M_{\mathrm{rw}} \quad . \tag{A.23}$$

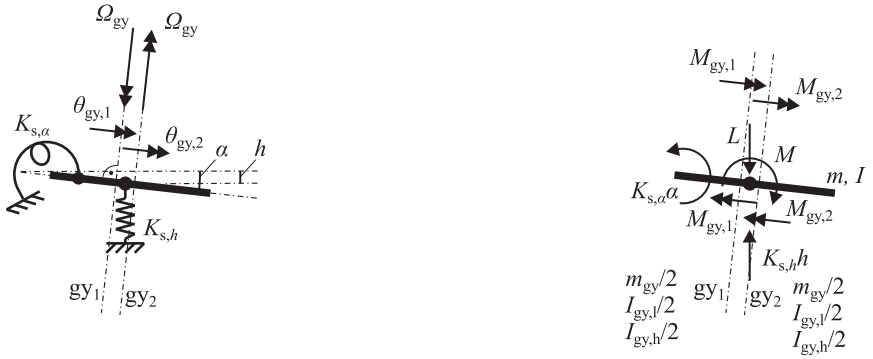

(a) Kinematic variables and spring constants. (b) Forces and mass properties.

Figure A.4: Rigid body equipped with a twin control moment gyroscope.

Control Moment Gyroscope as Actuator

Applying a virtual displacement on the whole system in vertical direction yields

$$(m\,\mathrm{d}x)\ddot{h} + 2\frac{m_{gy}}{2}\ddot{h} = -(K_{s,h}\,\mathrm{d}x)h + (L\,\mathrm{d}x) \quad . \tag{A.24}$$

A virtual rotation of the whole system around the centre of gravity results in

$$\begin{aligned}(I\,\mathrm{d}x)\ddot{\alpha} + (\frac{I_{gy,l}}{2}\ddot{\alpha} + \frac{I_{gy,h}}{2}\Omega_{gy}\dot{\theta}_{gy,1}) + (\frac{I_{gy,l}}{2}\ddot{\alpha} - \frac{I_{gy,h}}{2}\Omega_{gy}\dot{\theta}_{gy,2}) \\ = -(K_{s,\alpha}\,\mathrm{d}x)\alpha + (M\,\mathrm{d}x) \quad .\end{aligned} \tag{A.25}$$

Virtual rotations of the rotors around the gimbal axes lead to the following equations

$$-\frac{I_{gy,h}}{2}\Omega_{gy}\dot{\alpha} + \frac{I_{gy,l}}{2}\ddot{\theta}_{gy,1} = M_{gy,1} \tag{A.26a}$$

$$\frac{I_{gy,h}}{2}\Omega_{gy}\dot{\alpha} + \frac{I_{gy,l}}{2}\ddot{\theta}_{gy,2} = M_{gy,2} \quad , \tag{A.26b}$$

where $M_{gy,j}$ is the actuating moment around a gimbal axis. The gimbal rotations are kinematically coupled.

$$\begin{pmatrix} \theta_{gy,1} \\ \theta_{gy,2} \end{pmatrix} = \begin{pmatrix} 1 \\ -1 \end{pmatrix} \theta_{gy} \tag{A.27}$$

The resulting input torque M_{gy} that acts between the gimbals and the bridge girder, which energetically corresponds to θ_{gy}, follows according to Section 1.3.

$$M_{gy} = \begin{pmatrix} 1 \\ -1 \end{pmatrix}^{T} \begin{pmatrix} M_{gy,1} \\ M_{gy,2} \end{pmatrix} \tag{A.28}$$

The total torque $(M_{gy,1} + M_{gy,2})$ between the actuator and the bridge equals zero due to the special gearing mechanism.

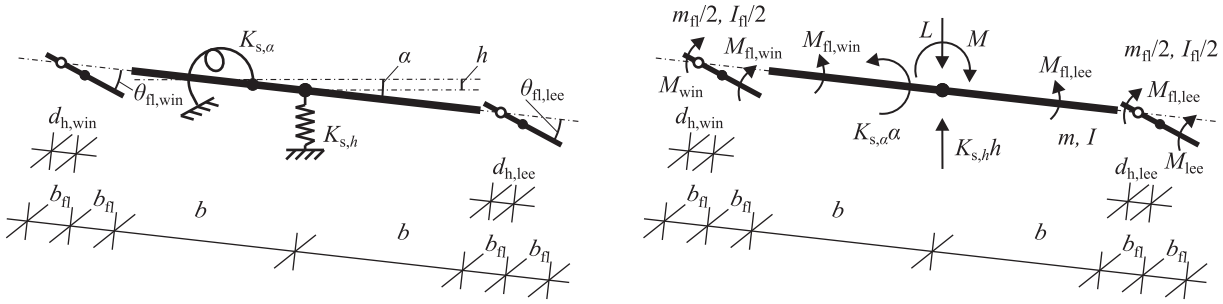

(a) Kinematic variables and spring constants. (b) Forces and mass properties.

Figure A.5: Rigid body equipped with rigid flaps.

Flaps as Actuating Elements

The following variables are introduced to abbreviate the vertical displacements of the centres of gravity of the flaps.

$$h_{\mathrm{fl,win}} = h - (b + b_{\mathrm{fl}})\alpha + d_{\mathrm{h,win}}\theta_{\mathrm{fl,win}} \tag{A.29a}$$

$$h_{\mathrm{fl,lee}} = h + (b + b_{\mathrm{fl}})\alpha + d_{\mathrm{h,lee}}\theta_{\mathrm{fl,lee}} \tag{A.29b}$$

A virtual displacement of the whole system in vertical direction leads to

$$m\ddot{h} + \frac{m_{\mathrm{fl}}}{2}(\ddot{h}_{\mathrm{fl,win}} + \ddot{h}_{\mathrm{fl,lee}}) = -K_{\mathrm{s},h}h + L \quad . \tag{A.30}$$

From a virtual rotation of the whole system around the centre of gravity it follows that

$$\begin{aligned} I\ddot{\alpha} + \frac{I_{\mathrm{fl}}}{2}((\ddot{\alpha} + \ddot{\theta}_{\mathrm{fl,win}}) + (\ddot{\alpha} + \ddot{\theta}_{\mathrm{fl,lee}})) + \frac{m_{\mathrm{fl}}}{2}(b + b_{\mathrm{fl}})(-\ddot{h}_{\mathrm{fl,win}} + \ddot{h}_{\mathrm{fl,lee}}) \\ = -K_{\mathrm{s},\alpha}\alpha + M \quad . \end{aligned} \tag{A.31}$$

A virtual rotation of the windward flap around its hinge results in

$$\frac{I_{\mathrm{fl}}}{2}(\ddot{\alpha} + \ddot{\theta}_{\mathrm{fl,win}}) + \frac{m_{\mathrm{fl}}}{2}\ddot{h}_{\mathrm{fl,win}}d_{\mathrm{h,win}} = M_{\mathrm{win}} + M_{\mathrm{fl,win}} \quad , \tag{A.32}$$

and a virtual rotation of the leeward flap around its hinge leads to

$$\frac{I_{\mathrm{fl}}}{2}(\ddot{\alpha} + \ddot{\theta}_{\mathrm{fl,lee}}) + \frac{m_{\mathrm{fl}}}{2}\ddot{h}_{\mathrm{fl,lee}}d_{\mathrm{h,lee}} = M_{\mathrm{lee}} + M_{\mathrm{fl,lee}} \quad . \tag{A.33}$$

The variables $M_{\mathrm{fl},j}$ represent the hinge moments. Static moments around the hinges that are caused by the self-weight of the flaps are not modelled. As with all gravity effects, they need not be considered when they are compensated with elastic connections. Hence, it is supposed that a part of the hinge moments finally originates from springs and that the zero position of the flaps complies with the static equilibrium position under the effect of the self-weight.

References

Abel 1979

ABEL, I.: An analytical technique for predicting the characteristics of a flexible wing equipped with an active flutter-suppression system and comparison with wind-tunnel data / NASA. 1979 (NASA-TP-1367). – Technical Paper

Abramowitz & Stegun 1984

ABRAMOWITZ, M. ; STEGUN, I. A.: *Pocketbook of Mathematical Functions*. Abridged Edition of the Original Handbook. Frankfurt a. M. : Harri Deutsch, 1984

Cobo del Arco & Aparicio 1999

ARCO, D. Cobo d. ; APARICIO, Á. C.: Improving suspension bridge wind stability with aerodynamic appendages. in: *Journal of Structural Engineering* 125 (1999), pp. 1367–1375

Argyris & Mlejnek 1988

ARGYRIS, J. ; MLEJNEK, H.-P.: *Methode der Finiten Elemente in der elementaren Strukturmechanik, Band III — Einführung in die Dynamik*. Braunschweig : Vieweg, 1988 (in German)

Argyris 1957

ARGYRIS, J. H.: Die Matrizentheorie der Statik. in: *Ingenieur-Archiv* 25 (1957), pp. 174–192 (in German)

Arnold 1973

ARNOLD, L.: *Stochastische Differentialgleichungen*. München : Oldenbourg, 1973 (in German)

Aslan & Starossek 2008

ASLAN, H. ; STAROSSEK, U.: Passive control of bridge deck flutter using tuned mass dampers and control surfaces. in: *EURODYN 2008 — 7th European Conference on Structural Dynamics*. Southampton / UK, 2008, Paper E298

Augusti & al. 2001

AUGUSTI, G. ; BORRI, C. ; NIEMANN, H.-J.: Is aeolian risk as significant as other environmental risks? in: *Reliability Engineering and System Safety* 74 (2001), pp. 227–237

Bai & al. 2010

BAI, Y. ; SUN, D. ; LIN, J.: Three dimensional numerical simulations of long-span bridge aerodynamics, using block-iterative coupling and DES. in: *Computers & Fluids* 39 (2010), pp. 1549–1561

Barelli & al. 2006

BARELLI, M. ; WHITE, J. ; BILLINGTON, D. P.: History and aesthetics of the Bronx-Whitestone Bridge. in: *Journal of Bridge Engineering* 11 (2006), pp. 230–240

Bendat & Piersol 2000

BENDAT, J. S. ; PIERSOL, A. G.: *Random Data: Analysis and Measurement Procedures*. 3rd Edition. New York : Wiley, 2000

Bergmann 2004

BERGMANN, D.: *Experimentelle Ermittlung der instationären aerodynamischen Eigenschaften von Brückenprofilen im Wasserkanal*, Universität Stuttgart, Dissertation, 2004 (in German)

Bisplinghoff & al. 1951

BISPLINGHOFF, R. L. ; ISAKSON, G. ; O'BRIEN, T. F.: Gust loads on rigid airplanes with pitching neglected. in: *Journal of the Aeronautical Sciences* 18 (1951), pp. 33–42

Bleich 1949

BLEICH, F.: Dynamic instability of truss-stiffened suspension bridges under wind action. in: *Transactions of the American Society of Civil Engineers* 114 (1949), pp. 1177–1232

Boonyapinyo & al. 1999

BOONYAPINYO, V. ; MIYATA, T. ; YAMADA, H.: Advanced aerodynamic analysis of suspension bridges by state-space approach. in: *Journal of Structural Engineering* 125 (1999), pp. 1357–1366

Boyd & al. 1994

BOYD, S. ; EL GHAOUI, L. ; FERON, E. ; BALAKRISHNAN, V.: *Linear Matrix Inequalities in System and Control Theory*. Philadelphia : Society for Industrial and Applied Mathematics (SIAM), 1994

Brigham 1997

BRIGHAM, E. O.: *FFT-Anwendungen*. München : Oldenbourg, 1997 (in German)

Buchek 1974

BUCHEK, P. M.: Modern Control Techniques in Active Flutter Suppression Using a Control Moment Gyro / NASA. 1974 (NASA-CR-138494). – Contractor Report

Caracoglia & Jones 2003

CARACOGLIA, L. ; JONES, N. P.: A methodology for the experimental extraction of indicial functions for streamlined and bluff deck sections. in: *Journal of Wind Engineering and Industrial Aerodynamics* 91 (2003), pp. 609–636

Chambers 2005

CHAMBERS, J. R.: Innovation in Flight: Research of the NASA Langley Research Center on Revolutionary Advanced Concepts for Aeronautics / NASA. 2005 (NASA SP-2005-4539). – Special Publication

Chen & Kareem 2001a

CHEN, X. ; KAREEM, A.: Aeroelastic analysis of bridges under multicorrelated winds: Integrated state-space approach. in: *Journal of Engineering Mechanics* 127 (2001), pp. 1124–1134

Chen & Kareem 2001b

CHEN, X. ; KAREEM, A.: Nonlinear response analysis of long-span bridges under turbulent winds. in: *Journal of Wind Engineering an Industrial Aerodynamics* 89 (2001), pp. 1335–1350

Chen & al. 2000

CHEN, X. ; MATSUMOTO, M. ; KAREEM, A.: Time domain flutter and buffeting response analysis of bridges. in: *Journal of Engineering Mechanics* 126 (2000), pp. 7–16

Clobes 2008

CLOBES, M.: *Identifikation und Simulation instationärer Übertragung der Windturbulenz im Zeitbereich*, Technische Universität Braunschweig, Dissertation, 2008 (in German)

Clough & Penzien 1993

CLOUGH, R. W. ; PENZIEN, J.: *Dynamics of Structures*. 2nd Edition. New York : McGraw-Hill, 1993

Davenport 1962

DAVENPORT, A. G.: Buffeting of a suspension bridge by storm winds. in: *Journal of the Structural Division (ASCE)* 88 (1962), pp. 233-268

Den Hartog 1985

DEN HARTOG, J. P.: *Mechanical Vibrations*. Dover Edition. New York : Dover Publications, 1985

Dyrbye & Hansen 1996

DYRBYE, C. ; HANSEN, S. O.: *Wind Loads on Structures*. Chichester / UK : Wiley, 1996

Edwards 1977

EDWARDS, J. W.: Unsteady Aerodynamic Modeling and Active Aeroelastic Control / NASA. 1977 (NASA-CR-148019). – Contractor Report

Ernst 1965

ERNST, H.-J.: Der E-Modul von Seilen unter Berücksichtigung des Durchhangs. in: *Der Bauingenieur* 40 (1965), pp. 52–55 (in German)

Eusani 2005

EUSANI, R.: *Zur numerischen Zeitbereichssimulation der aeroelastischen Instabilität bei Seilbrücken*, Universität Wuppertal, Dissertation, 2005 (in German)

Eversman & Tewari 1991a

EVERSMAN, W. ; TEWARI, A.: Consistent rational-function approximation for unsteady aerodynamics. in: *Journal of Aircraft* 28 (1991), pp. 545–552

Eversman & Tewari 1991b

EVERSMAN, W. ; TEWARI, A.: Modified exponential series approximation for the Theodorsen function. in: *Journal of Aircraft* 28 (1991), pp. 553–557

Ferry 1932

FERRY, E. S.: *Applied Gyrodynamics*. New York : Wiley, 1932

Föllinger 2003

FÖLLINGER, O.: *Laplace-, Fourier- und Z-Transformationen*. 8. Auflage. Heidelberg : Hüthig, 2003 (in German)

Fujisawa 1995

FUJISAWA, N.: Control of coupled flutter of a bridge deck by mechanical damper. in: *Proceedings of the 50th Annual Conference of the Japan Society of Civil Engineers*. Tokyo, 1995, pp. 1508–1509 (in Japanese)

Garrick 1938

GARRICK, I. E.: On Some Reciprocal Relations in the Theory of Nonstationary Flows / NACA. 1938 (NACA-TR-629). – Technical Report

Gasch & Knothe 1987

GASCH, R. ; KNOTHE, K.: *Strukturdynamik — Band 1: diskrete Systeme*. Berlin : Springer, 1987 (in German)

Gasch & Knothe 1989

GASCH, R. ; KNOTHE, K.: *Strukturdynamik — Band 2: Kontinua und ihre Diskretisierung*. Berlin : Springer, 1989 (in German)

Giesing & al. 1970

GIESING, J. P. ; RODDEN, W. P. ; STAHL, B.: Sears function and lifting surface theory for harmonic gust fields. in: *Journal of Aircraft* 7 (1970), pp. 252–255

Gilbert 1963

GILBERT, E. G.: Controllability and observability in multivariable control systems. in: *Journal of the Society for Industrial and Applied Mathematics, Series A: Control* 2 (1963), pp. 128–151

Goßmann 1981

GOSSMANN, E.: *Kovarianzanalyse mechanischer Zufallsschwingungen bei Darstellung der mehrfachkorrelierten Erregung durch stochastische Differentialgleichungen*, Ruhr-Universität Bochum, Dissertation, 1981 (in German)

Graham & al. 2011

GRAHAM, J. M. R. ; LIMEBEER, D. J. N. ; ZHAO, X.: Aeroelastic control of long-span suspension bridges. in: *Journal of Applied Mechanics* 78 (2011), pp. 041018-1–041018-12

Hansen 1998

HANSEN, H. I.: *Active Vibration Control of Long Suspension Bridges*, Aalborg University, Dissertation, 1998

Hansen & Thoft-Christensen 2001

HANSEN, H. I. ; THOFT-CHRISTENSEN, P.: Active flap control of long suspension bridges. in: *Journal of Structural Control* 8 (2001), pp. 33–82

Hansen & al. 2000

HANSEN, H. I. ; THOFT-CHRISTENSEN, P. ; MENDES, P. A. ; BRANCO, F. A.: Wind-tunnel tests of a bridge model with active vibration control. in: *Structural Engineering International* 10 (2000), pp. 249–253

Hautus 1970

HAUTUS, M. L. J.: Stabilization, controllability and observability of linear autonomous systems. in: *Indagationes Mathematicae (Proceedings)* 73 (1970), pp. 448 - 455

Hübner 2003

HÜBNER, B. C.: *Simultane Analyse von Bauwerk-Wind-Wechselwirkungen*, Technische Universität Braunschweig, Dissertation, 2003 (in German)

Higashiyama & al. 1998

HIGASHIYAMA, H. ; YAMADA, M. ; KAZAO, Y. ; NAMIKI, M.: Characteristics of active vibration control system using gyro-stabilizer. in: *Engineering Structures* 20 (1998), pp. 176–183

Horri & al. 2010

HORRI, N. M. ; PALMER, P. ; GIFFEN, A.: *Chapter* 265: Active Attitude Control Mechanisms in: BLOCKLEY, R. (ed.) ; SHYY, W. (ed.): *Encyclopedia of Aerospace Engineering*. Vol. 5: Dynamics and Control. Wiley, 2010, pp. 3221–3231

Housner & al. 1997

HOUSNER, G. W. ; BERGMAN, L. A. ; CAUGHEY, T. K. ; CHASSIAKOS, A. G. ; CLAUS, R. O. ; MASRI, S. F. ; SKELTON, R. E. ; SOONG, T. T. ; SPENCER, B. F. ; YAO, J. T. P.: Structural control: Past, present and future. in: *Journal of Engineering Mechanics* 123 (1997), pp. 897–971

Huynh 2000

HUYNH, T.: *Suspension Bridge Aerodynamics and Active Vibration Control*, Aalborg University, Dissertation, 2000

Huynh & Thoft-Christensen 2001

HUYNH, T. ; THOFT-CHRISTENSEN, P.: Suspension bridge flutter for girders with separate control flaps. in: *Journal of Bridge Engineering* 6 (2001), pp. 168–175

ISO 31000 2009

Risk management - Principles and guidelines. 2009. – ISO 31000:2009-11

Jacot & Liska 1966

JACOT, A. D. ; LISKA, D. J.: Control moment gyros in attitude control. in: *Journal of Spacecraft and Rockets* 3 (1966), pp. 1313–1320

Jancauskas & Melbourne 1986

JANCAUSKAS, E. D. ; MELBOURNE, W. H.: The aerodynamic admittance of two-dimensional rectangular section cylinders in smooth flow. in: *Journal of Wind Engineering and Industrial Aerodynamics* 23 (1986), pp. 395–408

Jones 1938

JONES, R. T.: Operational treatment of the nonuniform-lift theory in airplane dynamics / NACA. 1938 (NACA-TN-667). – Technical Note

Jung & al. 2012

JUNG, K. ; KIM, H.-K. ; LEE, H. S.: Evaluation of impulse response functions for convolution integrals of aerodynamic forces by optimization with a penalty function. in: *Journal of Engineering Mechanics* 138 (2012), pp. 519–529

von Kármán & Sears 1938

VON KÁRMÁN, T. ; SEARS, W.: Airfoil theory for non-uniform motion. in: *Journal of the Aeronautical Sciences* 5 (1938), pp. 379–390

Karpel 1981

KARPEL, M.: Design for Active and Passive Flutter Suppression and Gust Alleviation / NASA. 1981 (NASA-CR-3482). – Contractor Report

Karpel & Strul 1996

KARPEL, M. ; STRUL, E.: Minimum-state unsteady aerodynamic approximations with flexible constraints. in: *Journal of Aircraft* 33 (1996), pp. 1190–1196

Karpel & Tiffany Hoadley 1991

KARPEL, M. ; TIFFANY HOADLEY, S.: Physically weighted approximations of unsteady aerodynamic forces using the minimum-state method / NASA. 1991 (NASA-TP-3025). – Technical Paper

Kautsky & al. 1985

KAUTSKY, J. ; NICHOLS, N. K. ; VAN DOOREN, P.: Robust pole assignment in linear state feedback. in: *International Journal of Control* 41 (1985), pp. 1129–1155

Kirch 2010

KIRCH, A.: Berechnung der Flatterwindgeschwindigkeit zweidimensionaler Modelle aeroelastischer Systeme — Untersuchungen zu Näherungsformeln / VDI. Düsseldorf, 2010 (Reihe 4, Nr. 216). – VDI Fortschritt-Bericht (in German)

Kirch & Peil 2009

KIRCH, A. ; PEIL, U.: Fundamental restrictions for the closed-loop control of wind-loaded, slender bridges. in: *Wind and Structures* 12 (2009), pp. 457–474

Kirch & Peil 2011

KIRCH, A. ; PEIL, U.: Transfer function approximation of motion-induced aerodynamic forces with rational functions. in: *Wind and Structures* 14 (2011), pp. 133–151.

Kirch & Peil 2012

KIRCH, A. ; PEIL, U.: Limitations for the control of wind-loaded slender bridges with movable flaps. in: *Wind and Structures* 15 (2012), pp. 441–462

Klein & al. 1972

KLEIN, R. E. ; CUSANO, C. ; STUKEL, J. J.: Investigation of a method to stabilize wind induced oscillations in large structures. in: *ASME Winter Annual Meeting*. New York, 1972, Paper 72-WA/Aut-11

Klöppel & Thiele 1967

KLÖPPEL, K. ; THIELE, F.: Modellversuche im Windkanal zur Bemessung von Brücken gegen die Gefahr winderregter Schwingungen. in: *Der Stahlbau* 36 (1967), pp. 353–365 (in German)

Kobayashi & Nagaoka 1992

KOBAYASHI, H. ; NAGAOKA, H.: Active control of flutter of a suspension bridge. in: *Journal of Wind Engineering and Industrial Aerodynamics* 41 (1992), pp. 143–151

Kobayashi & Nita 1996

KOBAYASHI, H. ; NITA, Y.: Active flutter control of suspension bridge by control surfaces. in: *Proceedings of the Third International Conference on Motion and Vibration Control*. Chiba, 1996, pp. 42–46

Kobayashi & al. 1998

KOBAYASHI, H. ; OGAWA, R. ; TANIGUCHI, S.: Active flutter control of a bridge deck by ailerons. in: *Proceedings of the Second World Conference on Structural Control*. Kyoto, 1998, pp. 1841–1848

Körlin & Starossek 2004

KÖRLIN, R. ; STAROSSEK, U.: Active mass dampers for flutter control of bridges. in: *Proceedings of the 8th International Conference on Flow-Induced Vibration*. Paris, 2004

Körlin & Starossek 2007

KÖRLIN, R. ; STAROSSEK, U.: Wind tunnel test of an active mass damper for bridge decks. in: *Journal of Wind Engineering and Industrial Aerodynamics* 95 (2007), pp. 267–277

Krätzig & Başar 1997

KRÄTZIG, W. B. ; BAŞAR, Y.: *Tragwerke 3 — Theorie und Anwendung der Methode der finiten Elemente*. Berlin : Springer, 1997 (in German)

Küssner 1936

KÜSSNER, H. G.: Zusammenfassender Bericht über den instationären Auftrieb von Flügeln. in: *Luftfahrtforschung* 13 (1936), pp. 410–424 (in German)

Küssner 1940

KÜSSNER, H. G.: Das zweidimensionale Problem der beliebig bewegten Tragfläche unter Berücksichtigung von Partialbewegungen der Flüssigkeit. in: *Luftfahrtforschung* 17 (1940), pp. 355–361 (in German)

Küssner & Göllnitz 1964

KÜSSNER, H. G. ; GÖLLNITZ, H.: Tabellen der aerodynamischen Derivativa des schwingenden Streckenprofils mit Knicken und Stufen / Deutsche Luft- und Raumfahrt. 1964 (DLR FB 64-05). – Forschungsbericht (in German)

Küssner & Schwarz 1940

KÜSSNER, H. G. ; SCHWARZ, L.: Der schwingende Flügel mit aerodynamisch ausgeglichenem Ruder. in: *Luftfahrtforschung* 17 (1940), pp. 337–354 (in German)

Kwon 1996

KWON, S.-D.: *Flutter Analysis and Active Aerodynamic Control of Long-Span Bridges under Wind Loads*, Seoul National University, Dissertation, 1996

Kwon & Chang 2000

KWON, S.-D. ; CHANG, S.-P.: Suppression of flutter and gust response of bridges using actively controlled edge surfaces. in: *Journal of Wind Engineering and Industrial Aerodynamics* 88 (2000), pp. 263–281

Larose & Mann 1998

LAROSE, G. L. ; MANN, J.: Gust loading on streamlined bridge decks. in: *Journal of Fluids and Structures* 12 (1998), pp. 511–536

Larsen 2000

LARSEN, A.: Aerodynamics of the Tacoma Narrows Bridge — 60 years later. in: *Structural Engineering International* 10 (2000), pp. 243–248

Larsen & al. 2000

LARSEN, A. ; ESDAHL, S. ; ANDERSEN, J. E. ; VEJRUM, T.: Storebælt Suspension Bridge — Vortex shedding excitation and mitigation by guide vanes. in: *Journal of Wind Engineering and Industrial Aerodynamics* 88 (2000), pp. 283–296

Larsen & Walther 1998

LARSEN, A. ; WALTHER, J. H.: Discrete vortex simulation of flow around five generic bridge deck sections. in: *Journal of Wind Engineering and Industrial Aerodynamics* 77–78 (1998), pp. 591–602

Larsen & Walther 2003

LARSEN, A. ; WALTHER, J. H.: Discrete vortex simulation of vortex excitation and mitigation in bridge engineering. in: *Vortex and Particle Methods — Proceedings of the 2nd MIT Conference on Computational Fluid and Solid Mechanics*. Cambridge, Massachusetts, 2003, pp. 1397–1400

Limebeer & al. 2011

LIMEBEER, D. J. N. ; GRAHAM, J. M. R. ; ZHAO, X.: Buffet suppression in long-span suspension bridges. in: *Annual Reviews in Control* 35 (2011), pp. 235–246

Luke & Dengler 1951

LUKE, Y. L. ; DENGLER, M. A.: Tables of the Theodorsen circulation function for generalized motion. in: *Journal of the Aeronautical Sciences* 18 (1951), pp. 478–483

Lunze 2004

LUNZE, J.: *Regelungstechnik 1: Systemtheoretische Grundlagen, Analyse und Entwurf einschleifiger Regelungen*. 4. Auflage. Berlin : Springer, 2004 (in German)

Lunze 2005

LUNZE, J.: *Regelungstechnik 2: Mehrgrößensysteme, Digitale Regelung*. 3. Auflage. Berlin : Springer, 2005 (in German)

Magnus 1971

MAGNUS, K.: *Kreisel — Theorie und Anwendungen*. Berlin : Springer, 1971 (in German)

Mannini & al. 2010

MANNINI, C. ; ŠODA, A. ; VOSS, R. ; SCHEWE, G.: Unsteady RANS simulations of flow around a bridge section. in: *Journal of Wind Engineering and Industrial Aerodynamics* 98 (2010), pp. 742–753

MATLAB 2007

MATLAB, The Language of Technical Computing. Version 7.5.0.342 (R2007b). The MathWorks, Inc., 15. August 2007. – Operating system Windows XP

Matsuda & al. 1999

MATSUDA, K. ; HIKAMI, Y. ; FUJIWARA, T. ; MORIYAMA, A.: Aerodynamic admittance and the strip theory for horizontal buffeting forces on a bridge deck. in: *Journal of Wind Engineering and Industrial Aerodynamics* 83 (1999), pp. 337–346

Miyata & al. 1994

MIYATA, T. ; YAMADA, H. ; DUNG, N. N. ; KAZAMA, K.: On active control and structural response control of the coupled flutter problem for long span bridges. in: *Proceedings of the First World Conference on Structural Control*. Los Angeles, 1994, pp. WA4-40 – WA4-49

Morino & al. 1995

MORINO, L. ; MASTRODDI, F. ; DE TROIA, R. ; GHIRINGHELLI, G. L. ; MANTEGAZZA, P.: Matrix fraction approach for finite-state aerodynamic modeling. in: *AIAA Journal* 4 (1995), pp. 703–711

Murata & Ito 1971

MURATA, M. ; ITO, M.: Suppression of wind-induced vibration of a suspension bridge by means of a gyroscope. in: *Proceedings of the Third International Conference on Wind Effects on Buildings and Structures*. Tokyo, 1971, pp. 1057–1066

Muravskii 2007

MURAVSKII, G. B.: Linear models with nearly frequency independent complex stiffness leading to causal behaviour in time domain. in: *Earthquake Engineering and Structural Dynamics* 36 (2007), pp. 13–33

Nelder & Mead 1965

NELDER, J. A. ; MEAD, R.: A simplex method for function minimization. in: *The Computer Journal* 7 (1965), pp. 308–313

Nissen & al. 2004

NISSEN, H. D. ; SØRENSEN, P. H. ; JANNERUP, O.: Active aerodynamic stabilisation of long suspension bridges. in: *Journal of Wind Engineering and Industrial Aerodynamics* 92 (2004), pp. 829–847

Nissim 1971

NISSIM, E: Flutter suppression using active controls based on the concept of aerodynamic energy / NASA. 1971 (NASA-TN-D-6199). – Technical Note

Okada & al. 2003

OKADA, T. ; HONKE, K. ; SUGII, K. ; SHIMADA, S.: Aerodynamic stability improvements in super-long-span suspension bridge through the use of gyroscopic dampers. in: *Kobe Steel Engineering Reports* 53 (2003), pp. 59–63 (in Japanese)

Okada & al. 2001

OKADA, T. ; HONKE, K. ; SUGII, K. ; SHIMADA, S. ; KOBAYASHI, H.: Suppression of coupled flutter of a bridge deck by gyroscopic damper. in: *IABSE Conference on Cable-Supported Bridges*. Seoul, 2001, Paper 130

Omenzetter & al. 2000a

OMENZETTER, P. ; WILDE, K. ; FUJINO, Y.: Suppression of wind-induced instabilities of a long span bridge by a passive deck-flaps control system; Part I: Formulation. in: *Journal of Wind Engineering and Industrial Aerodynamics* 87 (2000), pp. 61–79

Omenzetter & al. 2000b

OMENZETTER, P. ; WILDE, K. ; FUJINO, Y.: Suppression of wind-induced instabilities of a long span bridge by a passive deck-flaps control system; Part II: Numerical simulations. in: *Journal of Wind Engineering and Industrial Aerodynamics* 87 (2000), pp. 81–91

Omenzetter & al. 2002a

OMENZETTER, P. ; WILDE, K. ; FUJINO, Y.: Study of passive deck-flaps flutter control system on full bridge model. I: Theory. in: *Journal of Engineering Mechanics* 128 (2002), pp. 264–279

Omenzetter & al. 2002b

OMENZETTER, P. ; WILDE, K. ; FUJINO, Y.: Study of passive deck-flaps flutter control system on full bridge model. II: Results. in: *Journal of Engineering Mechanics* 128 (2002), pp. 280–286

Ostenfeld & al. 1970

OSTENFELD, C. ; HAAS, G. ; FRANDSEN, A. G.: Motorway bridge across Lillebælt — Model tests for the superstructure of the suspension bridge. in: *Bygningsstatiske Meddelelser* 41 (1970), pp. 99-112

Ostenfeld & Larsen 1992

OSTENFELD, K. H. ; LARSEN, A.: Bridge engineering and aerodynamics. in: *Aerodynamics of Large Bridges — Proceedings of the First International Symposium on Aerodynamics of Large Bridges*. Copenhagen, 1992, pp. 3–22

Ostenfeld & Larsen 1997

OSTENFELD, K. H. ; LARSEN, A.: Elements of active flutter control of bridges. in: *IABSE Conference on New Technologies in Structural Engineering*. Lisbon, 1997, pp. 683–694

Petersen 1996

PETERSEN, C.: *Dynamik der Baukonstruktionen*. Braunschweig : Vieweg, 1996 (in German)

Peterson & Crawley 1988

PETERSON, L. D. ; CRAWLEY, E. F.: Improved exponential time series approximation of unsteady aerodynamic operators. in: *Journal of Aircraft* 25 (1988), pp. 121–127

Phan & Kobayashi 2011

PHAN, D.-H. ; KOBAYASHI, H.: An experimental study of flutter and buffeting control of suspension bridge by mechanically driven flaps. in: *Wind and Structures* 14 (2011), pp. 153–165

Piésold & Corney 1999

PIÉSOLD, D. D. A. ; CORNEY, J. M.: Active aerofoil stabilization of cable-supported bridge decks. in: *Proceedings of the Institution of Civil Engineers — Structures and Buildings* 134 (1999), pp. 67–76

Pliefke & al. 2007

PLIEFKE, T. ; SPERBECK, S. T. ; URBAN, M. ; PEIL, U. ; BUDELMANN, H.: A standardized methodology for managing disaster risk — an attempt to remove ambiguity. in: *Proceedings of the 5th International Probabilistic Workshop*. Ghent, 2007, pp. 283–294

Preidikman & Mook 1997

PREIDIKMAN, S. ; MOOK, D. T.: A new method for actively suppressing flutter of suspension bridges. in: *Journal of Wind Engineering and Industrial Aerodynamics* 69–71 (1997), pp. 955–974

Preidikman & Mook 1998

PREIDIKMAN, S. ; MOOK, D. T.: On the development of a passive-damping system for wind-excited oscillations of long-span bridges. in: *Journal of Wind Engineering and Industrial Aerodynamics* 77–78 (1998), pp. 443–456

Preumont 2011

PREUMONT, A.: *Vibration Control of Active Structures*. Berlin : Springer, 2011

Preumont & Seto 2008

PREUMONT, A. ; SETO, K.: *Active Control of Structures*. Chichester / UK : Wiley, 2008

Remmert & Schumacher 2002

REMMERT, R ; SCHUMACHER, G.: *Funktionentheorie 1*. 5. Auflage. Springer, 2002 (in German)

Roger 1977

ROGER, K.: Airplane math modelling methods for active control design. in: *Structural Aspects of Active Controls — AGARD Conference Proceedings 228*. Lisbon / Portugal, 1977, pp. 4-1 – 4-11

Sakata 1971

SAKATA, H.: A study of flutter of suspension bridge with shallow box-type suspended structure. in: *Wind Effects on Buildings and Structures*. Tokyo, 1971, pp. 953–964

Sarkar & al. 1994

SARKAR, P. P. ; JONES, N. P. ; SCANLAN, R. H.: Identification of aeroelastic parameters of flexible bridges. in: *Journal of Engineering Mechanics* 120 (1994), pp. 1718–1742

Scanlan 1978a

SCANLAN, R. H.: The action of flexible bridges under wind, I: Flutter theory. in: *Journal of Sound and Vibration* 60 (1978), pp. 187–199

Scanlan 1978b

SCANLAN, R. H.: The action of flexible bridges under wind, II: Buffeting theory. in: *Journal of Sound and Vibration* 60 (1978), pp. 201–211

Schewe 2001

SCHEWE, G.: Reynolds-number effects in flow around more-or-less bluff bodies. in: *Journal of Wind Engineering and Industrial Aerodynamics* 89 (2001), pp. 1267–1289

Schlitt 2005

SCHLITT, H.: *Systemtheorie für stochastische Prozesse*. Berlin : Springer, 2005 (in German)

Schwarz 1940

SCHWARZ, L.: Berechnung der Funktionen $U_1(s)$ und $U_2(s)$ für größere Werte von s. in: *Luftfahrtforschung* 17 (1940), pp. 362–369 (in German)

Scott 2001

SCOTT, R.: *In the Wake of Tacoma*. Reston / Virginia : ASCE Press, 2001

Sears 1940

SEARS, W. R.: Operational methods in the theory of airfoils in non-uniform motion. in: *Journal of the Franklin Institute* 230 (1940), pp. 95–111

Sears 1941

SEARS, W. R.: Some aspects of non-stationary airfoil theory and its practical application. in: *Journal of the Aeronautical Sciences* 8 (1941), pp. 104–108

Sevart 1975

SEVART, F. D.: Development of Active Flutter Suppression Wind Tunnel Testing Technology / Air Force Flight Dynamics Laboratory. 1975 (AFFDL TR-74-126). – Technical Report

Simiu & Scanlan 1996

SIMIU, E. ; SCANLAN, R. H.: *Wind Effects on Structures: Fundamentals and Applications to Design*. 3rd Edition. New York : Wiley, 1996

Stark 1984

STARK, V. J. E.: General equations of motion for an elastic wing and method of solution. in: *AIAA Journal* 22 (1984), pp. 1146–1153

Starossek 1992

STAROSSEK, U.: *Brückendynamik – Winderregte Schwingungen von Seilbrücken*. Braunschweig : Vieweg, 1992 (in German)

Starossek & Aslan 2007

STAROSSEK, U. ; ASLAN, H.: A novel aero-elastic damper for long-span bridges. in: *Proceedings of the ICWE 12 — 12th International Conference on Wind Engineering*. Cairns, 2007, pp. 2167–2174

Sternberg 1991

STERNBERG, A.: Stability investigation of long-span bridges using indicial functions with oscillatory terms. in: *Probabilistic Engineering Mechanics* 6 (1991), pp. 164–174

Theodorsen 1934

THEODORSEN, T.: General Theory of Aerodynamic Instability and the Mechanism of Flutter / NACA. 1934 (NACA-TR-496). – Technical Report

Theodorsen & Garrick 1938

THEODORSEN, T. ; GARRICK, I. E.: Mechanism of Flutter: A Theoretical and Experimental Investigation of the Flutter Problem / NACA. 1938 (NACA-TR-685). – Technical Report

Theodorsen & Garrick 1941

THEODORSEN, T. ; GARRICK, I. E.: Nonstationary Flow about a Wing-Aileron-Tab Combination Including Aerodynamic Balance / NACA. 1941 (NACA-TR-736). – Technical Report

Thiesemann 2008

THIESEMANN, L.: *Zur Ermittlung von Flatterderivativa mittels Versuchen und numerischer Strömungsmechanik*, Technische Universität Hamburg-Harburg, Dissertation, 2008 (in German)

Tiffany Hoadley & Adams Jr. 1988

TIFFANY HOADLEY, S. ; ADAMS JR., W. M.: Nonlinear programming extensions to rational function approximation methods for unsteady aerodynamic forces / NASA. 1988 (NASA-TP-2776). – Technical Paper

Ukeguchi & al. 1966

UKEGUCHI, N. ; SAKATA, H. ; NISHITANI, H.: An investigation of aeroelastic instability of suspension bridges. in: *Symposium International sur les Ponts Suspendus*. Lisbonne, 1966, pp. 273–284

Unbehauen 2007

UNBEHAUEN, R.: *Regelungstechnik II*. 9. Auflage. Wiesbaden : Vieweg, 2007 (in German)

Van der Hoven 1957

VAN DER HOVEN, I. : Power spectrum of horizontal wind speed in the frequency range from 0.0007 to 900 cycles per hour. in: *Journal of Meteorology* 14 (1957), pp. 160–164

Vepa 1977

VEPA, R.: Finite State Modeling of Aeroelastic Systems / NASA. 1977 (NASA-CR-2779). – Contractor Report

Wagner 1925

WAGNER, H.: Über die Entstehung des dynamischen Auftriebs von Tragflügeln. in: *Zeitschrift fur Angewandte Mathematik und Mechanik,* 5 (1925), pp. 17–35 (in German)

Walther & Larsen 1997

WALTHER, J. H. ; LARSEN, A.: Two dimensional discrete vortex method for application to bluff body aerodynamics. in: *Journal of Wind Engineering and Industrial Aerodynamics* 67 & 68 (1997), pp. 183–193

Wilde & Fujino 1998

WILDE, K. ; FUJINO, Y.: Aerodynamic control of bridge deck flutter by active surfaces. in: *Journal of Engineering Mechanics* 124 (1998), pp. 718–727

Wilde & al. 1999

WILDE, K. ; FUJINO, Y. ; KAWAKAMI, T.: Analytical and experimental study on passive aerodynamic control of flutter of a bridge deck. in: *Journal of Wind Engineering and Industrial Aerodynamics* 80 (1999), pp. 105–119

Wilde & al. 1996

WILDE, K. ; FUJINO, Y. ; MASUKAWA, J.: Time domain modelling of bridge deck flutter. in: *Structural Engineering, Earthquake Engineering* 13 (1996), pp. 93–104

Wilde & al. 2001

WILDE, K. ; OMENZETTER, P. ; FUJINO, Y.: Suppression of bridge flutter by active deck-flaps control system. in: *Journal of Engineering Mechanics* 127 (2001), pp. 80–89

Xie & Xiang 1985

XIE, J.-M. ; XIANG, H.-F.: State-space method for 3-D flutter analysis of bridge structures. in: *Proceedings of the First Asia-Pacific Symposium on Wind Engineering*. Roorkee, India, 1985, pp. 269–276

Yamada & al. 1997

YAMADA, M. ; HIGASHIYAMA, H. ; NAMIKI, M. ; KAZAO, Y.: Active vibration control system using a gyro-stabilizer. in: *Control Engineering Practice* 5 (1997), pp. 1217–1222

Yang & Giannopolous 1979

YANG, J. N. ; GIANNOPOLOUS, F.: Active control and stability of cable-stayed bridge. in: *Journal of the Engineering Mechanics Division (ASCE)* 105 (1979), pp. 677–694

Yoshimura & Nakamura 1979

YOSHIMURA, T. ; NAKAMURA, Y.: On the indicial aerodynamic moment responses of bridge deck sections. in: *Proceedings of the ICWE 11 — 5th International Conference on Wind Engineering*. Fort Collins, 1979, pp. 877–885

ZAERO 2004

ZAERO, Engineers Toolkit for Aeroelastic Solutions. Version 7.2. ZONA Technology, Inc., Dezember 2004. – Theoretical Manual

Zhou & al. 1996

ZHOU, K. ; DOYLE, J. C. ; GLOVER, K.: *Robust and Optimal Control*. Upper Saddle River, New Jersey : Prentice Hall, 1996

Zurmühl & Falk 1984

ZURMÜHL, R. ; FALK, S.: *Matrizen und ihre Anwendung — Teil 1: Grundlagen*. 5. Auflage. Berlin : Springer, 1984 (in German)